2020

A Spectropolarimetric Study of Southern WR + O Binaries

Andrew G. Fullard

A Spectropolarimetric Study of Southern WR + O Binaries

A Dissertation
Presented to
the Faculty of the College of Natural Sciences and Mathematics
University of Denver

In Partial Fulfillment
of the Requirements for the Degree
Doctor of Philosophy

by
Andrew G. Fullard
August 2020
Advisor: Dr. Jennifer L. Hoffman

Author: Andrew G. Fullard
Title: A Spectropolarimetric Study of Southern WR + O Binaries
Advisor: Dr. Jennifer L. Hoffman
Degree Date: August 2020

Abstract

The classical Wolf-Rayet (WR) state is the evolved stage of a massive star, post main-sequence. They are characterized by their strong emission line spectra and stellar winds that are often more than 10 times denser than that of their progenitor O-type stars, which have mass loss rates of $10^{-6}\ M_{\odot}\ \mathrm{yr}^{-1}$. The evolution of WR stars and their connection to specific types of supernovae (SNe) is an open question. Current theory suggests that rapidly rotating massive stars may be the progenitors of SNe that produce long-duration gamma-ray bursts. The interaction between WR stars and their companion in binary systems may provide sufficient angular momentum to create such progenitors.

Angular momentum (and therefore rotation) tends to create aspherical structures in astronomical objects (e.g. Be star disks, T Tauri jets caused by decretion and accretion respectively) that can be investigated using linear polarimetry, even for unresolved sources. I have investigated WR stars in detail to determine the geometric structure of their winds using spectropolarimetry. I began by using archival broadband polarimetric data to search for intrinsic polarization in a sample of more than 40 single and binary WR stars, finding that 12 of the stars exhibit intrinsic continuum polarization or line polarization effects that indicate aspherical or non-uniform winds.

In the later stages of the project, I used the Southern African Large Telescope (SALT) to obtain time-dependent spectropolarimetric observations of 10 of the stars in that sample, along with 8 additional targets. These targets are all WR + O binary systems, whose complex winds are best observed over time with spectropolarimetry to determine the geometry of the wind across different emission lines and the continuum. I investigated two stars in the sample, WR 42 and WR 79, and found that they exhibit classic continuum polarization

signatures of binary orbits, as well as intriguing orbital line polarization effects. I compared the line polarization behaviour with the predictions of existing spectrally-derived models of the systems to obtain new information about the structure of the colliding wind regions.

Finally, I have modified an existing 3-D Monte Carlo radiative transfer code to include an additional source of photons that represents a companion star. This allows the code to treat the asymmetric structures seen in massive binary systems. I used this updated code to simulate the well-observed WR + O system V444 Cygni. I created a set of emission regions to simulate line emission from both the WR wind and wind-wind collision regions, finding that the wind-wind collision creates very strong polarimetric signals that appear similar to those in other systems in my SALT sample. The results shed new light on the relationships among WR + O binaries and yield clues to their subsequent evolution and potential roles as SN and GRB progenitors.

Acknowledgements

I am eternally grateful to my advisor Dr. Jennifer Hoffman for her unerring support, advice and knowledge during my doctoral studies. My immediate research group and friends, Dr. Manisha Shrestha, Dr. Leah Huk, Dr. Jamie Lomax, and Rachel Johnson are all excellent scientists who have improved this work through their advice and assistance. I thank my friends and colleagues Dr. Rachel Bennet and Tristan Wolfe for making graduate school a much better experience. I thank all of the DU Physics and Astronomy Department graduate students, professors and staff for making the department a place I could complete this work. I especially thank the tireless administrators Faun Lee and Barbara Stephen who helped me through so many bureaucratic hoops. Outside of DU, I must thank Dr. Nicole St-Louis and Dr. Tony Moffat for their brilliant advice, imparting their extensive scientific and professional experience to me. Dr. Kenneth Nordsieck has made much of this dissertation possible through his support and advice regarding SALT observations and polarimetry. I thank my family for supporting my career from the very beginning. They have done so much to help me reach where I am today. Finally, I thank my partner Rissa, who has been there for me through all the ups and downs of this PhD. I could not have asked for a better companion through such a difficult time.

Table of Contents

List of Tables

List of Figures

Chapter 1

Introduction

1.1 Project summary

The massive, mass-losing, evolved stars known as Wolf-Rayet (WR) stars represent important links between massive stars and their late-time evolution into supernovae. They produce metals to enrich the interstellar medium from both their mass-loss and supernovae, providing the building blocks of life. The goal of this project is to understand the stellar wind geometries of WR stars to constrain their later evolution. In this dissertation work, I investigate the stellar wind geometries of WR stars, both single and binary systems, using a range of techniques centered around multiwavelength polarimetry. I include both observations and models in my work. Observations are important to sample the reality of stellar populations, and I acquired new spectropolarimetric data with the aim of gaining the first multi-object spectropolarimetric sample of known Galactic Wolf-Rayet binaries. My models are necessary to interpret the complex nature of spectropolarimetric data. Modern polarimetric models have not been used to interpret electron scattering in WR binary systems, or they have not been sophisticated enough to treat the complex structures and illumination sources in these systems.

1.2 Evolution of massive stars

The evolution of stars is an extensive topic that could warrant multiple review articles. I present a summary of stellar evolution that is relevant to the objects discussed in this dissertation, namely high-mass stars in the Milky Way, those with an initial mass greater than 8 $M_\odot$ and a metallicity comparable to that of the Sun. The focus of this section will be single stars. The impact of companion stars on stellar evolution will be covered in Section 1.4.

High-mass stars in the Milky Way necessarily form in young star formation regions due to their short prestellar lifetimes of less than $1 - 7{\times}10^4$ yr (Tigé et al. 2017). There is no clear evolutionary sequence for high-mass star formation. The latest theories suggest that "massive dense clumps", which are mass reservoirs of 100s or 1000s of solar masses, collapse into multiple hydrogen-fusing cores at the same time as the stellar envelope of hydrogen gas coalesces. Once the stellar UV field ionizes the envelope, accretion ceases (Motte, Bontemps, and Louvet 2018).

Once formed, massive stars join the Main Sequence (MS), a period of stable hydrogen fusion delineated by the continuous band of stars on a color-luminosity (Hertzsprung-Russell, or HR) diagram (Fig. 1.1). These stars are all fusing hydrogen into helium in their cores (the core boundary being defined as the radius where fusion ends). In high-mass stars, the dominant fusion process is the CNO cycle, where carbon, nitrogen and oxygen are used as catalytic intermediaries to form helium nuclei via collisions with hydrogen nuclei (Böhm-Vitense 1992). Their high mass requires high energies to prevent core collapse, so the high-mass main sequence stars are both hot ($> 10^5$ K) and bright ($> 10^4$ $L_\odot$) (Langer 2012). Even on the MS, very massive stars (> 28 $M_\odot$) can exhibit significant mass loss as their high luminosities provide sufficient radiation pressure to expel more than 10% of their mass (Brott et al. 2011).

The accumulation of helium in the core of massive stars increases as the CNO cycle continues to fuse hydrogen, until the triple-α process can begin at core temperatures $> 10^8$

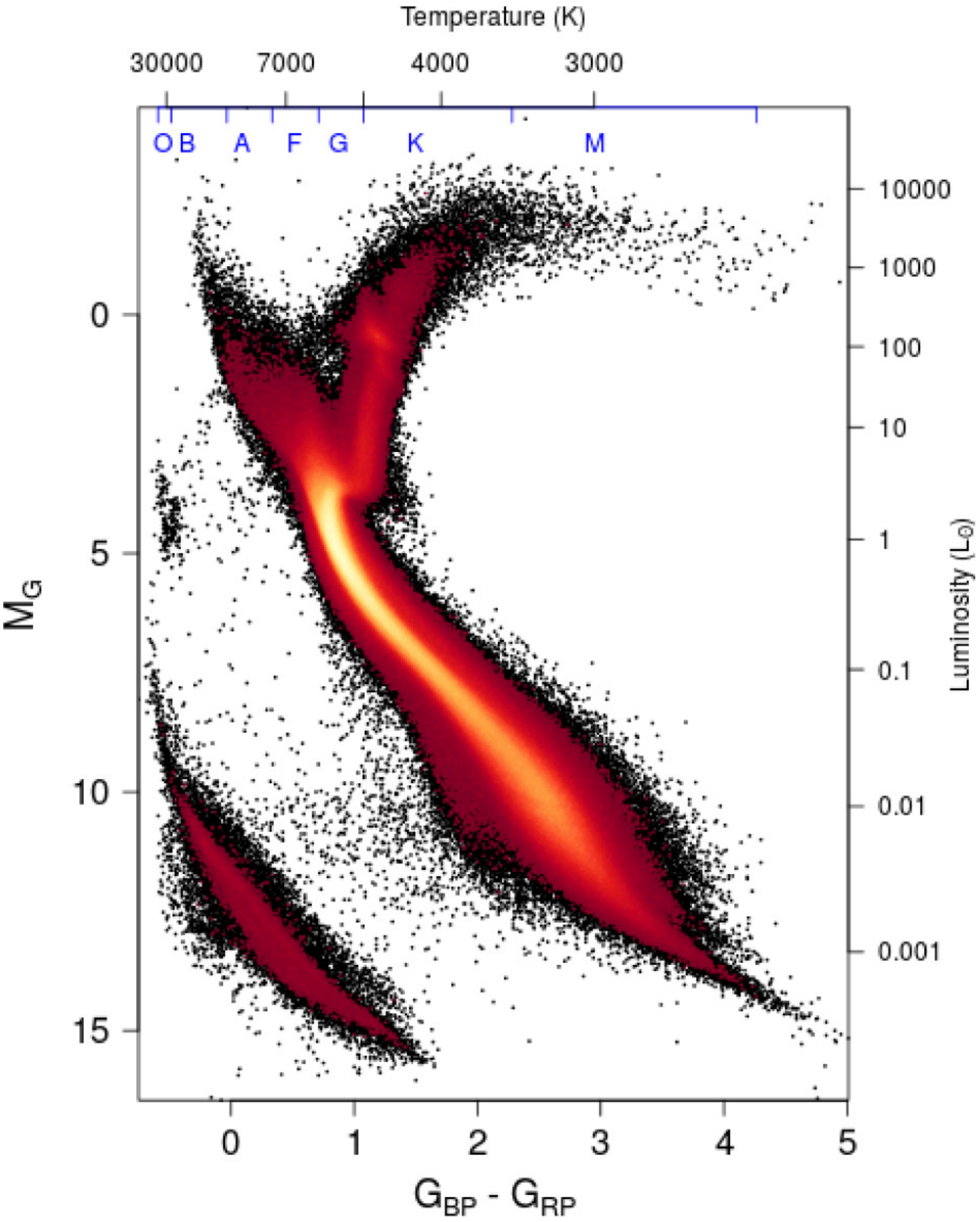

Figure 1.1: Hertzsprung-Russell diagram from Fig. 5 of Gaia Collaboration et al. (2018). M_G is the measured *Gaia* space telescope magnitude, while G_{BP} and G_{RP} are the blue and red colors respectively. This diagram contains 4,276,690 stars. The color scale represents the square root of the density of the stars. The main sequence is shown by the densest region of the diagram. The temperature and luminosity scales are approximate.

K (Hoyle 1946). In this process, three helium nuclei fuse into carbon. For stars in the $10-30\ M_\odot$ mass range, this process leads to expansion of the stellar envelope (and associated cooling) as hydrogen fusion resumes in layers around the helium-fusing core (Ekström et al. 2012). These stars will follow horizontal supergiant paths in the HR diagram, i.e. paths of constant luminosity in Fig. 1.1. Stars with masses greater than $30\ M_\odot$ cannot cool sufficiently to become red supergiants, instead remaining in the blue part of the HR diagram.

For stars up to $\sim 17\ M_\odot$, post-MS evolution abruptly ends in a Type IIP or IIL supernova (SN), defined by their plateaued and linear light curves respectively, and lacking hydrogen in their spectra (hence Type II; Smartt 2009). More massive stars are thought to follow paths that include periods of greatly enhanced mass-loss (Langer 2012). This evolutionary stage is discussed in detail in the next section.

1.3 Wolf-Rayet stars

Wolf-Rayet (WR) stars are a class of evolved, massive star that exhibit strong mass loss (Crowther 2007). The mass loss occurs due to radiation-driven, optically thick winds. Their progenitors are typically massive O stars (> 18 M$_\odot$). These massive stars evolve along the MS (and sometimes into a red or blue supergiant stage) before entering the WR stage, in which they spend $\sim 10\%$ of their ~ 5 Myr lifetime (Meynet and Maeder 2005).

WR stars were initially detected by Wolf and Rayet (1867). The class is categorized observationally by the stars' emission-line spectra, based on both the line strengths and ratios of the line strengths (Smith 1968). There are two major types: WC stars have strong He, C and O emission lines, while WN stars have strong He and N emission lines. Within these broad types, WC and WN stars are split into early (2–5) and late (6–11) subtypes, where early-type stars are hotter and late-type are cooler. The classification of these subtypes is based on the relative strengths of N III λ4634, 4642, N IV λ4508 and N V λ4603, 4619 for WN stars. WC stars are classified by the relative strengths of O V λ5592, C III λ5696 and C IV λ5608, 5612. Example spectra for these WR types are shown in Figure 1.2. These strong emission lines are the result of rotational mixing, hydrogen stripping by a close companion star through Roche lobe overflow (RLOF), or by the strong stellar winds of the O-star stage removing the outer hydrogen envelope (or a combination of these factors). These processes reveals the products of the CNO cycle from the previous MS stage (WN type), and with further evolution products of the triple-α process become visible (WC type. Lamers et al. 1991). These products are expelled from the star in their stellar winds, where they become ionized in the high temperatures ($> 10^4$ K, Gräfener, Koesterke, and Hamann 2002). Rare early-type WC stars that have strong oxygen lines after even more mass loss occurs are placed into the WO classification (Crowther, De Marco, and Barlow 1998). The cause of WO rarity is their proximity to core collapse, which is expected to occur within a few thousand years of reaching the WO stage (Tramper et al. 2015). Additional subtypes include "WNH", luminous WN stars that show both WN emission lines and hydrogen in their spectra. Stars of this type are thought to still be in the hydrogen fusing phase (specifically near the end of the phase), and the class was proposed to make it clear that such stars could not be Type Ia SN progenitors (Smith and Conti 2008).

The evolution of single WR stars has been thoroughly investigated in the last decade. The Potsdam Wolf-Rayet models (PoWR; Gräfener, Koesterke, and Hamann 2002) have been used to predict a set of evolutionary pathways for different initial masses at Solar metallicity ($Z_{\odot}$), shown in Table 1.1 (Sander et al. 2019). Other evolutionary models by Georgy et al. (2012) have been used to produce paths on the H-R diagram, shown in Figure 1.3. In this figure, the left panel shows single-star stellar evolution models without rotation. The right panel shows the same models including the effects of rotation. In general, an O-type star ($< 35\ M_{\odot}$, black paths in Fig. 1.3) evolves into a red supergiant (RSG, red paths in Fig. 1.3) and then may have a luminous blue variable (LBV[1]) phase before becoming a classical WN star (green and purple paths in Fig. 1.3). O stars with

---

[1] LBVs are named for their periods of photometric variability predicted to coincide with increased mass-loss (Smith 2017).

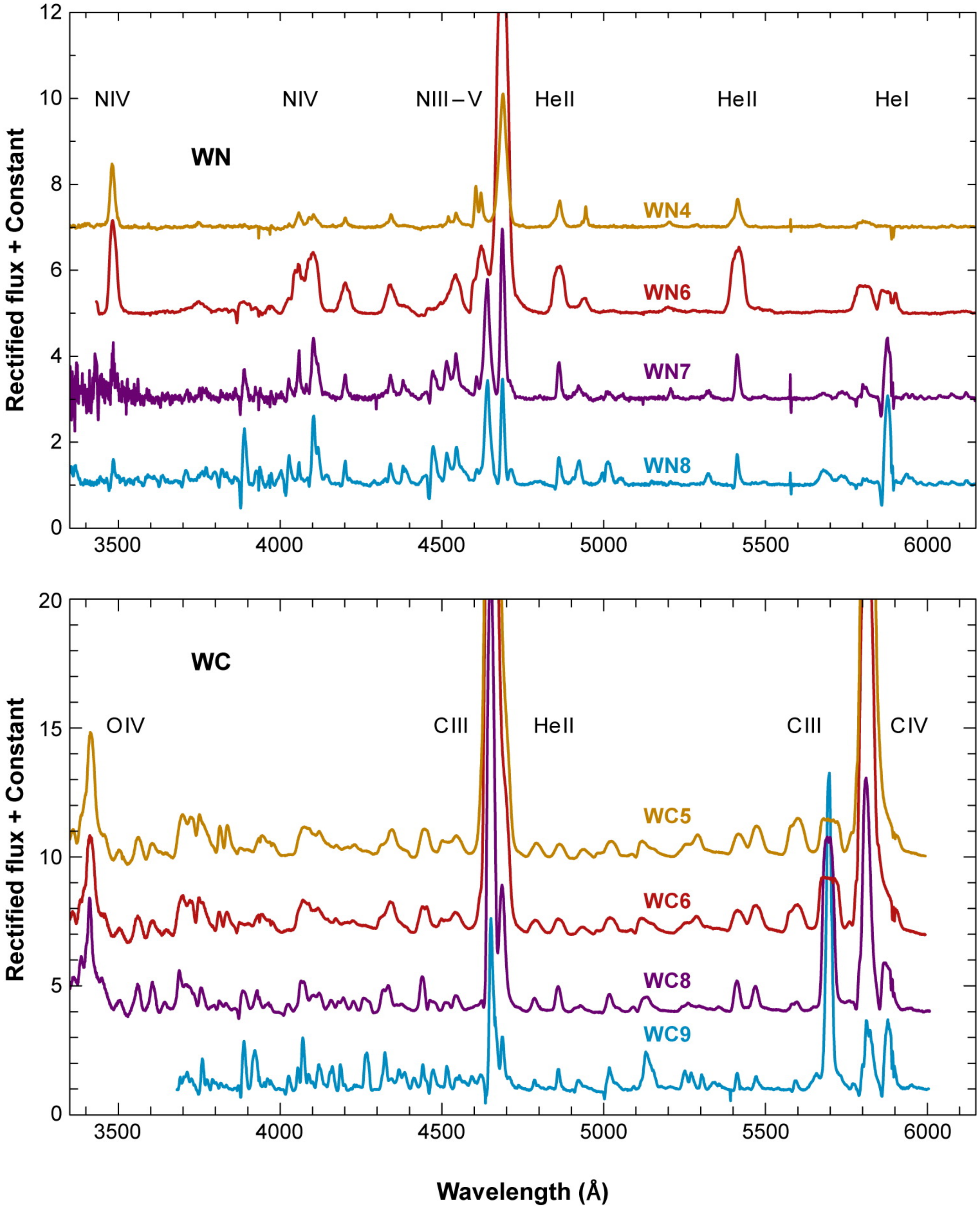

Figure 1.2: Typical optical spectra of Wolf-Rayet stars, adapted from Crowther (2007). WR types are labeled along with major emission lines.

Table 1.1: Single-star evolutionary paths reproduced from Sander et al. (2019). Mass ranges are rough estimates based on empirical luminosities and current evolutionary calculations. CC are core collapse events that may or may not be luminous.

M_i ($M_\odot$)	Evolutionary path
8–18	OB $\rightarrow$ RSG [$\rightarrow$ BSG] $\rightarrow$ SN II
18–35	O $\rightarrow$ RSG $\rightarrow$ WNL [$\leftrightarrow$ LBV] $\rightarrow$ WN $\rightarrow$ WC $\rightarrow$ WO $\rightarrow$ CC
35–80	O $\rightarrow$ Of/WNH $\leftrightarrow$ LBV $\rightarrow$ WN $\rightarrow$ WC $\rightarrow$ WO $\rightarrow$ CC
> 80	O $\rightarrow$ Of/WNH $\leftrightarrow$ LBV [$\rightarrow$ WNH] $\rightarrow$ SN IIn

MS masses greater than 35 $M_\odot$ skip the RSG stage. In some cases the star may oscillate between LBV and WNH types. Following the WN stage, the stars progress through WC and WO subtypes for $M_i > 18$ $M_\odot$ (blue paths in Fig. 1.3). WO stars in the $18 - 80$ $M_\odot$ initial mass range undergo core collapse (CC), as gravity overcomes the radiation pressure provided by nuclear fusion, and form a compact object such as a black hole or neutron star. Usually the CC of a WO star results in a Type Ib or Ic SN[2], because there is no hydrogen left in the star. This means we can conclude that Type Ic SNe originate from objects that have had both hydrogen and helium exhaustion occur (Smith 2014). However there is evidence, both theoretical and observational, that a fraction of massive stars may fail to produce SNe, instead collapsing directly into a compact object (e.g. Adams et al. 2017; Smartt 2015; Sukhbold and Woosley 2016).

Rotation has a strong effect not only on a star's evolution to the WR stage (Figure 1.3), but also on the star's subsequent evolution beyond this transition (Section 1.4). Because of this, investigating the rotational properties of WR stars has been of great interest for many years (e.g. Harries, Hillier, and Howarth 1998; Stevance et al. 2018; Vink and Harries 2017a). The effects of rotation can be seen in Fig. 1.3. The right panel of Fig. 1.3 shows that rotation allows lower-mass O stars to evolve to the WR stage. Rotation decreases the mass threshold required for the WR stage to be reached by mixing CNO cycle products into the stellar envelope and increasing the mass of the convective core (Maeder and Meynet 2012;

---

[2] SN Type Ib and Ic are distinguished by the presence (Ib) or absence (Ic) of strong helium emission lines in their spectra (Filippenko 1997).

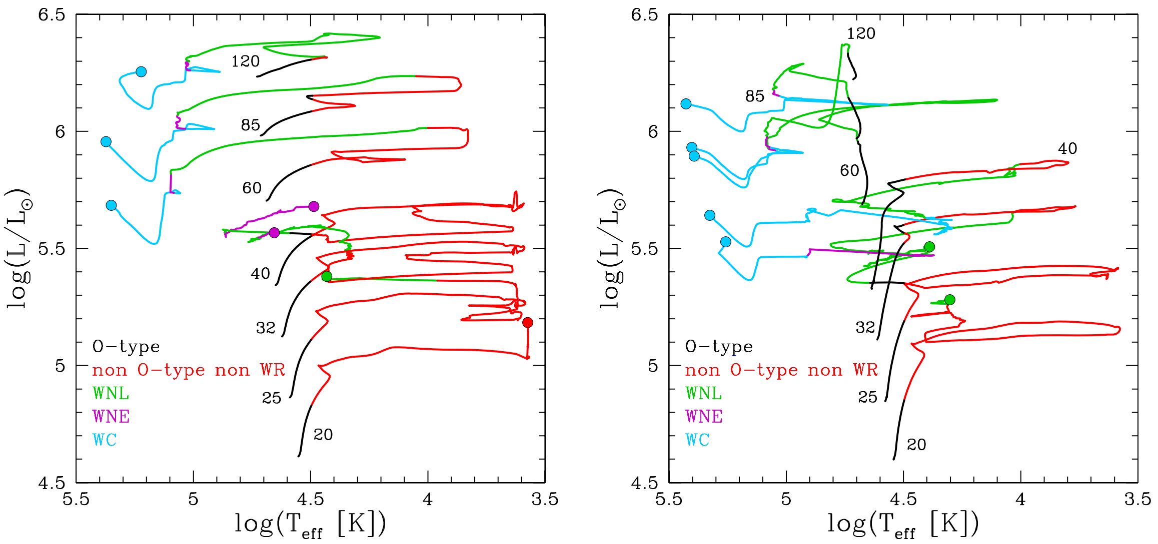

Figure 1.3: Hertzsprung-Russell diagram of stellar models from Georgy et al. (2012). Left panel shows single star models without rotation. Right panel shows models with initial main sequence rotation velocities of 40% of the breakup velocity. Numbers show initial mass in $M_\odot$. Evolutionary stage is indicated by color (see plot legend). Track endpoints are indicated by circles.

Meynet and Maeder 2017). This enhances the “surface” abundances of heavy elements, which are then expelled and ionized in the stellar wind.

The winds of WR stars are radiatively driven to high velocities ($\sim$2000 km s^{-1} Crowther 2007). Historically, CAK theory (see Appendix A.3 for a brief review) was used to determine velocity structure and mass-loss rates. However, this theory completely breaks down in the dense winds of WR stars where multiple scattering is important (Crowther 2007; Sander, Vink, and Hamann 2020). Instead, hydrodynamic modeling is required to derive correct $\dot{M}$ and v_∞ values. Sander, Vink, and Hamann (2020) has shown that $\dot{M}$ is strongly dependent on the Eddington factor, Γ, as well as the metallicity of the WR star. The quantity Γ_e is called the Eddington factor for electron scattering. It is defined as the ratio of radiative acceleration (provided by Thomson scattering) to surface gravity, and is written in Equation 1.1, where q_e is the number of electrons per atomic mass (Crowther 2007). WR stars are both hot (thus have high q_e) and have lost most of their mass via stellar winds or stripping (thus have high M/L). This pushes them towards the $\Gamma_e = 1$ limit. As a result, radiative pressure provides sufficient acceleration to create a stellar wind with high velocity.

$$\Gamma_e = 10^{-4.5} q_e \frac{L/L_\odot}{M/M_\odot} \tag{1.1}$$

Grassitelli et al. (2018) has shown that proximity to the Eddington limit defines the transition between the subsonic optically thick wind and the supersonic wind regime.

The broad emission-line spectra of WR stars originate[3] in their high-velocity winds, which move radially outwards from the center of the WR star and therefore produce velocity dispersion effects in the observed spectra. The optically thick ($\tau > 1$) nature of these winds makes detecting a stellar surface (and therefore determining the stellar radius and temperature) very difficult. The surface is typically defined at a Rosseland optical depth of $\tau_{Ross} \sim 10$ (c.f. § A.1 Schmutz, Hamann, and Wessolowski 1989). The observer only sees through the optically thin part of the wind, resulting in a visible "photosphere" of optical continuum emission at $\tau_{Ross} = 2/3$ where the transition from the subsonic to supersonic wind occurs. The emission lines originate beyond this radius, stratified at different temperatures in the wind (Hamann and Gräfener 2004; Hillier 1989). Figure 1.4 shows the change from a blackbody continuum to a complex emission (and at short wavelengths, absorption) spectrum with increasing radius. As one would expect, at higher temperatures closer to the helium-fusing layers, more strongly ionized species are found. The precise stratification of WR atmospheres can only be found using non-LTE (Local Thermodynamic Equilibrium) models such as CMFGEN (Hillier 2011) and PoWR (Gräfener, Koesterke, and Hamann 2002). Figure 1.5 shows the ionization stratification with density of a representative model WR star atmosphere (Gräfener, Koesterke, and Hamann 2002)[4]. The observed optical spec-

---

[3] For an overview of radiative transfer and line formation concepts used in this paragraph, see Appendix A.

[4] The model shown in this figure includes line blanketing, an effect whereby large numbers of spectral lines from iron group elements redistribute extreme UV flux to longer wavelengths. It is a critical process in WR modeling because it affects the derived temperatures and luminosities (Crowther 2007; Gräfener, Koesterke, and Hamann 2002; Hillier 2011).

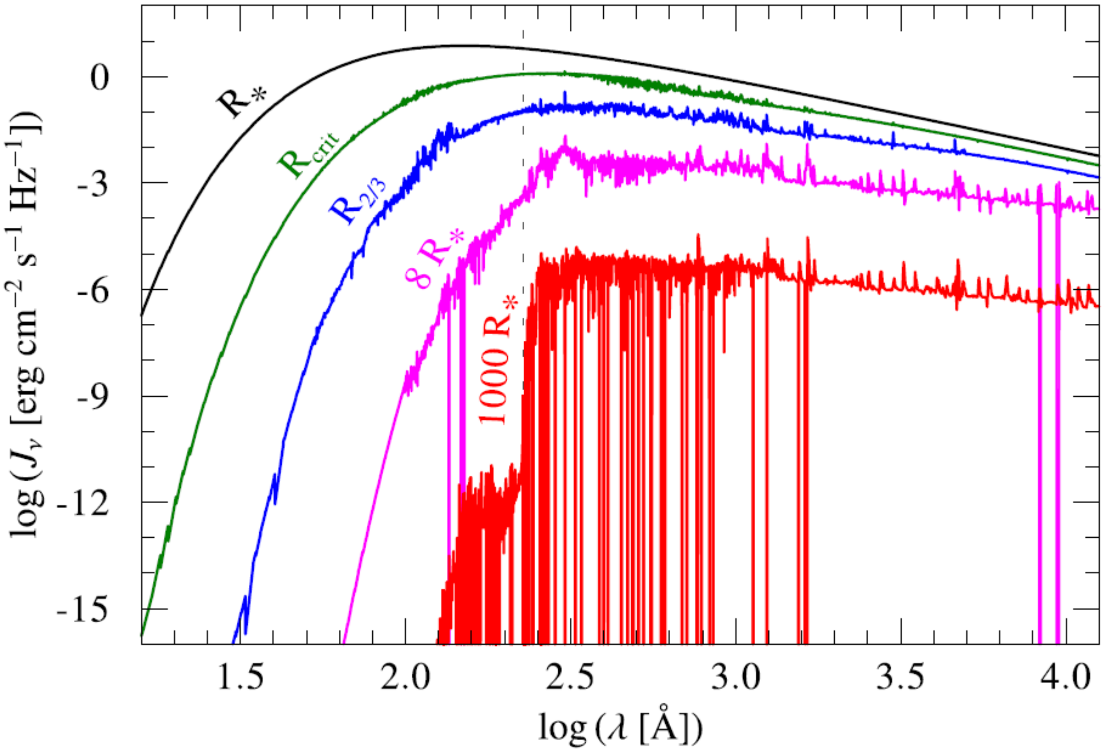

Figure 1.4: The layering of a WR radiation field with radius from Sander, Vink, and Hamann (2020). R_* corresponds to a Rosseland mean optical depth of 20. The model is of a WNE type star at solar metallicity.

tral lines can be thought of as recombination lines, though the reality is more complicated (Hillier 1989). As recombination lines are dependent on both ion and electron density, the strength of the emission lines scales as the square of the density (see Equation A.4). This is why WR stars produce emission-line spectra despite a factor of only ∼10 greater wind density over O supergiants (see Repolust, Puls, and Herrero 2004, for an overview of O star wind parameters).

These optically thick winds are an impediment to measuring stellar rotation directly, so methods such as polarimetry are typically used as indirect methods of inferring stellar rotation (see Section 1.5 and references therein). However, a recent study of the WR binary system 2XMM J160050.751424 (“Apep”) found that both companions are WR stars, and that the low velocity of the dust plume (measured by imaged proper motion over the span

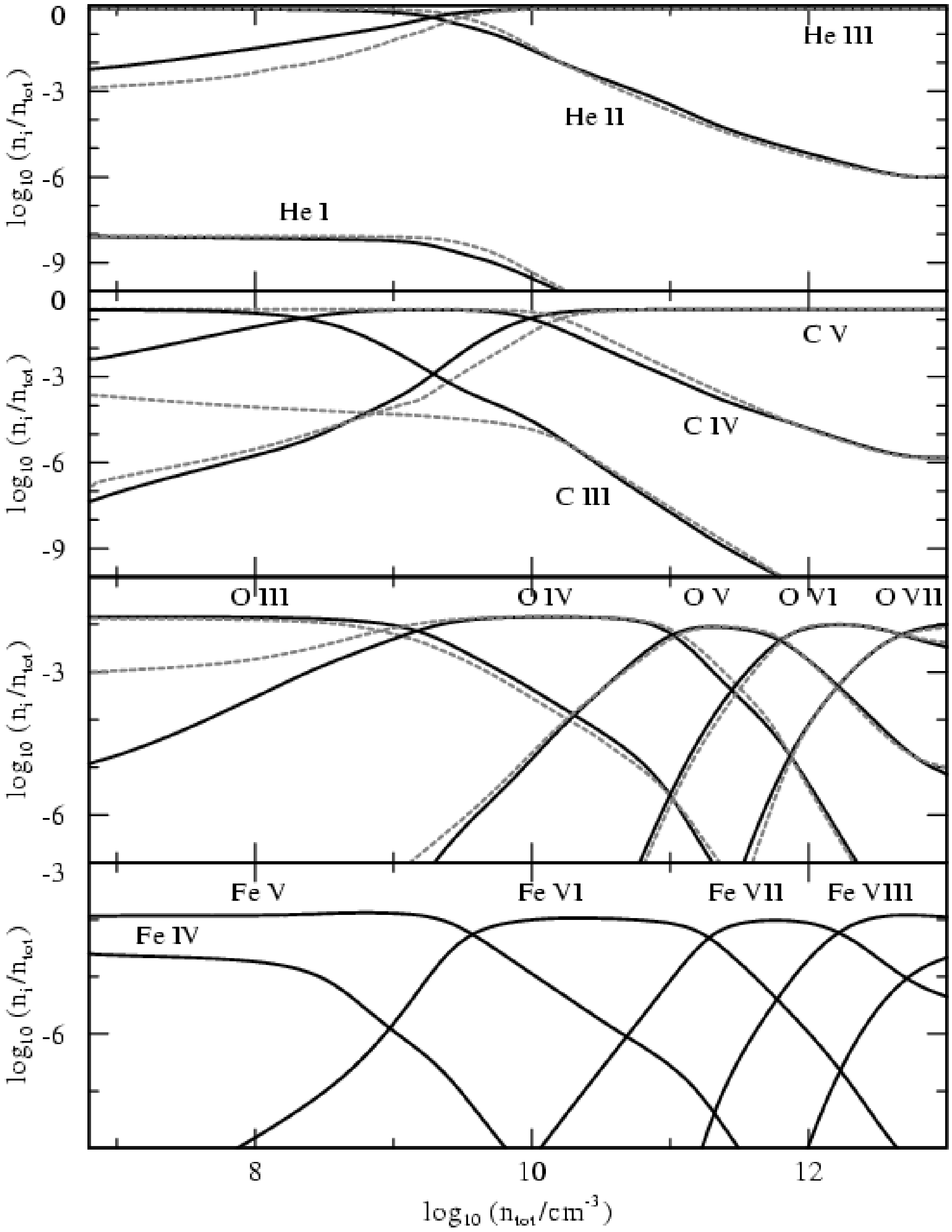

Figure 1.5: WR wind ionization stratification from Gräfener, Koesterke, and Hamann (2002) for the early-type WC star WR 111. The ground state populations (n_i/n_{tot}) are plotted asa function of the atomic density (n_{tot}). Thus distance from the WR "surface" decreases with increasing n_{tot}. The solid black line is a model including line blanketing, while the dashed line is without line blanketing.

of a year, Callingham et al. 2019) can be explained if one of the stars, a WC8 type, is rotating at near-critical[5] velocity (Callingham et al. 2020).

1.4 WR stars in binary systems

Massive stars are commonly found in binary systems, with approximately 70% thought to engage in mass exchange with a companion (Sana et al. 2012). Since stars with $M > 18$ $M_\odot$ are expected to evolve into the WR stage (see Table 1.1), WR stars are likely to be found in binary systems with other massive stars (though this is at least partially due to observational effects making low-mass companions difficult to observe; see Duchêne and Kraus 2013). Furthermore, mass exchange in a binary system means that the lower mass limit for the WR stage can be extended down below 18 $M_\odot$ (Podsiadlowski, Joss, and Hsu 1992; Smith, Götberg, and Mink 2018).

The known Galactic population of WR stars is incomplete due to extinction effects in the Galaxy. The most up-to-date catalog of Milky Way WRs is maintained by P. Crowther[6] and contains 666 objects. The observed binary fraction in this catalog is around 40% (Van Der Hucht 2001a). Foellmi, Moffat, and Guerrero (2003a,b) found a similar fraction in the Magellanic Clouds. Thus WR binaries make up a significant population, but not a majority, of known WR stars.

Binarity affects massive star evolution in two main ways: via rotation and mergers (Langer 2012). I concentrate on rotational effects because they are most relevant to this work. Packet (1981) showed with a simple model that a star gaining mass from its companion via an accretion disk can reach critical velocity after a mass increase of $\sim 5-10\%$. How does this mass transfer happen? In a close binary, Roche lobe overflow (RLOF) transfers mass from the primary (more massive) star to the secondary (also called the donor and

---

[5] The critical or break-up velocity can be defined as $v_{crit} = \sqrt{GM_*/R_*}$ where M_* is the stellar mass and R_* is the stellar radius. It is the rotational velocity above which the star will begin to be pushed apart by centrifugal force (Gräfener et al. 2012).

[6] www.pacrowther.staff.shef.ac.uk/WRcat/

gainer, respectively). RLOF occurs when the primary star evolves to a giant or supergiant stage and fills (then overflows) the gravitational equipotential region called the Roche lobe, which represents the gravitational equilibrium between the two stars. Then matter transfers to the secondary star across the first Lagrangian point (Paczyński 1971). For initial orbital periods of several days, the primary will undergo RLOF while still burning hydrogen in its core, and transfer most of its H-rich envelope to the secondary (this scenario is known as Case A). For initial periods of a few weeks, the mass transfer will occur during the H-shell burning (Case B). Longer initial periods result in He-shell burning mass transfer (Case C; the three cases A, B and C are from Kippenhahn and Weigert 1967). The cases are separated by period because binaries with longer initial periods have larger separations and thus require a more inflated envelope of the primary star to fill the Roche lobe. Given the larger range of orbital periods encompassed by Cases B and C, they are accordingly more common (Crowther 2007). In WR binaries, in Cases A and B, the primary star will evolve to the WR stage due to mass transfer removing hydrogen, while the secondary remains on the main sequence but with a higher mass than its initial mass (Petrovic, Langer, and Hucht 2005). In Case C, the WR stage will only be reached if the primary is > 18 $M_\odot$ due to the large orbital separations; hydrogen stripping does not occur in this case.

Shenar et al. (2019) used the BPASS (Binary Population and Spectral Synthesis) code (Eldridge et al. 2017) to define 4 tracks for WR evolution (noting that the individual tracks are extremely dependent on the model chosen). The tracks correspond to the following WR formation scenarios:

- Main Sequence WR stars (“born this way”), which inhabit the WNH classification mentioned in the previous section.
- Wind-stripped WR stars (w-WR), formed through mass loss via only their winds, following the single-star evolution in Table 1.1.

- Wind+binary-stripped WR stars (wb-WR), formed by both mass loss from winds and binary mass-exchange via RLOF.
- Binary-stripped WR stars (b-WR), formed only by binary interaction removing outer layers. Not all of these have sufficient mass to display a WR spectrum.

Figure 1.6 shows WR evolutionary tracks from the zero-age main sequence (the point where the star first joins the main sequence) through the WC/WO stage for the Large Magellanic Cloud. Surface hydrogen fractions are indicated by different coloured line segments, with green showing WN types with no hydrogen present. In the Milky Way's galactic environment, it is expected that the minimum mass required to reach each stage is lower due to the direction relationship between metallicity and mass loss (Sander, Vink, and Hamann 2020).

In the case of a WR + O binary system, my focus in this research, both stars have stellar winds. This leads to a wind collision region arising in the system. The shape of this region is dependent on the relative momentum flux ρv^2 that the two winds produce (Stevens, Blondin, and Pollock 1992). This is in turn dependent on the mass-loss rate $\dot{M}$ of each star. In the case of winds that have reached v_∞, one-dimensional momentum balance can be used to find the distance to the contact point where the winds meet:

$$\left(\frac{\dot{M}_1 v_1}{\dot{M}_2 v_2}\right)^{1/2} = \frac{d_1}{d_2}, \tag{1.2}$$

where the subscripts 1 and 2 represent the two stars, v is the wind velocity, and d is the distance from each star to the contact point. Accelerating winds, important for binaries where the stars are close enough that v_∞ is not reached, lead to the more complex case where the momentum flux changes with radius; thus the contact point is found where both the difference in momentum flux is zero and the change in that difference with radius is less than zero (Stevens, Blondin, and Pollock 1992). If the momentum flux difference between

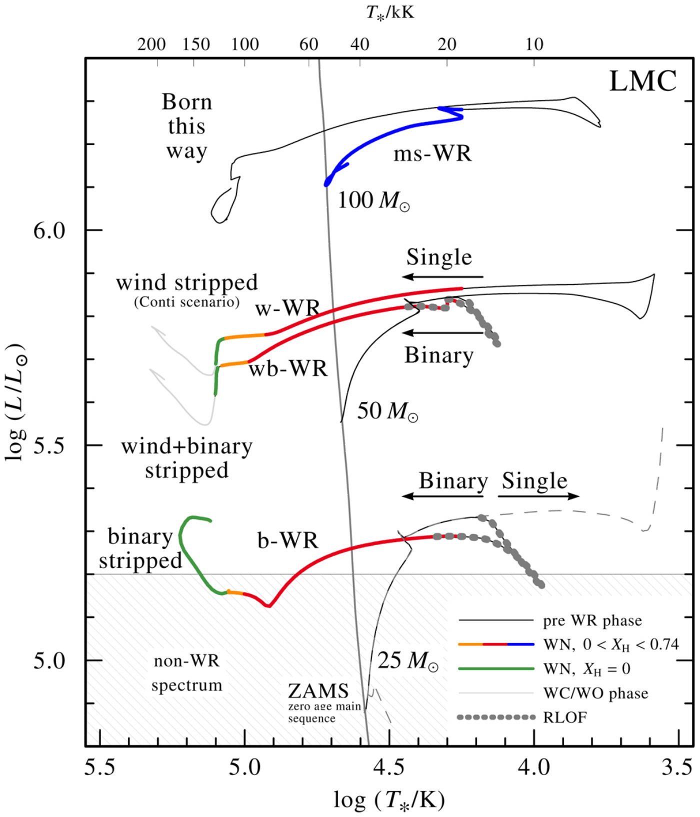

Figure 1.6: Evolutionary tracks on the H-R diagram of WR stars with different amounts of binary influence, from Shenar et al. (2019). X_H is the surface hydrogen fraction. The models were computed for the environment of the Large Magellanic Cloud. The binary models were computed for orbital periods of 25 days. Based on observations, stars are not expected to show WR spectra in the hashed region below 5.2 $log(L/L_\odot)$.

the two stars is sufficiently large, the wind of the weaker star can be crushed completely to its surface and the stronger wind dominates entirely (Stevens, Blondin, and Pollock 1992).

A full picture of the wind structure in a WR + O system requires hydrodynamic simulations (e.g. Parkin and Pittard 2008; Stevens, Blondin, and Pollock 1992). Figure 1.7 shows an example hydrodynamic model from Parkin and Pittard (2008). However, simpler models have shown promising results. In particular, the model of Luehrs (1997), adapted by Hill et al. (2000), has been able to accurately fit line profiles of WR + O binaries (Hill, Moffat, and St-Louis 2002, 2018; Hill, Moffat, and St-Louis 2003). In this model, excess emission of the wind-wind collision region that is observed in the C III $\lambda5696$ line is modelled as fast-streaming, optically thin plasma. The emission is known to arise from the wind-wind collision region because the excess emission is out of phase with the binary orbit. The plasma is emitting and cooling around a conical cavity created by the collision between the O star's wind and that of the WR star. The apex of the cone corresponds to the contact point between the winds. Figure 1.8 shows a sketch of the Hill et al. model. The cone axis is offset from the line that joins the WR and O stars by a Coriolis angular deviation $\delta\phi$, and has a defined thickness $\Delta\theta$ and opening angle θ. The thickness angle is bisected by the opening angle so that $\Delta\theta/2$ thickness is on either side of the streaming line shown in Fig. 1.8. The density of the thick region decreases quadratically towards and away from the θ line so that even if $\Delta\theta/2 = \theta$, the O star wind region is not uniformly filled. This model was updated by Hill et al. to extend the conical cavity into the WR wind shell and add the effects of turbulence. Although I use a simple spherical cavity to represent the O star wind region in Chapter 4, I plan to incorporate the conic model described above in future stages of the modeling project.

1.4.1 The fates of WR stars in binary systems

As discussed in the above section, binary interactions have a strong impact on the evolution of massive stars. Mass transfer can accelerate the transition to the WR stage and

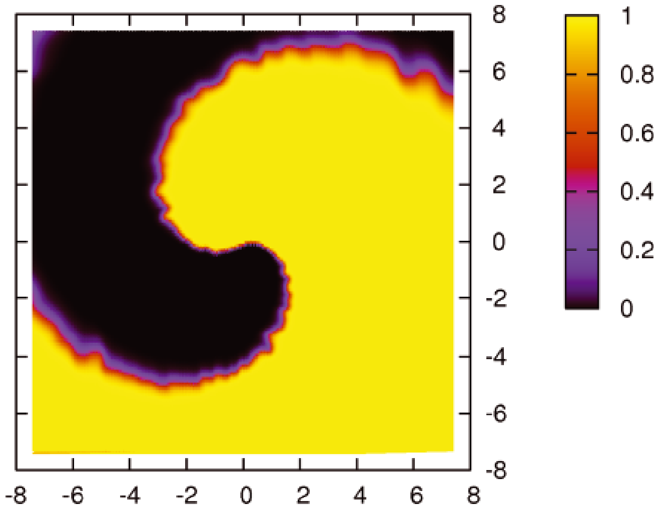

Figure 1.7: Hydrodynamic wind-wind collision model from Parkin and Pittard (2008). Viewed from above the orbital plane, the axes are measured in AU. The color at 0.5 represents the contact point between the winds. The two extremes 0 and 1 represent the winds of each star. The mass-loss ratio of the two stars is 3:1 and this defines the stars in the model.

greatly reduce the minimum mass needed to reach this stage (see Fig. 1.6). Therefore, it is important to understand the mass loss and transfer in massive binary systems because a quantitative knowledge of these processes will inform stellar evolution models and allow us to clarify the relationships between initial and final mass for stars above $\sim 25\ M_\odot$ (Langer 2012). Characterizing binary orbits also allows for mass determinations via constraints on inclination angles[7]. Orbital inclination angles can be determined independently with polarimetric modeling (see Section 1.5.2).

As discussed in Section 1.3, Type Ib and Type Ic SNe must originate from WR stars that have lost all their hydrogen (and helium for Type Ic) to their strong winds. Because of their similar progenitors, these classes are often combined under the label of Type Ibc (e.g. Smartt 2009; Smith 2014). A currently unanswered question regarding Type Ibc SNe is their observed frequency compared to that of the expected progenitors, WR stars. Single WR stars are not numerous enough to explain the rate of Type Ibc SNe (Smartt 2009; Smith

---

[7] Time-dependent spectroscopy can provide $M \sin i$, i.e. mass dependent on the inclination angle i.

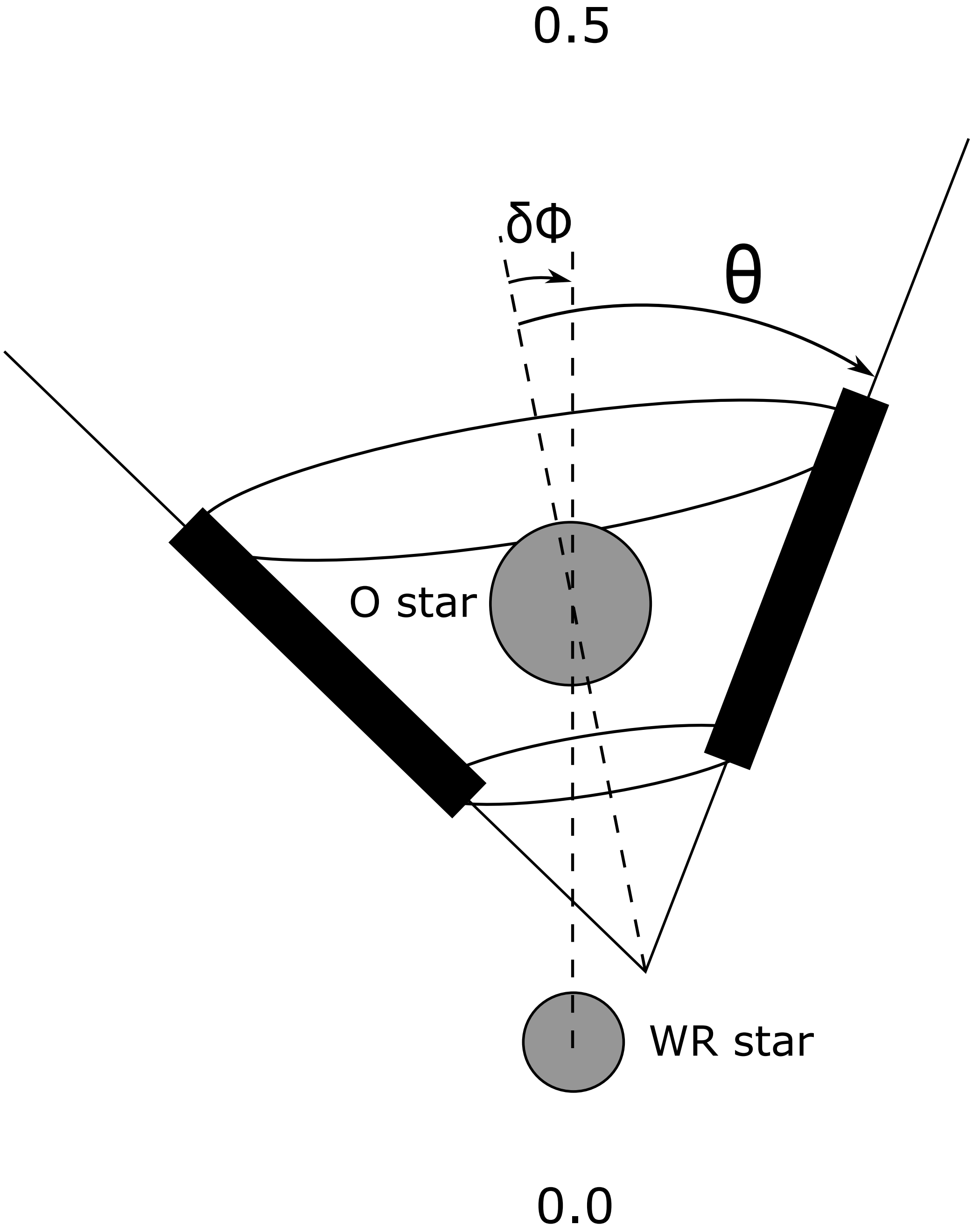

Figure 1.8: Sketch of the C III λ5696 emission model presented in Hill, Moffat, and St-Louis (2002). Phases 0.0 and 0.5 mark the viewing direction at primary and secondary conjunction, respectively. θ denotes the half-opening angle of the cone and $\delta\phi$ is the aberration/Coriolis angular deviation of the cone. The thick region of the shock cone represents the tangentially-enhanced fast-streaming C III λ5696 emission.

2014). Therefore, binary interaction has been proposed to explain the mass-loss required to reveal helium cores (c.f. the wb-WR and b-WR classifications in the previous section); stellar evolution models that include binary mass transfer have been successful in replicating the observed Type Ibc rate (e.g. Eldridge et al. 2013). The uncertainty around this topic means that it is essential to quantify the mass loss and mass transfer in massive binary systems (including WR binaries in particular) to investigate the validity of these models and their assumptions. Moreover, a better characterization of mass-loss and mass transfer in WR binaries allows us to identify the progenitor systems of SNe that may produce exotic objects like binary black holes or black hole-neutron star pairs that are likely to produce gravitational waves (Heuvel et al. 2017; Vink and Harries 2017a).

A further question arises regarding Type Ic SNe: how do they produce gamma-ray bursts? Some Type Ic SNe have shown extremely broad emission lines (2000–3000 km s^{-1}), and these are the only SNe that have been observed to be associated with long gamma-ray bursts (LGRBs) (Cano et al. 2017; Smith 2014). GRBs are short (time of seconds) flashes of gamma-rays that arrive regularly on Earth (Woosley and Bloom 2006). They are divided into two groups, short (median duration 0.3 s) and long (median duration 20 s). At least 18 LGRBs have been associated with SNe of Type Ic (Cano et al. 2017). They are expected to have kinetic energies of $\sim 2.5 \times 10^{52}$ erg, more than 10 times that of a typical SN (Cano et al. 2017).

To produce LGRBs requires focused jets far from the star with a high power of $\sim 10^{50}$ erg s^{-1} (Woosley and Bloom 2006). The most favored theoretical framework for LGRB production is the collapsar "central-engine" model, whereby the collapse of the progenitor into a black hole also creates a centrifugally-supported accretion disk. The interaction of the disk and the black hole produces bipolar relativistic jets that give rise to gamma-ray emission (Cano et al. 2017; Woosley and Bloom 2006; Woosley, Langer, and Weaver 1993). High angular momentum (greater than 10^{16} cm^2 s^{-1}) is required to support the accretion disk (Woosley 1993). The other possible central-engine scenario is the millisecond magnetar model, which requires a rapidly rotating ($P\sim$1–10 ms) magentized neutron star to act as the jet production mechanism (Metzger et al. 2011). Both of these models require the stellar core to be rapidly rotating before core-collapse, around 400 km s^{-1} (Woosley and Heger 2006). As a result, there have been many attempts to search for rapidly rotating WR stars as they are the best candidates for these progenitors due to their connection with SNe Ibc (e.g. Shenar, Hamann, and Todt 2014; Stevance et al. 2018; Vink, Gräfener, and Harries 2011). To date, these surveys have not taken binary systems into account, despite the fact that they are potentially very important to producing LGRBs (Cano et al. 2017; Smith et al. 2011). For example, in a binary, a common envelope phase (where both stars in the system share the same hydrogen or helium atmosphere) can convert orbital angular momentum to rotational angular momentum of the resulting merged object (Chevalier 2012). This would occur late in the evolution of a binary system, after one star has produced a SN and become a neutron star. As the compact object inspirals, angular momentum is imparted to the core via disk accretion and produces a GRB upon merging (Fryer and Heger 2005). Alternatively, RLOF mass transfer may provide enough momentum transfer to spin up the gainer in the system; high rotation rates up to 500 km s^{-1} have been found in the O star companions of WR stars (Shara et al. 2017; Vanbeveren et al. 2018) though these results have been called into question by Reeve and Howarth (2018). A recent study by St-Louis et al. (2020) of the long-period binary WR 137 showed that the O star has a disk, and the authors posit that this is due to earlier mass-transfer in the system.

Given the importance of rapidly rotating WR stars as possible progenitors of LGRBs, detecting them in binary systems is a high priority. The optically thick atmospheres make direct rotation measurement with spectroscopy difficult, so indirect measurements need to be used. Rapid rotation changes the shape of the WR wind, deforming it into either a high density equatorial region (Ignace, Cassinelli, and Bjorkman 1996) or a prolate geometry parallel to the rotation axis (Gayley 2004). These density and geometry changes in a hot, ionized wind are best detected using polarimetry.

In order to investigate the roles of WR binaries as SN and LGRB progenitors, we need to understand the mass transfer between WR stars and their main sequence companions to discover whether, how, and how much angular momentum is being transferred between the stars or lost from the system. To do this, we use the observational tool of spectropolarimetry, which allows us to detect the elongated and distorted winds indicative of mass loss and mass transfer. With radiative transfer modeling to interpret these data, we can constrain the inclination angles of binary orbits (and therefore the stellar masses), locate the material being transferred between the stars or lost from the system (which can ultimately probe mass-loss and mass-transfer rates), and search for signatures of rapid rotation (see Sections 1.5 and 1.5.2).

1.5 Polarization of light

In the ionized stellar winds of WR stars, linear polarization is created by the process of electron (Thomson) scattering of starlight. Thus the polarization of light is a possible avenue to investigate the stellar winds of WR stars. Here I briefly discuss the formalism of polarization and the characteristics of Thomson scattering.

In the wave theory of light, light waves are made up of electric and magnetic fields oscillating in planes perpendicular to one another and to the direction of travel. The polarization state of a light ray is defined by the amplitude and angle of the electric field's oscillation measured in the plane of the electric and magnetic fields. It can be linear (a constant angle of the electric field) or circular (an angle changing constantly with time clockwise or counterclockwise about the direction of travel; Clarke 2010).

Astrophysical polarimetry quantifies the extent to which the electric field of light detected by a telescope is oriented in a particular direction. This direction, called the polarization position angle, is measured East from North following the IAU convention (Clarke 2010). The polarization state of a light ray can be described by the Stokes parameters I, Q, U, and V (Chandrasekhar 1947; Stokes 1851). The Q and U vectors represent linear polarization in two different orientations (positive Q is parallel to North-South, negative Q is parallel to East-West; positive U is parallel to NE/SW, negative U is parallel to NW/SE, all following the IAU convention), while V represents circular polarization (positive for increasing E-field angle with time with respect to the $+Q$ direction, negative for decreasing angle with time, following the IAU convention). Given that

$$\vec{S} = \begin{pmatrix} I \\ Q \\ U \\ V \end{pmatrix}, \tag{1.3}$$

the possible states of totally polarized light are

$$\text{Linear horizontal} = \begin{pmatrix} 1 \\ 1 \\ 0 \\ 0 \end{pmatrix}, \qquad \text{Linear vertical} = \begin{pmatrix} 1 \\ -1 \\ 0 \\ 0 \end{pmatrix}, \tag{1.4}$$

$$\text{Linear } +45^\circ = \begin{pmatrix} 1 \\ 0 \\ 1 \\ 0 \end{pmatrix}, \qquad \text{Linear } -45^\circ = \begin{pmatrix} 1 \\ 0 \\ -1 \\ 0 \end{pmatrix}, \tag{1.5}$$

$$\text{Right hand circular} = \begin{pmatrix} 1 \\ 0 \\ 0 \\ 1 \end{pmatrix}, \qquad \text{Left hand circular} = \begin{pmatrix} 1 \\ 0 \\ 0 \\ -1 \end{pmatrix}. \tag{1.6}$$

Because the light from most sources is not totally polarized, the individual Stokes parameters are usually considered as fractions of total intensity, e.g. $q = Q/I$, $u = U/I$. This means that the relation $p = \sqrt{q^2 + u^2 + v^2}$ can be used to calculate the total fractional polarization p, where q, u and v are the fractional Stokes parameters. However, this positive definite quantity is biased towards larger values for q and u with low signal-to-noise ratio (Clarke 2010; Wardle and Kronberg 1974), so considering the fractional parameters individually is more accurate. Another quantity of interest is the linear polarization position angle, $\theta = \frac{1}{2}\ \arctan \frac{u}{q}$ (Hough 2006). This defines the orientation of the polarization vector in $q - u$ space, measured counterclockwise from the $+q$ axis. Note that because the polarization states in equations 1.4–1.6 are degenerate, $q - u$ space only encompasses position angles in the range $0 \leq \theta < \pi$. The degeneracy arises because the electric field vector oscillates in a plane (Jackson 1998).

Other important equations relating the Stokes parameters to the total polarization p and the polarization position angle θ are

$$q = p \cos 2\theta \tag{1.7}$$

$$u = p \sin 2\theta. \tag{1.8}$$

These are derived from simple trigonometry of a vector defined by length p and angle 2θ in $q - u$ space. A benefit of investigating polarization in $q - u$ space is that both rotation and translation in the space can be accomplished by simply rotating or translating the axes, the same as any other coordinate system. Rotation is particularly useful. If a dominant position angle axis of a set of polarization observations can be found, rotating the polarization data so that the dominant axis aligns with the $+q$ direction allows interpretation of the data *relative* to that dominant axis; in the case of Thomson scattering (discussed in detail below), this axis is perpendicular to the geometrical extent of the aspherical polarizing region (Wang and Wheeler 2008). After rotation, the total polarization p remains the same as before, but one can take q polarization to indicate a scattering geometry that is parallel (negative q) or perpendicular (positive q) to the dominant axis. Similarly, u polarization probes scattering material that is at 45° to the dominant axis; in the case of an axisymmetric scattering region, the rotated u parameter scatters around 0.

In the case of Thomson scattering, an incoming photon of energy $<<$ 0.511 MeV (corresponding to the electron rest mass and frequencies in the X-ray regime) interacts with a free electron. The election oscillates at the same frequency as the incoming photon, due to the Lorentz force (Irwin 2007). Oscillation is acceleration, and an accelerating charge will radiate, so the incoming photon is effectively absorbed and re-emitted in a new direction, assuming elastic scattering (valid for the range of photon energies considered here). The degree of linear polarization Π caused by Thomson scattering is dependent on the observer's viewing angle with respect to the incident photon direction, with a maximum when observed perpendicularly to the incident wave as shown in equation 1.9 (Rybicki and Lightman 1986):

$$\Pi = \frac{1 - \cos^2\theta}{1 + \cos^2\theta} \tag{1.9}$$

Thomson scattering produces no circular polarization. The second important property of Thomson scattering is that it is wavelength-independent below 0.511 MeV. This is because the classical electron cross-section $\sigma_T = 0.655 \times 10^{-24}$ cm^2 can be used in this energy regime, which is itself based on the classical electron radius, a quantity independent of frequency (Rybicki and Lightman 1986).

In distributed scattering material, the geometry of the material on the sky affects the observed polarization. Figure 1.9 shows how different centrally-illuminated geometries can create observed polarization in unresolved scattering regions. Radially emitted photons scatter in the material, producing polarization perpendicular to the scattering plane (and therefore tangential to a circular surface at an arbitrary distance from the central source). If the scattering region is not circular in the plane of the sky, the polarization will have additional contributions from the parts of the region that are not circular. The same

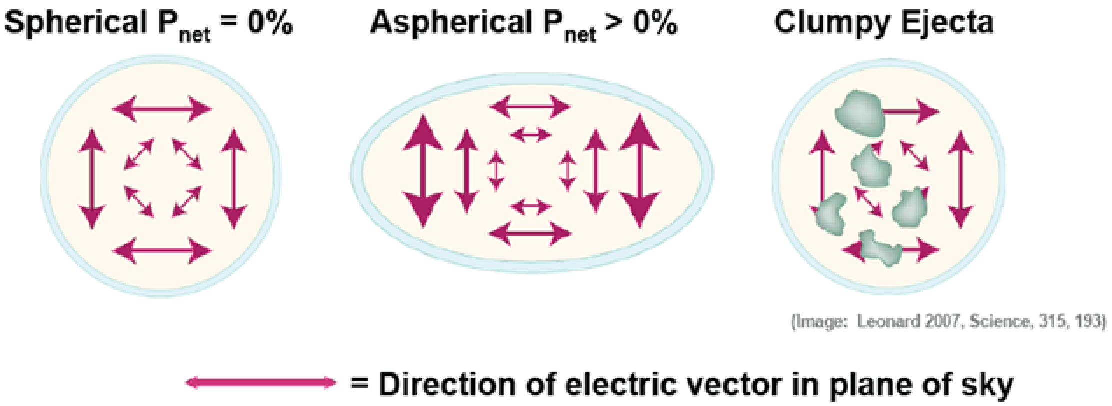

Figure 1.9: Centrally-illuminated scattering regions and the polarization they produce. Left: a spherically symmetric region produces no net polarization. Center: an aspherical region with no density variation produces net polarization perpendicular to its longest axis. Right: absorbing clumps in an otherwise spherical scattering region produce net polarization by means of obscuration. Image from Leonard (2007).

situation occurs when there is a change in density of the scattering region that is not radial. For an unresolved scattering region, the polarization vectors sum to produce the observed polarization. Thus any deviation from central illumination of a circular (on the plane of the sky) scattering region results in a net observed polarization. This means that external illumination will also produce a net polarization.

The alignment of dust grains in the interstellar medium also results in linear polarization of starlight. This imprints an additional polarization regardless of the origination or polarization state of the light. The grains may be aligned by the Galactic magnetic field, mechanically by colliding atoms, or through radiative torques (Clarke 2010). This alignment typically manifests as interstellar polarization (ISP), and in the Milky Way Galaxy it follows the Serkowski Law (Serkowski, Mathewson, and Ford 1975), an empirically-derived law describing the magnitude and wavelength dependence of the ISP at optical wavelengths. The empirical form was modified by Wilking et al. (1980) and Whittet et al. (1992). The descriptive function $p(\lambda)$ is smooth, and peaks at optical wavelengths. It is defined as

$$p(\lambda) = p(\lambda_{max}) \exp \left[-K\lambda_{max} \ln^2 \left(\frac{\lambda_{max}}{\lambda} \right) \right] \tag{1.10}$$

where $p(\lambda_{max})$ is the polarization at the peak wavelength λ_{max}, and $K = 0.01 \pm 0.05 + (1.66 \pm 0.09)\lambda_{max}$ (Whittet et al. 1992) though often the approximation $K = 1.7$ is used. An in-depth discussion of ISP measurement and subtraction is presented in Chapter 2.

1.5.1 Spectropolarimetry and the line effect

A natural extension of polarimetry is to observe polarization at multiple wavelengths, i.e. spectropolarimetry. All the same principles of polarimetry apply, the observations are simply a function of wavelength. For grey processes such as Thomson scattering, spectropolarimetry can be used to investigate the geometry of scattering regions illuminated by different emission processes. Spectropolarimetry allows us to obtain accurate measurements of the spectral shape of the ISP (e.g. Bagnulo et al. 2017) and precisely extract it from measurements rather than performing a fit to a small number of broadband polarization measurements (see Chapter 2 for applications of the broadband method).

Spectropolarimetry allows us to investigate the “line effect”, a long-sought observational property of some WR stars that serves as a signature of rapid rotation (Vink and Harries 2017a). Observationally, the line effect manifests as a reduction in polarization across WR emission line profiles relative to the continuum with no corresponding change in position angle, as shown in Figure 1.10 from Harries, Hillier, and Howarth (1998). This occurs because the continuum originates nearer the stellar surface, so continuum photons scatter through a greater optical depth of material and acquire a higher polarization than the emission lines, which originate farther out in the stellar wind. In fact, recombination lines are produced unpolarized, and are therefore expected to show no polarization if they do not scatter before exiting the WR wind (St-Louis 2013). The line effect has been detected in

$\sim 20\%$ of WR stars (Gräfener et al. 2012; Harries, Hillier, and Howarth 1998; McLean et al. 1979; Schulte-Ladbeck et al. 1991). The line effect has also been found to correlate with ejecta nebulae by Vink, Gräfener, and Harries (2011) and Gräfener et al. (2012). Ejecta nebulae are predicted to last for only $\sim 10^5$ yr (Marle, Langer, and García-Segura 2005), so depolarization in emission lines could indicate that a given star has only recently reached the WR stage.

The importance of the line effect is that it can provide a diagnostic for asymmetric winds, because net observed polarization must arise from asymmetric scattering geometry, asymmetric scatterer density, or asymmetric illumination of scatterers. Logically, the most likely cause for an asymmetric wind is rapid rotation causing elongation parallel to the rotation axis (Gayley 2004; Owocki, Cranmer, and Gayley 1996); thus, the line effect can identify rapidly-rotating WR stars that may be LGRB progenitors (see Section 1.4.1) as the elongated wind produces an ellipse projection in the sky at inclination angles $0° < i < 180°$. However, Stevance et al. (2018) found that they could not rule out the presence of rapid rotation using the lack of a line effect as the sole diagnostic (though they used the wind-compressed model that has been called into question by e.g. Gayley 2004).

1.5.2 Polarization in WR + O binary systems

Although Fig. 1.9 shows the simple case of a centrally-illuminated scattering region, net polarization can also be caused by the asymmetric illumination of an otherwise spherically symmetric density distribution for the same reason: Stokes vector addition. This means that WR + O binary systems can produce variable polarization as their orbits progress, due to the changing illumination of the WR stellar wind from the observer's perspective. Given that WR + O systems produce only linear polarization (the magnetic fields and other effects that give rise to circular polarization are weak in WR stars; see Chevrotière et al. 2014; Hubrig et al. 2016), the q and u Stokes parameters introduced in Section 1.5 are the focus of the observational campaign presented in this dissertation. Since emission

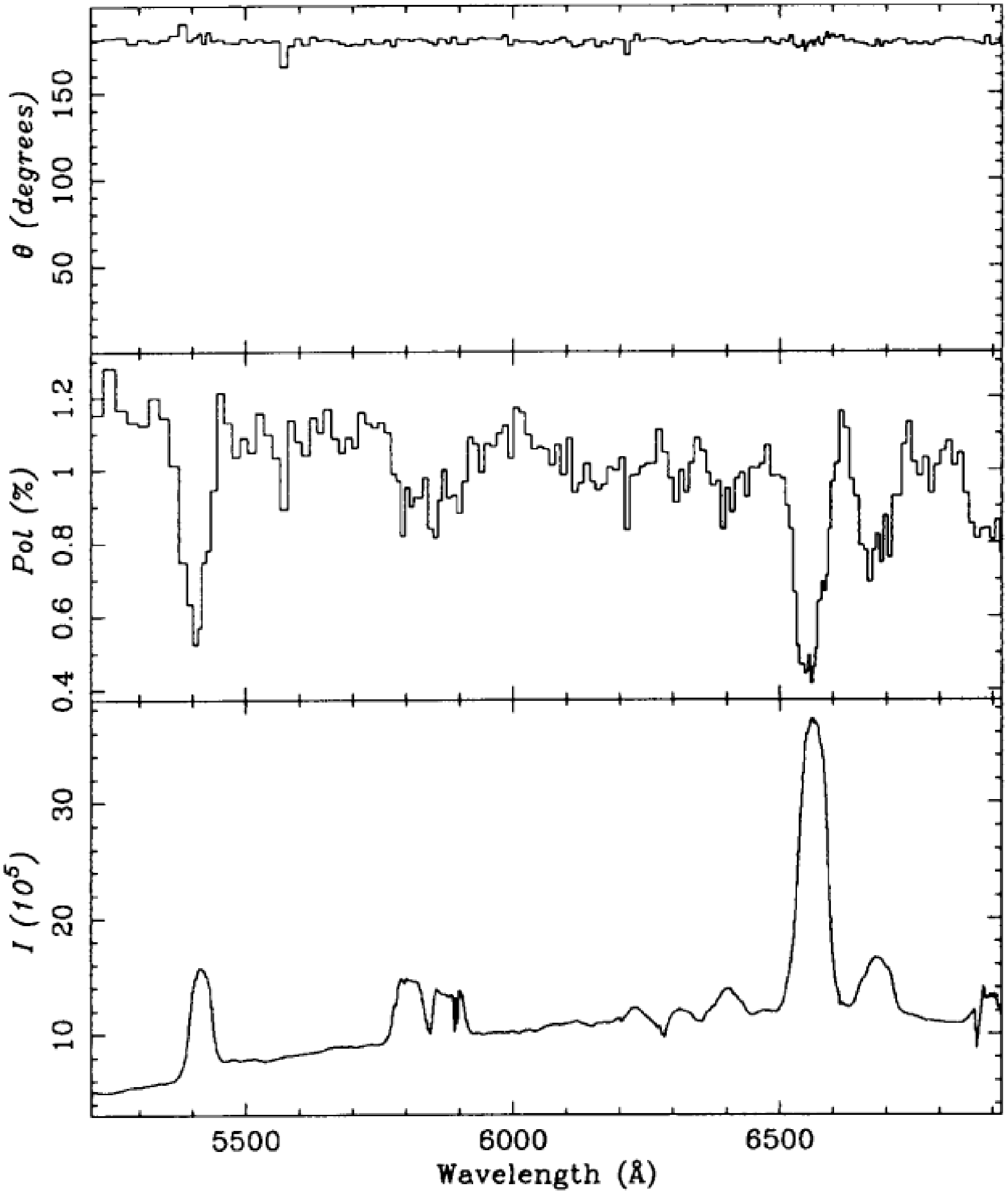

Figure 1.10: WR 134 data showing the line effect, from Fig. 1 of Harries, Hillier, and Howarth (1998). The top panel shows the polarization position angle, middle shows the total polarization binned to a constant error of 0.05% in P, and bottom shows the unbinned intensity spectrum.

lines arise in different regions of the WR + O system than the continuum (see Section 1.4), we can expect them to show different polarization variability than the continuum (which is primarily produced via the O star light illuminating the WR wind). Figure 1.11 shows examples of the possible phased and unphased effects in a WR binary that are described in this section (Hoffman 2015). It should be noted that although the Coriolis effect creates a spiral-like pattern of density fluctuations in the wind out to large distances (e.g. Callingham et al. 2019), the density and temperature of the winds has dropped such that polarization is dominated by scatterers much closer to the WR + O stars (e.g. Kurosawa, Hillier, and Pittard 2002; Lomax et al. 2015).

The time-varying continuum polarization caused by illumination of the WR wind can be approximated by the classic model of Brown and McLean (1977) and Brown, McLean, and Emslie (1978), hereafter the BME model. In this model, the scattering region is described as an optically thin electron gas with optical depth τ_0 (integrated over all directions). Only polarization caused by Thomson scattering is considered by the model, and the envelope is assumed to be co-rotating with the illumination sources. The parameters γ_n, $n = (0, 1, 2, 3)$ are defined as measures of the 3D envelope geometry. γ_0 quantifies the flattening of the envelope towards the orbital plane, with $\gamma_0 = 1$ for a plane envelope, 0 for a spherical envelope, and -2 for a fully prolate envelope in the polar direction. γ_1 and γ_2 are measures of the degree of asymmetry about the orbital plane. They are usually set equal to 0 because it is less likely to see asymmetry than symmetry about the orbital plane (e.g. St-Louis et al. 1988; Moffat and Piirola 1993). γ_3 and γ_4 measure the concentration of material in the orbital plane. In particular, γ_3 represents material along the line connecting the two stars in the binary case, while γ_4 represents material perpendicular to that line. The illuminators consist of one point source at the center of the scattering region and an additional point source at an arbitrary location along the direction $\theta = 90°$, $\phi = 0°$ relative to the central source (which may be either interior or exterior to the scattering region).

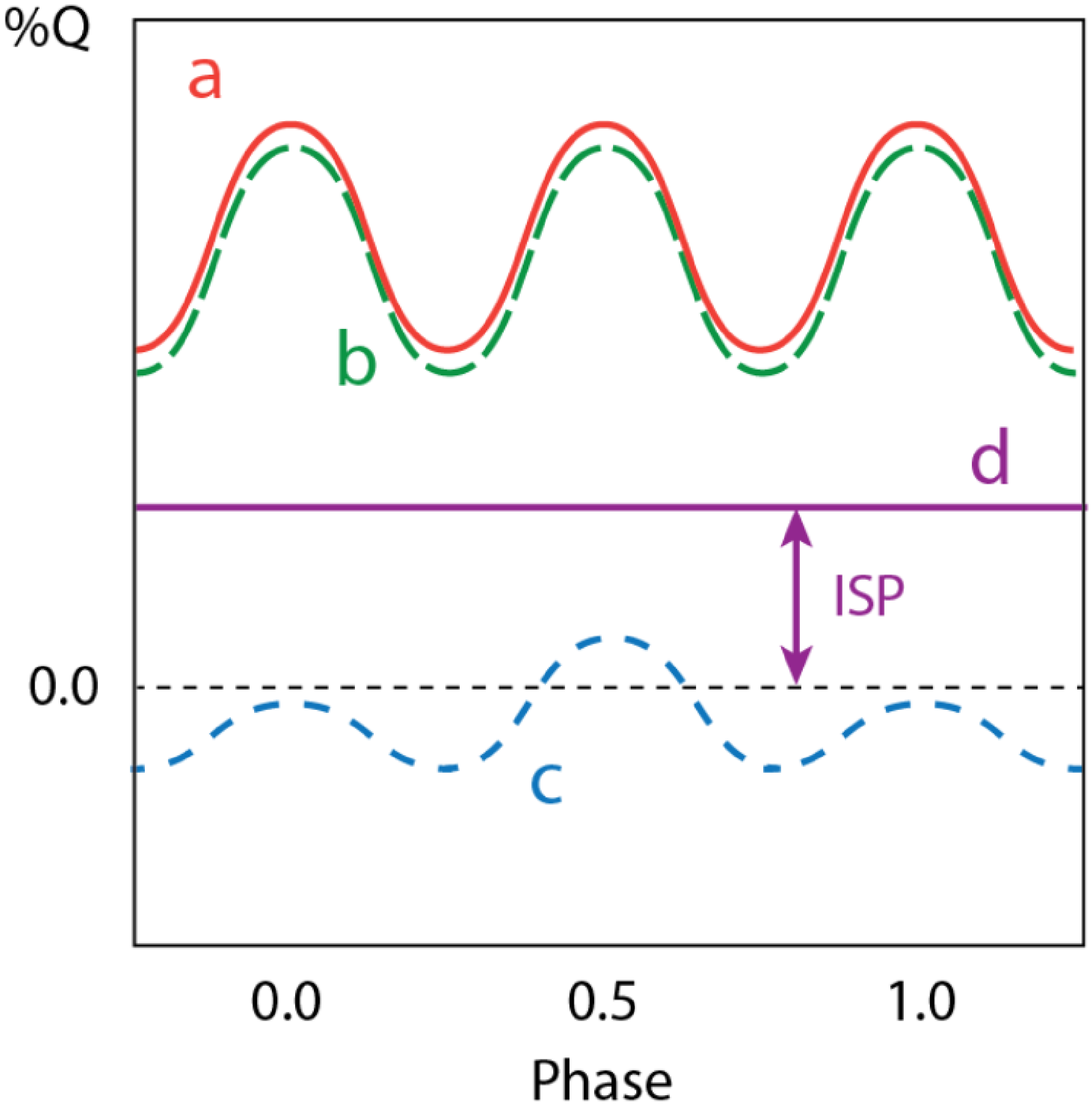

Figure 1.11: Sources of polarization variation in WR binaries. *a)* is continuum variation (Brown, McLean, and Emslie 1978); *b)* is an emission line arising and scattering like the continuum; *c)* is an emission line arising and scattering differently than the continuum (e.g., Lomax et al. 2012); *d)* is an emission line arising and scattering far from the orbital plane with 0% intrinsic polarization (the "line effect"). Figure from Hoffman (2015).

The model is encapsulated in two equations for q and u:

$$q = q_0 + q_1 \cos\lambda + q_2 \sin\lambda + q_3 \cos 2\lambda + q_4 \sin 2\lambda \tag{1.11}$$

$$u = u_0 + u_1 \cos\lambda + u_2 \sin\lambda + u_3 \cos 2\lambda + u_4 \sin 2\lambda \tag{1.12}$$

where q_0, u_0 are constant fractional polarization terms (that includes both ISP and any constant intrinsic polarization of the system), q_i, u_i $(i = 1, 2, 3, 4)$ are coefficients with units of fractional polarization and $\lambda = 2\pi\phi$ for circular orbits, where ϕ is the orbital phase (ranging from $0 - 1$ over the orbit). The terms in λ rather than 2λ can be neglected because they correspond to cases where γ_1 or γ_2 are nonzero. With that simplification, Robert et al. (1992) showed that for binary systems (with one internal and one external illuminator)

$$q = q_0 + \Delta q \cos\Omega - \Delta u \sin\Omega, \tag{1.13}$$

$$u = u_0 + \Delta q \sin\Omega + \Delta u \cos\Omega, \tag{1.14}$$

where

$$\Delta q = -\tau_3[(1 + \cos^2 i)\cos 2\lambda - \sin^2 i] \tag{1.15}$$

and

$$\Delta u = -2\tau_3 \cos i - \sin 2\lambda\,. \tag{1.16}$$

In these expressions, Ω is the position of the line of nodes on the sky, measured counterclockwise from the north, and i is the orbital inclination with respect to the line of sight (see Figure 1.12 for a visual definition of these values). τ_3 is given by $\tau_3 = \tau_*(a/r)^\gamma$, with τ_* representing the mean optical depth of the envelope, a the mean orbital separation, and r the instantaneous separation. The parameters a and r are equal for circular orbits, which means the equation for τ_3 simplifies to $\tau_3 = \tau_*$. In the expression for τ_3, γ is a power index that reflects the actual free-electron density in the envelope. Using this model, it is easy to recover orbital quantities of interest (i, Ω) and the mean optical depth of the envelope τ_*. The model also recovers any constant polarization so that ISP can be subtracted vectorially from q_0 and u_0.

Figure 1.13 shows how illumination by an orbiting source produces polarization from a spherical scattering region, at two different inclination angles (this is a special case of the BME formulation; Brown and McLean (1977). We use capital Q, U here following their convention). For face-on orbits ($i = 0°$), the polarization varies evenly between positive and negative Q and positive and negative U, repeating twice per cycle. This produces a circle in the $Q - U$ plane with a radius proportional to the optical depth of the scattering region τ_0. When plotted versus phase, the observed polarization produces a sine wave in both Q and U that repeats twice (i.e. equations 1.13 and 1.14). For edge-on orbits ($i = 90°$), the polarization varies from 0 to positive Q. The inset panel in Figure 1.13 shows how the ellipse in $Q - U$ space can be used to derive orbital quantities. The eccentricity of the ellipse e can be used to determine i, the semi-major axis of the ellipse can be used to determine the quantity $2\tau_0(\gamma_3^2 + \gamma_4^2)^{1/2}$, related to the optical depth τ_0 of the scattering region and the two density measures γ_3 and γ_4 (for material along the line connecting the stars and perpendicular to that line, respectively). λ_2 is the angle of the concentration of material relative to the line between the stars, $0.5 \arctan \gamma_4/\gamma_3$ (recall that $\lambda = 2\pi\phi$, similarly λ_2 is a phase). Rotating the orbital plane with respect to north in the figure produces the angle Ω shown in Fig. 1.12. It also rotates the ellipse major axis in $Q - U$ space by angle Ω relative to north. It can be seen that as the orbit becomes more face-on, Ω becomes harder to determine as the ellipse becomes more circular and the major axis more difficult to determine. The centre of the ellipse is located at $Q = \tau_0(1 - 3\gamma_0)\sin^2 i$, $U = 0$. For a sphere $\gamma_0 = 0$ so this reduces to $Q = \tau_0 \sin^2 i$. Thus any constant polarization q_0, u_0

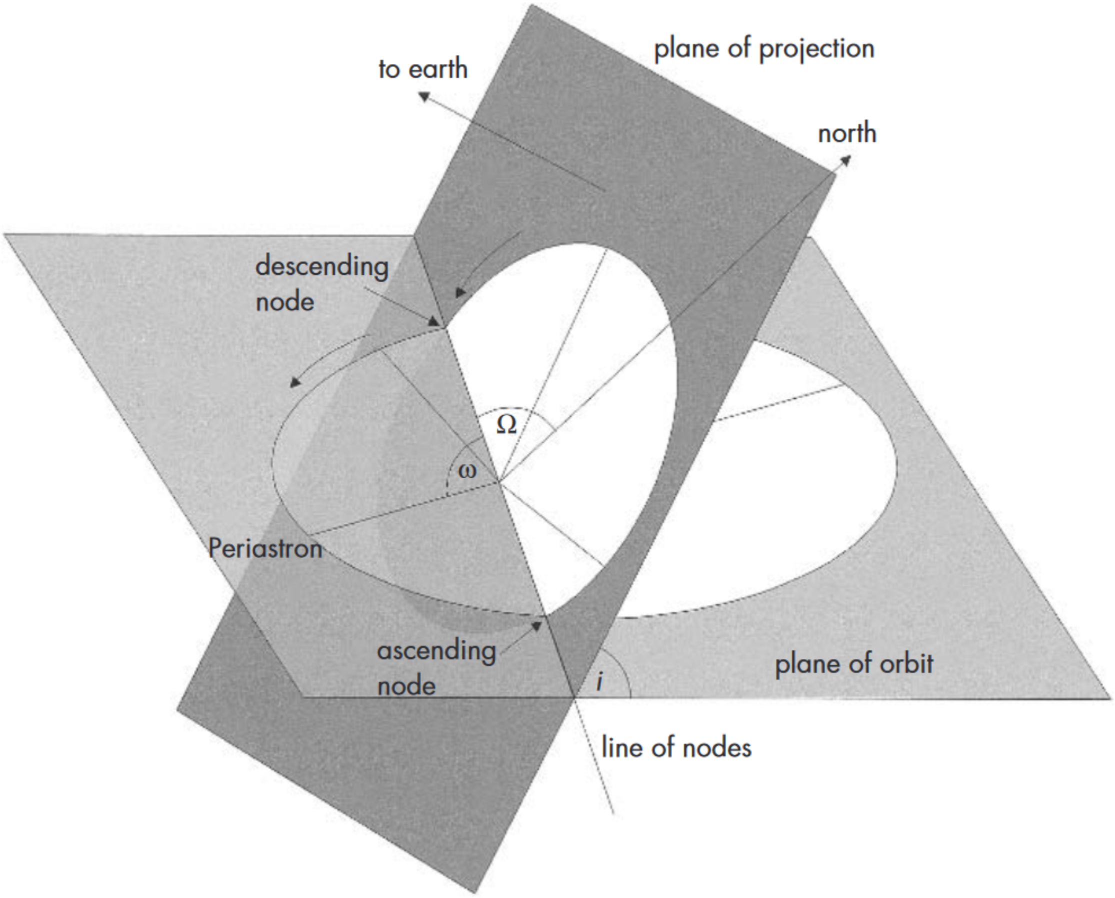

Figure 1.12: Schematic of binary orbit elements (stellar sources only, no scattering regions) from Fig. 7.4 of Alzner and Argyle (2012). Ω is the position angle of the line of nodes, measured counter-clockwise from north. The line of nodes is the line of intersection between the true and projected orbit planes. i is the inclination angle of the orbit, i.e. the angle between the true and projected orbital planes. ω is the argument of periastron measured from the line of nodes to the periastron (not applicable for circular orbits).

produces an offset from this location and shifts the origin. Non-spherical distributions of material ($\gamma \neq 0$) will also produce a constant offset in Q.

As noted in Section 1.5, rotating and translating the axes in $q - u$ space can allow for investigation of polarization compared to a dominant axis; naturally for binary polarization, the dominant axis is Ω, and the origin is shifted by sources of constant polarization (such as interstellar polarization). Using the continuum polarization to find the orbital axis of the system means that other sources of polarization, such as line polarization (discussed in more detail later), can be compared relative to the plane of the orbit rather than in isolation.

The BME model has been shown to describe WR binary systems well in general (e.g. St-Louis et al. 1993; St-Louis et al. 1988; Moffat and Piirola 1993) and is therefore depicted as curve a) in Fig. 1.11. However, it also makes an assumption of point sources that mean it cannot explain eclipse effects in close binary systems alone (e.g. for V444 Cygni St-Louis et al. 1993). Fox (1994a) developed extensions to the BME model to account for the occultation of scattering material by finite sized sources. The extensions rely on a spherically symmetric scattering region, which is unlikely to be physical for WR + O binaries with wind-wind collision (see Fig. 1.7). Another problem with the BME model is its reliance on extremely high-precision polarimetric measurements. Aspin, Simmons, and Brown (1981), Simmons, Aspin, and Brown (1982), and Wolinski and Dolan (1994) investigated the required polarimetric precision required to accurately estimate binary orbit parameters from the BME model. They found that the model becomes biased towards high inclination angles such that even for measurements with negligible uncertainty, $i < 20°$ cannot be estimated with any confidence (in particular, the 1-σ confidence interval extends down to $i = 0°$). Although Ω is unbiased, it cannot be reliably estimated below $i = 20°$. The shortcomings of these analytic models led to the numerical approach detailed in Section 1.8 and Chapter 4.

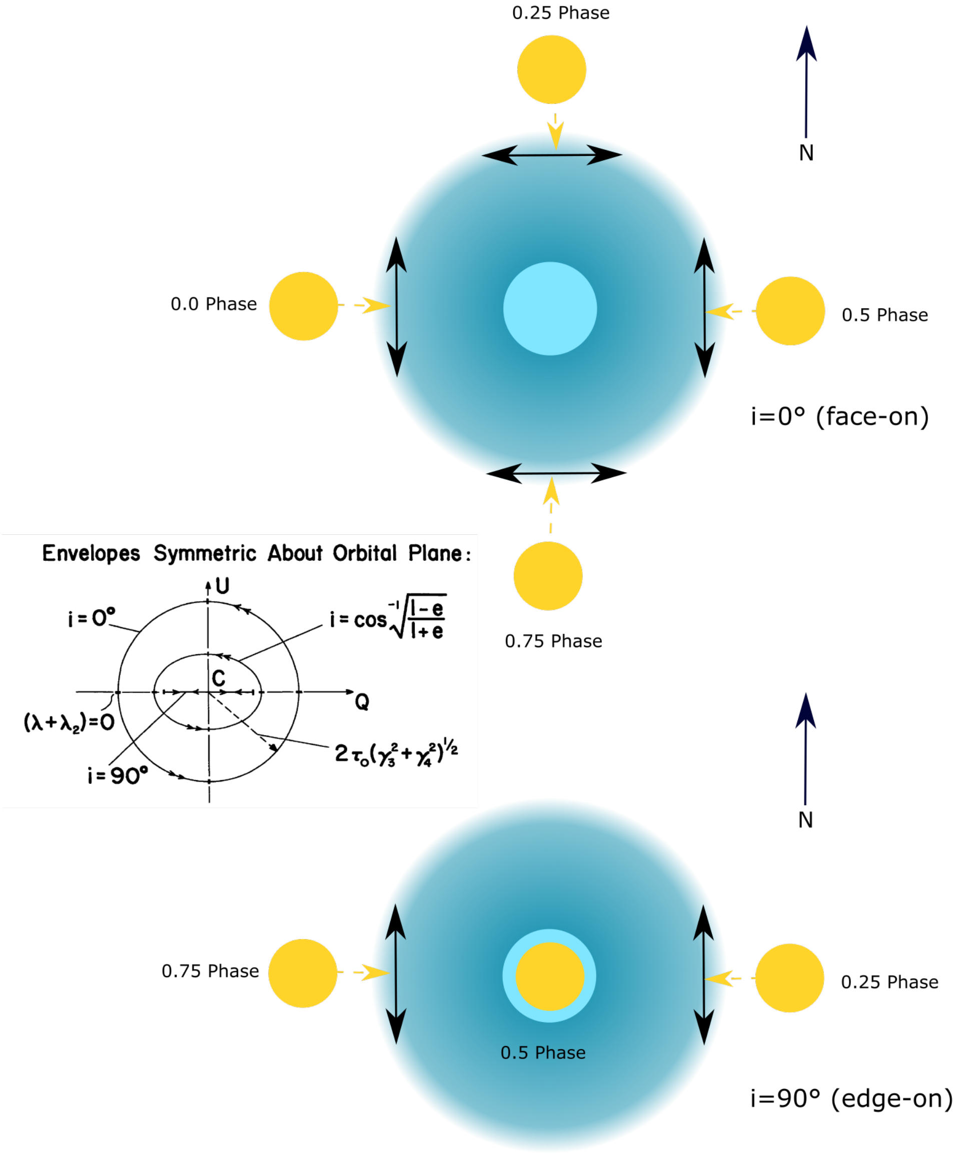

Figure 1.13: Sketch of the theoretical polarization variation of a binary system with phase and inclination angle, discussed in detail in § 1.5.2. The schematic shows the simplified case of a star surrounded by a spherical distribution of scatterers (blue circle and region respectively), illuminated both by a central star and by an orbiting star (yellow circle, illumination shown by dashed arrows). Polarization is shown by the black lines with double arrows and corresponds to $+q$ (vertical) and $-q$ (horizontal) polarization. Two extreme cases are shown, face-on ($i = 0^\circ$) and edge-on ($i = 90^\circ$) The inset figure shows how the BME model can be used to derive orbital quantities geometrically in $q - u$ space, given simplifying assumptions such as point sources and optically thin scattering material (Brown, McLean, and Emslie 1978).

One interesting analytic approach was devised by St-Louis et al. (1988), who showed that the mass-loss rate of WR stars in binary systems changes the amplitude of polarization variation with phase. I confirm this result with numerical models in Chapter 4.

Scattering by astrophysical dust also produces linear polarization. The extremely hot environments around WR + O systems tend to preclude the formation of dust, although some work suggests that dust may be present in the shielded regions created by colliding winds (Harries, Hillier, and Howarth 1998; Williams 2014) or in shells around the binary (e.g. Lau et al. 2017). Dust has been shown to form around some single late-type WC stars as well (e.g. Williams 2014). Only one star in my observational sample, WR 113 (discussed in Section 1.6.2), has shown evidence of dust production (Cohen, Barlow, and Kuhi 1975). Therefore, I assume that large-scale wavelength-dependent polarization effects are dominated by ISP (see Section 1.5 for a short summary and Chapter 2 for details of ISP). Because ISP is time-independent, it manifests as a constant polarization offset as a function of phase (curve d in Fig. 1.11).

Although Thomson scattering is spectrally grey, i.e., independent of wavelength, the amount of scattering (and thus degree and angle of polarization) occurring in a particular part of an observed spectrum is a function of the location of the material that produces emission or absorption at those wavelengths, and the geometry (projected onto the plane of the sky) and optical depth of the region that scatters that part of the spectrum. For example, an emission line arising in a WR + O binary wind collision region effectively orbits the WR star wind and illuminates it similarly to the O star companion, but this only occurs at the wavelengths of the emission line. This allows a further diagnostic: with spectropolarimetric measurements, not only can I determine the geometry and optical depth of the scattering region where the continuum light is polarized, but also constrain the location and distribution of specific elements in the system as well, based on models that predict their location in the WR wind or collision region (see Figures 1.5 and 1.8).

Theoretical and computational models have been used extensively in the interpretation of spectropolarimetric observations to determine scattering region geometries and optical depths for many different astronomical objects (e.g. Hoffman, Whitney, and Nordsieck 2003; Huk 2017; Shrestha et al. 2018; Wood et al. 1996a,b). When the observed system is a binary, time-dependent line polarization information can be used to constrain the properties of line emission and scattering regions in the system through interpretation of their phase-dependent behavior (Fig. 1.11). As our view of the scattering region changes over time due to the orbital motion in the system, we can obtain 3D information about the scattering geometry and emission sources with the aid of modeling (either analytical models such as that of Brown, McLean, and Emslie (1978) or numerical models as in Chapter 4). Of course, this is only true if the structures are stable over greater than the timescale of our observations. Previous observations of WR binary systems have shown stability of their polarization variation over a timescale of years (e.g. Drissen et al. 1987; St-Louis et al. 1993). I can also determine the optical depth of the scattering region and therefore its density. This provides a measure of the mass-loss and mass-transfer in the system, which I can use to investigate its subsequent evolution.

What happens to the polarization signal when a wind-wind collision region exists in a system, with a geometry such as that shown in Fig. 1.8? Kasen et al. (2004) investigated a similar scattering geometry for Type Ia SNe, in which one star in a binary system explodes while the other may create a low-density region in its "wake" as the ejecta engulf it. In this model, a sphere with a cone-shaped "cutout" was used as the scattering geometry. The cone had 5% of the density of the sphere. Their radiative transfer models showed that the q polarization signal was the greatest when the cone axis was perpendicular to the line of sight, shown in Figure 1.14. In this figure, the polarization of the lighter region is removed by the cutout, leaving a net positive polarization defined by the vectors in the darker region. Kasen et al. (2004) also found that the magnitude of the polarization in this model is dependent on the cone opening angle and filling density. In a binary system viewed at $i = 90°$, the model shown in Fig. 1.14 would correspond to the phases of quadrature, i.e. 0.25 and 0.75, when the q polarization due to the binary illumination is lowest[8]. Therefore one would expect some $-q$ polarization at those phases in a WR binary, with the polarization magnitude depending on the wind-wind collision region density and opening angle. At phases 0 and 0.5, the contribution of the cutout to polarization would be zero, and this contribution would smoothly transition between zero and the $-q$ value at quadrature. For inclination angles other than 90°, the cutout would always be partially visible and contribute to the polarization. In this scenario, the amplitude of variation with phase decreases, while the maximum $-q$ value stays constant, as i approaches 0° (or 180°) because the inclination angle approaches a constant perpendicular view of the cut out (i.e. where Kasen et al. showed the maximum polarization contribution would occur). Thus, at low inclination angles, the cutout contributes an almost constant polarization signal with phase.

By combining phased spectropolarimetric observations with 3D numerical modeling, then, I can investigate the structures in WR + O binary winds. In particular, analysis of the behavior of emission line polarization as a function of phase will enable constraints on mass loss and mass transfer and thus yield new insights into the possible evolution of such systems, as described in Section 1.4.1. The combination of strong emission lines arising in known locations (see Section 1.3) and possible continuum polarization from elongated winds (see discussion of the "line effect below") make WR + O binaries excellent targets for this kind of analysis. We are obtaining spectropolarimetric observations for a range of WR + O binary systems (see Section 1.6.2). I discuss 2 of these objects, WR 42 and WR 79, in Chapter 3. I am developing models to interpret the observations, and these are described in Chapter 4.

Spectropolarimetry has been successfully used to constrain the properties of the shock cone in the WN5 + O6 binary system V444 Cyg by Lomax et al. (2015). These authors

---

[8] Note that the rotation of the cone by 90° to match the orbital plane in Fig. 1.13 means that the polarization would be in negative q (the opposite of what Kasen et al. considered). This is equivalent to a position angle rotation in $q - u$ space.

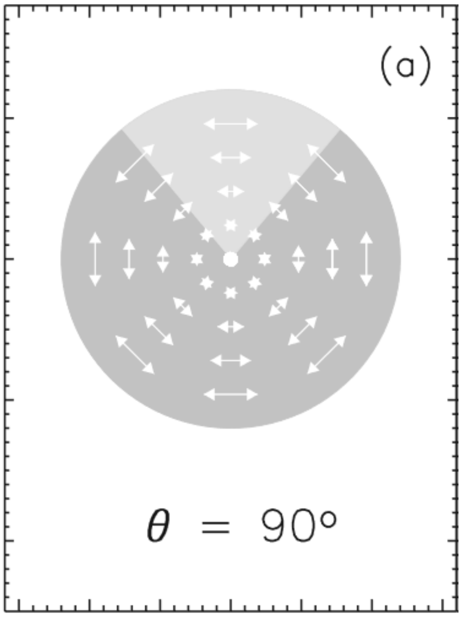

Figure 1.14: Spherical scattering region with conic cutout from Kasen et al. (2004). The lighter region shows the cutout, whose polarization is effectively subtracted from the total. The arrows show polarization vectors.

used constraints from X-ray observations to create a hydrodynamical model of a wind cavity produced by the O star within the WR star wind. They found that the polarization of the He II λ4686 emission line showed variations that correlated with the orientation of the wind cavity in the X-ray model. Additional observations showed that the polarization in this line increases at orbital phases corresponding to the edges of the opening angle of the wind cavity (Hoffman 2015). However, no analytical or numerical model has been produced to explain this behavior in more detail, nor has it been established whether other WR+O systems show similar line polarization behavior. In Chapter 4 I present a numerical model to investigate whether existing V444 Cygni models (Lomax et al. 2015; Marchenko et al. 1997) can explain the system's line polarization variations, and how applicable the model is to other WR + O systems.

As noted in §1.4.1, rapidly rotating WR stars may have density and/or geometry variation in their winds such as an equatorially compressed wind or a prolate optical photosphere.

The can lead to the empirical "line effect" (see §1.5). In WR binary systems, detecting the line effect becomes more complex. The WR wind is illuminated from multiple sources, and wind-wind interaction regions can create areas of enhanced density, increasing the polarization of emission lines by increasing asymmetry. This can create phase-dependent line polarization, as in case c) of Fig. 1.11, based on the well-studied mass-transfer binary β Lyrae (Lomax et al. 2012). Vink and Harries (2017a) used spectropolarimetry to search for the line effect in a sample of WR stars, including binaries, although they did not perform phased observations of the binary systems. Therefore, we need time-dependent spectropolarimetric observations to accurately determine if a WR star in a binary system has an elongated wind (case d) in Fig. 1.11). This means we can search for rapidly rotating WR stars in the systems where they may be forming. I show in Chapter 3 that as in Lomax et al. (2015), the amplitude of line polarization can vary with phase so a single observation of a binary system is not sufficient to clearly diagnose a line effect.

1.6 The Southern African Large Telescope and Robert Stobie Spectrograph

1.6.1 Instrument

The primary instrument used to collect new data for this dissertation was the Robert Stobie Spectrograph (RSS), attached to the Southern African Large Telescope (SALT) near Sutherland, South Africa (Buckley, Swart, and Meiring 2006; Potter et al. 2016). SALT has a fixed 11-m primary mirror, with the secondary mirror tracking across the primary to follow targets. The telescope is operated by an onsite observer and runs on a queue schedule, under which observations are assigned priorities and an algorithm chooses the observations that will be carried out during a given night. Because of the fixed primary, observations occur in two "tracks" on the sky separated by the secondary mirror housing.

Our access to RSS/SALT is courtesy of our collaborator Ken Nordsieck at the University of Wisconsin-Madison.

The RSS is a linear spectrograph covering a wavelength range of $3200 - 9000$ Å, with resolving power $R = 800 - 10000$. It is based on holographic gratings to minimise polarimetric effects (Burgh et al. 2003). The attached polarimeter can be used with any other mode, including multi-object spectroscopy, and has a field of view of 4×8 arcmin. It is based on half- and quarter-wave plate rotators with a Wollaston prism used as a beamsplitter to obtain the ordinary and extraordinary[9] beams and measure Stokes q, u, v (Potter et al. 2016). The polarimeter is calibrated to match the IAU conventions for polarimetry defined in Section 1.5. For the observations presented here, we chose to limit the wavelength range to $4200 - 7200$ Å to minimize the systematic error from RSS. Because we are only interested in linear polarization (see Section 1.5.2), we used only the half-wave plate in the instrument.

1.6.2 Target selection

We selected initial targets using the following criteria, designed to meet the observational goal of the project: to conduct the first study of WR+O binary systems using spectropolarimetry with good orbital coverage, in order to characterize their colliding winds and other mass transfer structures. We do not aim for a complete sample; rather, we chose a variety of WR types to investigate the corresponding range of spectropolarimetric behavior.

- WR binary system, spectroscopically confirmed
- Observable by SALT
- Visual-band apparent magnitude between approximately 5 and 15 for best spectropolarimetric precision
- Orbital period between 3 and 30 days

---

[9] This method uses the birefringance of the prism material to split the polarized light into polarized and unpolarized (Stokes I) beams. Comparing the beam intensity provides the normalized Stokes parameters q, u and v for different rotations of the wave plates aligned with the Stokes parameters (Clarke 2010).

The orbital period (and target selection in general) was chosen to allow for reasonable completion of 20 observations evenly spaced across each system's orbit. The short maximum orbital period also makes it extremely likely that there will be colliding winds in the target systems. The visual-band apparent magnitude range keeps exposure times below 1 hour per object while preventing saturation of the CCD, based on SALT/RSS sensitivity. I determined the visibility of targets using the SALT sky coverage guide and VISIBILITY CALCULATOR[10].

I checked for spectroscopic confirmation using the ninth catalog of spectroscopic binary orbits (Pourbaix et al. 2004) and the seventh catalog of Wolf-Rayet stars (Van Der Hucht 2001b). For newer targets, I used SIMBAD[11] to investigate the literature for applicable information. Additional references for the chosen targets are given in Table 1.2.

This has resulted in a sample of 18 targets – 7 WC type, 10 WN type and 1 WO type – out of a possible 68 WR binary stars visible from SALT. Their basic parameters are provided in Table 1.2. Of note are three stars in the main sample (non-italicized) that do not have known companions. WR 6 has most recently been considered a candidate for complex wind density structures (St-Louis, Tremblay, and Ignace 2018) but may also be an eccentric precessing binary orbit (Schmutz and Koenigsberger 2019). WR 12 has been clearly shown to have colliding winds (Fahed and Moffat 2012) and a period has been derived for it; however, the companion cannot be identified in the spectra. Similarly, WR 14 has shown significant radio variability that was interpreted as particle acceleration from a colliding wind (De Becker and Raucq 2013) as well as polarimetric variability over a long time-scale (Drissen, Robert, and Moffat 1992), but no strong spectral signatures from a binary companion (Sander et al. 2019). Italicized stars are part of the "fishing pool", a set of low-priority targets designed to take up gaps in the SALT observing queue and provide quick tests for interesting polarized spectral features. They do not necessarily meet all our

---

[10] http://astronomers.salt.ac.za/software/#VisibilityCalculator

[11] http://simbad.u-strasbg.fr/simbad/

Table 1.2: SALT targets with relevant parameters.

WR Number	Spectral type	RA (°)	Dec (°)	m_V	Period (d)	P. ref.	i (°)	Observations
6	WN4b + ?	103.554	-23.928	6.94	3.77	1	?	9
9	WC4 + O7	116.460	-34.330	10.9	14.3	2	64	10
12	WN8h + ?	131.197	-45.982	11.0	23.9	3	79	12
14	WC7 + ?	133.747	-47.592	8.80	2.42	4	79	12
21	WN5o + O4-6	156.631	-58.641	9.76	8.25	2	69	16
29	WN7h + O	162.693	-60.478	12.7	3.16	5	44	1
30	WC6 + O7.5V	162.775	-62.284	11.7	18.8	3	70	14
30a	WO4 + O5-5.5	162.912	-60.943	13.3	4.63	6	?	3
31	WN4o + O8V	163.437	-59.513	10.7	4.83	7	62	4
42	WC7 + O7V	167.517	-60.979	8.25	7.89	8	38	14
43a	WN6ha + WN6ha	168.781	-61.261	11.2	3.77	9	71	2
47	WN6 + O5V	190.963	-63.087	11.1	6.24	3	67	14
48	WC6 + O6-7V(+ O9.5/B0lab)	197.030	-65.306	16.8	18.3	10	?	3
62a	WN5 + O5.5-6	218.157	-61.498	13.8	9.14	11	45	2
71	WN6o + ?	240.956	-62.693	10.2	7.69	12	?	5
79	WC7 + O5-8	253.582	-41.820	6.95	8.89	2	34	10
97	WN5b + O7	264.223	-34.044	11.1	12.6	2	31-85	4
113	WC8d + O8-9IV	274.781	-11.633	9.43	29.7	13	62-78	16

Italicized stars are part of the “fishing pool”. Orbital periods are individually sourced, and have rigorous ephemeris measurements. Spectral types and visual apparent magnitudes are from SIMBAD. Inclination angles were sourced from the seventh catalog of WR stars (Van Der Hucht 2001b). References: 1) Georgiev et al. (1999); 2) Lamontagne et al. (1996); 3) Fahed and Moffat (2012); 4) Van Der Hucht (2001b); 5) Niemela and Gamen (2000); 6) Bartzakos, Moffat, and Niemela (2001); 7) Gamen and Niemela (1999); 8) Hill et al. (2000); 9) Schnurr et al. (2008); 10) Moffat and Seggewiss (1977); 11) Collado, Gamen, and Barbá (2013); 12) Isserstedt, Moffat, and Niemela (1983); 13) David-Uraz et al. (2012).

observing criteria e.g. WR 71's binary status is not clear (Isserstedt, Moffat, and Niemela 1983; Marchenko, Moffat, and Eenens 1998).

1.6.3 Observations

The observing plan for the project is intended to provide maximum orbital phase coverage (20 phase bins per object) for the objects in the sample. The queue-scheduling process for the telescope is well suited to this goal. Planning multiple visits targeting bright short-period binaries means that the observations can be accomplished in slots that are unsuitable for other projects, such as during bright time and in short time slots. Exposure times range from 1500–2400 seconds depending on the apparent magnitude of the target (i.e. dimmer targets have longer exposure times). Signal-to-noise ratios are typically greater than 100 for Stokes parameters. Observed R is greater than 1000 to facilitate line profile analysis.

Our completed observation counts are listed in the Observations column in Table 1.2. These are the result of four successful RSS-SALT proposals for the project (2017-1-SCI-040, 2017-2-SCI-014, 2018-1-SCI-008, 2018-2-MLT-005). A major setback occurred to the project in 2019. From December 3, 2018 to October 2019, a sensor in the wave plate rotator was mistakenly disabled. This caused a $\sim 5°$ random position angle uncertainty in the data taken in this timeframe. It was not detected earlier because of the previously well-calibrated instrument. These observations were thus discarded from the sample and are not shown as part of the count in Table 1.2. We also lost about 6 weeks' worth of observation time (approx. 12 observations) when the telescope was shut down due to COVID-19 in late March through early May 2020.

1.6.4 Data reduction

Polarimetric data reduction for RSS data is accomplished using the POLSALT Python software package[12]. First, basic CCD image reductions are run to prepare the images for

---

[12] https://github.com/saltastro/polsalt

polarization reduction. This includes overscan subtraction, gain correction, crosstalk correction and mosaicing. Then, wavelength calibration is done initially by eye by identifying bright lines in calibration data taken from a Xenon arc lamp that is exposed to the instrument for both the ordinary and extraordinary beams from the polarimeter. Previous identifications from prior calibrations can be used to guide this process. After identifying the first set of lines, the rest are automatically identified by the software. Next, cosmic ray rejection is done for each spectropolarimetric image (with a typical rate of 25 cosmic rays per second of exposure). The beams are corrected for distortion, then the brightest object in the spectrometer slit is assumed to be the science target, and its polarization spectrum extracted using a window defined around the object, typically 10". Waveplate position pairs (waveplate positions 45° apart) are used to calculate raw, unnormalized Stokes parameters with respect to the IAU conventions defined in Section 1.5. These parameters are evaluated for systematic error, and combined into Stokes Q and U fluxes. Flux calibration is performed using previously measured calibration targets and includes airmass correction. If systematic errors are higher than the expected 0.03%, the data can be culled to reduce the systematic error. Systematic uncertainties arise from the instrumental polarization, which for SALT is primarily due to the mirror's short focal length (Nordsieck et al. 2003).

The instrument suffers from a major source of additional systematic error when observing targets with high total polarization ($> 1\%$[13]). The two types of glass that are glued in sheets to form the wave plates are not aligned absolutely perfectly. This results in a wavelength-dependent and track-dependent "ripple" in the polarization position angle spectrum similar to that predicted by Nordsieck et al. (2003) for the mirror polarization response. An example is shown in Figure 1.15, measured using a 100% polarized lamp. Developing a robust method to correct the data for this effect is an ongoing effort that will become part of the reduction pipeline.

---

[13] This is not a flux dependence because a dim target can be highly polarized.

I have produced a first-order method to account for these effects, which takes the pure ripple spectrum from the lamp and fits it to existing reduced spectra using χ^2 minimization, scaling and translating the polarized lamp spectrum as necessary. This method is not an attempt to remove the effects of the ripple from the data; rather, it allows me to estimate appropriate uncertainties on continuum and line polarization values derived from uncorrected data. The lamp spectrum was interpolated with a cubic spline after any attempts to fit functions (such as a Fourier series or high-order polynomials) failed to produce accurate results.

I validated the method by producing synthetic data from the interpolated ripple spectrum. The synthetic data was generated by randomly scaling the interpolated ripple spectrum in the range 0–5, then Gaussian noise was added at each wavelength bin of the synthetic data at a level similar to observations (1.1° position angle standard deviation of the Gaussian distribution). I found that the fitting procedure could reproduce the input translation and scaling of the synthetic data within the fit uncertainties. Figure 1.16 shows 20 fits to the randomly scaled and noisy synthetic data. The scaling of the instrumental ripple data (the most important parameter to determine the uncertainty) matched the randomly produced scaling factor within fit uncertainties for all cases.

An example fit to science data is shown in Figure 1.17, for the star WR 42. The panels show the position angle data for multiple phases fit with the ripple spectrum. The fits are different for each observation because the observations were taken at different times and therefore arise on different tracks across the primary mirror. The polarization dependence means that each observation of each target needs to be fit to estimate uncertainties. The Python code that was written to perform this reduction is displayed in Appendix A.4.

Once the fitting process is completed, half the maximum amplitude of the fitted spectrum is used as an estimate of the 1-σ uncertainties on any computed continuum or line polarization values. This is because both of the processes used to extract such values (as described below) necessitate integration across multiple wavelength bins and can therefore

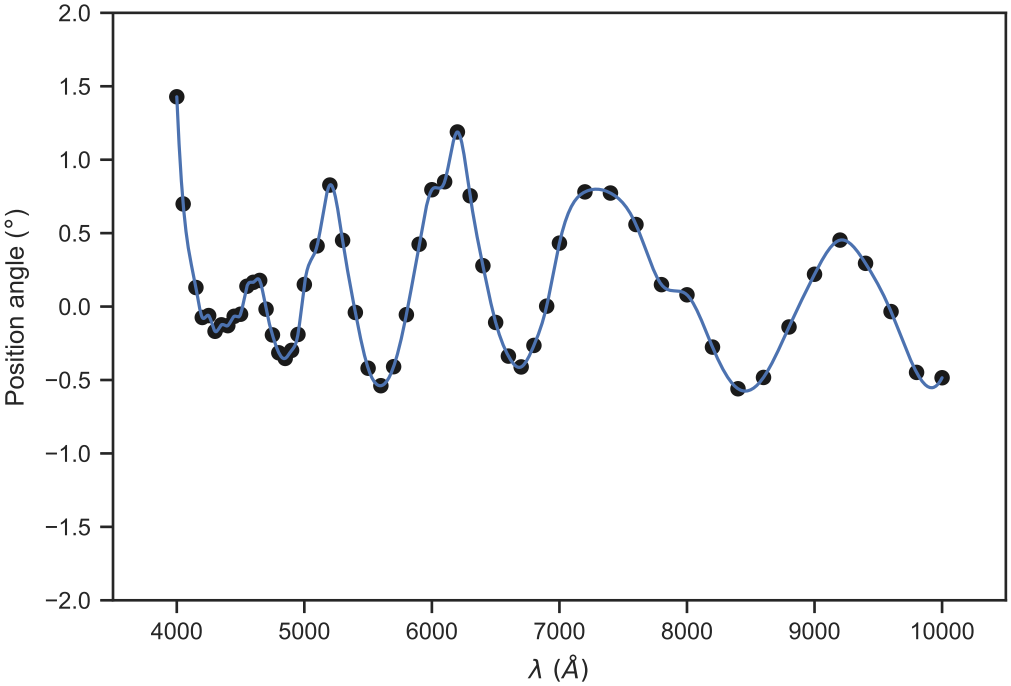

Figure 1.15: RSS/SALT instrumental polarization spectrum "ripple". The black points are the smoothed result of a 100% polarized Xe lamp observed by the instrument. The blue line is the cubic spline interpolation of the data (see Section 1.6.4).

cover some arbitrary part of the ripple spectrum. Half the maximum amplitude is used to provide the most conservative uncertainty estimate as an upper bound on the true uncertainty. Nordsieck is developing a calibration procedure that will allow us to reliably subtract the ripple from RSS data, producing more reliably polarization measurements.

Polarization spectra are complex and difficult to analyze without further reduction. Two different sources of polarization can be extracted from the spectra: continuum polarization, which for WR + O originates primarily from O-star companion light scattering in the WR wind, and line polarization, which originates from emission line light scattering in ionized material, primarily the WR wind. These two polarization signals can be expected to behave differently with the orbital phase of the binary, allowing us to interpret them separately (see Section 1.5.2).

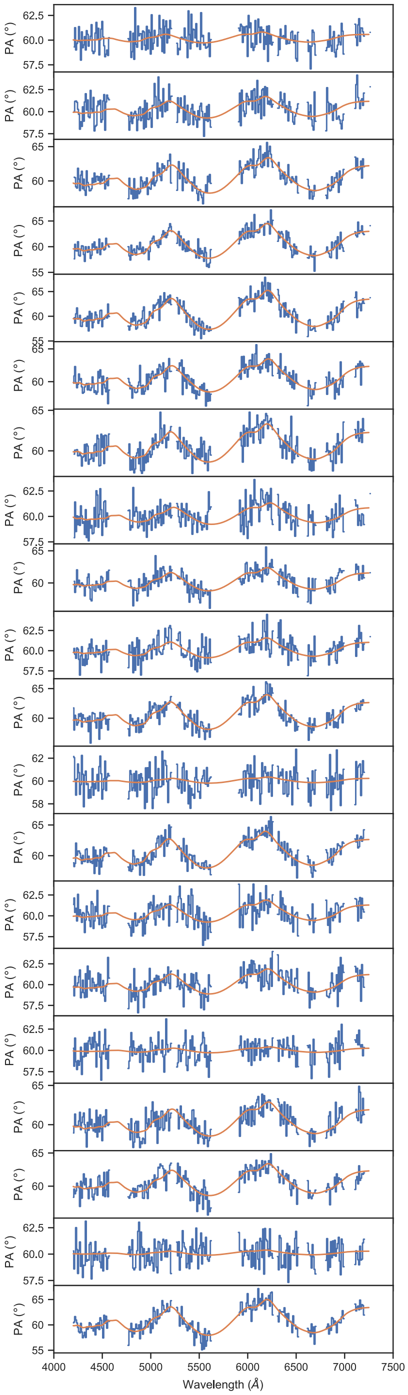

Figure 1.16: Fitted RSS position angle spectrum to synthetic data. The orange line is the interpolated instrumental position angle spectrum. The blue line is synthetic data with empty regions where strong emission lines would be removed from real data (see § 1.3).

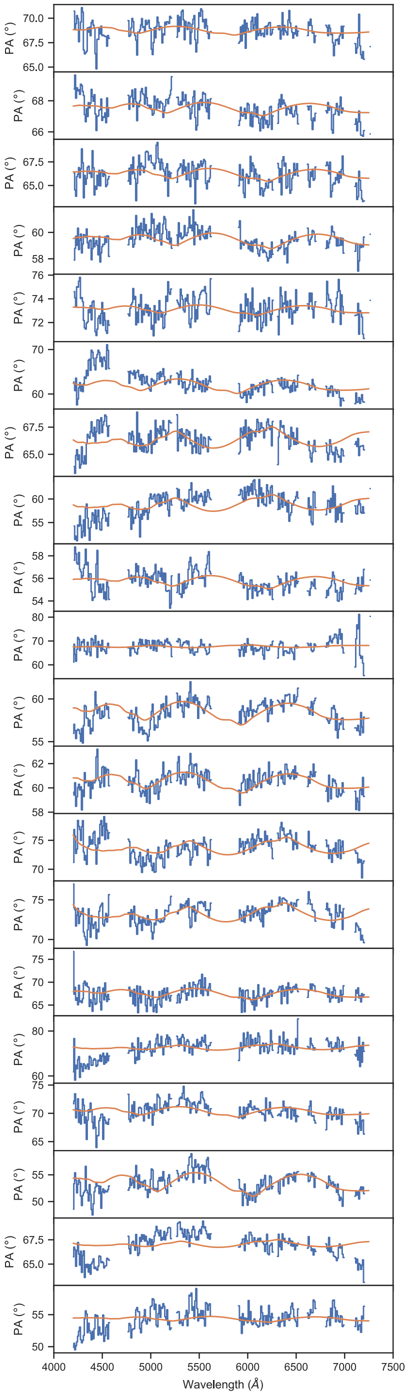

Figure 1.17: Fitted RSS polarization spectrum to WR 42 data. The orange line is the interpolated instrumental position angle spectrum. The blue line is the data with strong emission lines removed (see § 1.3).

Table 1.3: Narrow-band filter characteristics from Massey (1984). λ_c is the central wavelength.

Filter	λ_c (Å)	FWHM (Å)
b	4270	70
v	5160	130
r	6000	100

Continuum polarization can be easily extracted by performing a weighted integration of narrow-band filters with the observed spectra. In particular, the *bvr* filters from Smith (1968) and Massey (1984) are designed to avoid the strong emission lines present in WR spectra (see Figure 1.18). I wrote a Python script to extract continuum polarization from reduced SALT data, which is presented in Appendix A.5. The script linearly interpolates the narrow-band filters to the same wavelength scale as the input spectrum. It integrates the input flux and polarization weighted to the filter, following equation 1.17:

$$q_{out} = \frac{\int F_{obs}(\lambda) q_{obs}(\lambda) f(\lambda) d\lambda}{\int F_{obs}(\lambda) f(\lambda) d\lambda}, \tag{1.17}$$

where q_{out} is the filtered fractional polarization, $q_{obs}(\lambda)$ is the observed fractional polarization, $F_{obs}(\lambda)$ is the observed flux, and $f(\lambda)$ is the narrow-band filter function, approximated by Gaussians with central wavelengths and full-width half maximum (FWHM) given in Table 1.3. The integration limits are the region where $f(\lambda) > 0$.

To extract emission line polarization, a more complex method is required. For this project, I adopted the polarization flux equivalent width (*pfew*) method described in Hoffman, Nordsieck, and Fox (1998) and successfully used in Lomax et al. (2015) for analyzing the WR + O binary system V444 Cyg. Using this method, I can separate the polarization spectrum into its continuum and line components without making assumptions about the system. This is accomplished by estimating and subtracting the continuum polarization in a given line region. Thus the total polarization within a given emission line region can

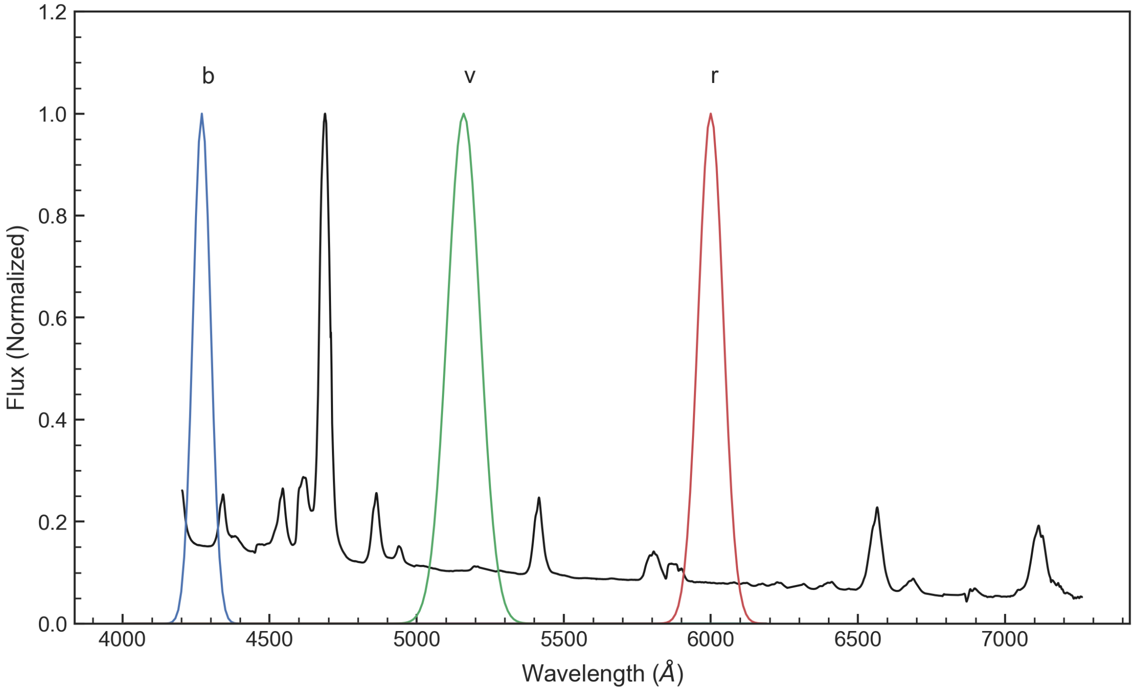

Figure 1.18: Example WR star spectrum with narrow-band filters overlaid, showing how the *bvr* filters avoid strong emission lines. The observation is from RSS/SALT of WR 6 (see Table 1.2).

be calculated. The method is as follows. The observed polarization spectrum $\%q_{obs}$ is composed of several parts:

$$\%q_{obs} = \frac{Q_c F_c + Q_L F_L + Q_{ISP} F_{total}}{F_{total}} \tag{1.18}$$

The polarization in a bin centered on a line is given by $Q_c + Q_l + Q_{ISP}$ where c is continuum polarization, L is line polarization and ISP is the interstellar polarization component (see Section 1.5 for information about the ISP). The flux in the bin is given by $F_{total} = F_c + F_L$ (for optical wavelengths where emission from interstellar material is negligible). Here I am using only Q for simplicity; the equations apply to U with simple substitution of U for Q. I must first estimate the continuum flux F_c and polarized continuum flux $Q_c F_c$ in the wavelength bin. Subtracting $Q_c F_c$ from the numerator and F_c from the denominator of equation 1.18 yields equation 1.19 for the flux equivalent width polarization $\%q_{few}$:

$$\%q_{few} = \frac{Q_c F_c + Q_L F_L + Q_{ISP} F_{total} - (Q_c F_c + Q_{ISP} F_c)}{F_{total} - F_c}, \tag{1.19}$$

This becomes

$$\%q_{few} = \frac{Q_L F_L + Q_{ISP} F_L}{F_L} = \%q_L + \%q_{ISP}, \tag{1.20}$$

where $\%q_L$ is the polarization percentage of the line radiation and $\%q_{ISP}$ is the interstellar polarization caused by line radiation. I find the total polarization of the line by summing Equation 1.19 over the chosen line region. Given that the ISP changes very slowly with wavelength compared to the width of a typical emission line (Serkowski, Mathewson, and Ford 1975; Whittet et al. 1992), the value of Q_{ISP} is effectively constant and the total polarization of an emission line of width w (or number of bins w) is given by

$$\%q_{\text{entire line}} = \frac{\sum_{i=1}^{w}(Q_{L,i}F_{L,i} + Q_{ISP}F_{L,i})}{\sum_{i=1}^{w} F_{L,i}} \tag{1.21}$$

$$= \frac{\sum_{i=1}^{w} Q_{L,i}F_{L,i}}{\sum_{i=1}^{w} F_{L,i}} + \frac{Q_{ISP}\sum_{i=1}^{w} F_{L,i}}{\sum_{i=1}^{w} F_{L,i}} \tag{1.22}$$

$$= \%q_L + \%q_{ISP}. \tag{1.23}$$

These equations hold for both Q and U, and for positive or negative values in either Stokes parameter.

My application of the *pfew* method to SALT data is presented in Appendix A.6. The Python code runs a graphical user interface that provides the user with a step-by-step process to load data, select the lines to measure and define the widths of the continuum and line regions, and extract the line polarization. It also displays the selected regions on a plot of the loaded data, and the plot window can be used to choose the regions graphically (see Figure 1.19).

1.7 Monte Carlo radiative transfer

As the name suggests, Monte-Carlo radiative transfer uses the Monte Carlo numerical method to solve the radiative transfer equation (see Appendix A).

The Monte Carlo method is based on pseudorandom number generation that samples a probability density function (PDF) in order to reproduce physical effects in a statistical way (Whitney 2011). To sample a value x_0 from a PDF, the cumulative probability distribution (CPD) $\psi(x_0)$ must be inverted. The CPD is defined as the normalized integral of the PDF $P(x)$:

$$\psi(x_0) = \frac{\int_a^{x_0} P(x)dx}{\int_a^b P(x)dx}. \tag{1.24}$$

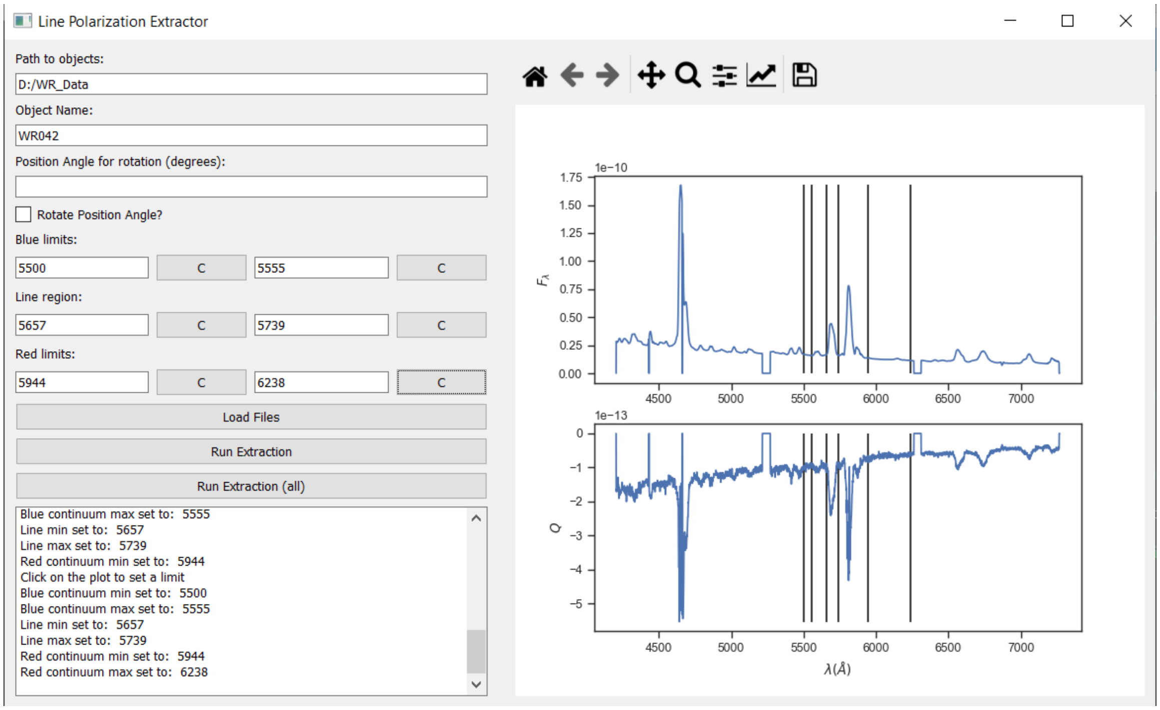

Path to objects: D:/WR_Data

Object Name: WR042

Position Angle for rotation (degrees):

☐ Rotate Position Angle?

Blue limits: 5500 5555

Line region: 5657 5739

Red limits: 5944 6238

```
Blue continuum max set to:  5555
Line min set to:  5657
Line max set to:  5739
Red continuum min set to:  5944
Click on the plot to set a limit
Blue continuum min set to:  5500
Blue continuum max set to:  5555
Line min set to:  5657
Line max set to:  5739
Red continuum min set to:  5944
Red continuum max set to:  6238
```

Figure 1.19: Example of integrated line polarization extraction from RSS/SALT data using my code.

As x_0 ranges from a to b, $\psi(x_0)$ uniformly ranges from 0 to 1 (Duderstadt and Martin 1979). Thus, one samples for x_0 by using a random number generator to choose a $\psi(x_0)$ value between 0 and 1, and then solving Eq. 1.24 for x_0. This method can be straightforwardly applied to sample the distance that a virtual photon packet will travel in a region of optical depth τ before being absorbed or scattered. The PDF for this situation, based on the equation of radiative transfer (Eq. A.1), is given by

$$P(\tau)d\tau = e^{-\tau}d\tau. \tag{1.25}$$

Converting this to a CPD, where ξ is the generated random number between 0 and 1 and τ_0 is the desired sampled quantity, we find

$$\psi(\tau) = \frac{\int_0^{\tau_0} e^{-\tau}d\tau}{\int_0^{\infty} e^{-\tau}d\tau} = 1 - e^{-\tau_0} = \xi. \tag{1.26}$$

Inverting this result provides

$$\tau_0 = -\ln(1-\xi). \tag{1.27}$$

This means that if the sampled optical depth τ_0 is greater than τ, the photon is statistically likely to interact with the scattering region (it may "interact" by scattering or becoming absorbed, depending on the albedo of the material inside the region[14]).

The concept of the photon packet is used to simulate radiative transfer. Photon packets (usually referred to in this context simply as "photons") are virtual particles that at each step has a direction and location in the model. Photons are emitted from a source location, passed through the model, and in the most straightforward case are collected into directional bins once they exit the model. If the photon is scattered while traveling, it may gain polarization. The amount of polarization acquired in a given scattering event can be described by the Stokes vector (see Section 1.5)

$$\mathbf{S}(\theta,\phi) = [I(\theta,\phi), Q(\theta,\phi), U(\theta,\phi), V(\theta,\phi)], \tag{1.28}$$

following Chandrasekhar (1960) and Whitney (2011). The polarization is defined in the observer's frame, therefore Mueller matrices (Müller 1948) need to be used to rotate into and out of the photon propagation direction (Chandrasekhar 1960). After scattering from direction $\mathbf{P_1}(\theta_1,\phi_1)$ to $\mathbf{P_2}(\theta_2,\phi_2)$ across angle Θ, where i_1 is the initial scattering angle and i_2 is the final scattered angle (in the photon's frame; see Figure 1.20), the Stokes vector becomes:

$$\mathbf{S} = \mathbf{L}(\pi - i_2)\mathbf{R}(\boldsymbol{\Theta})\mathbf{L}(-i_1)\mathbf{S}' \tag{1.29}$$

---

[14] Albedo can be sampled directly using ξ since it is between 0 and 1. If ξ is greater than the specified albedo of the scattering region, the photon will be absorbed instead of scattered.

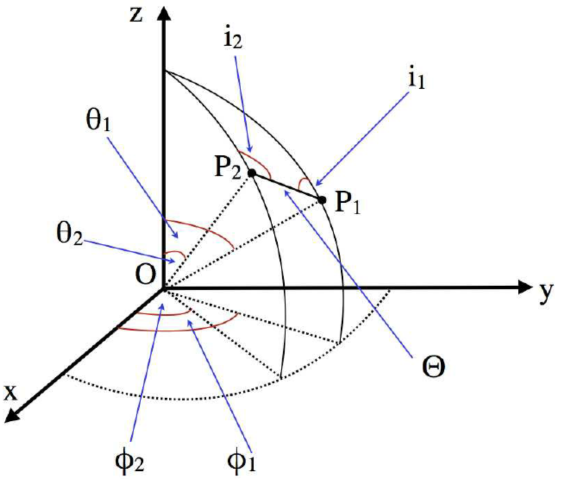

Figure 1.20: Scattering geometry from Chandrasekhar (1960).

where $\mathbf{S}'$ is the incident Stokes vector and $\mathbf{L}$ is the Mueller matrix used to rotate in and out of the photon packet's frame by angle ψ:

$$\mathbf{L}(\psi) = \begin{bmatrix} 1 & 0 & 0 & 0 \\ 0 & \cos 2\psi & \sin 2\psi & 0 \\ 0 & -\sin 2\psi & \cos 2\psi & 0 \\ 0 & 0 & 0 & 0 \end{bmatrix}. \tag{1.30}$$

The matrix $\mathbf{R}(\Theta)$ is the scattering matrix, defined in the photon's frame for electron scattering (and also Rayleigh scattering; Whitney 2011):

$$\mathbf{R}(\Theta) = \frac{3}{4} \begin{bmatrix} \cos^2\Theta + 1 & \cos^2\Theta - 1 & 0 & 0 \\ \cos^2\Theta - 1 & \cos^2\Theta + 1 & 0 & 0 \\ 0 & 0 & 2\cos\Theta & 0 \\ 0 & 0 & 0 & 2\cos\Theta \end{bmatrix}. \tag{1.31}$$

With these equations, we need to sample Θ and i_1. We can calculate the intensity for a scattered photon from $I = (\cos^2\Theta + 1)I' + (\cos^2\Theta - 1)\cos 2i_1 Q' - 2\cos\Theta \sin 2i_1 U'$ (where the primed values refer to the incident vector $\mathbf{S}'$). This can be accomplished using the rejection method (Whitney 2011). i_1 and $\cos\Theta$ are sampled from an isotropic distribution of angles, so $i_1 = 2\pi\xi_1$ and $\cos\Theta = 2\xi_2 - 1$, where ξ_1 and ξ_2 are two different random numbers. $I(\cos\Theta, i_1)$ is calculated from the sampled values. The PDF is sampled as $P(\cos\Theta, i_1) = \xi P_{max}$ where P_{max} is the maximum PDF value determined analytically or numerically. If $P(\cos\Theta, i_1) < I(\cos\Theta, i_1)$, the Θ and i_1 values can be accepted; otherwise $P(\cos\Theta, i_1)$ is sampled again until it is less than $I(\cos\Theta, i_1)$. With values for $\cos\Theta$ and i_1, the final θ, ϕ and i_2 angles can be calculated following the laws for sines and cosines in spherical geometry (Green 1985). The matrices can be multiplied following Equation 1.29 to calculate the Stokes parameters, and the resultant vector is normalized to $P(\cos\Theta, i_1)$ so that I remains equal to 1 as the photon packet propagates (correct for Thomson scattering).

Uncertainties in the resulting Stokes parameters are calculated using the standard deviation of the summed outgoing Stokes parameters in each θ, ϕ directional output bin (I, Q, U, V), normalized by $\sqrt{N}$ where N is the number of photons in the output bin (Wood et al. 1996a). The output Stokes parameters in each bin are summed and normalized by the number of photons in the bin, then divided by the solid angle of the bin. Flux values are obtained by dividing by the total number of photons emitted across the model (Chandrasekhar 1960).

1.8 *SLIP* Code overview

SLIP (Supernova LIne Polarization) is a Fortran + MPI[15] code based on the Monte Carlo radiative transfer methods outlined in Whitney (2011) and summarized in Section 1.7. I have upgraded it to use methods such as dynamic array allocation. The simulation grid is a linearly spaced spherical polar coordinate system in r, θ and ϕ. Photon packets are emitted from user-specified locations in the grid and propagate through the user-defined scattering region. At each grid cell the optical depth is integrated until the photon scatters

---

[15] MPI is the Message Passing Interface, used to send variables between processors for parallel operations https://www.open-mpi.org/.

or exits the grid cell. The photon packets are collected as they exit the simulation limits and are binned into different observational directions in θ and ϕ. In this way, a single model can be viewed from multiple angles, greatly reducing computation time. Orbits can be simulated by simply moving around the grid in the ϕ direction. The code is parallel via MPI, so that each processor on a high-performance cluster can propagate photons, and then the photons are summed at the end following the normalization described in Section 1.7.

The spherical polar model grid is defined in 3 dimensions, but the user can restrict it to 2 or 1 by limiting the θ or ϕ grids to one cell each. This model grid defines the maximum resolution of a given scattering material geometry. Regardless of the grid resolution, photon packet location and direction are defined to floating point precision. A spherical polar grid was chosen for *SLIP* because this makes it easier to define frequently-used ϕ-symmetric geometries.

Output bins are defined in θ_o and ϕ_o, which can be higher or lower resolution than the model grid through which the photons move. Photon packet counting follows Poisson statistics, so increasing the output bin resolution by a factor of 2 requires a factor of 4 increase in photon counts to maintain the same measurement uncertainty for a given output bin.

The scattering region in *SLIP* is defined by the user from a range of preset geometry types: ellipsoids, bow shocks, toroids, and a sphere with a spherical region removed. This last scattering material arrangement is most relevant to this dissertation and bears some extra explanation. In this case, the scattering material is defined with an input file that defines density as a function of radius. Then, a spherical region is defined by its radius and position in the $x - y$ ($\theta = 90^\circ$) plane. Within this spherical region, all scattering material is removed and density is set to 0. See Chapter 4 for the physical reasoning behind this case. All other scattering regions have a constant density defined by the optical depth at $\theta = 90^\circ$. This means that for the bow shock and ellipsoidal cases the optical depth changes with θ as the column depth changes with θ, because the scattering region boundary is not constant with θ.

Emission regions are also defined by the user. They can consist of 1 or 2 spherical emitting surfaces (referred to as stars), or 3 different volume emission regions. One star is placed at the origin of the model grid, while the companion star is placed by the user at an arbitrary point along the x-axis ($\theta = 90°$, $\phi = 0°$). The radius of each star is also user-defined. The user can use point sources instead of extended surfaces by setting the radius to 0. The volume emission regions are based on the scattering region geometry. One region can emit from anywhere within the scattering region where density is present. Another can emit from a user-defined shell within the scattering region. The final option is to emit from 2 individual wedge-shaped regions whose size and position in r and ϕ is controlled by the user. The θ extent of these wedge-shaped regions can also be controlled by the user. The wedge shape is the result of using the ϕ axis to control the size of the regions: as the radial coordinate of the region increases, so does the arc length defining the outside edge of the region. Figure 1.21 shows the different possible emission regions in the $x - y$ plane.

1.9 Broader impacts and this dissertation

Although WR stars are rare, they have a significant impact on their surroundings because of their strong winds and deaths as SNe with or without LGRBs. Their SN provide enrichment of the interstellar medium with metals is critical for the development of the complex molecules necessary for life. Though we have population-scale models for the impact of rotation, mass loss, and binary interactions on the evolution of massive stars (e.g. Dorn-Wallenstein and Levesque 2020), we lack the observational evidence of these effects. In this dissertation, I use observational spectropolarimetry and 3D radiative transfer modeling to constrain the geometric and mass-loss characteristics of WR winds and WR + O binary wind collision regions. These measurements provide new insight into these complex

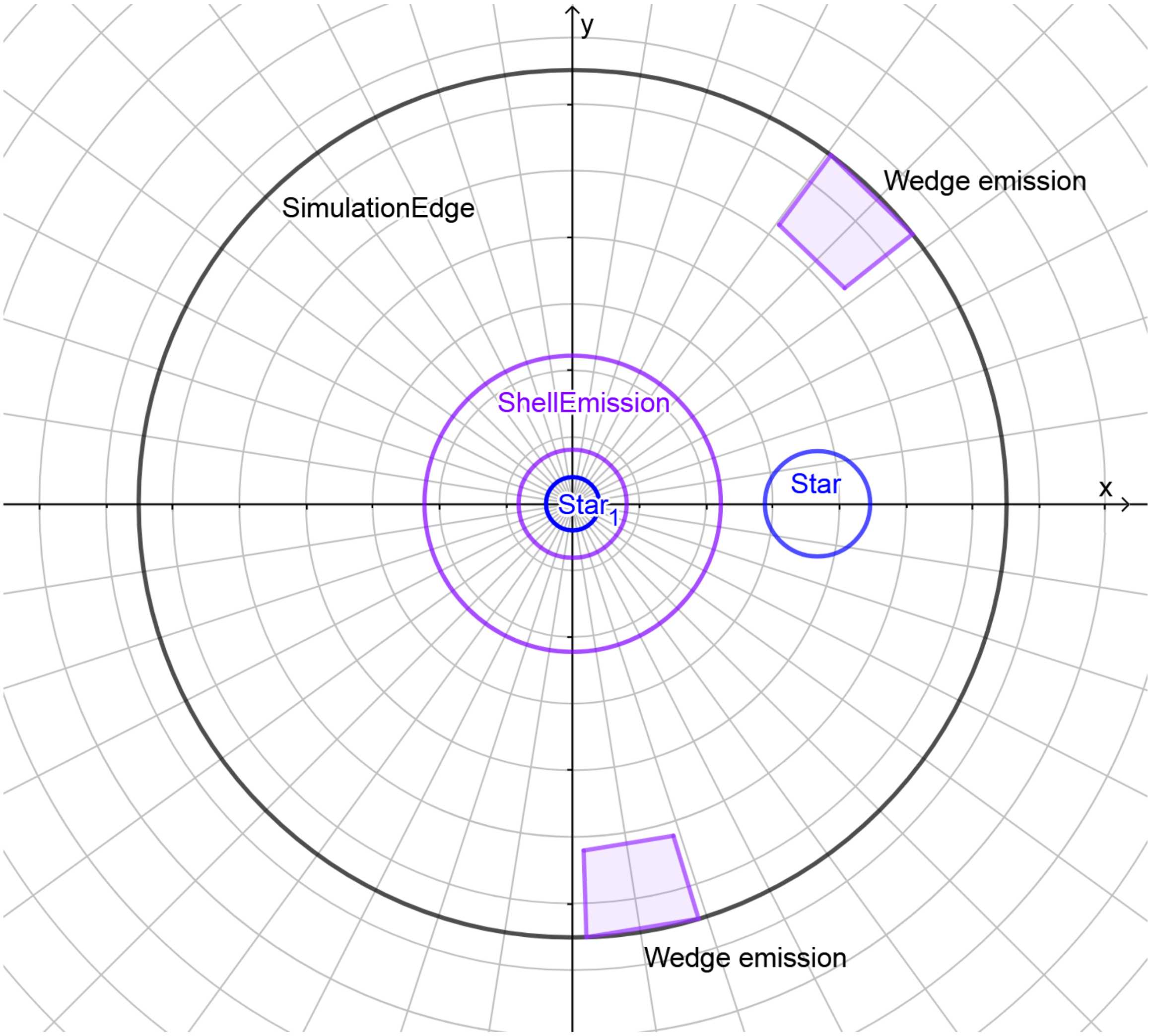

Figure 1.21: *SLIP* emission regions shown here in the $x - y$ plane. A polar grid is shown to approximate the model grid. The solid black circle is the edge of the model. The stars are spherical emitting surfaces. The shell and wedge emission regions are volume emission.

systems, and form the basis of future work that will extend the analysis to more systems, and take full advantage of the detailed spectropolarimetry from RSS/SALT.

In Chapter 2, I investigate the bulk geometry of WR winds using polarization to search for the signatures of binary interaction and rapid rotation that are expected to influence stellar evolution. This work contains the largest single sample of WR polarization measurements published to date.

Chapter 2 was previously published in *The Astronomical Journal* as Fullard et al. (2020), and is reproduced in full here. It may necessarily repeat some of the information provided in this introductory chapter. The data in Chapter 2 were reduced using the standard polarimetric methods described in Piirola (1988). Extinction is not relevant for polarimetry; instead the equivalent interstellar polarization correction is discussed in detail.

In Chapter 3, I extend this method further using time-dependent spectropolarimetric data from RSS/SALT to explore the geometries of two very similar WR + O binary systems in more detail. These spectropolarimetric data allow me to conduct the first detailed investigation of the behavior of emission line polarization in WR binary stars. The results yield information about the geometry and orbital behavior of different layers of the WR stellar wind, and the wind collision regions.

Finally, I have constructed new radiative transfer simulations, presented in Chapter 4, that will enable interpretation of the RSS/SALT spectropolarimetric data by including both continuum and line polarization output in 3D. These models will allow me to determine the extent to which the WR + O systems observed with SALT are, for example, very similar in structure but observed at different inclination angles. I test the model against the well-observed system V444 Cygni, and match the observations of the continuum polarization behaviour. In Chapter 5, I conclude and discuss future work resulting from this dissertation.

Chapter 2

A multi-wavelength search for intrinsic linear polarization in Wolf-Rayet winds

2.1 Abstract

Wolf-Rayet stars have strong, hot winds, with mass-loss rates at least a factor of ten greater than their O-star progenitors, although their terminal wind speeds are similar. In this paper we use the technique of multiband linear polarimetry to extract information on the global asymmetry of the wind in a sample of 47 bright Galactic WR stars. Our observations also include time-dependent observations of 17 stars in the sample. The path to our goal includes removing the dominating component of wavelength-dependent interstellar polarization (ISP), which normally follows the well-known Serkowski law. We include a wavelength-dependent ISP position angle parameter in our ISP law and find that 15 stars show significant results for this parameter. We detect a significant component of wavelength-independent polarization due to electron scattering in the wind for 10 cases, with most WR stars showing none at the ~0.05% level precision of our data. The intrinsically polarized

stars can be explained with binary interaction, large-scale wind structure, and clumping. We also found that 5 stars out of 19 observed with the Strömgren *b* filter (probing the complex λ4600–4700 emission line region) have significant residuals from the ISP law and propose that this is due to wind asymmetries. We provide a useful catalogue of ISP for 47 bright Galactic WR stars and upper limits on the possible level of intrinsic polarization.

2.2 Introduction

Massive hot stars have high luminosities and as a result they drive strong winds via line-driving radiation pressure, mainly through UV photons interacting with ions in their hot wind. Those massive stars evolved to the cool part of the H-R diagram drive strong winds via radiation pressure mainly on dust grains (e.g. Lafon and Berruyer 1991). Above initial masses of $\sim$20 $M_\odot$, massive stars evolve into a classical Wolf-Rayet (cWR) stage of He-burning, with most of their outer H-rich envelopes removed by pulsating winds in an intervening, relatively short LBV stage (or possibly an RSG stage for the least massive among them; Smith 2014, 2017). The extremely strong winds of cWR stars exceed those of their main-sequence (MS) O-star progenitors by at least an order of magnitude, even though their luminosities are rarely greater than those of their progenitors (Crowther 2007). The prime reason for this difference between MS and cWR stars is that cWR can reach the Eddington limit, at which the luminosity to mass ratio approaches unity. In most cases they also have high surface temperatures, from which the enhanced UV flux can drive strong winds due mainly to the large number of atomic transitions of iron in various ionization stages in the UV (Hillier 1989).

Another branch of stars with WR-like spectra are the most massive and luminous MS stars known, mostly of generic type WNLh or O/WNLh (with h sometimes replaced by ha or (h)). We include such stars if they are in the updated online general WR catalogue (Crowther 2015). For convenience, we group cWR and these luminous H-rich stars under one designation, i.e."WR".

With typical mass-loss rates of 10^{-5} $M_{\odot}$/yr and terminal velocities of 2000 km/s, WR winds are optically thick out to about 2 R_{*} (where R_{*} is the radius at a Rosseland optical depth of 20) and optically thin beyond this (Hamann et al. 2019). The outer, thin part is stratified under the spherically symmetric assumption, with emission lines of higher ionization formed closer to the hotter lower boundary and lines of lower ionization formed further out, although with a degree of overlap between the ionization groups (e.g. Hillier 1989). The inner thick wind remains essentially unobservable, making it impossible to directly probe the key stellar properties at R_{*}. But one can nevertheless get a reasonable indirect handle on these parameters by modelling the emerging emission-line spectrum (Hamann et al. 2019). Another technique is to track the trajectories of inhomogeneities in the outer, observable wind, such as clumps and co-rotating interaction regions (CIRs) as seen in O stars, which have their origin in the inner wind region, if not at R_{*} itself (Ramiaramanantsoa et al. 2019, 2018).

Another factor affecting WR winds is the rotation of the underlying star; rapid rotation is likely an important element in creating Long-duration Gamma-Ray Bursts (LGRBs; Woosley and Bloom 2006). Rapid rotation of some WR stars has been inferred by Harries, Hillier, and Howarth (1998) and others using line depolarization, also known as the line effect. In this model, the flattened wind leads to higher polarization in continuum light, which mostly arises from near the base of the optically thin wind. This is accompanied by less polarization of lines with lower ionization states as they are formed further out in the wind where there are fewer free electrons off which to scatter. The scattering of light by free electrons (or ions, to a much lesser degree) leads to polarization in an *asymmetric* wind, whereas a spherically symmetric wind will show no net polarization for any lines or continuum. However, Stevance et al. (2018) found that they could not rule out the presence of rapid rotation using the lack of a line effect as the sole diagnostic.

Any Galactic polarimetric measurement contains an interstellar polarization (ISP) contribution due to scattering of starlight by aligned dust grains in the interstellar medium.

There are multiple ways to extract the intrinsic stellar polarization from such measurements (e.g., Quirrenbach et al. 1997). For example, observing the target using spectropolarimetry allows one to use time invariant line polarization to estimate and then subtract the ISP contribution (Harrington and Collins 1968). Since the ISP does not change rapidly with time, fitting observed polarization variability using models such as that of Brown, McLean, and Emslie (1978) can also recover the intrinsic polarization component. We use a third method, characterizing the ISP by obtaining multi-wavelength broadband polarimetric observations and simultaneously fitting the empirical Serkowski law describing the ISP behavior (Serkowski, Mathewson, and Ford 1975; Whittet et al. 1992; Wilking et al. 1980) along with a wavelength-independent, constant level of polarization assumed intrinsic to the star. This achieves both characterization of the ISP and identification of any significant continuum polarization caused by free-electron scattering in a flattened wind. In this work, we apply this Serkowski + constant fit method to continuum-dominated polarimetry of a sample of 47 Galactic WR stars. Our observations (taken between 1989 and 1991) used broadband $UBVRI$ filters, as well as a Strömgren b filter in some cases to isolate the WR emission-line complex at ∼4650Å. We present our data in Section 2. In Section 3, we discuss in more detail the cases of six stars that show polarimetric time variability. Our fits to the ISP and intrinsic polarization are the subject of Section 4. Finally, we discuss our results in Section 5 and conclude in Section 6.

2.3 Data

We obtained our multiband polarimetry in two observing runs by A. F. J. Moffat, one in the North at the 1.25m Crimean Observatory telescope in Sept 1989, the other in the South at the 1.5m ESO/La Silla telescope in May 1991. Both these telescopes were equipped with a simultaneous 5-channel polarimeter designed and built by V. Piirola (Korhonen, Piirola, and Reiz 1984; Piirola 1973; Piirola 1988). At La Silla the photo-tube in the I-band was malfunctioning, so we replaced this filter with a medium band Strömgren b filter to simulate partial spectropolarimetry. Only the brightest stars had enough flux to give useful data in this filter due to its width compared to the standard Johnson filters. Fortunately, the lack of *I*-band data proved not to be a major handicap when we fit the data as a function of wavelength (Section 2.5). We calibrated the polarization angles in each filter using standard polarized stars as in (Moffat and Piirola 1993). We also observed unpolarized standard stars to eliminate the instrumental polarization (which was very small, less than 0.01% in all bands).

Table 2.1 lists the stars we observed, along with their *V* magnitudes, spectral types, binary status, and, if applicable, their periodicities (including those due to non-binary variation), all taken from the online WR catalogue of Crowther (2015) unless stated otherwise.

2.4 Mean polarization of time-dependent observations

For systems with multiple observations, we require a single mean polarization value per band so that we can calculate the constant intrinsic and ISP components. We obtained these mean values in one of two ways, depending on the system and number of observations. In the case of binaries with known orbital periods, we fitted theoretical binary polarization models to our data in each waveband and took the resulting constant q and u values to represent a "systemic mean" polarization for the system. To fit the models, we used previously derived binary parameters from Table 2.2. These fits also allowed us to derive new physical parameters for WR 133; see *a*) below. For single stars, we took an uncertainty-weighted mean of the polarization measurements in each band. Table 2.3 tabulates these mean $UBVRIb$ polarimetric values and uncertainties; we discuss individual cases in the subsections below.

a) WR 133 This is a binary WN5o + O9I system. Its observed polarimetric data are presented in the appendix, Table A.2. To calculate its systemic mean polarization, we followed Moffat et al. (1998), fitting both q and u simultaneously with an analytical polarization model for elliptical binary orbits derived from Brown et al. (1982), corrected

Table 2.1: Basic parameters for stars included in our sample. M_V taken from the SIMBAD database. Spectral type and binary status are taken from Crowther (2015) unless otherwise noted. Periods are taken from Van Der Hucht (2001a, 2006) unless otherwise noted.

WR	HD	Alt ID	m_V	Spectral type	Binary status	Period (d)	Ref.
ESO/La Silla							
6^{ac}	50896	EZ CMa	6.91	WN4b	CIR?	3.77	⋯
8	62910		10.10	WN7o/CE	SB1	38.4	⋯
9	63099	V443 Pup	10.50	WC4 + O7	SB2	14.305	1
14	76536		8.80	WC7+?	SB1	2.42	⋯
16^{a}	86161	V396 Car	8.36	WN8h	⋯	⋯	⋯
21	90657	V398 Car	9.65	WN5o + O4-6	SB2	8.25443	2
22^{a}	92740	V429 Car	6.42	WN7h + O9 V-III	SB2	80.336	⋯
23	92809		9.03	WC6	⋯	⋯	⋯
24	93131		6.48	WN6ha	⋯	⋯	⋯
25	93162		8.80	O2.5 If* / WN6 + O	SB2	207.85	3
40^{a}	96548	V385 Car	7.70	WN8h	⋯	⋯	⋯
42^{bc}	97152	V431 Car	8.07	WC7 + O7V	SB2	7.8912	4
43^{a}	97950	NGC3603abc	9.03	a=A1: WN6ha + WN6ha	SB2	3.7724	5
				c=C: WN6ha + ?	SB1	8.89	5
46	104994	DI Cru	10.93	WN3bp	?	0.28-0.33	6
48^{a}	113904	* θ Mus	5.53	WC6 + O6-7V(+ 09.7Iab)	SB1	19.1375	7
52	115473		9.00	WC4	⋯	⋯	⋯
57	119078		9.40	WC8	⋯	⋯	⋯
69	136488		9.10	WC9d + OB	SB2	2.293	⋯
71^{a}	143414	LT TrA	10.10	WN6o	SB2?	7.69	⋯
78	151932	V919 Sco	6.51	WN7h	⋯	⋯	⋯
79^{bc}	152270		6.59	WC7 + O5-8	SB2	8.8911	4
86	156327	V1035 Sco	9.32	WC7 (+ B0III-I)	VB	0.1385	⋯
90	156385		6.92	WC7	⋯	⋯	⋯
92	157451		10.20	WC9	⋯	⋯	⋯
103^{a}	164270	V4072 Sgr	8.74	WC9d + ?	SB1	1.7556	⋯
108	313846		9.89	WN9ha	⋯	⋯	⋯
110	165688		9.87	WN5-6b	CIR?	4.08	8
111^{a}	165763		7.82	WC5	⋯	⋯	⋯
113^{a}	168206	CV Ser	9.10	WC8d + O8-9IV	SB2	29.700	9
123	177230	V1402 Aql	11.12	WN8o	SB1?	2.3940	⋯

Table 2.1: (cont.)

WR	HD	Alt ID	M_V	Spectral type	Binary status	Period (d)	Ref.
Crimean Observatory							
1	4004	V863 Cas	10.14	WN4b	SB1?	...	...
3	9974		10.69	WN3ha	SB2	46.85	...
127	186943	QY Vul	10.69	WN5o + O8.5V	SB2	9.5550	10
128	187282	QT Sge	10.51	WN4(h)	SB2?	3.56	...
133[b]	190918	V1676 Cyg	6.75	WN5o + O9I	SB2	112.4	...
134[b]	191765	V1769 Cyg	8.08	WN6b	CIR	2.255	11
135	192103	V1042 Cyg	8.11	WC8	...	...	...
136	192163	V1770 Cyg	7.50	WN6b(h)	SB1?	4.554	...
137	192641	V1679 Cyg	7.91	WC7pd + O9	SB2	4766	12
138	193077		8.01	WN5o + B?	SB2	1538	13
139[bc]	193576	V444 Cyg	8.00	WN5o + O6V-III	SB2	4.212454	14
140	193793	V1687 Cyg	6.85	WC7ed + O5.5fc	SB2	2900	15
141[bc]	193928	V2183 Cyg	9.78	WN5o + O5V-III	SB2	21.6895	...
148	197406	V1696 Cyg	10.30	WN7ha + O4-6V	SB2	4.317336	16
153	211853	GP Cep	9.00	a1: WN6o/CE + O3-6	SB2	6.6887	17
				a2: B0:I + B1:V-III	SB2	3.4663	17
155[bc]	214419	CQ Cep	8.80	WN6o + O9II-Ib	SB2	1.6412436	...
157	219460B		10.75	WN5o (+ B1II)	VB	1.7860	...

[a] Denotes systems with 2–5 observations. [b] Denotes systems with more than 5 observations. [c] Denotes systems for which our data have been previously published. 1: Spectral Type Bartzakos, Moffat, and Niemela (2001), 2: Spectral Type Fahed and Moffat (2012), 3: Period Gamen et al. (2006), 4: Period Hill et al. (2000), 5: Period Schnurr et al. (2008), 6: Period Marchenko et al. (2000), 7: Period Hill, Moffat, and St-Louis (2002), 8: Binary status St-Louis et al. (2009), 9: Period Hill, Moffat, and St-Louis (2018), 10: Period La Chevrotière, Moffat, and Chené (2011), 11: Period Aldoretta et al. (2016), 12: Period Lefèvre et al. (2005), 13: Period Annuk (1990), 14: Period Eriș and Ekmekçi (2011), 15: Period Williams (2019), 16: Period Munoz et al. (2017), 17: Period Demers et al. (2002)

Table 2.2. Extant estimated parameters for systems with time-dependent data that were fit in Section 2.4.

WR	E_0 (HJD)	P(d)	e	i (°)	Ω (°)	$\omega_{\rm WR}$ (°)	Ref.
133	2447420.5 ± 0.036	112.4 ± 0.02	0.39 ± 0.007	···	···	18.9 ± 0.0107	1
134	···	2.255 ± 0.0008	···	···	···	···	2
139	2441164.311 ± 0.007	4.212454 ± 0.000004	0.00	80.8 ± 1.6	-41.8 ± 3.8	···	3
141	2448840.80 ± 0.002	21.6895 ± 0.00003	0.00	68 ± 12	103 ± 25	···	4

References. — 1: Robert et al. (1989) and Underhill and Hill (1994), 2: Aldoretta et al. (2016), 3: Eriş and Ekmekçi (2011)(E_0, P); St-Louis et al. (1993)(i, Ω), 4: Marchenko, Moffat, and Eenens (1998)

Table 2.3. Mean polarization data for all our targets, calculated as described in Section 2.4. The mean column key is: S = Snapshot observational data, SM = systemic mean polarization in the case of stars with fitted multiple observations, or weighted mean polarization in the case of stars without significant polarization variability.

WR	Variability	Mean	Obs. count	HJD 2,440,000+	Band	q (%)	σ_q (%)	u (%)	σ_u (%)
1	SB1?	S	1	7768.5470	U	-5.713	0.101	-1.148	0.204
					B	-6.243	0.053	-1.383	0.086
					V	-6.442	0.092	-1.423	-0.104
					R	-5.748	0.047	-1.360	0.059
					I	-5.122	0.065	-1.163	0.059

Note. — Table 2.3 is published in its entirety in the machine-readable format. A portion is shown here for guidance regarding its form and content.

by Simmons and Boyle (1984) and modified for an extended source of scatterers (see Robert et al. 1992). The model equations are

$$q = q_0 + \Delta q \cos\Omega - \Delta u \sin\Omega, \tag{2.1}$$

$$u = u_0 + \Delta q \sin\Omega + \Delta u \cos\Omega, \tag{2.2}$$

where

$$\Delta q = -\tau_3[(1+\cos^2 i)\cos 2\lambda - \sin^2 i] \tag{2.3}$$

and

$$\Delta u = -2\tau_3 \cos i - \sin 2\lambda\,. \tag{2.4}$$

The parameters q_0 and u_0, which we adopt as our systemic mean values, represent the interstellar (plus any constant intrinsic) polarization. As usual, Ω is the rotation of the line of nodes on the sky counter-clockwise from the north and i is the orbital inclination with respect to the line of sight. The quantity λ is defined by $\lambda = \nu + \omega_{\rm WR} + \pi/2$, where ν is the true anomaly and $\omega_{\rm WR}$ is the argument of periastron for the WR star. Finally, τ_3 is given by $\tau_3 = \tau_*(a/r)^\gamma$, with τ_* representing the mean optical depth, a the mean orbital separation, and r the instantaneous separation. The parameters a and r are related by

$$a/r = [1 + e\cos(\lambda - \lambda_p)]/(1-e^2)\,, \tag{2.5}$$

where e is the orbital eccentricity and λ_p is the periastron passage, with $\lambda_p = \omega_{\rm WR} + \pi/2$. In the expression for τ_3, γ is a power index that reflects the actual free-electron density around the WR star between two plausible extremes: $\gamma = 1$ for a uniformly ionized wind (reasonable for the hottest WR winds) and $\gamma = 2$ for an idealized global point source of scatterers. The second case means that the free electrons in the WR wind are located at the WR star radius so that we can ignore any extension in radius. This approximates a decrease in ionization in the outer wind of the WR star.

WR 133 was also observed polarimetrically by Robert et al. (1989). We used their blue single-filter broadband data in the 0.6–0.9 phase region to improve the overall fit, treating this source as though it was simply another observed band with its own q and u zero points to be fitted. We discarded the Robert et al. (1989) zero-point values because their data were not observed with the same instruments as ours.

The polarization in WR stars is caused by electron scattering in the hot, ionised outflow, and as a consequence we expect it to be largely wavelength-independent. Therefore, for WR 133 we kept all parameters the same for each band, except for the q and u zero points (q_0 and u_0), then fitted all bands simultaneously in q and u. We phased the data using the published ephemeris for the system (listed in Table 2.2). We fixed e, P and Ω using the estimates from Underhill and Hill (1994; Table 2.2). Lastly, we carried out the fit minimizing the uncertainty-weighted χ^2 values as a function of q_0, u_0, Ω, τ_3, and i with LMFIT (Newville et al. 2014). We used the least-squares Trust Region Reflective method with Huber loss function (Huber 1964) to provide a robust method of dealing with outliers. We found that fixing $\gamma = 1$ provided the best fit as measured by a Kolmogorov-Smirnov test of the Studentized residuals compared to a Gaussian distribution with $\mu = 0$ and $\sigma^2 = 1$, though the data are not complete enough to reliably discriminate between $\gamma = 1$ or 2. The systemic mean polarization values for each band are presented in Table 2.3, and we list the fitted orbital parameters in Table 2.4. The fits are displayed in Figure 2.1.

Given our fitted value for the inclination, $i = 115.9^\circ \pm 7.3^\circ$, we attempted to calculate the masses of the components using the $M \sin^3 i$ values provided by Underhill and Hill (1994). We derived $M_O = 1.12\,\mathrm{M}_\odot$ and $M_{WR} = 0.55\,\mathrm{M}_\odot$, unrealistically low masses for both spectral types, implying that our fitted inclination angle is too close to 90°. Using the polarization-derived orbital parameter confidence intervals from Wolinski and Dolan (1994), we find that our σ_P/A metric is approximately 0.6, where $\sigma_P \approx 0.038\%$ is the average uncertainty of our polarization measurements and $A = (|q_{max} - q_{min}| + |u_{max} - u_{min}|)/4 = 0.063\%$ describes the amplitude of the polarization variation fit. Using Fig. 5 from Wolinski and Dolan (1994), we estimate the critical value of i as $\sim 70°$ or $\sim 110°$, for which the upper limit of the possible inclination reaches 0° or 180°, respectively. Thus our fitted inclination is more properly expressed as $i = 115.9°^{+64.1°}_{-7.3°}$. This unfortunately makes it difficult to derive further parameters of interest from our inclination angle with any confidence. Given the expected inclination range of 15–30° (Underhill and Hill 1994), Fig. 5 of Wolinski and Dolan (1994) suggests that given our current estimate for A, measurement uncertainties of less than $\sim 0.0008\%$ are required to verify this small inclination angle polarimetrically.

Under the assumption that our τ_* value and the orbital separation values from Underhill and Hill (1994) are correct, we provide an estimate of the mass-loss rate $\dot{M}$ using the following equation from Moffat et al. (1998) (see also St-Louis et al. 1988):

$$\dot{M}_{WR}/2 \times 10^{-5} M_{\odot}\ \mathrm{yr}^{-1} = \frac{\tau_*(v_\infty/2000\ \mathrm{km\ s}^{-1})(a/0.5\ \mathrm{AU})}{0.0016(f_c/0.6)(\alpha/0.5)} \tag{2.6}$$

where f_c is the fraction of the total light from the companion star, α is the number of scattering electrons per nucleon, a is the mean orbital separation and v_∞ is the WR terminal wind velocity. We adopt $v_\infty = 1535$ km s^{-1} from Niedzielski and Skorzynski (2002), $\alpha = 0.5$ for fully ionized He, and calculate $f_c = I_O/(I_{WR} + I_O) = 10^{-6.55/-2.5}/(10^{-4/-2.5} + 10^{-6.55/-2.5}) = 0.913$ using absolute magnitudes from Bowen et al. (2008) and Crowther (2007) for the O and WR stars respectively. We adopt $a = 1.154$ AU from Underhill and Hill (1994). This results in a low mass-loss rate of $\dot{M}_{WR} = 6.52 \pm 0.6 \times 10^{-6} M_{\odot}\ \mathrm{yr}^{-1}$. This is within the upper limit reported by St-Louis et al. (1988), and provides a tighter constraint for this system.

b) WR 139 and WR 141 Although these data were previously published by Marchenko, Moffat, and Koenigsberger (1998; WR 139) and St-Louis et al. (1993; WR 141), these authors did not provide the fit parameters q_0 and u_0. We therefore recalculated the fits to recover the systemic mean values. Since these binaries both have circular orbits, the

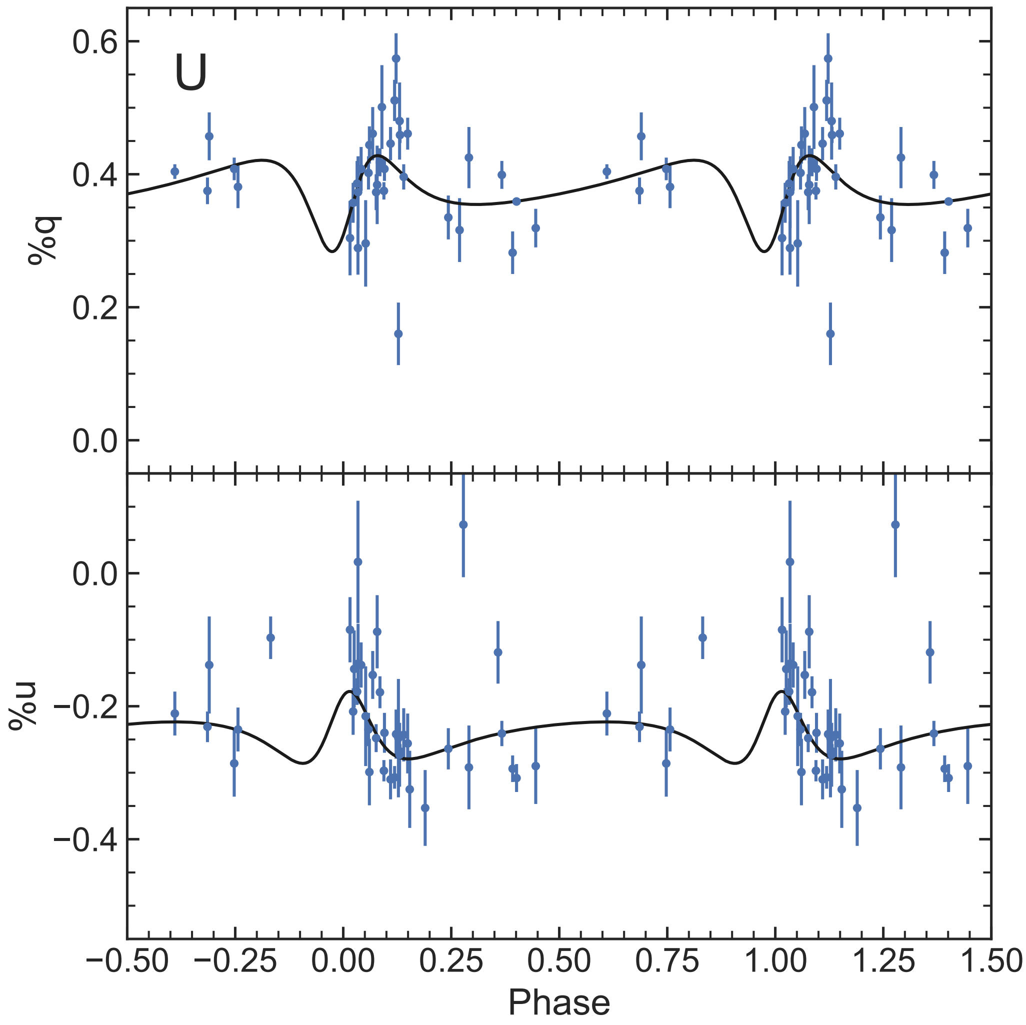

Figure 2.1: $UBVRI$ filter data and orbital fits for WR 133 (Section 2.4**a**). Panels correspond to U through I filters. The final panel displays data from Robert et al. (1989) for comparison. The black lines represent our fit to the data using equations 2.1 and 2.2. The data presented in this figure are available in the Appendix, Table A.2. Following convention, we display more than one full period in order to clarify behavior around primary eclipse.

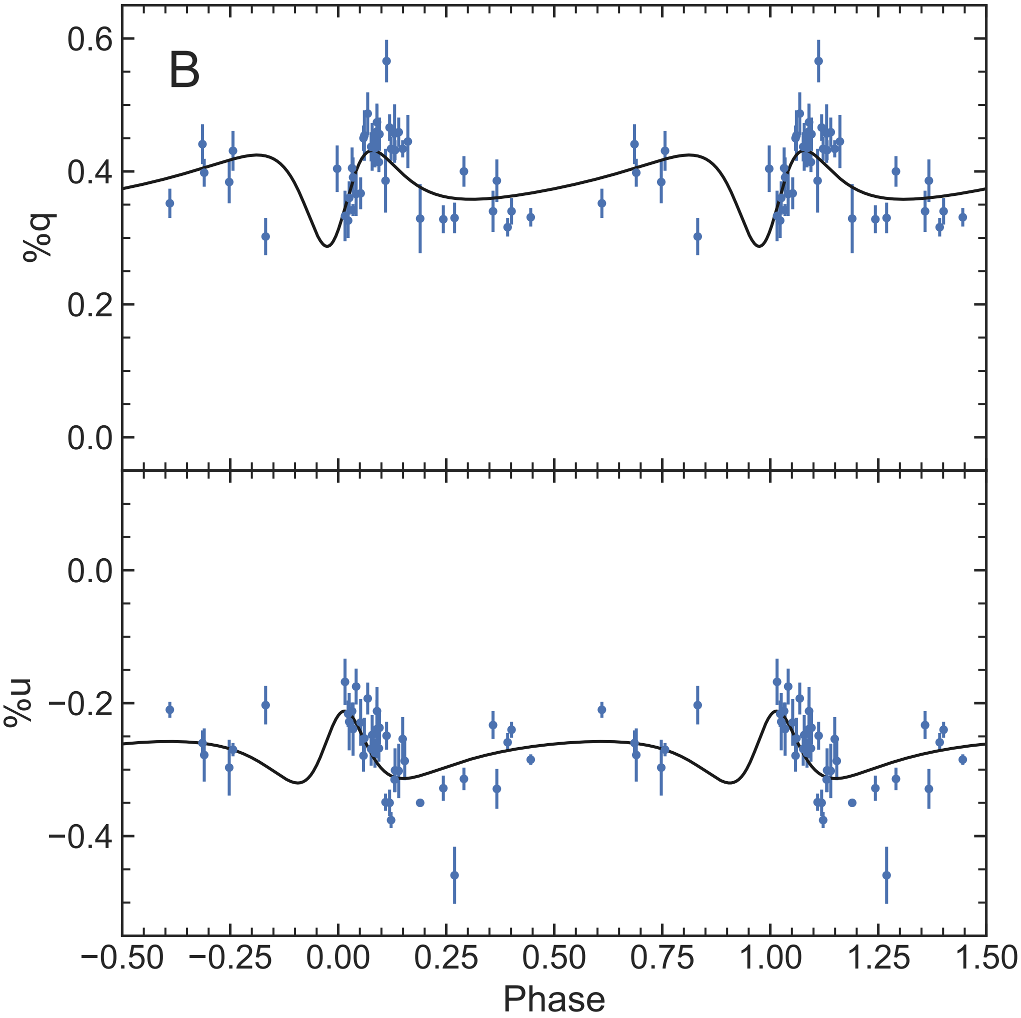

Figure 2.1: (cont.)

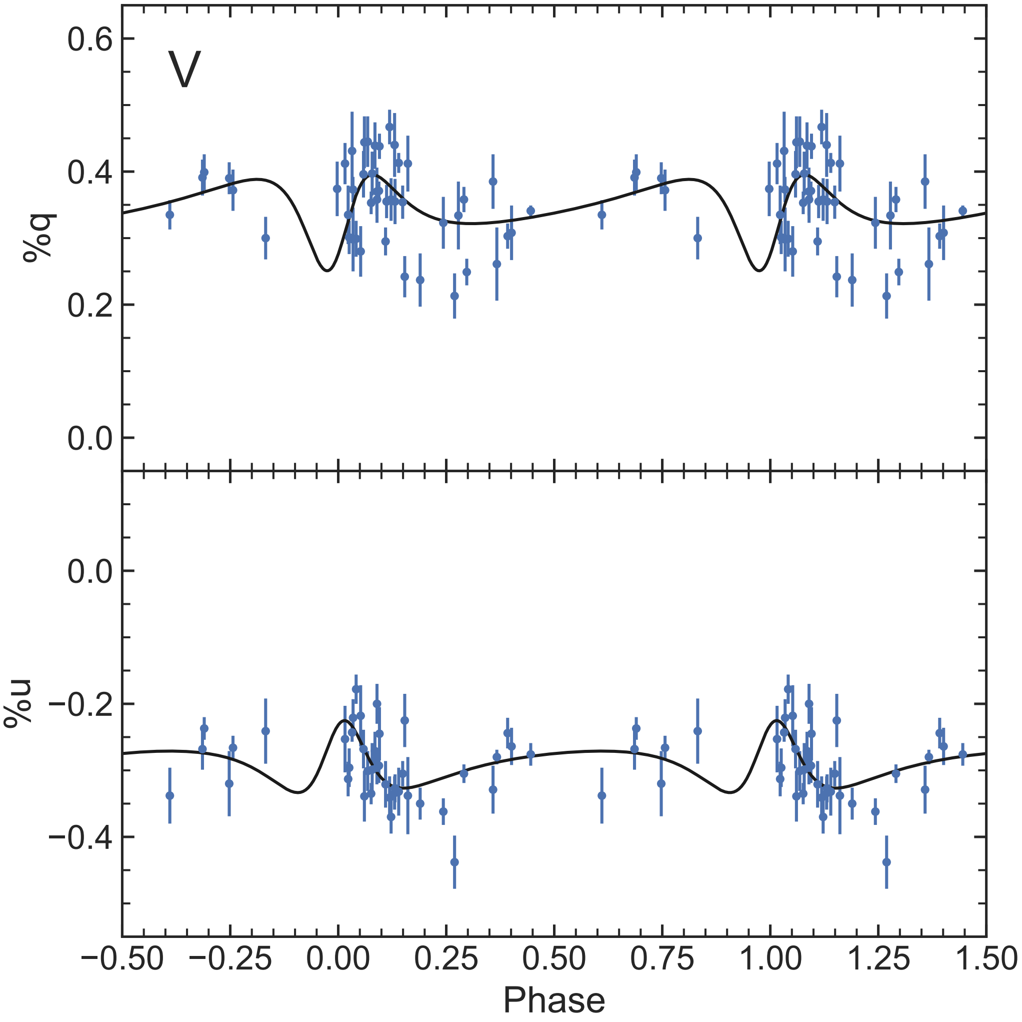

Figure 2.1: (cont.)

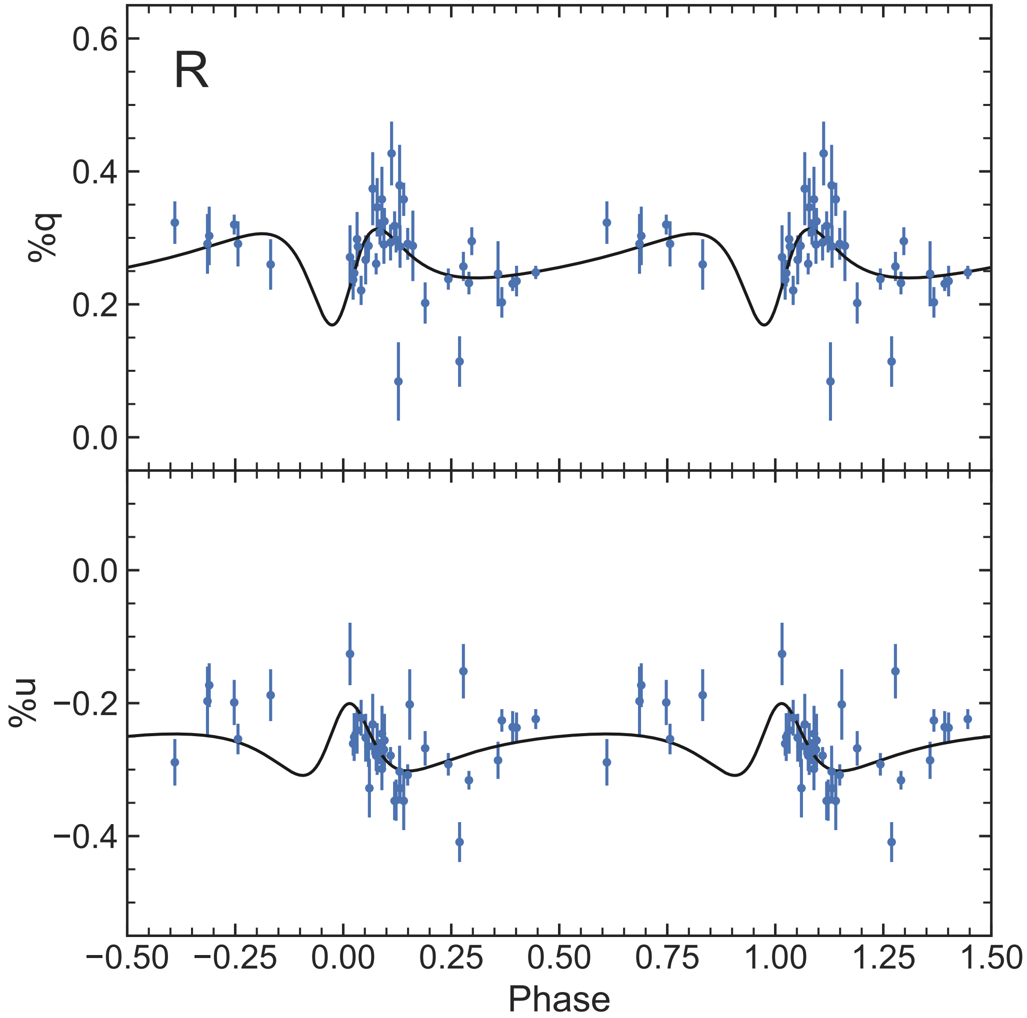

Figure 2.1: (cont.)

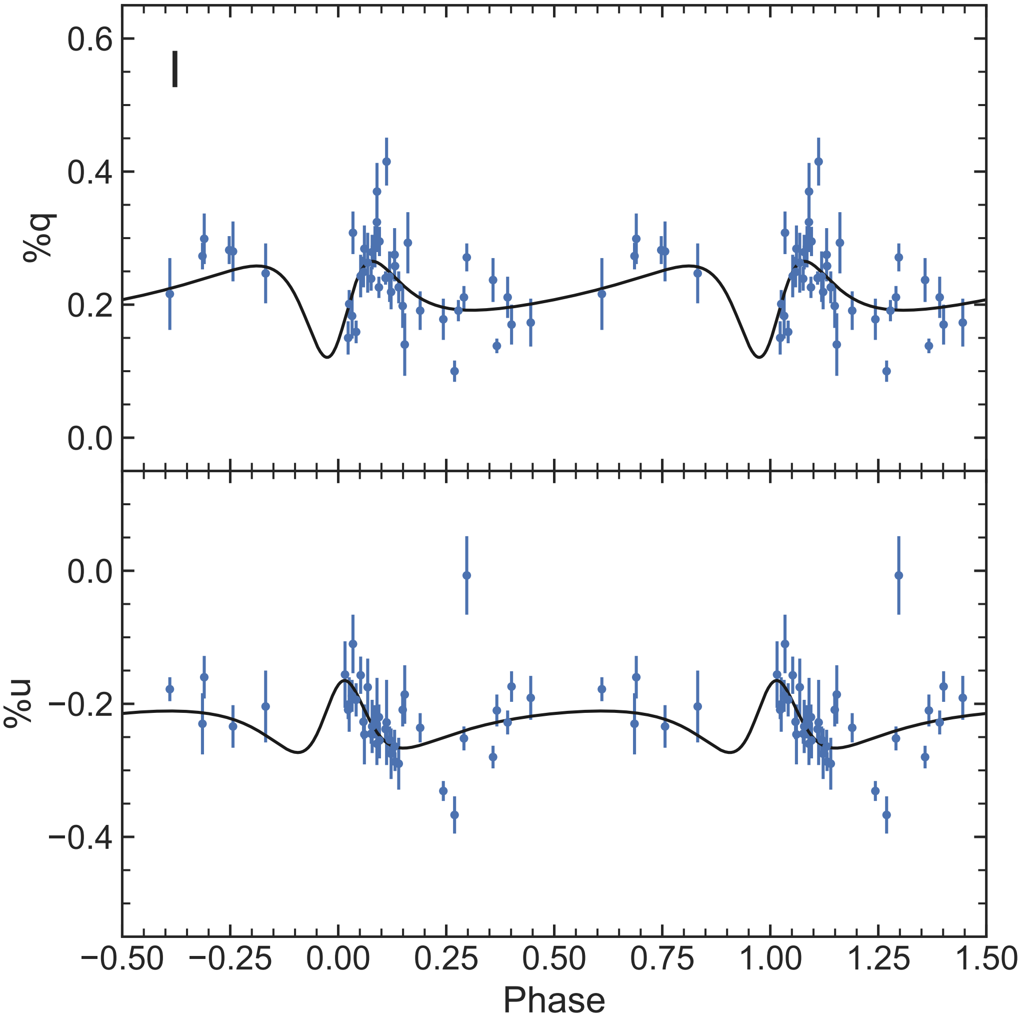

Figure 2.1: (cont.)

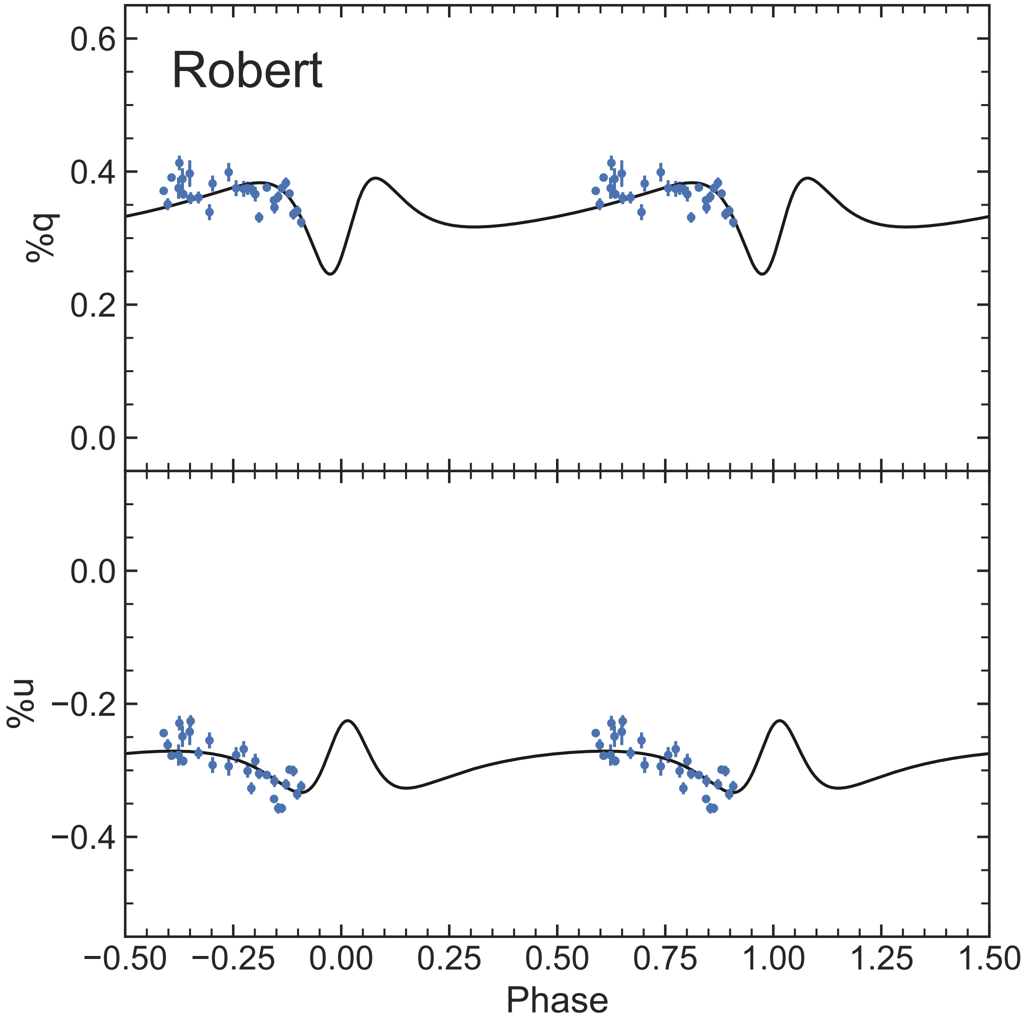

Figure 2.1: (cont.)

Table 2.4. Fitted binary parameters for WR 133 (Section 2.4**a**).

Parameter	Value
i (°)	115.9 ± 7.3
Ω (°)	162.4 ± 5.4
τ_*	$4.48 \pm 0.93 \times 10^{-4}$
$\dot{M}_{WR}$ ($M_\odot$ yr^{-1})	$6.52 \pm 0.6 \times 10^{-6}$

Note. — Based on the uncertainty analysis by Wolinski and Dolan (1994), the i presented here is a lower limit ($115.9° < i < 180°$).

elliptical prescription is not appropriate, so we fitted their data with circularized versions of equations 2.1 and 2.2, where $\lambda = 2\pi\phi$ in equations 2.3 and 2.4, and ϕ is the orbital phase. Also, because $a = r$ for a circular orbit, $\tau_3 = \tau_*$.

For WR 139, we did not fit the data in the region between phases 0.4–0.6 because of its strong departure from the simple model due to eclipse effects (St-Louis et al. 1993; Marchenko et al. 1997). The resulting binary parameters we found for both systems are the same within uncertainties as those previously published, so we do not present them here.

c) WR 134 This object has not been shown to have a luminous binary companion. Instead, the wind of WR 134 probably features rotating CIRs that come and go with a coherence timescale of about 40 days (Aldoretta et al. 2016). Therefore the binary models we used in **a)** and **b)** are not appropriate to describe its polarization variability. Instead, we phased our data to the period given in Aldoretta et al. (2016; Table 2.2) and took an uncertainty-weighted mean in each band to represent the mean polarization. We present the filter data in Figure 2.2. Its observed polarimetric data are presented numerically in the Appendix, Table A.3. The *UBVRI* mean values are presented in Figure 2.2 f) to better display the periodic behavior of the system. This periodic behavior has been seen in polarimetric data by Morel et al. (1999). However, in contrast to the Morel et al. results, our u data lack a clear periodicity. This may be related to the coherency timescale of the wind structures, or a different location of the structures in the wind. Our q data appear to phase well with the Aldoretta et al. (2016) period, suggesting that the period is related to a permanent feature of the star, such as its rotation rate.

d) WR 6 The binary status of this object has been in dispute for many years. It has been proposed that its periodic variability can be explained by CIRs (e.g. St-Louis, Tremblay, and Ignace 2018; Moffat et al. 2018), or by the apsidal motion of a binary companion (e.g. Schmutz and Koenigsberger 2019). Given the uncertainty surrounding the nature of the object, and the limited number of data points in our sample, we simply take a per-band weighted mean of the $UBVRb$ data presented in Moffat and Piirola (1993).

e) WR 42, WR 79, WR 155 These systems are all binaries, and their systemic means were already published by Moffat and Piirola (1993) (WR 42, WR 79) and Piirola (1988) (WR 155), produced using the model of Brown, McLean, and Emslie (1978). We provide their values for reference purposes in Table 2.3.

f) WR 48, WR 113 These systems are binaries, but we observed them only twice each. Thus, it is not feasible to fit binary models to these data, so we took an uncertainty-weighted mean in each band instead of attempting to fit each observation separately.

g) WR 16, WR 40, WR 103 These systems exhibit significant random polarization variation. As in **c)** and **d)**, we took an uncertainty-weighted mean in each band for each system.

h) WR 22, WR 43, WR 71, WR 111 These systems showed no polarization variability greater than 2σ over multiple nights. We took an uncertainty-weighted mean in each band, even for the binary WR 22 and the pair of binaries in WR 43.

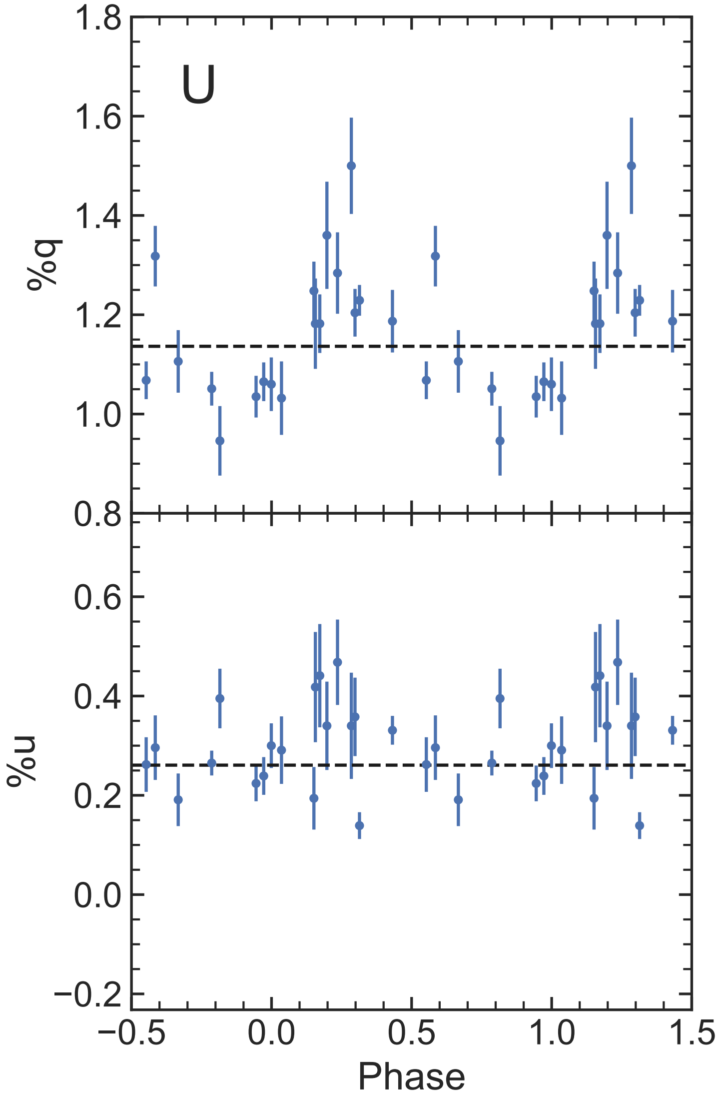

Figure 2.2: $UBVRI$ filter data for WR 134 (Section 2.4**c**). Panels correspond to U through I filters. The dashed line shows the weighted mean polarization value in each band. The final panel displays the uncertainty-weighted mean of the five filters. The data presented in this figure are available in the Appendix, Table A.3.

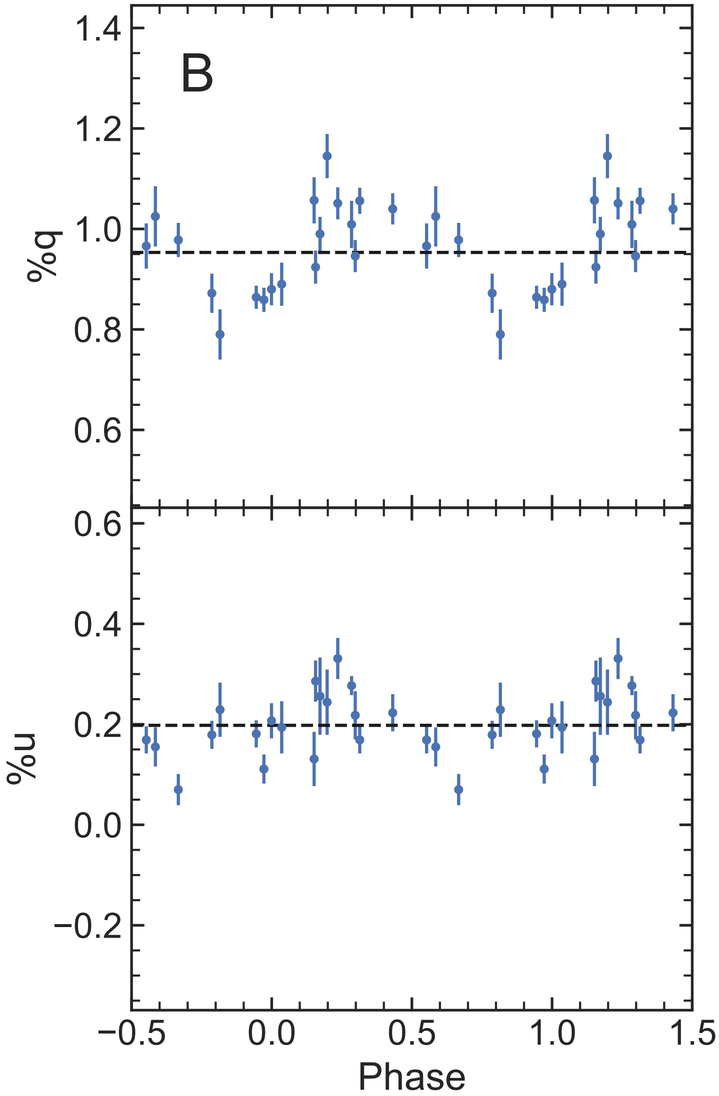

Figure 2.2: (cont.)

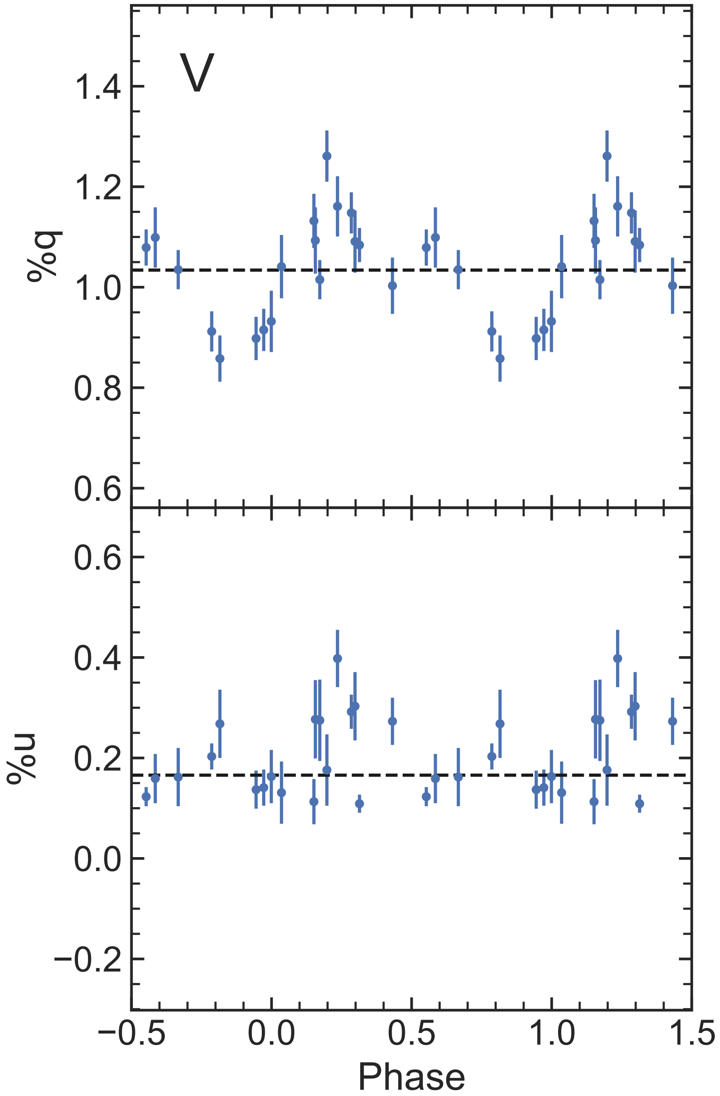

Figure 2.2: (cont.)

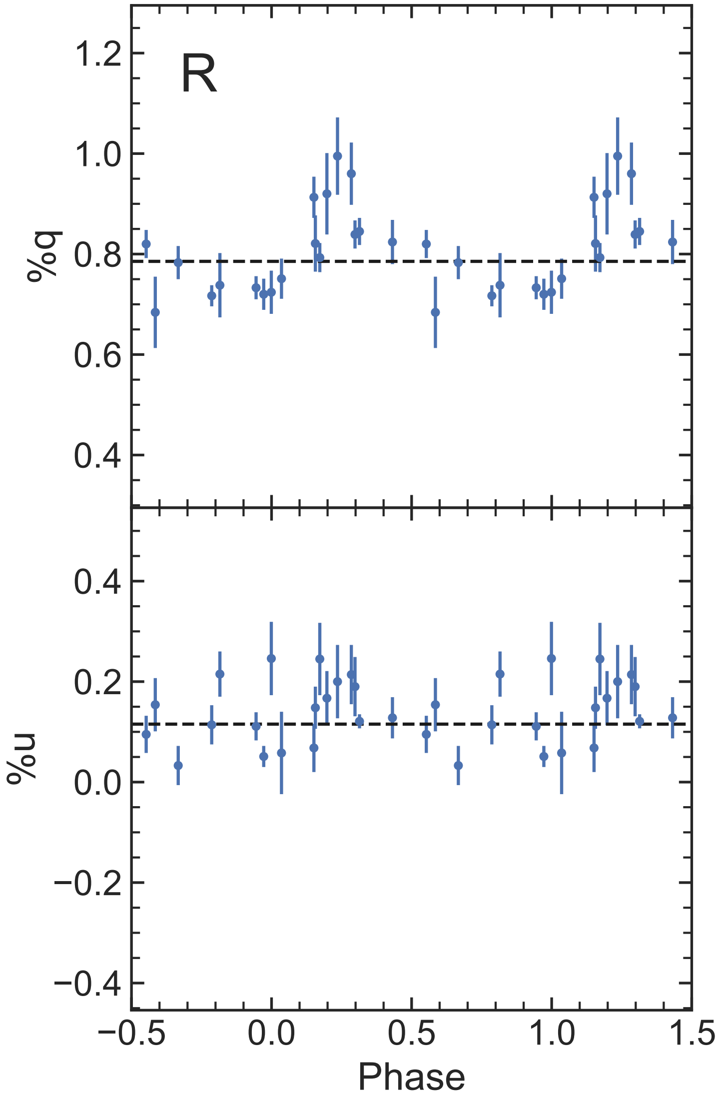

Figure 2.2: (cont.)

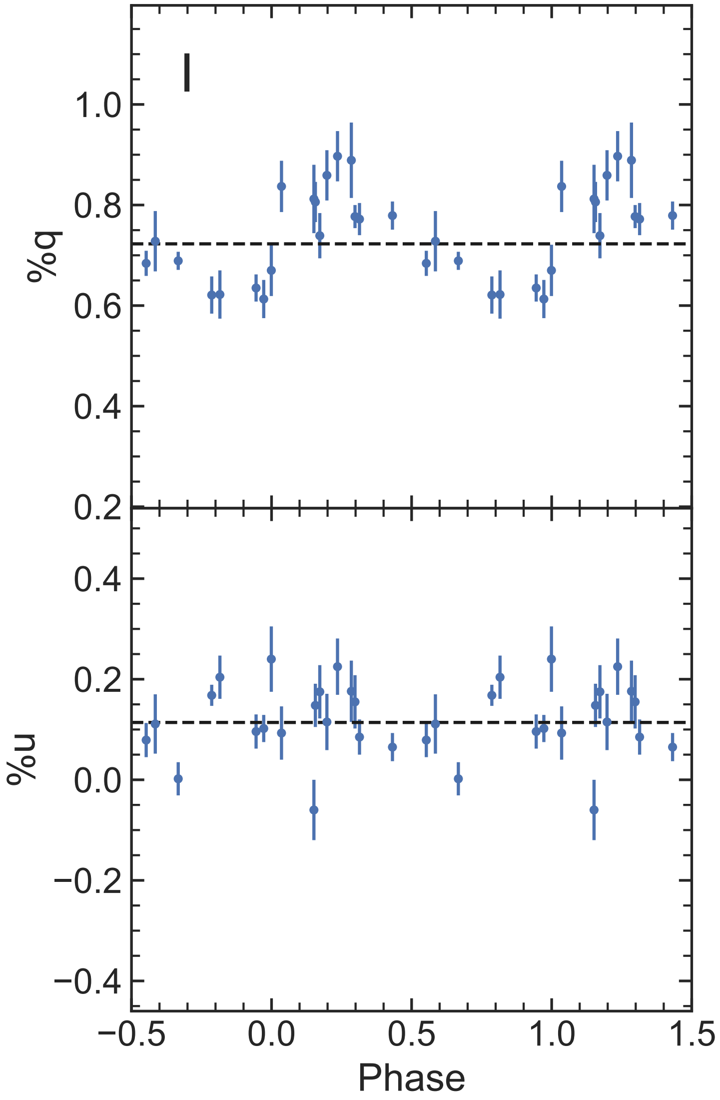

Figure 2.2: (cont.)

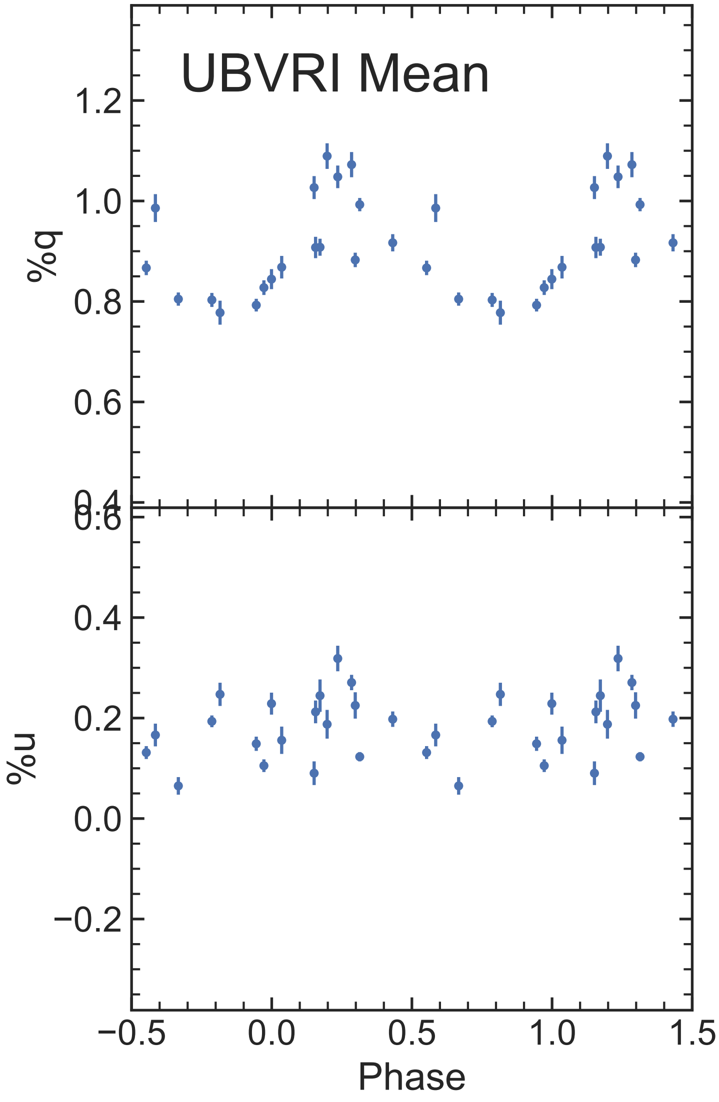

Figure 2.2: (cont.)

2.5 Simultaneous fit of interstellar and intrinsic polarization

We next investigated the contribution of interstellar polarization to each of our targets. Using the mean polarization values we derived in Section 2.4, we followed Moffat and Piirola (1993) to fit q and u simultaneously for all objects with a modified Serkowski law:

$$q = q_{00} + P_{\mathrm{IS,max}} \cos 2\theta_{\mathrm{IS}} \times \exp\left[-1.7\lambda_{\mathrm{max}} \ln^2(\lambda_{\mathrm{max}}/\lambda)\right] \tag{2.7}$$

$$u = u_{00} + P_{\mathrm{IS,max}} \sin 2\theta_{\mathrm{IS}} \times \exp\left[-1.7\lambda_{\mathrm{max}} \ln^2(\lambda_{\mathrm{max}}/\lambda)\right]. \tag{2.8}$$

In these equations, q_{00} and u_{00} represent constant polarization intrinsic to the system, which we expect to be independent of wavelength due to free-electron scattering in WR winds. Given the measurement uncertainties in our data, wavelength-dependent effects in this intrinsic ISP-corrected polarization (due to dust scattering or absorption in the WR environment) are unlikely to be detectable. $P_{\mathrm{IS,max}}$ represents the peak interstellar polarization value and λ_{max} the wavelength at which this peak occurs. These equations follow the prescription of Wilking et al. (1980), in which the constant K in the classic Serkowski law (Serkowski, Mathewson, and Ford 1975) is replaced by $1.7\lambda_{max}$. As in Moffat and Piirola (1993), we allow the position angle of the ISP to vary inversely with wavelength: $\theta_{\mathrm{IS}} = \theta_0 + k/\lambda$.

As in Section 2.4, we carried out the fits using LMFIT, beginning with the least-squares Levenberg-Marquadt method, then using the Markov-Chain Monte Carlo fitting module EMCEE (Foreman-Mackey et al. 2013) as part of the LMFIT module to refine the fits. We constrained the variable λ_{max} to lie in the range 0.35–1.0 μm as expected from other ISP surveys (e.g. Bagnulo et al. 2017). We chose initial parameter values from the data: $P_{\mathrm{IS,max}}$ began as the maximum total polarization across all bands, θ_0 began as the average position angle across all bands, and $\lambda_{\max}$ began as the central wavelength of the filter with the maximum total polarization value. We omitted data from La Silla in the additional Strömgren b filter because this filter can be potentially strongly affected by depolarization in the $\lambda4650$ line region (comprised of C III $\lambda4650$ + C IV $\lambda4658$ + He II $\lambda4686$ in WC stars, or He II $\lambda4686$ + N V $\lambda4601/4604/4619$ + N III $\lambda4634$-4642 in WN stars). While other filters may also be affected by line depolarization, the $\lambda4650$ region contains the strongest lines in the WR optical spectrum, and the Strömgren b filter is significantly narrower in wavelength than any of the Johnson filters. The $UBVRI$ data are therefore much less susceptible to line depolarization effects than the Strömgren b data. Thus, we neglect any line contributions to our broadband polarization results.

Figure 2.3 shows an example fit to the data for WR 22, using equations 2.7 and 2.8. The left panel shows the data that were fitted, while the right shows the same data and fit transformed to the usual p and θ space of the Serkowski law. In this case, the parameter k has $> 3\sigma$ significance (i.e. $|k| > 3\sigma_k$. In order to depict the wavelength dependence of θ_{IS}, we subtracted the fitted q_{00} and u_{00} parameters from the data and recalculated the position angle displayed in the figure.

After the first round of fits, we checked whether the fitted values for the intrinsic components q_{00} and u_{00} were significant, taking significant values to be at least 2σ above the estimated fit uncertainties, derived from the MCMC posterior probability distribution for each parameter. If the result for a given star was not significant for those parameters, we repeated the fit using the equations

$$q = P_{\mathrm{IS,max}} \cos 2\theta_{\mathrm{IS}} \exp\left[-1.7\lambda_{\max} \ln^2(\lambda_{\max}/\lambda)\right] \tag{2.9}$$

$$u = P_{\mathrm{IS,max}} \sin 2\theta_{\mathrm{IS}} \exp\left[-1.7\lambda_{\max} \ln^2(\lambda_{\max}/\lambda)\right]. \tag{2.10}$$

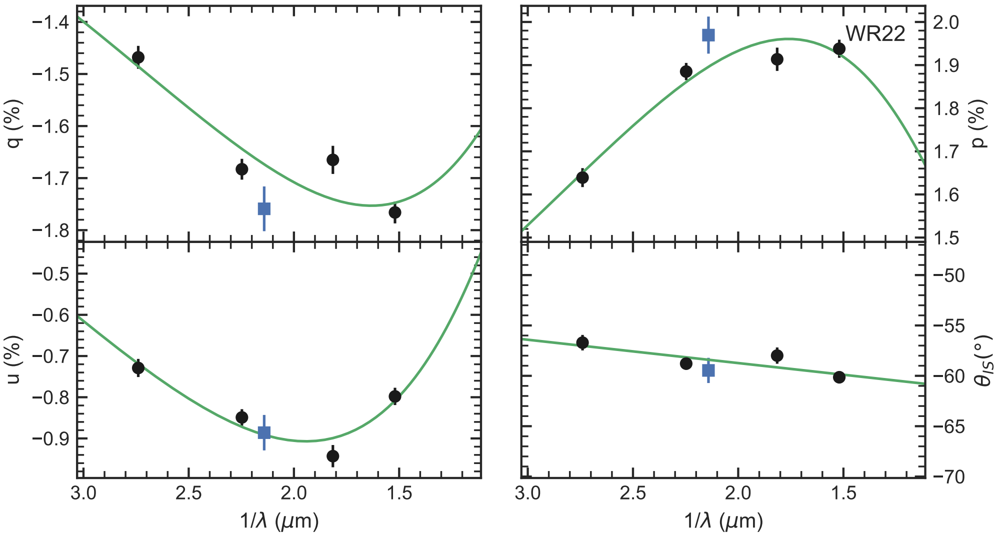

Figure 2.3: *UBVRI* polarization data for WR 22 (black points) fitted with equations 2.7 and 2.8 (green curves). Strömgren *b* filter polarization data are shown as blue points. The position angle points have been shifted by subtracting the fitted q_{00} and u_{00} values from the original data (Section 2.5).

This was done to ensure accurate ISP estimates in cases where the uncertainties on q_{00} and u_{00} were large. In those cases, the uncertainty in other parameters grew larger and reduced the significance of the k parameter result. Figure 2.4 shows an example fit to the data for WR 148 using equations 2.9 and 2.10.

We adopted final parameter values from the maximum likelihood estimates provided by EMCEE for all objects. We calculated 1σ error estimates from the 1σ Gaussian percentile of each parameter posterior probability distribution produced by EMCEE. We present the fitting results in Table 2.5, with values derived from equations 2.9 and 2.10 indicated with an ^{a}. Figures displaying fits for all systems are available as online material (see Figure Set A.8). We plot the results on a map of the sky in Galactic coordinates in Figure 2.5.

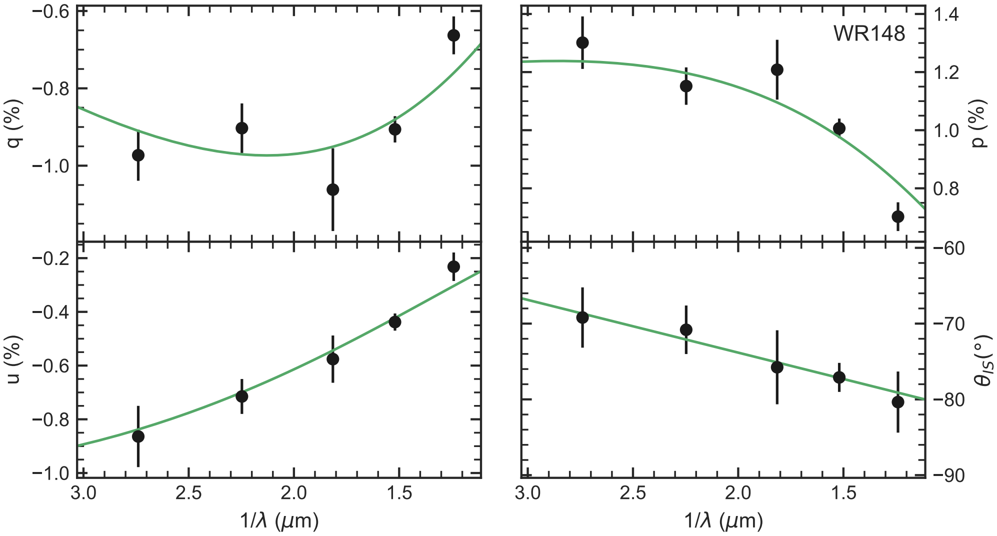

Figure 2.4: $UBVRI$ polarization data for WR 148 (black points), fitted with equations 2.9 and 2.10 (green curves).

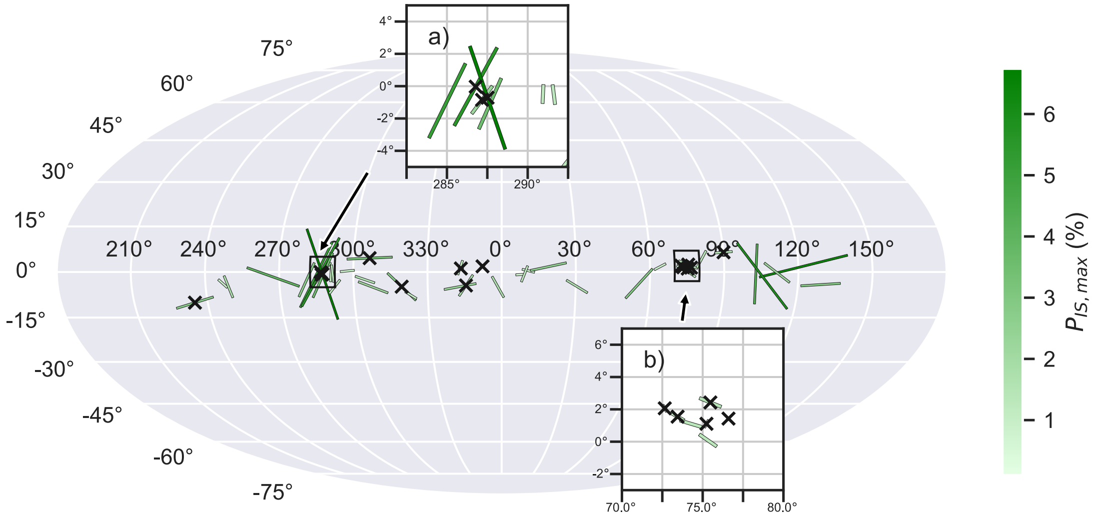

Figure 2.5: Map of our WR sample in Galactic coordinates, depicting our fitted polarization and position angle values for each star (Section 2.5; Table 2.5). The length of the bars is proportional to $P_{\mathrm{IS,max}}$. The angle of each bar represents θ_0, measured counterclockwise from the horizontal 0° line. Black crosses represent stars with $k/\sigma_k > 3$. Inset a) shows the region including WR 22, 23, and 25. Inset b) shows the region including WR 133, 134, 136, 138, and 139. We discuss these regions in Section 2.6.2.

Table 2.5: Results from our fits of interstellar + constant intrinsic polarization contributions to each of our targets (Section 2.5.)

WR	q_{00} (%)	$\sigma_{q_{00}}$ (%)	u_{00} (%)	$\sigma_{u_{00}}$ (%)	$P_{\rm IS,max}$ (%)	$\sigma_{P_{\rm IS,max}}$ (%)	λ_{max} (μm)	$\sigma_{\lambda_{max}}$ (μm)	θ_0 (°)	σ_{θ_0} (°)	k (°μm)	σ_k (°μm)
1^a	...	...	...	...	6.420	0.034	0.491	0.007	-83.0	0.7	-0.3	0.4
$3^{\ a}$	...	...	...	...	2.806	0.070	0.504	0.028	-88.2	2.2	1.0	1.2
6	$-2.220^{\rm b}$	0.143	$-0.782^{\rm b}$	0.139	2.721	0.147	0.521	0.004	-57.2	4.1	-3.2	1.2
8^a	...	...	...	...	0.860	0.023	0.499	0.035	-20.9	3.5	-1.9	1.7
9^a	...	...	...	...	1.657	0.214	0.600	0.148	-34.0	16.3	-6.1	8.8
14	$-1.151^{\rm b}$	0.281	0.129	0.267	3.918	0.289	0.539	0.004	-9.8	1.8	-0.1	0.2
16	0.293	0.426	0.957	0.468	2.632	0.500	0.548	0.023	-57.2	4.1	-3.2	1.2
21	0.878	0.512	$3.002^{\rm b}$	0.554	5.132	0.579	0.529	0.006	-58.0	2.8	-0.5	0.3
22	-0.728	0.325	0.979	0.354	2.135	0.371	0.538	0.015	-63.4	4.2	$2.3^{\rm b}$	0.7
23	0.000	0.350	$1.772^{\rm b}$	0.432	5.512	0.433	0.531	0.004	-59.4	1.9	$-1.1^{\rm b}$	0.2
24	-0.211	0.480	1.305	0.534	3.433	0.549	0.535	0.012	-56.9	3.6	0.8	0.6
25^a	...	...	...	...	6.741	0.042	0.631	0.006	-35.5	0.6	$-4.9^{\rm b}$	0.3
40^a	...	...	...	...	1.234	0.018	0.585	0.015	-63.9	1.7	0.2	0.8
42	$-0.409^{\rm b}$	0.124	$0.568^{\rm b}$	0.127	1.177	0.131	0.568	0.009	-46.3	2.5	-0.4	0.5
43^a	...	...	...	...	1.233	0.023	0.616	0.017	-41.4	2.0	-2.9	1.0
46^a	...	...	...	...	1.006	0.025	0.525	0.026	-87.2	2.7	0.1	1.2
48^a	...	...	...	...	1.446	0.014	0.551	0.013	80.6	1.3	-0.2	0.7
52^a	...	...	...	...	3.208	0.018	0.579	0.006	91.2	0.6	$-2.4^{\rm b}$	0.3
57^a	...	...	...	...	2.233	0.031	0.579	0.012	79.7	1.4	-1.4	0.7
69^a	...	...	...	...	2.775	0.020	0.540	0.008	68.1	0.9	$-4.1^{\rm b}$	0.4
71	0.171	0.336	0.592	0.254	0.939	0.373	0.586	0.110	74.3	9.2	-0.2	6.7
78^a	...	...	...	...	1.063	0.017	0.675	0.016	35.8	1.8	0.9	1.0
79^a	...	...	...	...	0.376	0.007	0.595	0.015	-81.5	1.8	$4.7^{\rm b}$	0.8
86^a	...	...	...	...	0.370	0.015	0.654	0.054	108.9	5.7	$-26.2^{\rm b}$	3.3
90	-0.918	0.647	$1.993^{\rm b}$	0.353	2.296	0.667	0.520	0.026	5.3	8.5	-4.1	2.2
92^a	...	...	...	...	1.770	0.022	0.560	0.013	28.4	1.4	$-3.0^{\rm b}$	0.7
103	$-0.889^{\rm b}$	0.232	0.561	0.257	1.682	0.268	0.518	0.008	-30.3	4.1	-0.2	0.4
108	$1.089^{\rm b}$	0.213	$0.759^{\rm b}$	0.155	0.585	0.255	0.701	0.190	2.0	49.2	-9.8	31.5
110^a	...	...	...	...	0.904	0.022	0.551	0.040	-6.7	3.7	-1.1	2.0
111	-0.111	0.212	0.940	0.376	1.208	0.392	0.544	0.036	-55.8	8.6	4.1	3.3
113^a	...	...	...	...	2.592	0.020	0.522	0.011	-84.0	1.1	-1.4	0.6
123^a	...	...	...	...	1.729	0.032	0.585	0.021	74.4	2.3	3.0	1.2
127^a	...	...	...	...	0.916	0.034	0.528	0.042	13.9	4.3	4.5	2.2
128	-0.621	0.440	$-1.696^{\rm b}$	0.470	2.811	0.494	0.496	0.022	23.8	6.5	0.0	0.9
133^a	...	...	...	...	0.491	0.009	0.400	0.020	-27.7	1.5	$4.4^{\rm b}$	0.7
134	0.112	0.065	$0.307^{\rm b}$	0.067	0.942	0.060	0.350	0.004	-14.7	5.0	$5.0^{\rm b}$	1.1

Table 2.5: (cont.)

WR	q_{00} (%)	$\sigma_{q_{00}}$ (%)	u_{00} (%)	$\sigma_{u_{00}}$ (%)	$P_{\mathrm{IS,max}}$ (%)	$\sigma_{P_{\mathrm{IS,max}}}$ (%)	λ_{max} (μm)	$\sigma_{\lambda_{max}}$ (μm)	θ_0 (°)	σ_{θ_0} (°)	k (°μm)	σ_k (°μm)
135^a	$\cdots$	$\cdots$	$\cdots$	$\cdots$	0.162	0.032	0.350	0.133	19.3	24.1	-3.5	12.7
136^a	$\cdots$	$\cdots$	$\cdots$	$\cdots$	1.454	0.018	0.490	0.017	-10.9	1.5	4.0^{b}	0.8
137^a	$\cdots$	$\cdots$	$\cdots$	$\cdots$	1.293	0.027	0.498	0.026	-8.3	2.3	-0.7	1.1
138^a	$\cdots$	$\cdots$	$\cdots$	$\cdots$	0.538	0.021	0.522	0.050	-62.1	4.8	-9.6^{b}	2.5
139	0.022	0.041	-0.267^{b}	0.089	0.098	0.083	0.970	0.065	83.8	19.6	-47.0^{b}	6.0
140^a	$\cdots$	$\cdots$	$\cdots$	$\cdots$	1.369	0.018	0.519	0.015	31.0	1.1	0.0	0.6
141^a	$\cdots$	$\cdots$	$\cdots$	$\cdots$	1.309	0.016	0.526	0.015	72.6	1.3	1.3	0.7
148^a	$\cdots$	$\cdots$	$\cdots$	$\cdots$	1.238	0.036	0.350	0.018	-87.8	2.6	7.0^{b}	1.4
153^a	$\cdots$	$\cdots$	$\cdots$	$\cdots$	4.242	0.017	0.541	0.005	43.7	0.8	1.2^{b}	0.4
155	0.412^{b}	0.119	-0.575^{b}	0.120	5.842	0.126	0.515	0.002	63.6	0.7	0.1	0.1
157^a	$\cdots$	$\cdots$	$\cdots$	$\cdots$	2.250	0.045	0.465	0.020	71.2	1.6	1.1	0.9

[a] Results fitted using equations 2.9 and 2.10.

[b] Results with 3σ significance.

Targets were fit using equations 2.7 and 2.8 unless marked.

2.6 Discussion

2.6.1 Intrinsic polarization

The intrinsic continuum polarization (q_{00}, u_{00} values) we detect in some of our targets could originate from the asymmetric illumination of a spherically symmetric free electron distribution or from a symmetric illumination of an asymmetric distribution (or both). For single WR stars the polarization is likely caused by light from the WR star scattering in an asymmetric wind (e.g., Harries, Hillier, and Howarth 1998; St-Louis 2013). In close WR binary systems all the above-mentioned effects can take place. In the case of the systems for which we estimated the binary polarization variations using the Brown, McLean, and Emslie (1978) model (§ 2.4), the remaining intrinsic polarization contributions could still be due to optically thick scattering or a finite stellar disk, which are not taken into account in that model. However, an examination of the results of Vink and Harries (2017b) for the SMC and LMC indicates that binaries are no more likely than single stars to posses intrinsic continuum polarization. For the Galaxy, the results of Harries, Hillier, and Howarth (1998) lead to similar conclusions. This seems to suggest that although a binary effect is expected in close WR + O systems (e.g. St-Louis et al. 1988), the probability of detecting it in a single snapshot observation is low. Therefore, in binaries for which we obtained only a single measurement of intrinsic continuum polarization at an arbitrary phase, or could not characterize the time-dependent polarization variations for other reasons, the intrinsic polarization may still include these binary effects. In these cases we cannot constrain the polarization source without additional phase-dependent observations.

Based on the fits described in Section 2.5, 12 stars in our sample showed intrinsic polarization above the 3σ level. However, WR 108 and WR 139 are outliers in this group because they do not have clearly defined values of $P_{\mathrm{IS,max}}$ within the observed $UBVR$ wavelength range. This means that the ISP toward them is also poorly defined, as shown by the large uncertainty on their polarization position angles (Table 2.5). As a result, their intrinsic polarization values are also poorly defined, regardless of the formal uncertainties, and we do not consider that we have detected significant intrinsic polarization for these stars.

Of the remaining 10 targets with intrinsic polarization, WR 21, WR 42, and WR 155 are known short-period binaries. In the case of WR 42, a short-period WC7 + O7V binary, we used the systemic mean polarization from binary fits made using the model of Brown, McLean, and Emslie (1978) (Section 2.4**e**). Thus the additional intrinsic polarization in WR 42 must be due to a wind asymmetry that is not incorporated into this model. Such an asymmetry could be caused by the binary interactions modeled by Hill et al. (2000) or rapid rotation of the WR star, and warrants further study with time-dependent polarimetry.

WR 155 is an extremely short-period WN6o + O9II-Ib system, for which we also used systemic mean polarization values from previous fits (Piirola 1988; Section 2.4**e**). This system undergoes sporadic periods of Roche lobe overflow, transferring mass between the O and WR stars (Koenigsberger, Schmutz, and Skinner 2017). It is therefore likely that the intrinsic polarization is caused by asymmetric wind structures produced due to these interactions between the stars.

We obtained only one snapshot observation of WR 21. The intrinsic Stokes u of $3.002\% \pm 0.554\%$ resulting from our fit should be treated with caution since it is much larger than any of our other measurements; further investigation is needed to check this result. Such a high polarization is not unprecedented, however; Villar-Sbaffi et al. (2006) found an intrinsic level of $3 - 4\%$ in the short-period WR + O binary WR 151 (CX Cep). For the range of inclination angles derived for WR 21 by Lamontagne et al. 1996 (48–62°), we calculate that the model of Brown, McLean, and Emslie (1978) produces a maximum polarization of $P = 0.1 - 0.4\%$ (regardless of the value of Ω). This is consistent with the amplitude of modulation we have found in additional unpublished data. If we take WR 21's large intrinsic polarization at face value, then, it is very unlikely to be due to binary effects alone. We thus hypothesize that WR 21 contains an asymmetric WR wind, which may be as extremely flattened as that of WR 151 (Villar-Sbaffi et al. 2006). Our Strömgren b filter results in § 2.6.3 show no significant line depolarization for this object, but this does not necessarily imply a spherical wind (Stevance et al. 2018). It is also important to note that our single observation does not preclude the existence of a transient, high-density clump. Further observations of WR 21 at different orbital phases would help clarify the situation.

Of the 7 other probably single stars with significant intrinsic polarization, WR 134 has been found to harbour complex wind structures (Aldoretta et al. 2016), which likely give rise to the observed intrinsic polarization. WR 128 is a WN4(h) type with small-scale spectral variability that may indicate inhomogeneities or clumps in the wind which could also cause a polarization signal (St-Louis et al. 2009).

WR 6 is a WN4b star with a possible companion (e.g. Schmutz and Koenigsberger 2019) or CIRs (e.g. St-Louis, Tremblay, and Ignace 2018; Moffat et al. 2018). Harries et al. (1999) measured the ISP using a different method from ours, and found a very different result of $P_{max} = 0.47 \pm 0.02\%$ at $\theta_0 = 164 \pm 2°$. This agreed with Robert et al. (1992) and Schulte-Ladbeck et al. (1991). However, they did not simultaneously fit the intrinsic polarization, nor did they include a wavelength-dependent position angle. On the other hand, as we discuss in Section 2.6.3, our B-band u measurement was strongly affected by the depolarization of emission lines in the system, and this may affect our fits. This complex system needs more spectropolarimetric observations to resolve its nature and measure the true value of its ISP.

The remaining 4 stars are all late-type WC types. WR 14, WR 23, and WR 103 display a relatively high level of small-scale spectral variability characteristic of strong clumping in their winds (Michaux et al. 2014), and this is most likely the cause of the (variable) intrinsic polarization. This variability was also detected in polarimetry by Drissen, Robert, and Moffat (1992) in the case of WR 14. WR 90 shows a residual in the b filter measurement; we discuss this object in more detail in Section 2.6.3 below.

Table 2.6 lists our findings for the intrinsic polarization (assumed constant with wavelength) of all objects in our sample. In cases where $|q_{00}| > 2\sigma_{q_{00}}$ or $|u_{00}| > 2\sigma_{u_{00}}$, we display our fitted quantities (uncertainties on these quantities are shown in Table 2.5). Otherwise, we quote upper absolute limits based on the 1σ observational uncertainties, or fit uncertainties in the case of stars with multiple observations. These were calculated as a mean over $UBVR$ uncertainties (and I when available; Table 2.3) in each of q and u. The band-to-band uncertainties are consistent at the $\sim 0.06\%$ level for U and V, and the $\sim 0.04\%$ level for B, R, and I. These values can be used to guide the required precision of future polarization observations of these systems.

2.6.2 The wavelength dependence of the ISP position angle

Dolan and Tapia (1986) studied the optical wavelength dependence of linear polarization in a number of strongly polarized stars. For 9 of 11 such stars they found a significant deviation from a constant polarization angle and fitted their data with a wavelength (λ) dependent function. These curves can be better linearized in most cases by using $1/\lambda$ as the independent variable, which we adopted in our fits in search of a significant slope in each of our targets (Section 2.5). Dolan and Tapia (1986) concluded that most of the nonzero slopes they derived could be intrinsic to the star, although they could not eliminate the presence of multiple dust clouds along the line of sight, each with different grain alignments. However, allowing for this effect is important, both to achieve the best possible fits to the ISP Serkowski law and to account for the possible presence of an intrinsic polarization component.

The recent ISP survey by Bagnulo et al. (2017) found that stars with strong wavelength dependence in the ISP position angles (large $|k|$) tend to have low interstellar polarization overall (small $P_{\mathrm{IS,max}}$). Our data confirm this trend, as shown in Figure 2.6, which displays a weak inverse relationship between $P_{\mathrm{IS,max}}$ and $|k|$. This likely reflects the fact that as P

Table 2.6: Intrinsic polarization values and limits for the WR stars in our sample.

WR	q_{00} (%)	u_{00} (%)
1	< 0.07	< 0.06
3	< 0.15	< 0.13
6	-2.220	-0.782
8	< 0.04	< 0.04
9	< 0.36	< 0.36
14	-1.151	< 0.02
16	< 0.03	0.957
21	< 0.04	3.002
22	-0.728	0.979
23	< 0.03	1.772
24	< 0.04	1.305
25	< 0.06	< 0.06
40	< 0.03	< 0.03
42	-0.409	0.568
43	< 0.03	< 0.03
46	< 0.04	< 0.04
48	< 0.03	< 0.03
52	< 0.03	< 0.03
57	< 0.05	< 0.05
69	< 0.03	< 0.03
71	< 0.03	0.592
78	< 0.03	< 0.03
79	< 0.01	< 0.01
86	< 0.04	< 0.04
90	< 0.04	1.993
92	< 0.0	< 0.04
103	-0.889	0.561
108	< 0.07	< 0.07
110	< 0.05	< 0.05
111	< 0.02	0.940

Table 2.6: (cont.)

WR	q_{00} (%)	u_{00} (%)
113	< 0.04	< 0.04
123	< 0.06	< 0.06
127	< 0.07	< 0.08
128	< 0.07	-1.696
133	< 0.01	< 0.01
134	< 0.01	0.307
135	< 0.08	< 0.07
136	< 0.04	< 0.04
137	< 0.06	< 0.06
138	< 0.05	< 0.05
139	< 0.04	-0.267
140	< 0.03	< 0.04
141	< 0.03	< 0.03
148	< 0.06	< 0.07
153	< 0.07	< 0.04
155	0.412	0.575
157	< 0.08	< 0.09

We present fitted results when they are at least 2× greater than the $\sigma_{q_{00}}$ or $\sigma_{u_{00}}$ uncertainty displayed in Table 2.5. Otherwise, we present upper limits computed using the mean 1σ broadband polarization uncertainties from our observational weighted means or systemic mean calculations. Band-to-band uncertainties are consistent at the $\sim 0.06\%$ level for U and V, and the $\sim 0.04\%$ level for B, R, and I.

values become small (declining redward from typical $\lambda_{\max}$ values of ~ 540 nm), θ becomes less well defined, giving rise to apparent rotations with wavelength.

Fifteen stars in our sample have ISP position angles (θ_{IS}) with significant wavelength dependence ($k > 3\sigma_k$). In cases with low $P_{\mathrm{IS,max}}$, this significance may simply be due to the relation shown in Fig. 2.6. However, within this subsample, two groups of stars stand out because they are clustered on the sky (as shown in the insets to Fig. 2.5). WR 22, WR 23, and WR 25 lie within $\sim 1^{\circ}$ and have distances in the range 2.1–2.8 kpc (Gaia Collaboration et al. 2018). WR 133, WR 134, WR 136, and WR 138 lie within $\sim 3^{\circ}$ and have distances in the range 1.9–2.7 kpc. This clustering of stars with significant θ_{IS} wavelength dependence supports the idea that this effect is due to scattering in multiple dust clouds along the line of sight. Figure 2.7, which displays the k values of the clustered stars versus their distance, reveals two different k trends with distance for the two clusters. This provides further evidence that in these stars, the significant position angle rotation is caused by a change in the ISM between observer and source, and that the behavior of k is strongly directional. This conclusion could be tested by using photometry of these stars and measuring their extinction, though this is beyond the scope of this paper.

WR 25 has had a previous ISP estimate produced by Drissen, Robert, and Moffat (1992). They found $P_{\max} = 6.74 \pm 0.02\%$ and $\lambda_{\max} = 6050 \pm 10$Å, using the standard Serkowksi law. Their $P_{\max}$ is identical to ours within uncertainties, though their $\lambda_{\max}$ is significantly smaller. This latter result is almost certainly due to the inclusion of k in our fits. Drissen, Robert, and Moffat (1992) noted that either there was a wavelength dependence of the ISP position angle or a wavelength-dependent intrinsic polarization of low magnitude. Since we find a significant k value for WR 25, but no significant intrinsic polarization, it is likely that we have detected the proposed wavelength-dependent ISP position angle. Drissen, Robert, and Moffat (1992) suggested that this could be due to the Carina nebula processing interstellar grains via shock waves. Our clustered k values for WR 22, WR 23 and WR 25

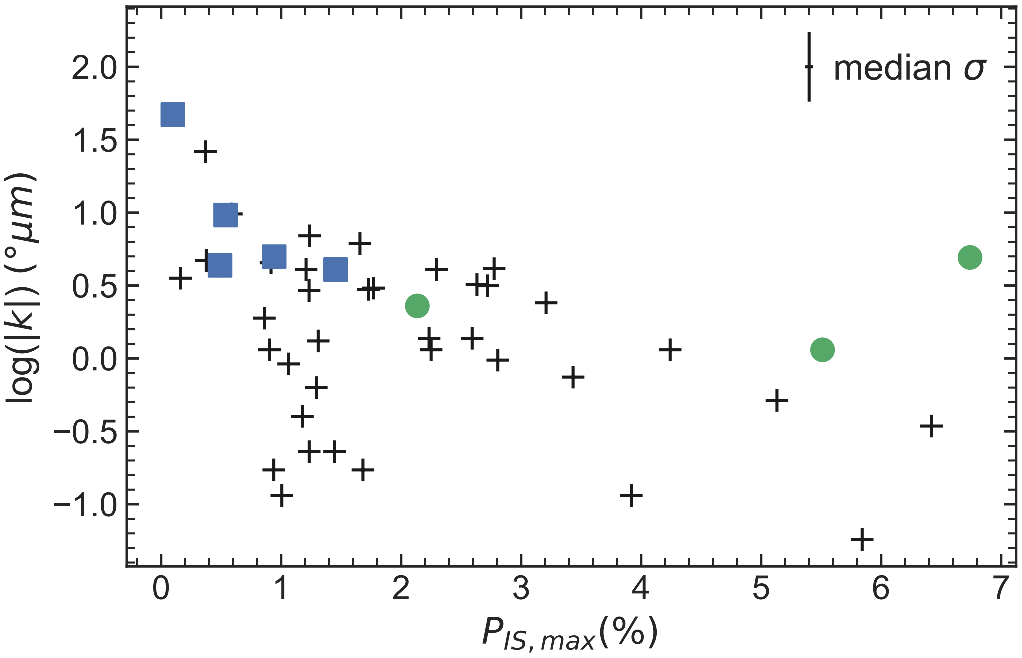

Figure 2.6: Interstellar position angle rotation coefficients (on a log scale) versus interstellar $P_{\mathrm{IS,max}}$ values for all stars in our sample. For clarity, we do not plot error bars on each point; median uncertainties for each quantity are represented by the cross-hairs in the upper right of the plot. Green circles correspond to the clustered stars in Fig. 2.5, inset a). Blue squares correspond to the clustered stars in Fig. 2.5, inset b).

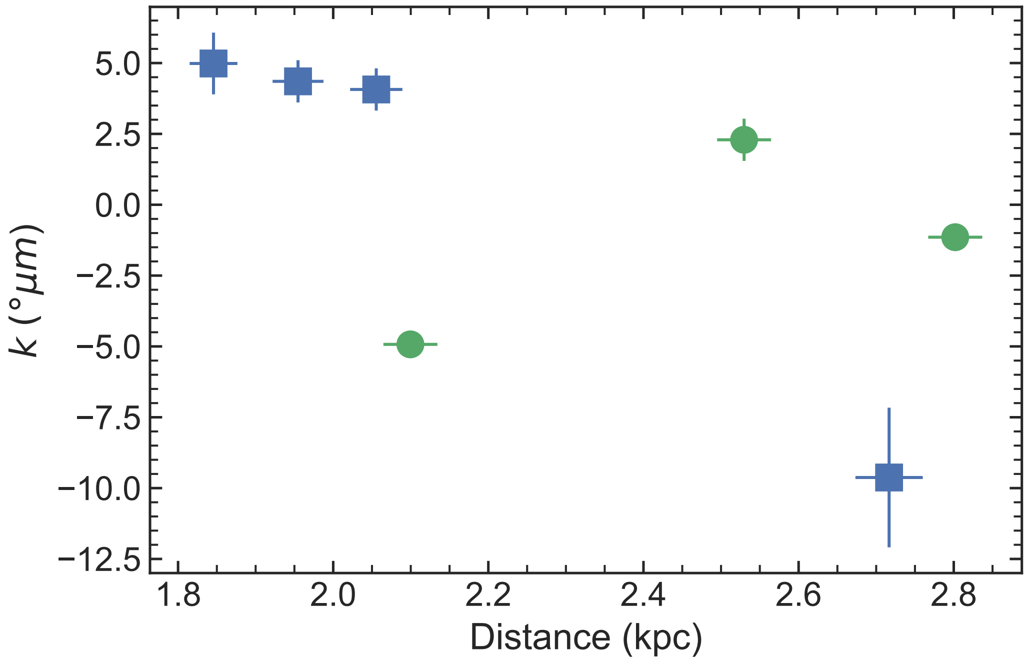

Figure 2.7: Interstellar position angle rotation coefficients versus *Gaia* DR2 distances for the two star clusters displayed in the insets in Fig. 2.5. Green circles correspond to systems in inset a) (WR 22, 23, 25). Blue squares correspond to systems in inset b) (WR 133, 134, 136, 138). Uncertainties in distance are derived from the *Gaia* data. WR 139 has been omitted due to its poorly defined $P_{\mathrm{IS,max}}$ (Section 2.6.1).

support this conclusion, and we make the same suggestion as Drissen, Robert, and Moffat, that the Carina nebula could benefit from a concentrated ISP survey.

2.6.3 Strömgren filter results

The narrow Strömgren b filter spans the complex $\lambda 4650$ line region, which includes several strong emission lines in both WC and WN spectral types (Section 2.5). We used this filter to observe 19 stars in our sample. To determine the significance of our measurements, we calculated the residual of the b filter data with respect to the fitted ISP equation in q, u and p, including the intrinsic polarization if present, by subtracting the fit results from the b filter data. We present the results in Table 2.6.3. We considered the residual to be significant if its absolute value was 3σ or more greater than the uncertainty on the measurement. Following the arguments by Vink and Harries (2017b), a b filter measurement that is depolarized in p compared to the intrinsic continuum polarization may be evidence of the line effect and thus imply an asymmetric WR wind and a rapidly rotating WR star. In the binary systems for which we could not define a systemic mean polarization, binary illumination of the WR wind may also contribute to the intrinsic continuum polarization.

Five stars showed a significant b filter residual in any Stokes parameter: WR 6, WR 48, WR 79, WR 90, and WR 113. We checked each residual in $q - u$ space to verify whether it corresponded to a depolarization or a polarization enhancement with respect to the fit result. Three objects with significant b residuals are known binaries: WR 48, WR 79 and WR 113. None of these binaries have a significant intrinsic continuum polarization using our 2σ significance criterion (§ 2.5). In these cases, the residual in the b filter may point to the existence of intrinsic continuum polarization (that was not sufficiently significant compared to our fitting uncertainties) at least equal to the b residual value. We discuss each of these cases in more detail below.

WR 48 was only observed twice; it has a significant b residual only in Stokes u, although we caution that because this result refers to a mean of two observations (§ 2.4f), the position

Table 2.7. Polarimetric residuals of our Strömgren b filter observations with respect to the ISP + intrinsic fits presented in Table 2.5 (in the sense $b-$ fit). We also list the uncertainty on each b measurement for comparison.

WR	b_q residual (%)	b_u residual (%)	b_p residual (%)	σ_b (%)
6	-0.045[a]	0.184[a]	-0.169[a]	0.009
16	-0.029	0.030	0.004	0.028
21	0.061	-0.030	-0.022	0.058
22	-0.085	0.005	0.073	0.043
24	0.052	0.054	-0.074	0.037
25	0.022	-0.027	0.026	0.063
40	0.001	0.024	-0.020	0.025
42	0.010	0.009	-0.013	0.011
48	-0.017	-0.108[a]	-0.017	0.023
52	-0.015	0.018	0.017	0.042
57	0.007	0.106	0.043	0.045
69	-0.072	0.010	0.043	0.068
71	-0.065	0.065	0.088	0.067
78	0.021	0.037	0.041	0.024
79	0.027[a]	-0.019	-0.009	0.009
90	-0.441[a]	0.333[a]	0.061	0.066
103	-0.080	0.016	-0.034	0.034
111	0.016	0.013	-0.020	0.015
113	-0.157[a]	0.073	0.150[a]	0.045

[a] Denotes $|b|$ residual values $> 3\sigma_b$.

The b_p residual corresponds to a magnitude difference only, not a vector difference as with the b_q and b_u residuals. A negative b_p value as defined here thus does not necessarily imply a depolarization in $q-u$ space.

angle of the residual is not well constrained. Given our uncertainties, this does not correspond to a significant line depolarization in p. Nonetheless, it does suggest some intrinsic continuum polarization, which may be due to an asymmetric WR wind, binary scattering effects, or both. Alternatively, WR 48 is a triple system whose third star, a O9.7Iab blue supergiant (BSG) is $\sim 10\times$ brighter than the WR + O binary, so it is possible that the BSG is the source of the polarization, although this is rare amongst BSGs. This matches the findings of St-Louis et al. (1987), who detected stochastic, quasi-periodic fluctuations in the polarization of the system that they attributed to the O9.7Iab star.

WR 79 had 6 observations, so its b uncertainty is low (§ 2.4e) and its b_q residual is significant despite being small. As in WR 48, this is not a robust line effect detection, but it could indicate a slightly asymmetric WR wind. In addition, Hill et al. (2000) detected a wind collision region that could be asymmetric enough to produce intrinsic continuum polarization in this system that was not significant given our 2σ criterion (§ 2.5). Additional phased observations at higher precision could further illuminate the nature of this continuum polarization.

WR 113 was observed twice (§ 2.4f) and thus, although its residual is significant in q and not u, the same position angle caveat applies as in the case of WR 48. However, its p residual is significant and positive. We verified in $q - u$ space that this residual is not a depolarization typical of the line effect, but rather an additional polarization in the b filter in excess of our ISP + continuum fit. This implies that instead of being unpolarized, the λ4650 line region contains its own constant or varying intrinsic polarization, a result that may complicate studies of the line effect in some binary systems. Time-dependent spectropolarimetry is required to assess this possibility.

As noted in Section 2.6.1, the binary status of WR 6 is ambiguous. The periodic nature of its polarization could be explained by the presence of CIRs or by a companion creating CIR-like structures in the wind (Harries et al. 1999). Such structures could also give rise to the significant intrinsic polarization we detect (§ 2.6.1). Harries et al. (1999) also found that the region covered by the b filter shows strong depolarization of the emission lines. Our negative b_p residual, which again we verified in $q-u$ space supports this line effect detection. This depolarization has also affected the B filter in our data, especially in Stokes u.

WR 90 is particularly interesting because it displays an intrinsic polarization with greater than 5σ significance, along with the significant Strömgren b filter residual. The residual shows a rotation of the polarization position angle of 71.5° with respect to the continuum, but no depolarization in p. Because this star has a WC7 spectral type, this deviation from the continuum angle is likely due to polarization effects in the C III λ4650 line region. This may be the first evidence that WR 90 has a structured or aspherical wind with a preferred orientation angle. However, a study by Chené and St-Louis (2011) showed only small-scale spectral variability, characteristic of clumps in the wind, without any sign of large-scale variability that could be attributed to the presence of a global wind structure. This may hint at transient structures, such as CIRs, in the WR 90 wind.

All five of the stars we found to contain a significant b residual would benefit from focused, time-dependent spectropolarimetric observing campaigns to provide more information about the emission line polarization and reveal more details about the structures of their winds and other circumstellar material.

2.7 Conclusions

We observed a sample of 47 WR systems, both single and binary, using broadband $UBVRIb$ filter polarimetry. We fit a modified Serkowski law to the data to characterise each star's intrinsic polarization and ISP contribution. We provide a table of fitted ISP values (Table 2.5) and a sky map of ISP vectors (Figure 2.5) as a resource for future polarimetric observations of these stars.

We found that 10 of the systems exhibit significant intrinsic polarization. Three of these stars (WR 21, WR 24 and WR 155) are short-period binaries and so their intrinsic polarization can be attributed to a combination of asymmetric winds due to rapid rotation of the WR star, illumination of the WR wind by the O star companion, and wind asymmetries caused by binary interaction. The intrinsic polarization in the other 7 systems is likely due to either complex wind structures (WR 6, WR 90, WR 134) or wind clumping (WR 14, WR 23, WR 103, WR 128), though WR 6 may have a binary companion. Six stars showed intrinsic polarization at 2–3σ significance, and we suggest further observations of these targets to improve the uncertainties. Table 2.6 presents 1σ upper limits to the intrinsic polarization for all other stars to guide future observations.

Fourteen stars in our sample showed a significant wavelength dependence of the ISP position angle. Some of these objects are clustered closely on the sky, suggesting that the wavelength dependence is due to the effects of multiple dust clouds along the line of sight. We also confirm the result of Bagnulo et al. (2017) that large $|k|$ values have a weak inverse relationship with $P_{\mathrm{IS,max}}$ (Fig. 2.6).

Nineteen systems were observed with the Strömgren b filter to investigate the λ4650 line complex present in most WR stars (Table 2.6.3). Five stars showed a significant residual relative to the Serkowski Law in the b filter: WR 6, WR 48, WR 79, WR 90, and WR 113. Three of these are binaries (WR 48, WR 79 and WR 113). The residual of WR 48 may be due to a combination of effects, including an asymmetric wind collision region. WR 79 is likely to have a wind collision region whose asymmetry contributes to the intrinsic polarization of the WR wind. WR 113 exhibits possible intrinsic line polarization, which is unusual and warrants further study. WR 6 has an ambiguous nature, so its residual could be explained either by CIR structures in its wind or by the motion of a binary companion creating structures in the wind. WR 90 is an interesting case, whose significant intrinsic polarization and position angle rotation in the b filter may indicate hitherto unknown asymmetries or structure in the wind.

We are currently monitoring 10 of the WR binary systems from this sample using spectropolarimetric observations obtained with the Robert Stobie Spectrograph on the Southern

African Large Telescope (Fullard et al. 2018; Johnson et al. 2019). These wavelength- and time-dependent data will enable us to characterize the colliding wind geometries and other binary properties in greater detail than has previously been possible. Similar observing campaigns focused on the other objects of interest highlighted here will reveal valuable information about the nature and structure of their WR winds.

2.8 Acknowledgements

The authors thank the referee for insightful comments that improved this manuscript, and the assistance provided by the AAS statistical review team. Thanks to M. Shrestha for her helpful suggestions for improving Table 2.1.

AGF and JLH acknowledge support from NSF award AST-1816944. AFJM and NSL are grateful to NSERC (Canada) for financial aid.

AGF and JLH respectfully acknowledge the Arapaho and Cheyenne peoples, upon whose traditional land the University of Denver was built. AGF and JLH also acknowledge the custodians and administrative staff at the University of Denver for their support.

This research has made use of the SIMBAD database, operated at CDS, Strasbourg, France. The original description of the VizieR service was published in 2000, A&AS 143, 9.

This research has made use of the VizieR catalogue access tool, CDS, Strasbourg, France (DOI: 10.26093/cds/vizier). The original description of the VizieR service was published in 2000, A&AS 143, 23.

Chapter 3

The "twin" Wolf-Rayet + O binary systems WR 42 and WR 79

3.1 Introduction

3.1.1 Wolf-Rayet + O binary stars

Despite being the rarest stellar mass group, massive stars (> 8 $M_\odot$) are the some of the most important originators of elements in the Universe, because they ultimately synthesize and distribute heavy elements when they explode as supernovae. Most massive stars spend a large fraction of their lives in binary systems with other massive stars (Sana et al. 2012). The interactions (such as mass transfer) between close companions drive the evolutionary paths that shape both stars' subsequent fates. Mass loss via stellar winds is another critical factor, as mass that leaves the system affects the stars' future evolution while enriching the ISM on a longer timescale. Thus, the study of massive binary stars can help us shed new light on how massive stars evolve, and their likely fate once nuclear burning has been exhausted.

A particular stage of a massive star's evolution after the main sequence is the population I classical Wolf-Rayet (WR) type (as opposed to other WR types that show strong emission lines, but either include hydrogen in their spectra, or are the central stars of some planetary nebulae). These core He-burning stars are characterized observationally by strong emission lines mainly of helium and nitrogen or carbon/oxygen, giving rise to the WN and WC/WO subtypes, respectively (Crowther 2007). The stars evolve from WN to WC (and then WO as a late extension of WC) as the stripping winds change from CNO cycle dominated to He-burning products, leading to stellar winds that are at least an order-of-magnitude denser than those of their immediate predecessor O-stars. As for all massive stars, WR stars are often found in binary systems, mostly with O-type companions (Crowther 2007; Van Der Hucht 2001b; Vanbeveren and Conti 1980). Those WR + O systems with short periods (< 10 years) are strongly influenced by mass transfer, while virtually all WR + O binaries reveal strong wind-wind interactions.

We have chosen to use the stellar wind regions in WR + O binaries to investigate their geometry and density distributions. We can use these properties of the stellar wind as well as established wind terminal velocities to calculate mass loss rates and mass transfer. The shape of the wind can also potentially help us investigate rapid rotation (Villar-Sbaffi et al. 2005), which could provide a link with long-duration gamma ray bursts that require it (Gräfener et al. 2012; Woosley and Bloom 2006, see also Section 1.4).

The observational technique of spectropolarimetry has been shown to be a useful tool for diagnosing large-scale wind asymmetries in single stars via the line effect (Harries, Hillier, and Howarth 1998; Vink and Harries 2017a). In this scenario, continuum photons travel through a greater optical depth of material than line photons, leading to an observed depolarization across strong emission lines. For there to be a net polarization, this effect also requires asymmetry in the wind, e.g. a wind elongated by rapid rotation (Shenar, Hamann, and Todt 2014) or enhanced magnetic fields (Cassinelli 1992; Poe, Friend, and Cassinelli 1989). While rapid rotation in WR binary systems has been recently inferred using spectroscopy and direct imaging (e.g., Callingham et al. 2019), spectropolarimetry allows us to probe the wind geometries in unresolved binary systems. To this end, we present and analyze phase-dependent spectropolarimetric data on two very similar WR + O binary systems, WR 42 and WR 79, obtained with the Robert Stobie Spectrograph at the Southern African Large Telescope (RSS/SALT; Potter et al. 2016).

3.1.2 WR 42 and WR 79

WR 42 (HD 97152; WC7 + O7 V) and WR 79 (HD 152270; WC7 + O5-8) are Galactic WR + O binary systems with very similar spectral types of both components, periods (∼ 8 days) and thus separations, and orbital inclinations (∼ 35°; St-Louis et al. 1987). Table 3.1 summarises the details of their stellar and orbital parameters. Because of their similarity, these systems have been the subject of comparison in the past: spectroscopically by Hill et al. (2000), updated in Hill, Moffat, and St-Louis (2002), and polarimetrically by St-Louis et al. (1987) and Moffat and Piirola (1993).

Despite being well studied, neither object has been the focus of a detailed spectropolarimetric analysis. Moffat and Piirola (1993) used the Strömgren b filter (in addition to broadband $UBVR$) to investigate the integrated polarization of the C III $\lambda4650$ + C IV $\lambda4658$ + He II $\lambda4686$ line complex in both stars, but they did not obtain enough observations for good orbital phase coverage. The sensitivity of RSS/SALT and the telescope's queue scheduling have allowed us to obtain high-quality spectropolarimetric observations that cover the entire orbit of each system. In this paper, we focus on the phase behavior of the continuum and integrated emission lines, comparing our new data with those of past studies.

3.1.3 Geometrical models

Geometrical models of WR 42 and WR 79 have been created using both polarimetric and spectroscopic results as a guide. St-Louis et al. (1987) found, using the binary polarization model of Brown, McLean, and Emslie (1978), that both systems have scattering electrons distributed approximately symmetrically about the line that connects the

Table 3.1: Spectral and orbital parameters of WR 42 and WR 79. The ephemerides we adopt for this work assume that phase 0.0 corresponds to the WR star at inferior conjunction, i.e. passing in front of the O star. See Section 3.7 for a discussion of the orbital parameters in relation to these data.

Parameter	WR 42	WR 79	Reference
Spectral type	WC7 + O7 V	WC7 + O5-8	1
P	7.8912 ± 0.0002 d	8.8911 ± 0.0001 d	2
e	0.00	0.00	2
E_0	2442463.34 ± 0.01	2441158.67 ± 0.07	2
i (Hill CW model)	36° ± 7°	29° ± 5°	3
i (Photometry)	40.3° ± 2.9°	33.6° ± 2.3°	4
i (Polarimetry)	43.5° ± 3.0°	44.8° ± 3.0°	5
i (Spectral type)	≈ 35°	≈ 25°	6
M (WR + O) $\sin^3 i$	3.7 + 6.2 $M_\odot$	1.8 + 4.9 $M_\odot$	4

References: (1) Crowther (2015); (2) Hill et al. (2000); (3) Hill, Moffat, and St-Louis (2002); (4) Lamontagne et al. (1996); (5) St-Louis et al. (1987); (6) Massey (1981).

two stars. However, the density of scattering material is aligned in the orbital plane at a preferred angle relative to the line between the stars, so that it either lags or precedes the O star in phase. The angle in both systems was found to lag the O star, but St-Louis et al. (1987) were unable to confirm the physical significance of the angle because of the propagation of uncertainty in the ephemerides they used.

The Hill, Moffat, and St-Louis (2002) model is the most detailed available for the systems at the time of this writing. It is based on that of Luehrs (1997), whereby emission in excess of the WR wind in the C III λ5696 line is modelled as fast-streaming optically thin plasma that is emitting and cooling around a conical cavity created by the collision between the O star's wind and that of the WR star. The cone axis is offset from the line that joins the WR and O stars by aberration plus a Coriolis angular deviation, and has a defined thickness and opening angle. This model was updated by Hill et al. to extend the conical cavity into the WR wind shell and add the effects of turbulence. Figure 3.1 shows a sketch of the Hill et al. model to aid in interpretation of the spectropolarimetric results presented in the rest of this paper. For more detail about this model, see Section 1.5.2.

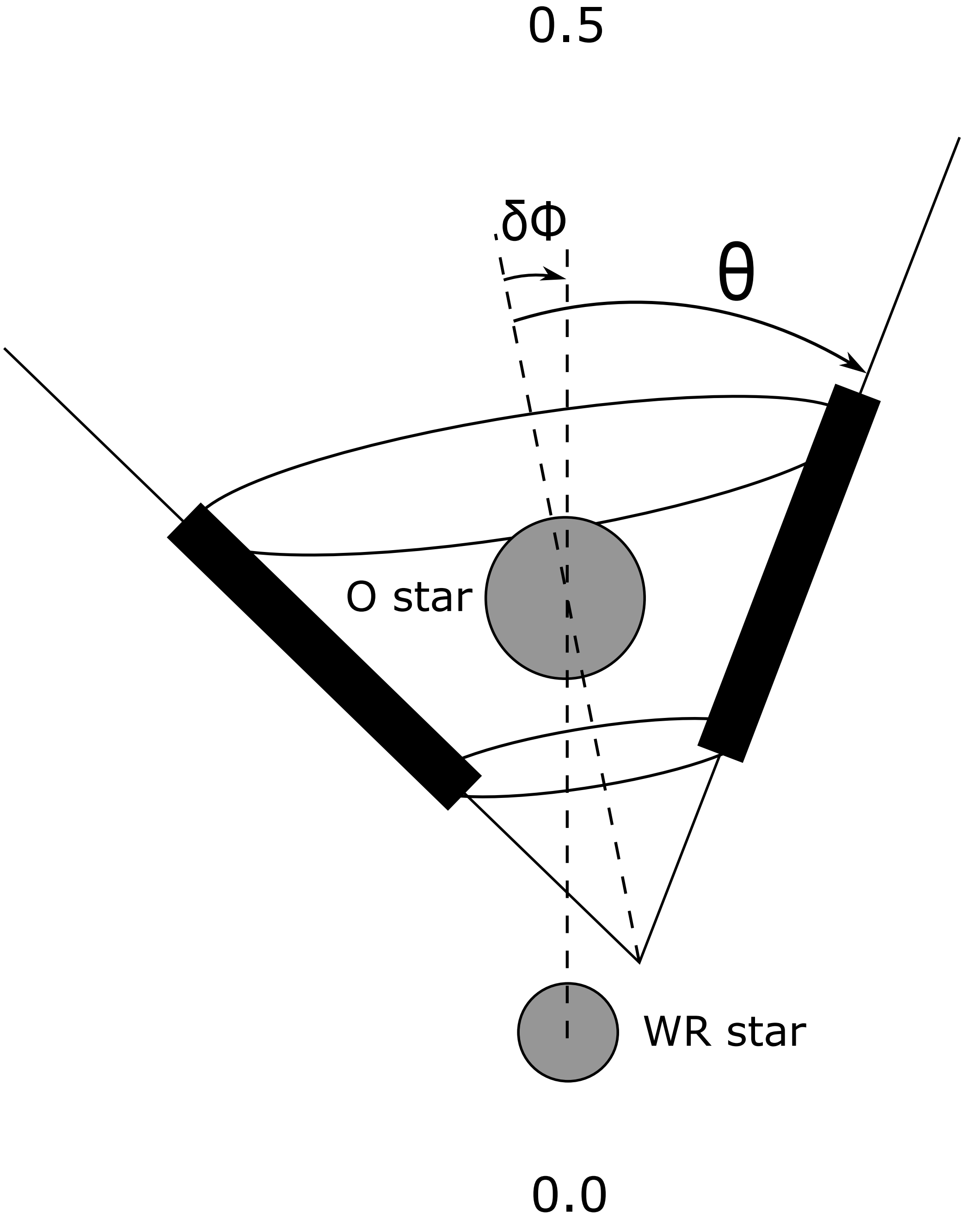

Figure 3.1: Sketch of the C III $\lambda5696$ emission model presented in Hill, Moffat, and St-Louis (2002). Phases 0.0 and 0.5 mark the viewing direction at primary and secondary conjunction, respectively. θ denotes the half-opening angle of the cone and $\delta\phi$ is the aberration/Coriolis angular deviation of the cone. The thick region of the shock cone represents the tangentially-enhanced fast-streaming C III $\lambda5696$ emission.

In this paper, we use spectropolarimetric observations at multiple orbital phases to investigate the colliding-wind geometries of both systems and assess the extent of their similarities. In Section 3.2, we present our data and observation methods. In Section 3.3, we discuss the interstellar polarization of our targets, and in Section 3.4 we describe and explain the phase behaviour of the spectropolarimetric observations in terms of continuum and line polarization. In Section 3.5 we discuss our results and how they relate to existing models of the two systems. We conclude in Section 3.6 with our findings and discussion of future work.

3.2 Data

We obtained the data from observations using the Robert Stobie Spectrograph (RSS) attached to the Southern African Large Telescope (SALT). RSS is a multi-object, medium-resolution spectrometer with polarimetric capabilities (Potter et al. 2016). We used it in long-slit grating spectropolarimetry mode covering 4200-7300 Å at resolution $R = 1200$. Observations were carried out between 2017 December and 2019 August; we summarize them in Tables 3.2 and 3.3 for WR 42 and 79 respectively.

We reduced the data using the SALT PYSALT and POLSALT packages (Crawford et al. 2010). Bin-to-bin polarimetric errors are consistent with photon statistics at a level of ∼0.01% polarization, but systematic uncertainties in absolute integrated polarization were larger, on the order of 0.06% polarization. The systematic uncertainties result from an optical-path anomaly caused by misaligned waveplate pieces, creating a wavelength dependent "ripple" (sinusoidal-like variation) in polarization position angle, which we characterize in § 3.3 (see also Fig. 1.15). In Figure 3.2, we display sample spectra from both stars, with major emission lines labeled.

We calculated the Julian date for each observation from the start of the observation date and time as recorded by SALT. The difference between observation start and end is negligible compared to the period of the stars. Observation times were on the order of 1200

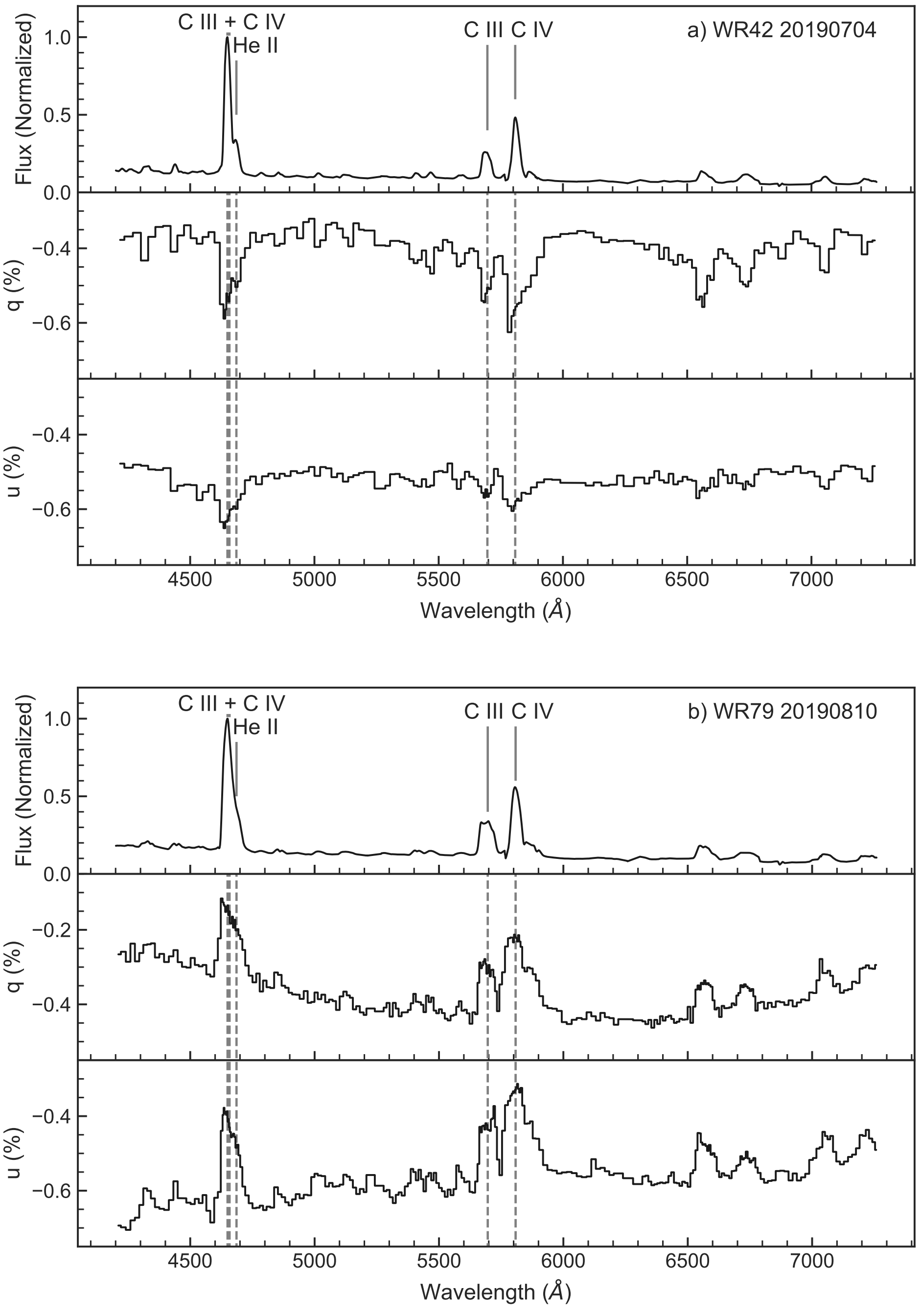

Figure 3.2: Typical spectropolarimetric data from RSS/SALT for WR 42 and WR 79. The $\%q$ and $\%u$ data are binned to an error of 0.01%. Major emission lines in carbon and helium are marked at their rest wavelengths in the observer's frame. C III + C IV are the lines at λ 4650 and λ 4658 respectively. a) WR 42 data, b) WR 79 data.

Table 3.2: Journal of RSS/SALT observations of WR 42. See Table 3.1 for the orbital parameters we used to determine orbital phase.

Observation Date	Julian Date	Orbital Phase
20171211	2458099.578	0.478*
20180103	2458122.518	0.385*
20180108	2458127.551	0.023
20180110	2458129.521	0.272
20180204	2458154.413	0.427
20180205	2458155.602	0.577
20180207	2458157.602	0.831
20180225	2458175.380	0.084
20180226	2458176.360	0.208
20180428	2458237.256	0.925*
20180512	2458251.355	0.712
20180613	2458283.290	0.758
20180705	2458305.241	0.540
20180708	2458308.241	0.920
20180719	2458319.211	0.310*
20191211	2458829.573	0.985
20191215	2458833.570	0.492
20191216	2458834.550	0.616
20191222	2458840.555	0.377
20191228	2458846.577	0.140

*Poor observational conditions or instrument error

seconds for WR 42 and 800 seconds for WR 79. We calculated orbital phases from the Julian dates (Tables 3.2 and 3.3; the JD here includes the observation time) following the prescription in the Appendix (Section 3.7).

In the phase plots below, we rely on the assumption that orbit-to-orbit variations are minimal, allowing observations to be “folded” onto a phase curve across multiple orbits. This assumption is based on previous observations of the systems conducted by St-Louis et al. (1987) that showed good long-term reproducibility of wide-band filter polarization.

3.3 Interstellar polarization and uncertainty estimates

Interstellar polarization (ISP) is an ever-present consideration for polarization measurements. In the Milky Way, it follows the empirical Serkowski law, derived from measure-

Table 3.3: Journal of RSS/SALT observations of WR 79. See Table 3.1 for the orbital parameters we used to determine orbital phase.

Observation Date	Julian Date	Orbital Phase
20180625	2458295.509	0.415
20180703	2458303.492	0.313
20180707	2458307.477	0.761*
20180709	2458309.222	0.957*
20180728	2458328.434	0.118
20180821	2458352.360	0.809
20180822	2458353.364	0.922
20180829	2458360.336	0.706*
20180911	2458373.322	0.167
20180914	2458376.309	0.503
20180928	2458390.252	0.071
20181005	2458397.258	0.859
20200319	2458928.530	0.612
20200320	2458929.530	0.725
20200508	2458978.395	0.221

*Poor observational conditions or instrument error

ments of intrinsically unpolarized standard stars in multiple directions in the sky (Serkowski, Mathewson, and Ford 1975). The effect of the ISP is to transform the intrinsic Q and U Stokes vectors as a function of wavelength. Thus a reasonable ISP estimate is necessary for extracting intrinsic polarization values and directly comparing the polarization values of emission lines that are separated in wavelength.

We investigated two methods to determine the ISP contribution for both our targets using the RSS/SALT data alone. We first attempted to fit a Serkowski law to the full polarized spectrum of each star, but the confusion introduced by the large number of polarized lines, combined with their large widths, prevented us from reliably determining the shape of the continuum polarization with wavelength. Second, we made the assumption that the most depolarized line in each object represented the maximum possible value of the ISP at that wavelength. This result produced reasonable agreement with the ISP values from the broadband polarization filter fits of Fullard et al. (2020), so we used values from that paper because it is not guaranteed that the lines are completely unpolarized. The ISP is described by equations 3.1 and 3.2 (Moffat and Piirola 1993).

$$q_{ISP} = q_{00} + P_{\mathrm{IS,max}} \cos 2\theta_{\mathrm{IS}} \exp\left[-1.7\lambda_{\mathrm{max}} \ln^2(\lambda_{\mathrm{max}}/\lambda)\right] \tag{3.1}$$

$$u_{ISP} = u_{00} + P_{\mathrm{IS,max}} \sin 2\theta_{\mathrm{IS}} \exp\left[-1.7\lambda_{\mathrm{max}} \ln^2(\lambda_{\mathrm{max}}/\lambda)\right] \tag{3.2}$$

In these equations, q_{00} and u_{00} are the constant components of the ISP, $P_{\mathrm{IS,max}}$ is the peak ISP, $\theta_{IS} = \theta_{IS}(0) + k/\lambda$ is the wavelength-dependent position angle of the ISP, and λ_{max} is the peak wavelength where the ISP is strongest. More detail can be found in Chapter 2.

The ISP is assumed to be constant over the 2-year timescale of our observations (Table 3.2 and 3.3). We use the ISP values from Fullard et al. (2020) (see Table 3.4) and subtract them from the data before fitting the position angle spectrum using equation 3.3. In the rest of this paper, "intrinsic" polarization refers to data from which we have subtracted the ISP estimates in Table 3.4.

3.3.1 Systematic uncertainty estimates

The "ripple effect" is an instrumental polarization described by the empirical function 3.3, where $f(\lambda)$ is the interpolated position angle ripple function taken from a 100% polarized Xe lamp fed through the instrument optics (see Fig. 1.15 and Section 1.6.4), x allows the ripple to translate in wavelength space, A is the scaled amplitude of the ripple, and ψ is the rotation of the ripple in polarization position angle. This effect is not currently corrected for by the instrument data reduction pipeline.

$$\theta_r = Af(\lambda + x) + \psi \tag{3.3}$$

Following the fit, we calculated the effect of the ripple on q and u uncertainty by first calculating $q_r = p \cos 2\theta_r$ and $u_r = p \sin 2\theta_r$, where $p = \sqrt{q^2 + u^2}$. The maximum amplitudes of q_r and u_r were taken to be estimates of σ_{q_r} and σ_{u_r}, respectively. These uncertainties are biased by the position angle of the data. Thus, we used the covariance of the ripple, $\sigma_{q_r u_r}$, to determine the uncorrelated uncertainties $\sigma_{q'}$ and $\sigma_{u'}$, following Montier et al. (2015). In this formulation,

$$\sigma_{q'}^2 = \sigma_{q_r}^2 \cos^2\theta + \sigma_{u_r}^2 \sin^2\theta + \sigma_{q_r u_r} \sin 2\theta, \tag{3.4}$$

$$\sigma_{u'}^2 = \sigma_{q_r}^2 \sin^2\theta + \sigma_{u_r}^2 \cos^2\theta - \sigma_{q_r u_r} \sin 2\theta, \tag{3.5}$$

and

$$\theta = \frac{1}{2} \arctan\left(\frac{2\sigma_{q_r u_r}}{\sigma_{q_r}^2 - \sigma_{u_r}^2}\right). \tag{3.6}$$

The resulting uncertainties $\sigma_{q'}$ and $\sigma_{u'}$ are on the order of 0.05% polarization for WR 42 and 0.04% for WR 79.

There are multiple caveats to this method. Firstly, the complex polarization spectra do not lend themselves well to fitting smooth curves; this results in even small line polarization features skewing the fit. Secondly, it is not certain whether the Xe lamp's position angle curve can simply be scaled and translated to correctly represent all of the possible instrumental effects. Finally, fitting first in position angle and then decomposing to the more fundamental q and u quantities introduces an additional source of bias, though we have attempted to correct for this using the uncorrelated uncertainties. However, this is a temporary measure to estimate uncertainties for data that are not fully calibrated to gain initial information about these systems.

3.4 Phase behaviour

The polarization variations of both stars have two major features: one, the continuum polarization oscillates sinusoidally with phase, as expected from theoretical binary polariza-

Table 3.4: Interstellar polarization estimates from Fullard et al. (2020), which we have subtracted from data presented as intrinsic.

Parameter	WR 42	WR 79
$P_{\mathrm{IS,max}}$ (%)	1.177 ± 0.131	0.376 ± 0.007
θ_{IS} (°)	-46.3 ± 2.5	-81.5 ± 4.8
k ($^\circ \cdot \mu$m)	0	4.7 ± 0.8
$\lambda_{\max}$ (μm)	0.568 ± 0.009	0.595 ± 0.015

tion models (Brown, McLean, and Emslie 1978); two, the emission line polarization varies with phase, but different emission lines have different phase behaviour. This suggests that they originate (and possibly scatter) in different parts of the WR-star wind-interaction region. We explore both of these behaviours in detail below.

3.4.1 Broadband continuum polarization

We extracted approximate continuum polarization values from our spectropolarimetric data by weighted integration of the data with Johnson BVR filter response curves. See Section 1.6.4 for more information about the filter procedure. Although Thomson scattering is spectrally grey, the strong line polarization effects at some phases mean that using a synthetic filter response allows us to compare our data with previous results by St-Louis et al. (1987) and Moffat and Piirola (1993). The St-Louis et al. (1987) data were observed with a broad blue filter, centered on 4700 Å with a FWHM of 1800 Å. The Moffat and Piirola (1993) data were observed with standard Johnson $UBVR$ filters. We tabulate the RSS BVR polarization values in Appendix B (Section A.8).

We combined our continuum results with those of St-Louis et al. (1987) and Moffat and Piirola (1993), and fit the combined data set with the analytical binary star polarization model from Moffat et al. (1998), itself an adaption of the model of Brown et al. (1982), Simmons and Boyle (1984), and Robert et al. (1992). The fitted equations are

$$q = q_0 + \Delta q \cos \Omega - \Delta u \sin \Omega, \tag{3.7}$$

$$u = u_0 + \Delta q \sin\Omega + \Delta u \cos\Omega, \tag{3.8}$$

where

$$\Delta q = -\tau_3[(1 + \cos^2 i)\cos 2\lambda - \sin^2 i] \tag{3.9}$$

and

$$\Delta u = -2\tau_3 \cos i - \sin 2\lambda. \tag{3.10}$$

The parameters q_0 and u_0 represent any constant polarization; this may be intrinsic or insterstellar polarization. Ω is the position angle of the line of nodes on the sky counter-clockwise from the north, and i is the orbital inclination with respect to the line of sight (where $i = 0$ is a face-on orbit and $i = 90$ is edge-on; see Section 1.5.2 and Fig. 1.12). The quantity λ is the orbital phase for a circular orbit. Finally, τ_3 is given by $\tau_3 = \tau_*(a/r)^\gamma$, with τ_* representing the mean optical depth, a the mean orbital separation, and r the instantaneous separation. Since both systems have circular orbits (Hill et al. 2000), $a = r$ and $\tau_3 = \tau_*$ (see Section 1.5.2).

To ensure consistency among data sets, before applying the fits, we recalculated the orbital phases for data from St-Louis et al. (1987) and Moffat and Piirola (1993) using their reported observation dates and the adopted ephemerides defined in Table 3.1. We discuss our choice of ephemerides for both systems in Section 3.7.

Even after this recalculation, however, the archival data did not align well in phase with our RSS data. It is unlikely that the real orbits of WR 42 and WR 79 have changed in the time between the observations reported in St-Louis et al. (1987) and Moffat and Piirola (1993), and the ephemeris of Hill et al. (2000) that we confirm in Section 3.7. If we can continue to use the Hill et al. (2000) ephemeris after ~ 20 years, but data from ~ 10 years prior do not match, it suggests the older data were not dated accurately. However, the wavelength resolution of our RSS spectra is not high enough to derive new ephemerides, so we cannot conclusively rule out a real orbital change. Instead, we adjusted the calculated

Table 3.5: Phase shifts and q, u zero-point shifts added to each archival data set for comparison with our RSS/SALT data.

Data set	Phase shift	q_{shift} (%)	u_{shift} (%)
WR 42			
St-Louis et al. (1987)	+0.08	0.00	0.00
Moffat and Piirola (1993)	+0.07	0.00	0.00
WR 79			
St-Louis et al. (1987)	+0.06	+0.152	-0.116
Moffat and Piirola (1993)	+0.05	+0.086	-0.115

phases for each archival data set by a constant shift to match our RSS data, under the assumption that the data should match because the Hill et al. (2000) ephemeris has not shown a change over time. To do this, we applied the analytical model functions (Eqns. 3.7 and 3.8) to the combined data set for each star allowing for the phases of both the archival data sets to shift by a constant value. We present our adopted phase shifts in Table 3.5.

We made further adjustments to the archival data by applying a zero-point shift to align their q_0 and u_0 values with those of the RSS data. This corrects for the different instrumental polarization effects produced by different instruments (up to 0.15%; Drissen et al. 1986). To determine these zero-point shifts, we added a constant term to each of Equations 3.7 and 3.8 (q_{shift} and u_{shift}) for the St-Louis et al. (1987) and Moffat and Piirola (1993) data. We then fit the three data sets simultaneously with these equations, keeping Ω, i and τ_* as the same values across all data sets but allowing the q_{shift}, u_{shift} values to change. We present our adopted zero point shifts in Table 3.5. WR 42 did not require a zero point shift. These range from $0 - 0.2\%$, which is typical for polarimetric shifts among different instruments (e.g. Moffat et al. 1998).

We carried out the final fits in q and u simultaneously, using the LMFIT package (Newville et al. 2014); we list the fit parameters for both stars in Table 3.6 and display the data and fits in Figs. 3.3 and 3.4. Following the uncertainty analysis of Wolinski and Dolan (1994), we calculated the upper and lower bounds of certainty on i. These are also presented in Table 3.6. The uncertainty on Ω is large enough for low i that Ω is consistent with zero

Table 3.6: Broadband continuum fit results for our RSS data combined with those of St-Louis et al. (1987) and Moffat and Piirola (1993).

Parameter	WR 42	WR 79
i (°)	38.8±38.8	34.0±34.0
τ_* ($\times 10^{-3}$)	1.17±0.17	1.48±1.39
Ω (°)	88.7	31.9

(see Wolinski and Dolan 1994, and Section 1.5.2 for a discussion of the bias in the BME model). The large uncertainties on the fitted values are the result of the inherent bias in the analytical model towards higher inclination angles, as well as the ratio of polarization uncertainties to polarization variability in the data. Future correction of the ripple in the SALT data will improve the fit uncertainties by greatly reducing the uncertainty of the SALT data (see Section 3.3.1).

3.4.2 Narrow-band continuum polarization

We extracted narrow-band continuum polarization from the RSS data by performing a weighted integration of the data with the synthetic narrow-band b, v and r filters from Massey (1984), which are explicitly different from the Johnson BVR filters applied in Section 3.4.1. The bvr filters are designed to avoid areas of strong line emission. See Section 1.6.4 for more information about the filter procedure. We carried out the same fitting procedure with these data as in § 3.4.1, using the RSS data only. We compared the results for different filters to determine whether there was any colour dependence in the continuum polarization. When we fit the filters individually with the analytical model, only the q_0 and u_0 parameters showed a difference between filters at the 3σ level; we attribute these differences to the (small) wavelength dependence of the ISP. Table 3.7 lists the error-weighted mean q and u polarization for each band. Taking advantage of the negligible differences between filters, we next calculated the error-weighted mean of all the time-dependent continuum polarization values to reduce the systematic uncertainties, and repeated the fitting process to obtain the results presented in Table 3.8. Once again, uncertainties were estimated using

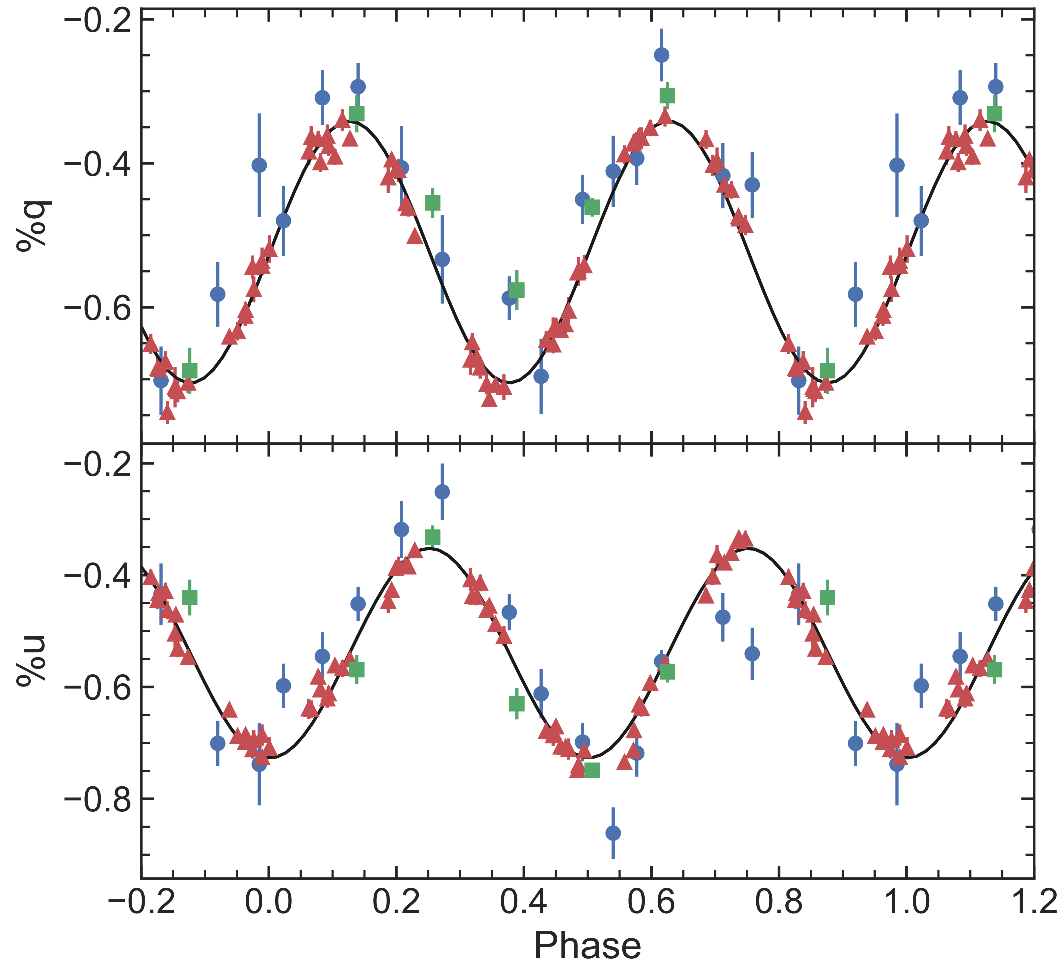

Figure 3.3: Broadband WR 42 polarization (Stokes q and u) from St-Louis et al. (1987, *red triangles*), Johnson B-band polarization from Moffat and Piirola (1993, *green squares*), and Johnson B-band polarization from RSS (*blue circles*). The error bars represent plus or minus 1σ uncertainties. The solid black curve is the fit of equations 3.7 and 3.8 to the continuum data. The fit results are presented in Table 3.6. The data from St-Louis et al. (1987) and Moffat and Piirola (1993) were shifted in both phase and zero point by the amounts listed in Table 3.5 (see Section 3.4.1

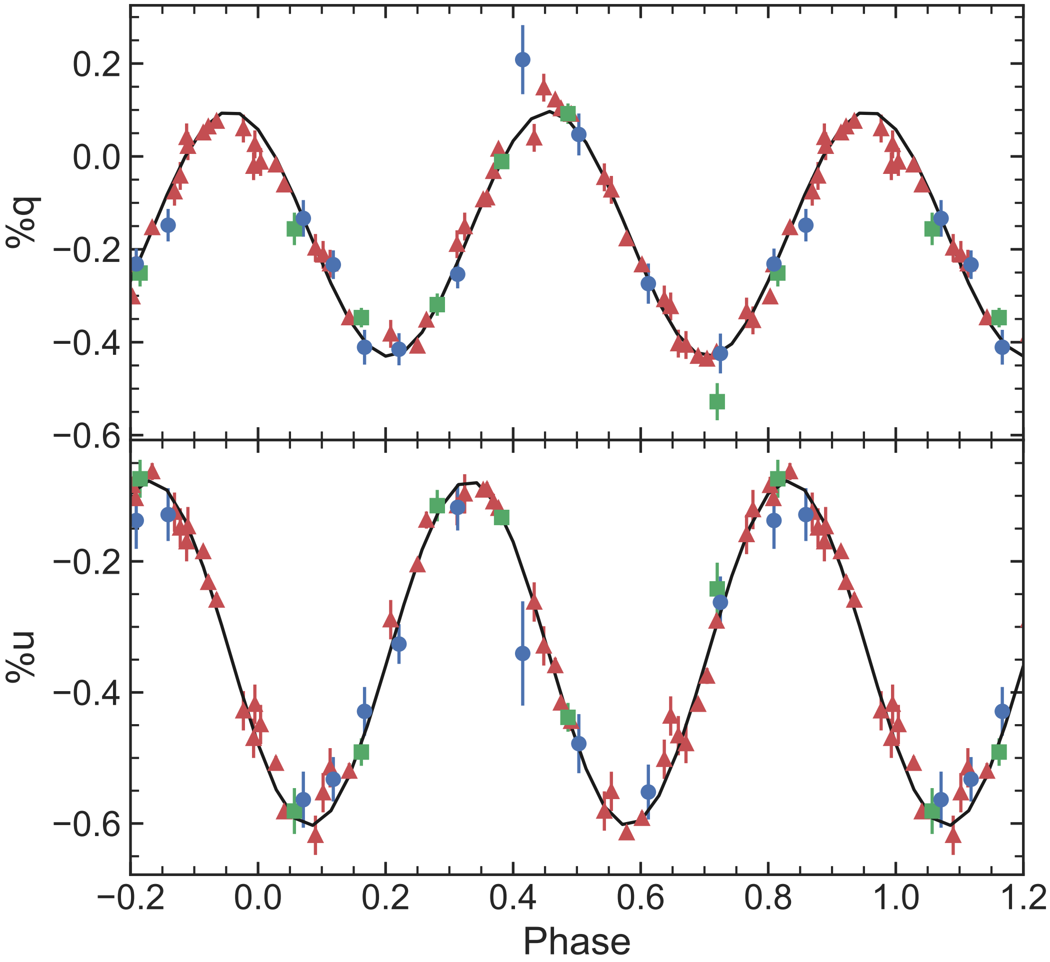

Figure 3.4: Same as Fig. 3.3, but for WR 79. The data from St-Louis et al. (1987) and Moffat and Piirola (1993) were shifted in phase and zero point by the amounts listed in Table 3.5.

Table 3.7: Error-weighted mean narrowband continuum polarization.

	WR 42	WR 79
b-filter		
$\bar{q}$ (%)	-0.425 ± 0.011	-0.259 ± 0.011
$\bar{u}$ (%)	-0.539 ± 0.010	-0.361 ± 0.012
v-filter		
$\bar{q}$ (%)	-0.480 ± 0.011	-0.339 ± 0.011
$\bar{u}$ (%)	-0.622 ± 0.010	-0.334 ± 0.012
r-filter		
$\bar{q}$ (%)	-0.470 ± 0.011	-0.352 ± 0.011
$\bar{u}$ (%)	-0.620 ± 0.010	-0.311 ± 0.012

Table 3.8: Fit results to the error-weighted mean narrowband continuum RSS data.

Parameter	WR 42	WR 79
i (°)	37.4±37.4	34.0±34.0
τ_* ($\times 10^{-3}$)	1.47±0.71	1.94±0.67
Ω (°)	86.0	28.7

the analysis of Wolinski and Dolan (1994), and this produced the large uncertainties making most results consistent with zero.

The fit results are presented in Figures 3.5 and 3.6. We expect these fits to produce different results from the broadband data, because the broad filter used by St-Louis et al. (1987) includes the strong C III λ4650 and He II λ4686 emission lines, which contain their own polarization signatures, as shown in Figure 3.2. Similarly, the standard Johnson filters used by Moffat and Piirola (1993) cover many of the emission lines of the systems. Our RSS data do not provide sufficient phase coverage of the orbits to draw strong conclusions from the narrow-band results alone; all the parameters we derive from the narrow-band fits are the same as those found in § 3.4.1.

3.4.3 Line polarization

We extracted the polarization of the strong emission lines using the `pfew` method following Lomax et al. (2015), whereby the integrated continuum polarization is estimated

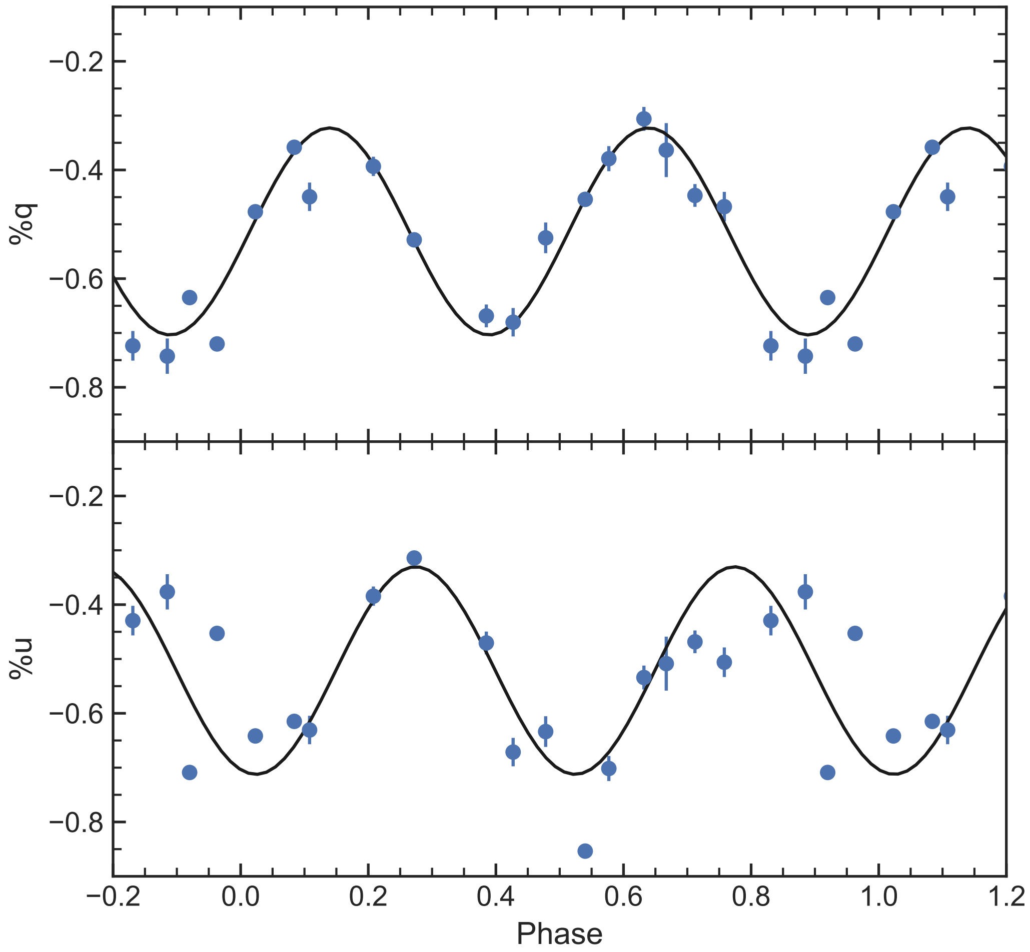

Figure 3.5: WR 42 measured polarization (Stokes q and u) plotted versus phase for the error-weighted mean narrow-band filter extracted from the RSS data only (blue points; see § 3.4.1 for details). The error bars represent 1σ uncertainties. The solid black curve is the fit of equations 3.7 and 3.8 to the continuum data. The fit results are presented in Table 3.8.

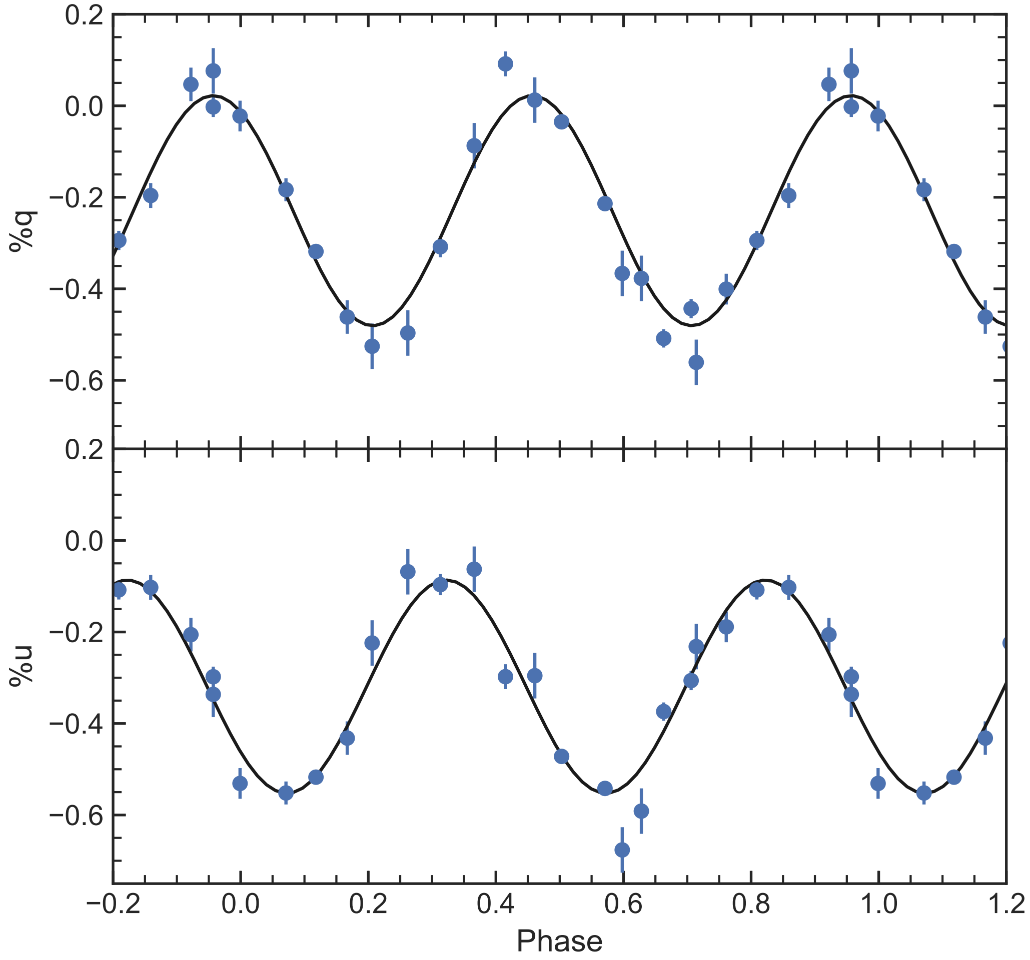

Figure 3.6: Same as Fig. 3.5, but for WR 79.

Table 3.9: Defined line and continuum regions used to measure integrated line polarization. The regions used were identical for both systems. They are displayed graphically in Figure 3.7.

Line region	Blue continuum (Å)	Line (Å)	Red continuum (Å)
C III λ 4650 + C IV λ 4658 + He II λ 4686	4491–4568	4579–4761	4767–4821
C III λ 5696	5500–5550	5629–5740	5928–6120
C IV λ 5801 + λ 5812	”	5760–5852	”

and subtracted from the integrated polarization of the line feature plus continuum (see §1.6.4). This produces a single polarization measurement for each emission line at each phase. Table 3.9 lists the values that were used to determine the integration region and the continuum values, and Figure 3.7 displays them graphically. The emission lines arise in different regions of the WR wind as discussed in Section 1.3. In general, higher ionization states occur deeper in the WR wind at higher densities. Thus C IV is probing further into the wind than C III, while He II arises in the outer regions of the wind (see Fig. 1.5).

We present the line polarization data in Figures 3.8 and 3.9 for WR 42 and WR 79, respectively. The data have been processed to subtract the ISP (see § 3.3) from both the line polarization and continuum models, and then rotated to the intrinsic error-weighted mean position angle of the combined broadband continuum (§ 3.4.1). This means that the Stokes parameters now contain geometrical information about the line scattering regions relative to the plane of the orbit. A particularly important result displayed by both stars is a phase shift of the C IV 5800 region line polarization compared to the continuum polarization. By eye, the shift appears to be about 0.25. This is discussed in more detail in Section 3.5.

We calculated the standard deviations of the continuum polarization and line polarization data. The line polarization in all cases shows less variation with phase than the broadband continuum. The lines have very low mean intrinsic (ISP-subtracted) polarization in both q and u. The results of the calculations are shown in Table 3.10. σ_q and σ_u are the standard deviations for the q and u data, respectively.

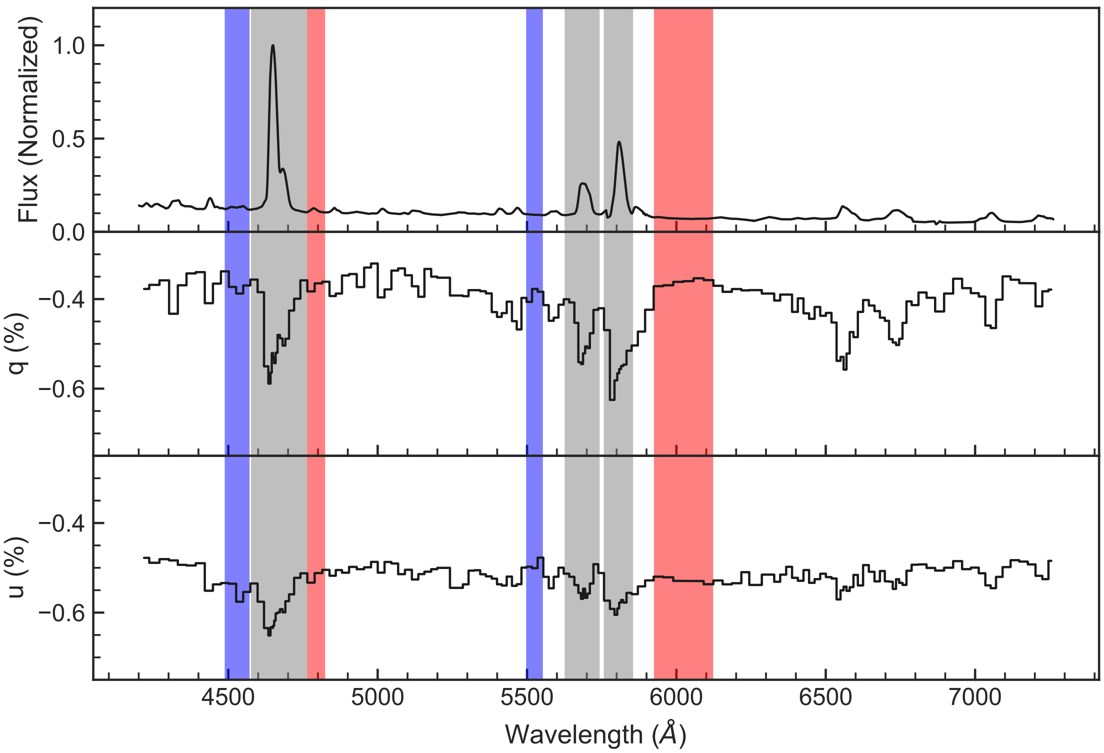

Figure 3.7: Highlighted regions for the polarized line integration method. Red and blue shading represents the red and blue side continuum values, respectively. The grey regions were used to integrate the major emission lines. From left to right, these are C III λ 4650 + C IV λ 4658 + He II λ 4686, C III λ 5696, C IV λ 5801 + λ 5812. The same regions were used for both stars.[1]

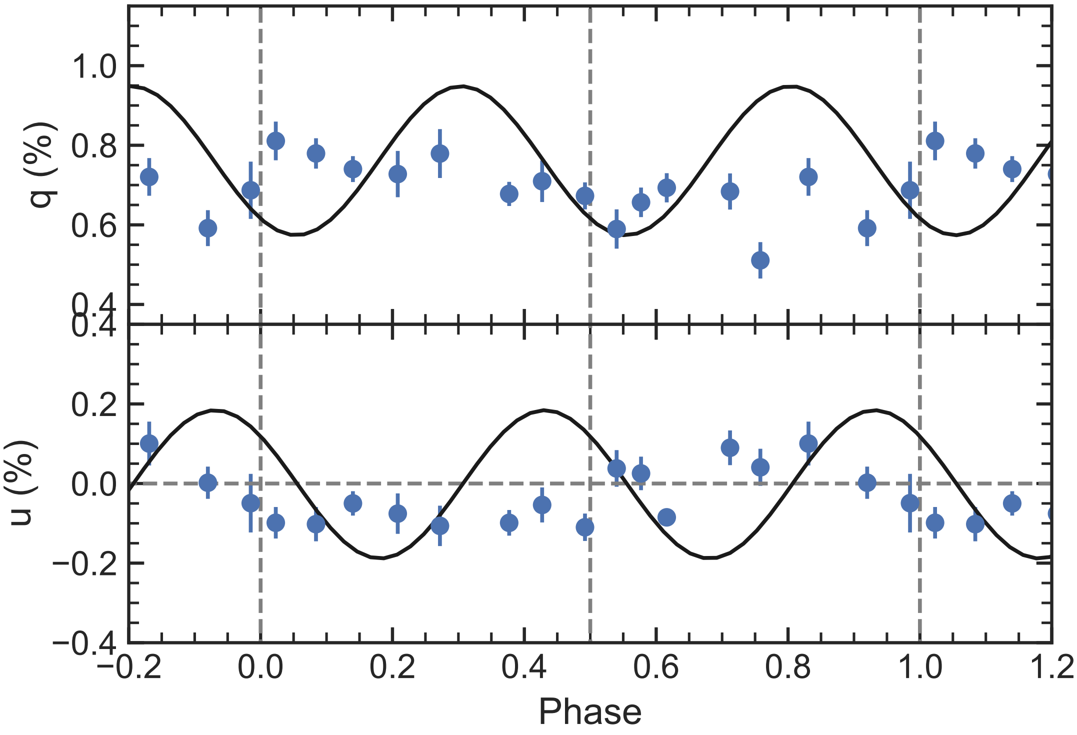

Figure 3.8: WR 42 integrated line polarization with phase. The points are the intrinsic $\%q$ and $\%u$ line polarization, rotated to the mean position angle of the **continuum** from § 3.4.1. The solid black curve is the fit of equations 3.7 and 3.8 to the combined broad-band continuum data with ISP subtracted, rotated to the mean position angle of the continuum. We set the variables q_0 and u_0 equal to zero. Blue circles are C III λ 4650 + C IV λ 4658 + He II λ 4686, green triangles are C III λ 5696 and red squares are C IV λ 5801 + λ 5812.

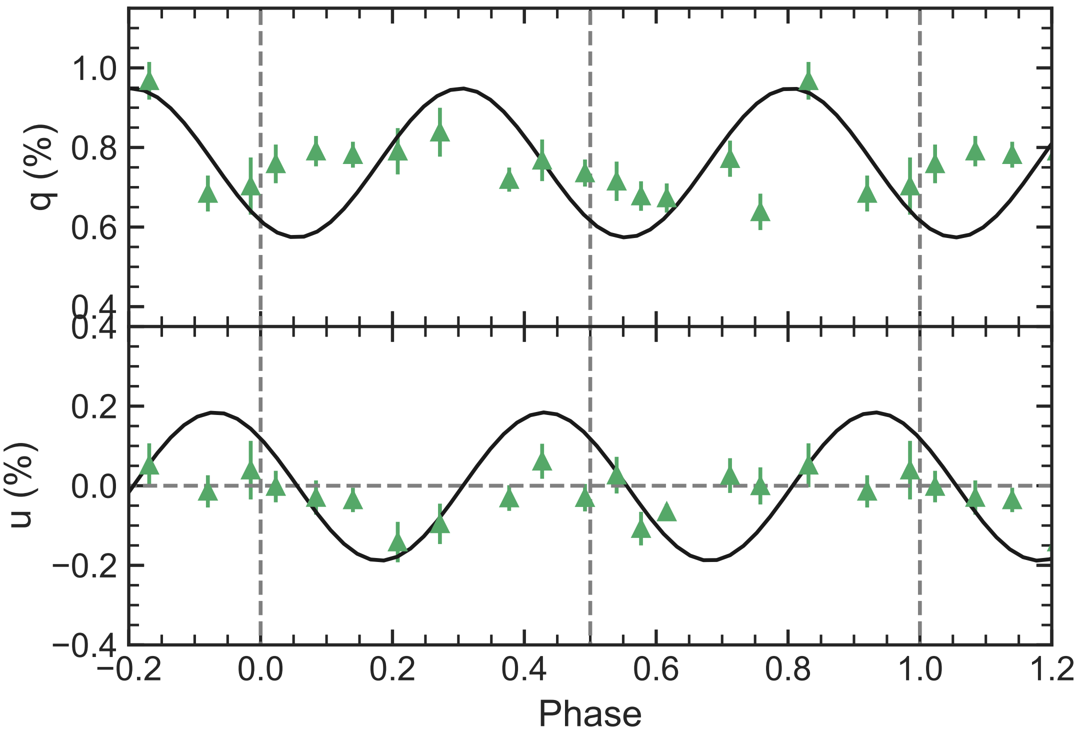

Figure 3.8: (cont...)

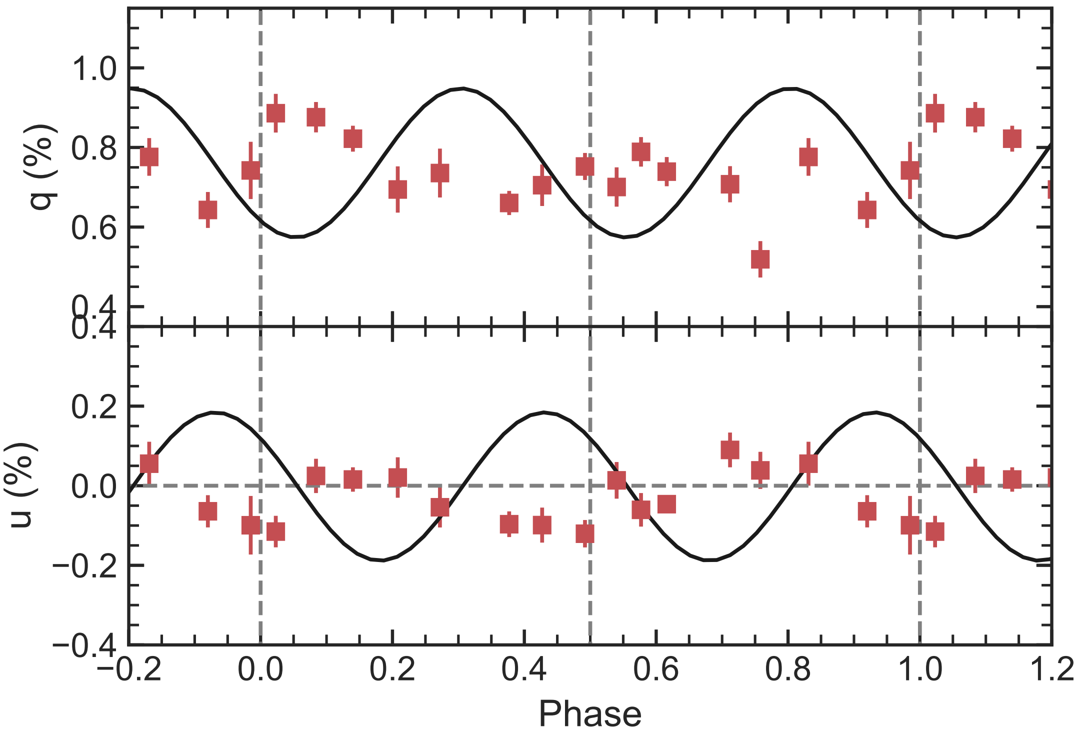

Figure 3.8: (cont...)

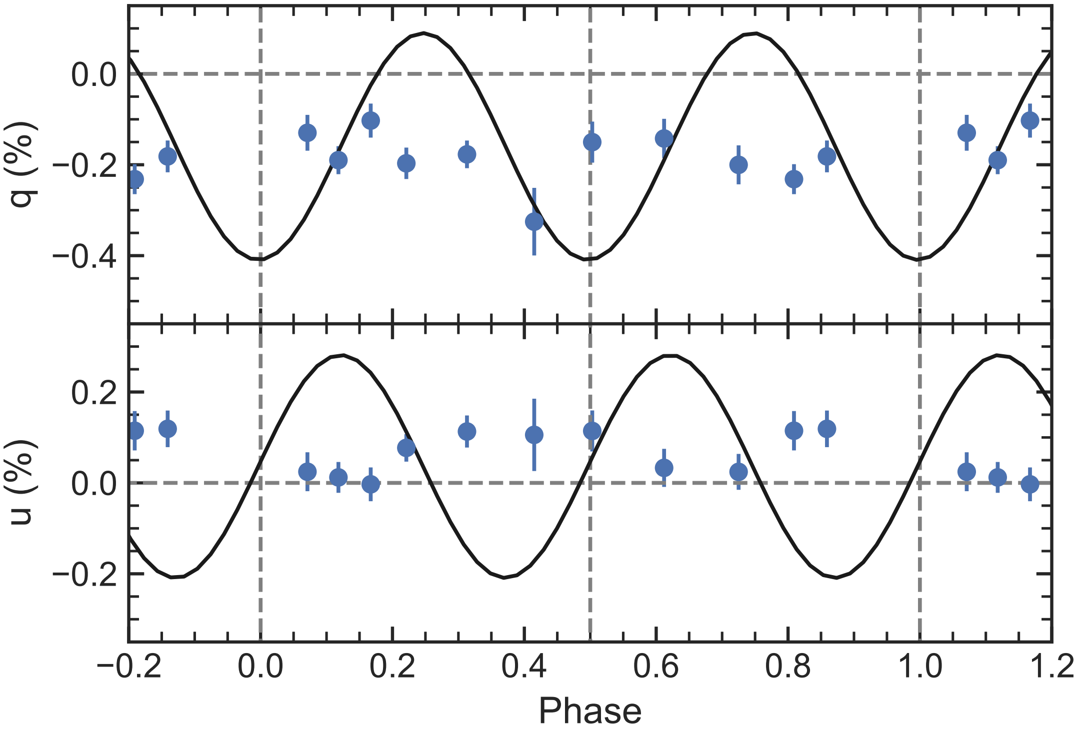

Figure 3.9: Same as Figure 3.8, but for WR 79.

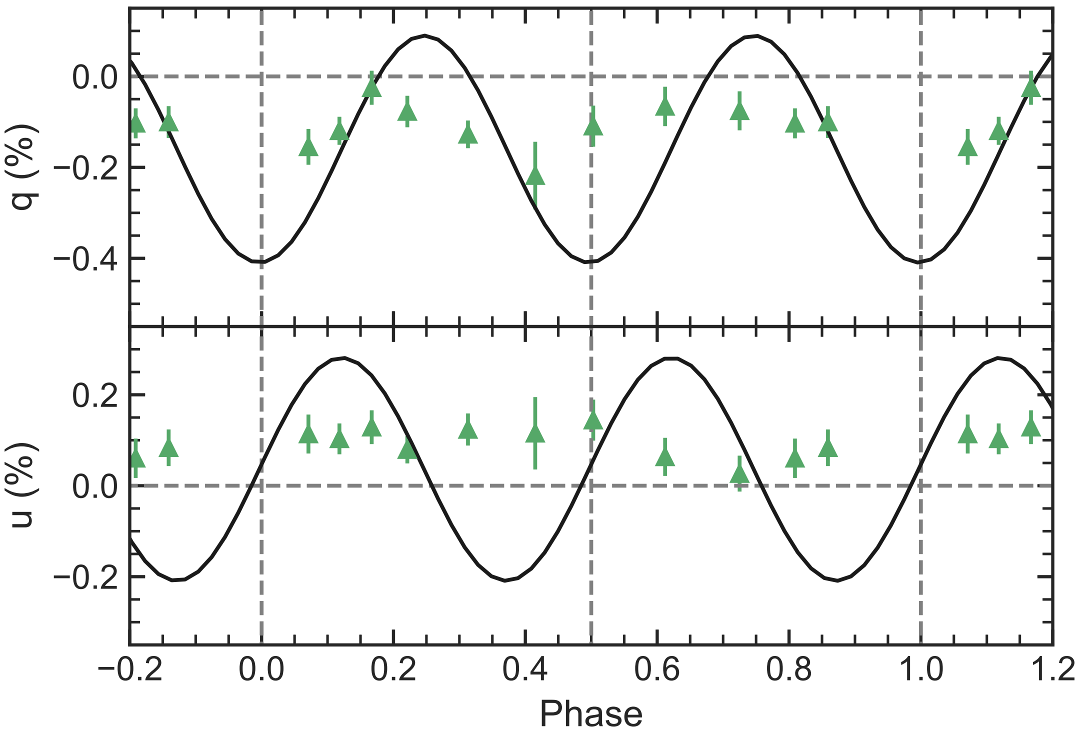

Figure 3.9: (cont...)

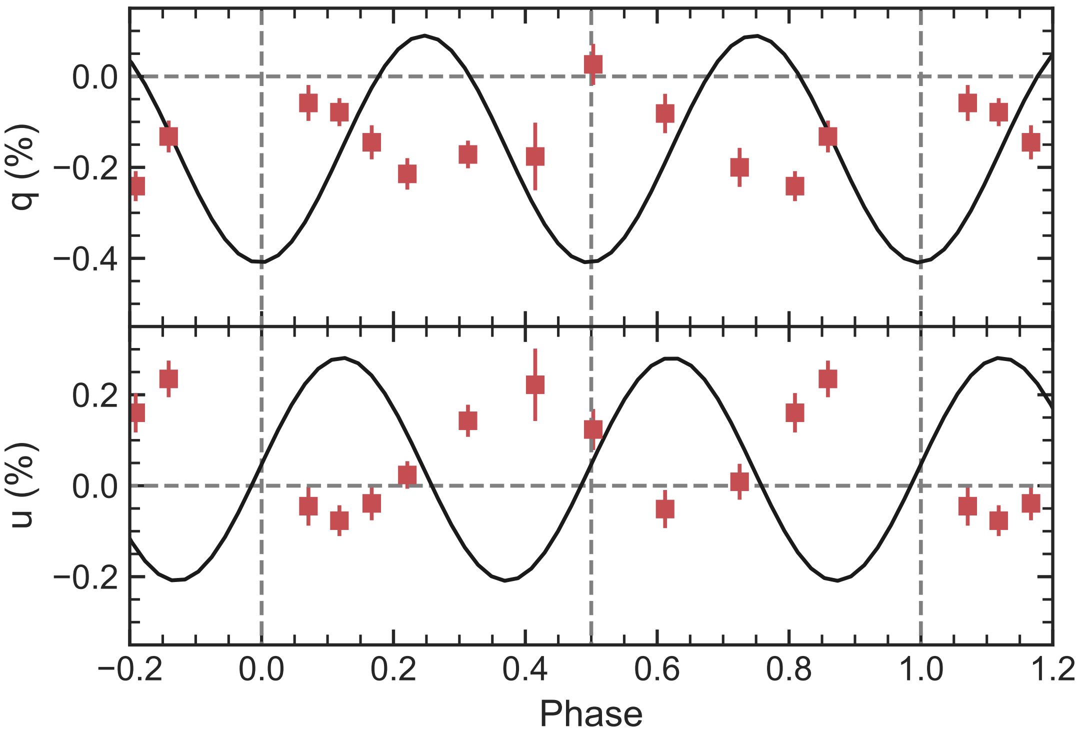

Figure 3.9: (cont...)

Table 3.10: Error-weighted mean intrinsic integrated line polarization, pre-rotation line position angle, and standard deviation for both WR 42 and WR 79. Analytic model intrinsic continuum values are provided for comparison purposes.

		$\bar{q}$ (%)	σ_q (%)	$\bar{u}$ (%)	σ_u (%)	$\bar{\theta}$ (°)
WR 42	Continuum	0.760	0.133	-0.001	0.132	64.2
	C III $\lambda4650$ + C IV $\lambda4658$ + He II $\lambda4686$	0.678	0.077	-0.028	0.072	62.8
	C III $\lambda5696$	0.737	0.079	-0.026	0.058	63.2
	C IV $\lambda5801$ + $\lambda5812$	0.714	0.090	-0.029	0.067	63.0
WR 79	Continuum	-0.162	0.178	0.036	0.173	75.3
	C III $\lambda4650$ + C IV $\lambda4658$ + He II $\lambda4686$	-0.186	0.059	0.061	0.049	155.8
	C III $\lambda5696$	-0.106	0.050	0.087	0.035	145.8
	C IV $\lambda5801$ + $\lambda5812$	-0.144	0.079	0.058	0.116	139.3

3.5 Discussion

3.5.1 Continuum polarization

The continuum polarization data, both narrow– and broad–band, are consistent with the analytical models based on Brown, McLean, and Emslie (1978) (after archival data were adjusted; § 3.4.1). This is probably due to the low inclination angles of both systems, which mean that eclipse effects like those in V444 Cyg (Lomax et al. 2015; St-Louis et al. 1993) do not play a role in producing the continuum polarization (see discussion in Section 1.5.2 regarding eclipse effects, and V444 Cyg data in Chapter 4). Following the analytical model, the continuum polarization variation is a measure of the mean optical depth of the scattering material, described by τ_* in Tables 3.6 and 3.8. The values we find for τ_* are typical for WR star winds (e.g. St-Louis et al. 1988). In general, the adherence to the model suggests that in both cases, the bulk of the scattering material can be approximated as optically thin, and it surrounds the WR star (i.e. its wind). Therefore, this polarization arises from continuum light emitted from the O star scattering in the WR star wind as expected from the illumination of a scattering region by two sources in the BME model (see Section 1.5.2).

Another important system parameter is the inclination angle i. Previous estimates for i are shown in Table 3.1. Our estimates lie within the ranges for each system, though the large uncertainties on the analytical polarization models at low inclination angles and our insufficient phase coverage means that no strong conclusions can be drawn about the systems from our continuum data.

Even after ISP subtraction, WR 42 contains a significant constant polarization (Table 3.10, $\bar{q}$ column). The rotation of all the data to the mean position angle of the continuum means that the majority of continuum polarization occurs along the q parameter. WR 42 has $\bar{q} \sim 0.7\%$. This could mean the wind is significantly distorted by the colliding wind region, creating asymmetries; or, the WR star is rapidly rotating, creating an elongated wind parallel to the rotation axis. It is also possible that the ISP estimate from Fullard et al. (2020) does not fully characterize the ISP of WR 42. However, Fullard et al. (2020) also found that WR 42 did have a significant constant intrinsic polarization component and attributed it to wind asymmetries that are not part of the analytical model. Together, this suggests that the classic analytical model is incomplete and numerical models are needed to account for all possible sources of polarization. I describe such a model in Chapter 4.

3.5.2 Integrated line polarization

The line regions presented in §3.4.3 have a lower magnitude of polarization variation on average when compared to the continuum (see Table 3.10). This occurs because the emission lines arise in both the WR star wind and in a streaming region in the colliding wind shock (Fig. 3.1). Thus, the orbital motion of the colliding wind region creates phase-varying polarization while the emission from the near-spherical unperturbed WR wind region dilutes the polarization percentage in the lines (see Section 1.5).

The phase behaviour of the emission line polarization can be directly compared to the continuum polarization, as shown in Figures 3.8 and 3.9. For both WR 42 and WR 79, the C IV λ5800 region displays phase behaviour that is out of phase with the analytical model by $\sim$0.25, or $\sim 90^{\circ}$ away from the O star in the orbit. This likely corresponds to the leading or trailing edges of the colliding wind shock as seen in the Hill, Moffat, and St-Louis (2002) model and Fig. 3.1. Both stars were shown by Hill, Moffat, and St-Louis (2002) to have a shock cone opening angle of $\theta \sim 25^{\circ}$ and a very large shock cone thickness of $\Delta\theta \sim 50^{\circ}$. The large thickness means that almost the entire volume of the cone in Fig 3.1 is filled by shocked material, though the density near the O star is lower (see Section 1.4). However, the polarization phase difference suggests that the majority of the C IV λ5800 region emission is occurring at the interface between the two winds, rather than closer to the O star. Usually we would expect two

What is surprising about the polarization variation of C IV λ5800 is that it is not typically modeled to determine shock cone parameters. Instead, the lower-ionization C III λ5696 line has been used by Hill, Moffat, and St-Louis (2002) and Hill et al. (2000) to model the colliding winds of both WR 42 and WR 79 because of its sensitivity to density. In polarization, this C III line does not show variations as significant as in C IV λ5800 (although they are still slightly greater than the uncertainty), nor is there a clear phase difference between the behavior of C III λ5696 compared to the continuum polarization. Figures 3.8 and 3.9 show that some of the C III λ5696 (green triangle) polarization matches the continuum in some parts of the orbit. If this effect is real (and better phase coverage and instrumental error correction are needed to be sure), then it suggests the C III λ5696 emission is occurring much closer to the O star than the C IV λ5800 emission. Alternatively, C IV λ5800 emission from the WR wind may not dilute the polarization signal as much as C III λ5696 emission.

Finally, the C III λ4650 spectral line region shows the lowest amount of polarization variation with phase for both stars. This implies that only a small amount of emission is occurring externally to the hot, optically thin parts of the WR wind, and the majority is likely to be originating from the WR wind itself. This implies that we may have detected the "line effect" (see §1.5), where depolarized emission lines indicate the presence of global wind asymmetries that could be caused by rapid rotation of the WR star (see § 1.5).

3.5.3 WR 42 and WR 79: spectropolarimetric twins?

As expected, our results show that both WR 42 and WR 79 are very similar in both continuum and line polarization variations. This tracks with the model of Hill, Moffat, and St-Louis (2002), who found very similar shock cone parameters for both systems. The major differences between the systems are shown in Table 3.10.

The strong, constant intrinsic continuum polarization of WR 42 is good evidence for an asymmetric wind. As noted above, this could be either the influence of the colliding wind shock cone, or rapid rotation of the WR star aligning the wind to a preferred axis. The former scenario is less likely given that WR 79 has a very similar colliding-wind structure; if this were the cause of the constant intrinsic polarization component, we would expect

WR 79 to display similar behaviour. However, the constant intrinsic polarization of WR 79 is much smaller ($|\bar{q}| \sim 0.2\%$). This difference in magnitude could also be due to our incorrectly characterizing the ISP towards WR 42, although this would not change any of our conclusions regarding the polarization variations of the object.

While WR 42 shows very little difference between the mean polarization position angles of its continuum and line polarization, WR 79 has a $\sim 75^\circ$ rotation between the two polarization regimes (see Table 3.10). WR 79 also shows greater variation in position angle between the different line emission regions (see Table 3.10 compared to WR 42). This could be related to the change in sign of the Coriolis angular deviation $\delta\phi$ (Fig. 3.1) that was found by Hill, Moffat, and St-Louis (2002) compared to WR 42. However, the likely cause for both differences is that WR 79 does not exhibit the strong constant intrinsic polarization of WR 42, which means that the position angle is not well-defined in $q - u$ space. Furthermore, the low inclination angle means that the analytical model fit is almost a circle in $q - u$ space. Because we have removed the ISP component, such a circle lies near the $q - u$ origin and thus does not have a well-defined average position angle. These results can be investigated using numerical models; see Chapter 4.

3.6 Conclusions

We observed two very similar WR + O binary systems, WR 42 and WR 79, using spectropolarimetry from RSS/SALT. The systems are known to be similar in period, inclination angle, and WR classification.

We found that the continuum polarization of both systems follows the classic analytical model of Brown, McLean, and Emslie (1978), suggesting that the continuum polarization variation can be explained by the illumination of the WR wind by the O-star companion. Our results agree with those of previous polarimetric studies by St-Louis et al. (1987) and Moffat and Piirola (1993), but only after the archival data were corrected for phase shifts and instrumental uncertainties. These phase shifts cannot be compensated for by considering observation exposure time, but it is also very unlikely that the stars' orbits have changed in ∼30 years.

We extracted integrated line polarization from both systems to investigate their phased behavior. We found that the C IV λ5800 shows a clear ∼ 0.25 phase difference from the continuum polarization, strongly suggesting that it arises from emission in the colliding wind shock region in the WR star wind. This is contrary to the expectation that the C III λ5696 line would be the clearest shock tracer because it is more sensitive to density variations than C IV λ5800 (Hamann et al. 1992). Instead we find that C III λ5696 seems to track the continuum, implying that most of this light originates from close to the O star. In general, the line polarization has a lower magnitude of phase variation than the continuum. This is expected, since much of the line emission originates as unpolarized light from optically thin regions of the WR wind and acts to dilute the line polarization.

As expected from their properties, WR 42 and WR 79 have similar broad-band and narrow-band continuum polarization behaviour overall. However, the ISP subtraction performed for the line polarization comparison shows that WR 42 contains a strong intrinsic component that is constant in phase, suggesting it possesses an asymmetric wind geometry that may be the result of rapid rotation of the WR star. It must be cautioned that this result could simply be an underestimate of the ISP, and better ISP characterization is needed to help determine whether this is the case. RSS has the capability to perform multi-object spectropolarimetry that will allow us to obtain accurate ISP for both stars once the data reduction process for the multi-object mode has been finished.

Future work will investigate the detailed polarimetric line profiles of the major lines covered in this chapter. We are also constructing numerical radiative transfer models to simulate the behavior of the line polarization in the context of existing system models (see Chapter 4). We are also continuing to gather more observations of both systems to improve phase coverage and the characterization of the ISP and instrumental uncertainties.

3.7 Orbital motion and ephemerides

The interpretation of our polarimetric data is highly dependent on accurately phased observations. When we compared our initial data with previously published data from Moffat and Piirola (1993) and St-Louis et al. (1987), we found that there was a phase shift between the datasets. This motivated our use of the most recent spectroscopically derived orbital solutions from Hill et al. (2000). We thus carried out the analysis below to ensure that the chosen ephemeris from Hill et al. (2000) for each star was correct. Hill et al. (2000) includes 2 possible periods for WR 42; we test both here.

For each object, we selected a flux observation as a template to cross-correlate with all other flux observations from the phase closest to zero for each star, using the Hill et al. (2000) ephemeris. Radial velocity variations will cause flux peaks to shift as a function of orbital phase, so is we can quantify these shifts via cross-correlation we can derive radial velocities. We interpolated this template using a cubic spline to 0.1 Å so as to obtain higher resolution in cross-correlation. We chose to analyze the emission lines C III λ5696 and C IV λ5812 due to their low blending with other lines. Although C III λ5696 displays complex phase-dependent behavior near its peak (Hill et al. 2000), the cross-correlation is only intended to confirm our choice of ephemeris, rather than deriving the orbit wholesale, so its complex behaviour simply introduces uncertainty to the determination of the cross-correlation.

Before cross-correlation, we performed an approximate continuum subtraction using a simple linear interpolation between blue- and red-side continuum points around the line of interest. This is justified by the fact that the stellar continuum in this region lies clearly in the Rayleigh-Jeans part of the spectrum for massive stars. Extinction can be neglected because it is unlikely to change in the timescale of our observations and neither WR 42 or WR 79 have been shown to produce dust. We normalized the emission lines used for the cross-correlation to their maximum values and smoothed the blue and red continuum cutoff points of the spectra with a sinusoidal function, so that they smoothly reduce to zero at the edges and prevent edge effects in the cross-correlation process (e.g. Gullberg and Lindegren 2002). We then performed cross-correlation using the CROSSCORRV function from PYASTRONOMY[2].

With radial velocities derived from the cross-correlation results at each phase, we performed a least-squares fit of the **phase space** model function

$$RV(\phi) = K \sin(2\pi(\phi - E_0)/P) + \gamma \tag{3.11}$$

to our RSS data for each star. In this function, K is the peak radial velocity, ϕ is the phase, E_0 is the time of primary conjunction in **phase space**, P is the period in **phase space**, and γ is the systemic radial velocity. Thus, if the data are well-phased to a given ephemeris, we expect $E_0 = 0$ and $P = 1$. We set these as the initial values for E_0 and P, and took the remaining initial fit parameters from Hill et al. (2000). Our aim was to check how well the chosen ephemeris produced the expected results, i.e., an observed radial velocity of ≈ 0 $\mathrm{km\,s^{-1}}$ at the calculated phase 0.0.

We display the cross-correlation radial velocity curves for the two stars in Figures 3.10 and 3.12 and list the corresponding fit parameters in Table 3.11. We note that the parameter γ is mostly determined by the choice of template spectrum, so our fit results are not intended to yield true values for γ. Additionally, our overestimation of K for C III λ5696 compared to the Hill et al. (2000) results can be explained by the complex phase behavior of the line shape. This is likely caused by the excess C III λ5696 emission from the colliding wind shock cone, which moves about 1/4 period out of phase with the RV orbit because of matter moving outward along the cone as opposed to along the orbit.

For both stars, the Hill et al. (2000) ephemerides produced good fits to the data, yielding E_0 and P values close to 0 and 1, respectively. Furthermore, the radial velocity varies with phase as expected and matches the behavior measured spectroscopically by Hill et al. (2000).

---

[2] https://github.com/sczesla/PyAstronomy

Table 3.11: Fitted radial velocity parameters for WR 42 and WR 79 in phase space.

WR 42	C III λ5696	C IV λ5812
P	1.00 ± 0.003	1.00 ± 0.003
E_0	-0.07 ± 0.003	0.003 ± 0.003
K (km s^{-1})	169 ± 3	140 ± 3
γ (km s^{-1})	-76 ± 2	-26 ± 2
WR 79	C III λ5696	C IV λ5812
P	1.00 ± 0.004	1.00 ± 0.006
E_0	-0.02 ± 0.004	0.02 ± 0.006
K (km s^{-1})	170 ± 3	158 ± 5
γ (km s^{-1})	20 ± 2	16 ± 4

In the case of WR 42, this phase behavior allows us to discriminate between the two distinct periods suggested by Hill et al. (2000), settling on $P = 7.8912$ d because it places the WR star in front at phase 0.0. The fits to the other period ($P = 7.8823$ d) are shown in Fig 3.11. Thus we are confident that the chosen Hill et al. (2000) ephemerides accurately represent the orbits of both WR 42 and WR 79 for our data.

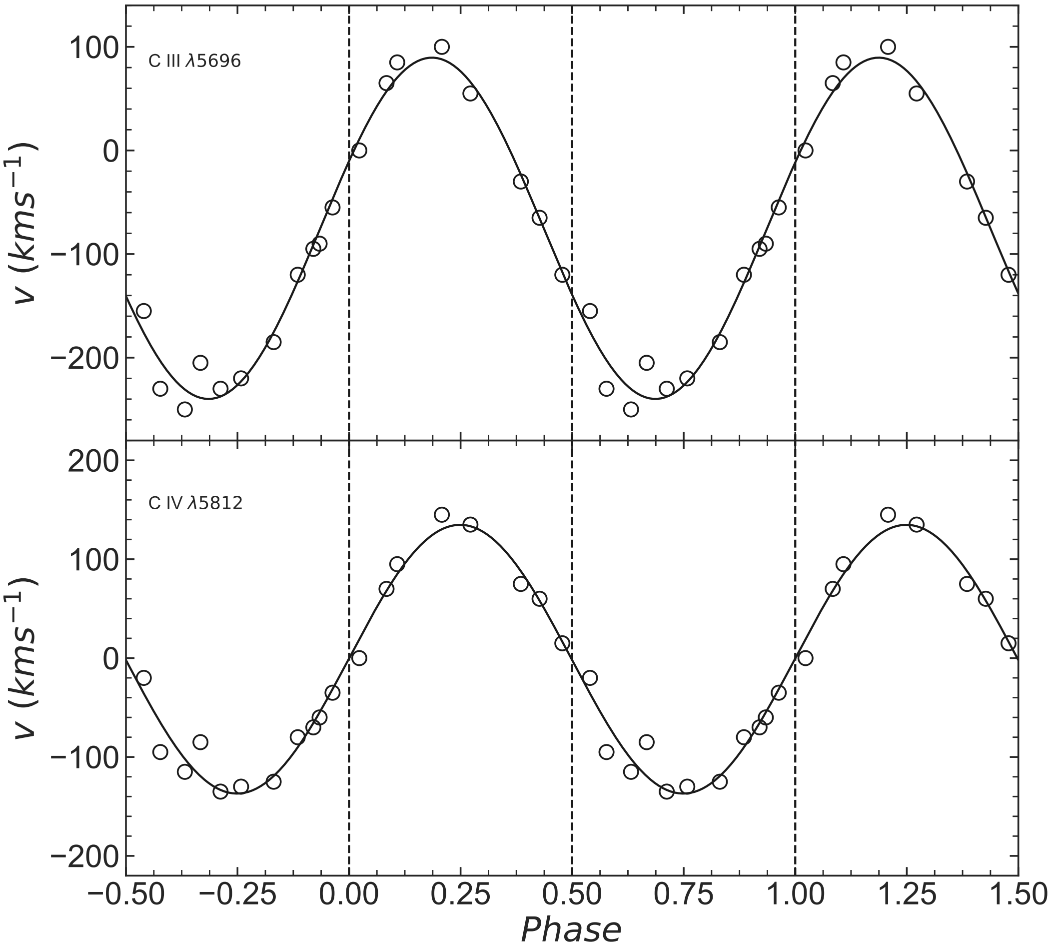

Figure 3.10: Radial velocity curves for WR 42, as measured via cross-correlation of our RSS flux spectra (Section 3.7). Error bars are smaller than the point size. The parameters of the overlaid fit are given in Table 3.11.

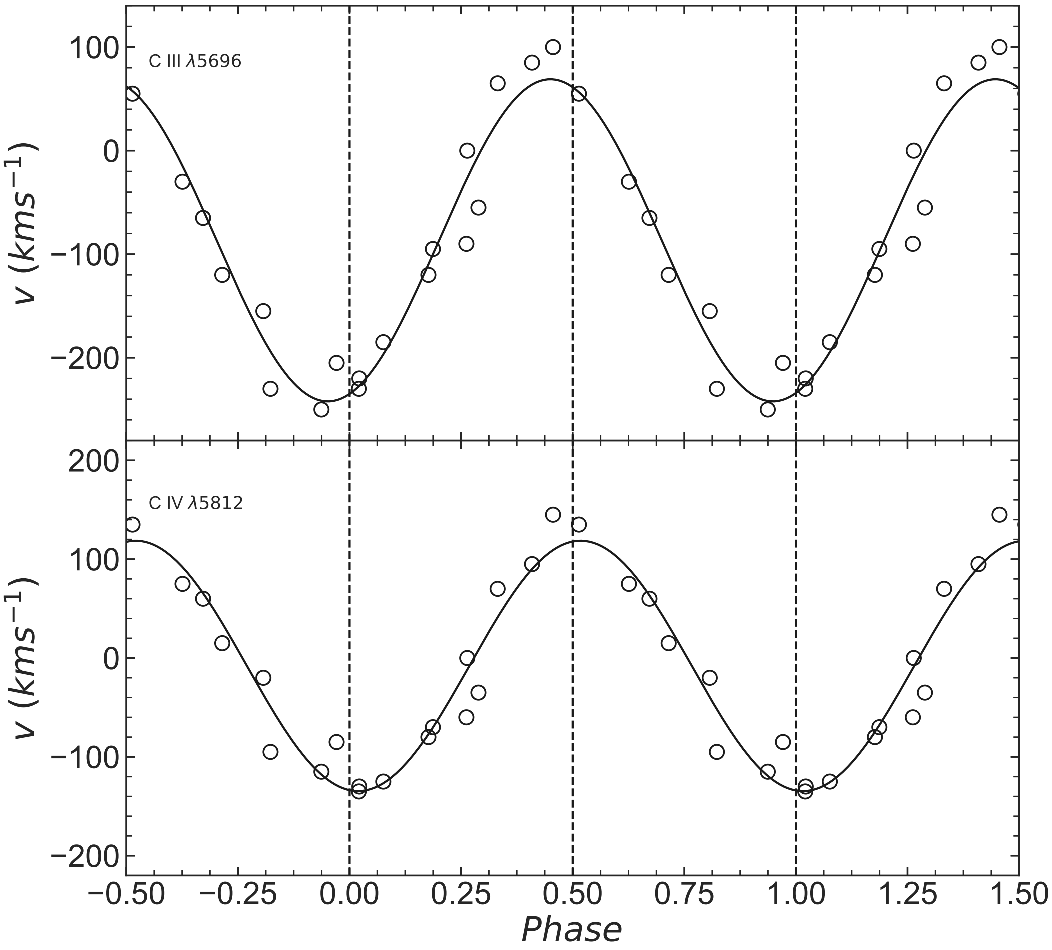

Figure 3.11: As in Fig 3.10, except the ephemeris in this case uses the Hill et al. (2000) alternate period, 7.8823 d. The resulting fit does not match our requirement of $E_0 = 0$, instead $E_0 = 0.19$ for C III λ5696 and $E_0 = 0.26$ for C IV λ5812.

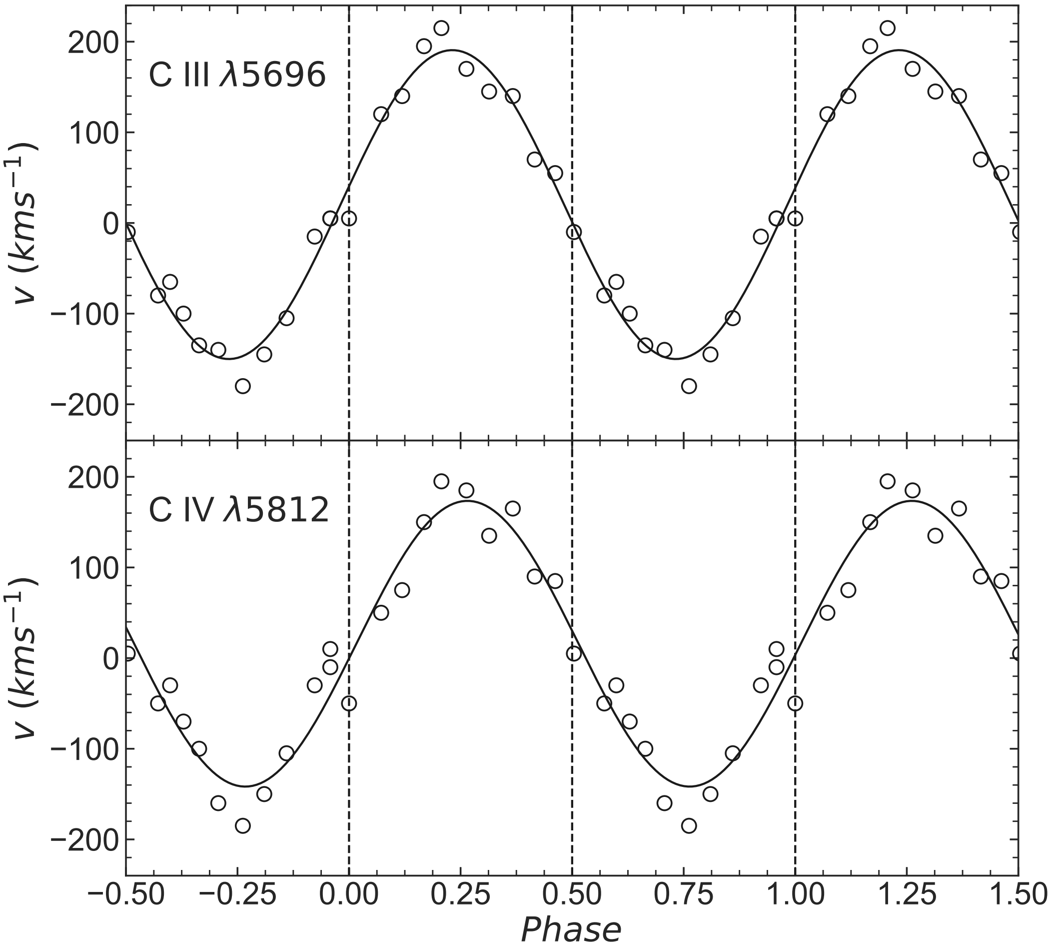

Figure 3.12: Radial velocity curves for WR 79, as measured via cross-correlation of our RSS flux spectra (Section 3.7). Error bars are smaller than the point size. The parameters of the overlaid fit are given in Table 3.11.

Chapter 4

MCRT modeling of WR + O binary systems

4.1 Introduction

Binary stars are a common feature of the universe, with over 40% of Solar-mass stars in a multiple-star system (Duchêne and Kraus 2013). In the case of massive stars, Sana et al. (2012) showed they make up more than half (and possibly more than 70%) of star systems containing a massive star. Therefore, it is of critical importance that we understand how binarity influences stellar evolution. Mass loss via stellar winds or mass transfer is known to have a dramatic impact on stellar evolution (Smartt 2009; Smith 2014). Binary interactions also produce circumstellar material (CSM), which can affect the morphologies and observable signatures of supernovae (SNe). Because massive stars have high temperatures and strong ionizing flux (Crowther 2007), the winds and nearby CSM in massive binaries are primarily made up of plasma, which produces polarization signals via Thomson scattering (Section 1.5). Although some WR binaries do produce dust, this dust typically condenses at large enough distances from the stars (e.g. Callingham et al. 2020) that we consider it part of the interstellar contribution to extinction and scattering for the purposes of this paper.

Polarimetry allows us to investigate the geometry and optical depth of material produced by mass loss and mass transfer even for unresolved systems. The polarimetric variations of massive binaries have been studied in some detail (e.g. Arora et al. 2019; Fullard et al. 2018; Harries, Hillier, and Howarth 1998; Hoffman, Nordsieck, and Fox 1998; Lomax et al. 2017; St-Louis et al. 1988; Moffat and Piirola 1993).

There have been numerous attempts to model the polarimetric behavior of binary systems, both analytical (e.g. Brown, McLean, and Emslie 1978) and numerical (e.g. Hoffman, Whitney, and Nordsieck 2003; Kurosawa, Hillier, and Pittard 2002). The analytical model of Brown, McLean, and Emslie (1978) has been widely used and modified by e.g. Moffat et al. (1998), but it is limited to optically thin scattering envelopes. It also integrates optical depth such that geometric detail is lost, and only information regarding density moments is produced. These moments describe the density distribution in different directions: flattening towards the orbital plane, symmetry about the orbital plane and concentration of material towards the orbital plane. The limitations of the analytic model are discussed in more detail in Section 1.5.2. Kurosawa, Hillier, and Pittard (2002) never released their model for use by others, and only used it to study one object, V444 Cygni. The otherwise feature-complete MCRT code Hyperion (Robitaille 2011) does not perform Thomson scattering, and is instead focused on dust radiative transfer and polarization. The DISK code by Hoffman, Whitney, and Nordsieck (2003) can perform Thomson scattering, but it has not received the updates that its sibling code *SLIP* has to handle additional density distributions, calculated albedo, or distributed emission from regions of varying density. More information about numerical methods can be found in Section 1.7.

In this chapter I detail modifications I have made to the existing Monte Carlo radiative transfer code Supernova Line Polarization (*SLIP*) (Hoffman 2007; Shrestha et al. 2018)) so that it can be used to simulate the polarization signals from binary star systems with complex wind geometries. Section 4.2 covers the basic operation of the code and my modifications, as well as validation of *SLIP*'s performance via comparison with the results of previous codes. Section 4.3 discusses *SLIP* simulations of WR+O binaries compared with archival and SALT data. In Section 4.4 I discuss the results and the future possibilities of the code.

4.2 Methods

SLIP is a Fortran + MPI code based on the Monte Carlo radiative transfer methods outlined in Whitney (2011). I have upgraded it to use methods such as dynamic array allocation. The simulation grid is a linearly spaced spherical polar coordinate system in r, θ and ϕ. Photon packets are emitted from user-specified locations in the grid and propagate through the user-defined scattering region. At each grid cell the optical depth is integrated until the photon scatters or exits the grid cell. The photon packets are collected as they exit the simulation limits and are binned into different observational directions in θ and ϕ. In this way, a single model can be viewed from multiple angles, greatly reducing computation time. Orbits can be simulated by simply moving around the grid in the ϕ direction. See Section 1.8, Hoffman (2007), Huk (2017), and Shrestha et al. (2018) for more information about the basics of *SLIP*.

I modified *SLIP* to include an additional spherical source located at an arbitrary distance along the x-axis ($\theta = 90^\circ$, $\phi = 0$) from the central spherical source (each source can be a finite size or a point). The number of photon packets emitted from each source is controlled as a fraction of the total. As with other versions of *SLIP*, the scattering region can also emit a fraction of the total photon packet count. Controlling the emission region is critical in understanding the effects of line polarization, because we know where line emission arises based on ionization stratification models (e.g. Hillier 1989).

I have also added new geometrical density distributions to account for the presence of a second star. The CSM radial density profile can be controlled by a loaded external input, so that e.g. an accurate stellar wind model can be placed around the central source. Additionally, a portion of the loaded radial density profile can be set to zero density using a sphere of arbitrary radius located at an arbitrary location in the $x-y$ plane of the simulation. Alternatively, 3D hydrodynamic simulation results can be loaded as CSM geometries to provide the most realistic density distribution.

To test the validity of the additions, I computed models that match three circumstellar geometries that can be easily compared with the analytical model of Brown, McLean, and Emslie (1978); that is, a radially constant spherical distribution of CSM, a radially and azimuthally constant disklike distribution in the orbital plane with an opening angle of 1.8°, and a radially constant prolate distribution (an ellipsoid with the major axis parallel to the z-axis, and the equation $\frac{x^2}{0.2^2} + \frac{y^2}{0.2^2} + \frac{z^2}{0.6^2} = 1$). The finite nature of the grid means that the disklike distribution is a single grid cell thick in the θ direction. All three geometries were centered on the sources located at the origin. Both stellar sources emitted an equal proportion of the photons, and both were set as point sources so eclipse effects are not important and photons will not be absorbed. I set the optical depth of all these CSM distributions at $\theta = 90^\circ$ to $\tau = 0.1$ to match the optically thin assumption of the analytical model (Carlos-Leblanc et al. 2019, found that this was the limit between optically thin and optically thick for their MCRT models). Note that the CSM density is set to be constant proportional to the optical depth at $\theta = 90^\circ$, so the prolate model shows an increase in optical depth towards $\theta = 0^\circ$ and 180° because of its increased radius towards those angles. I ran the models on the Stampede high-performance computing cluster at the Texas Advanced Computing Center[1], with 8×10^9 photons. The output was binned to 23 inclination and 40 orbital phase bins. The photon count was chosen to produce uncertainties less than the final expected uncertainties of data from the Robert Stobie Spectrograph (RSS) at the Southern African Large Telescope (SALT). Uncertainties are expected to be less than

---

[1] https://www.tacc.utexas.edu/systems/stampede. TACC is operated by the Extreme Science and Discovery Environment (XSEDE), which we access under allocation AST120067.

0.02% in polarization once systematic effects have been accounted for (see Section 1.6 and Chapter 3 for discussions of the uncertainty of RSS/SALT).

The comparisons between the numerical and analytical models are shown in Figures 4.1, 4.2, and 4.3 for the disklike, spherical, and prolate density distributions respectively. I fit the analytical models to the numerical results using LMFIT (Newville et al. 2014), and algebraically calculated the parameters from the Fourier coefficients (Drissen et al. 1986). The fit results for a selection of inclination angles are presented in Table 4.1. As examined by Wolinski and Dolan (1994), the analytical model requires very high precision measurements relative to the polarization variation amplitude to recover accurate derived parameters as the inclination angle decreases from 90° to 0°. This is why the truly low inclination angle numerical models are fitted with a biased higher inclination angle by the analytical model, despite the expectation that they should be identical given the high accuracy of the numerical model (see Section 1.5.2 for a discussion of the uncertainties in the analytical model). The disk model is most strongly affected because it has the lowest amplitude of polarization variation of the models. Further deviations from the analytical model are seen in the case of the prolate distribution (Figure 4.3). At orbital phase 0, the analytical model does not fit the negative q trough completely. This enhanced polarization is likely caused by scattered light from the star external to the density distribution, because it is behind the density distribution at phase 0. The strong negative q makes sense, because it is indicative of polarization parallel to the plane of the orbit, and therefore perpendicular to the scattering geometry creating the polarization, which must therefore be aligned with the z-axis (i.e., prolate).

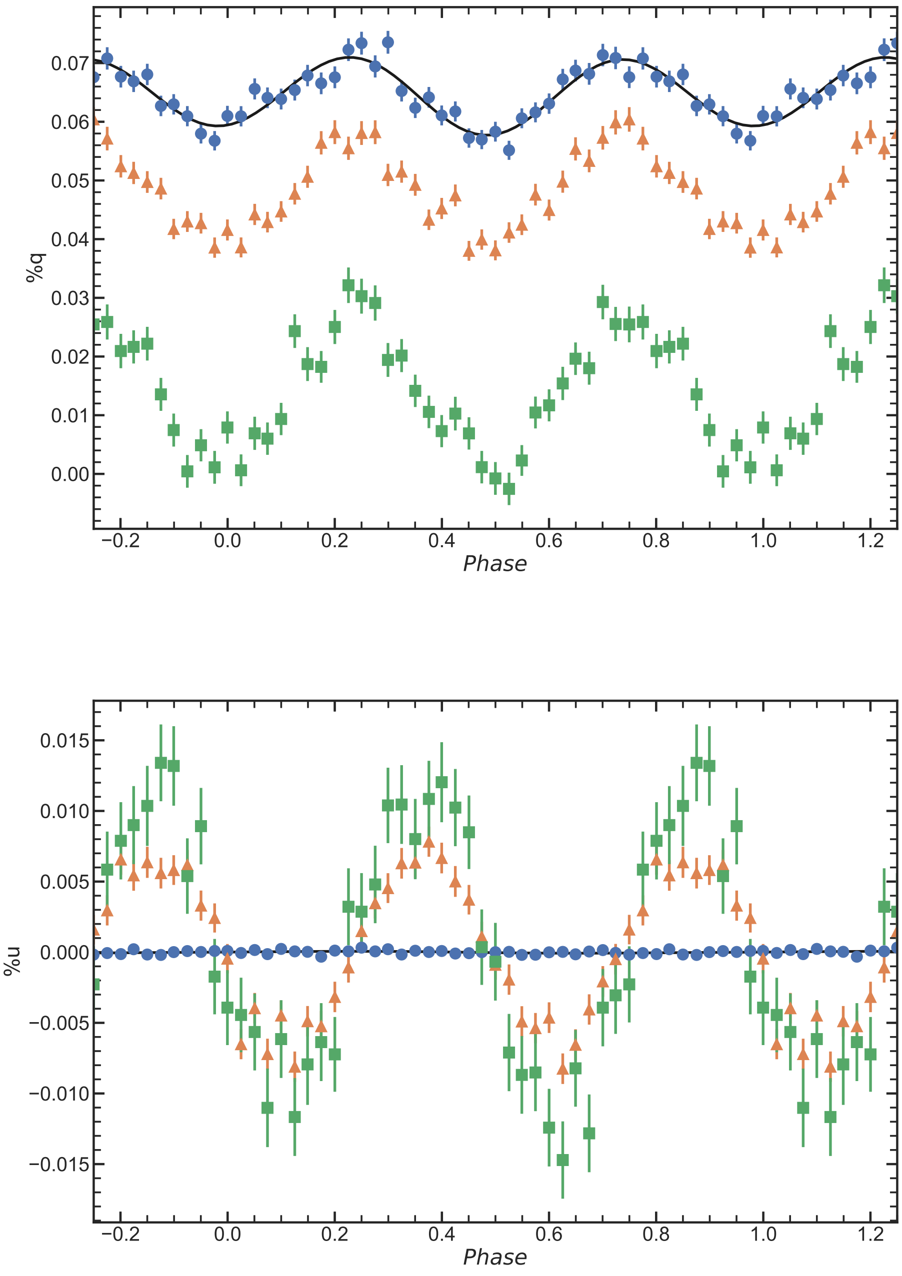

Figure 4.1: Comparison of *SLIP* results for a thin disk to the analytical model of Brown, McLean, and Emslie (1978). The blue circles represent $i = 90° \pm 4$, orange triangles represent $i = 58.7° \pm 4$, and the green squares represent $i = 27.4° \pm 4$. The $i = 90° \pm 4$ output has been fit by the model of Brown, McLean, and Emslie (1978) (black line).

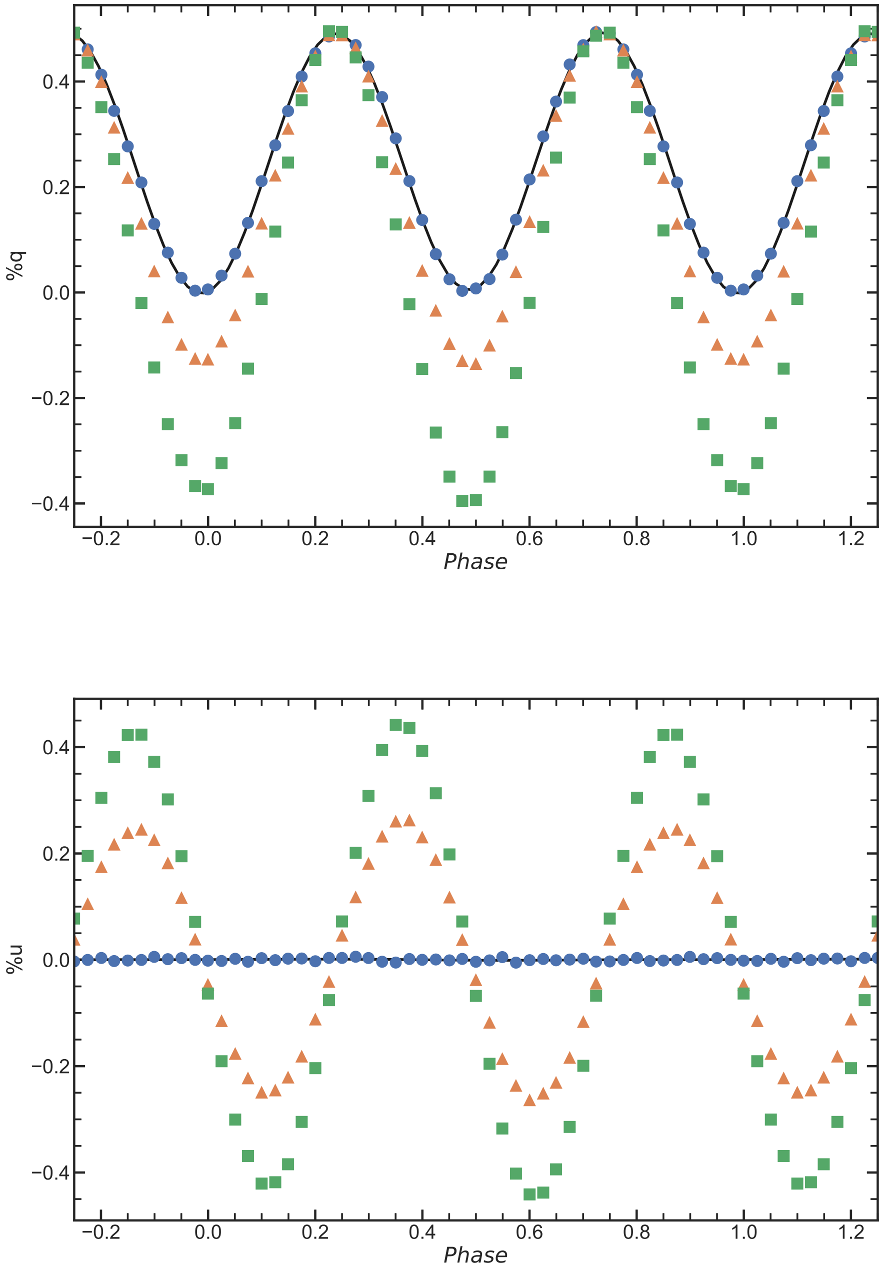

Figure 4.2: Comparison of *SLIP* results for a sphere to the analytical model of Brown, McLean, and Emslie (1978). The blue circles represent $i = 90^{\circ} \pm 4$, orange triangles represent $i = 58.7^{\circ} \pm 4$ and the green squares represent $i = 27.4^{\circ} \pm 4$. The $i = 90^{\circ} \pm 4$ output has been fit by the model of Brown, McLean, and Emslie (1978) (black line).

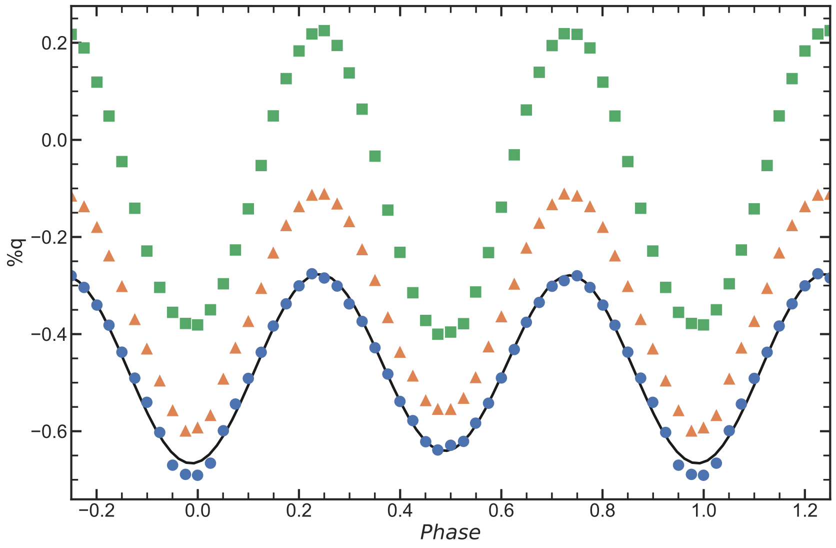

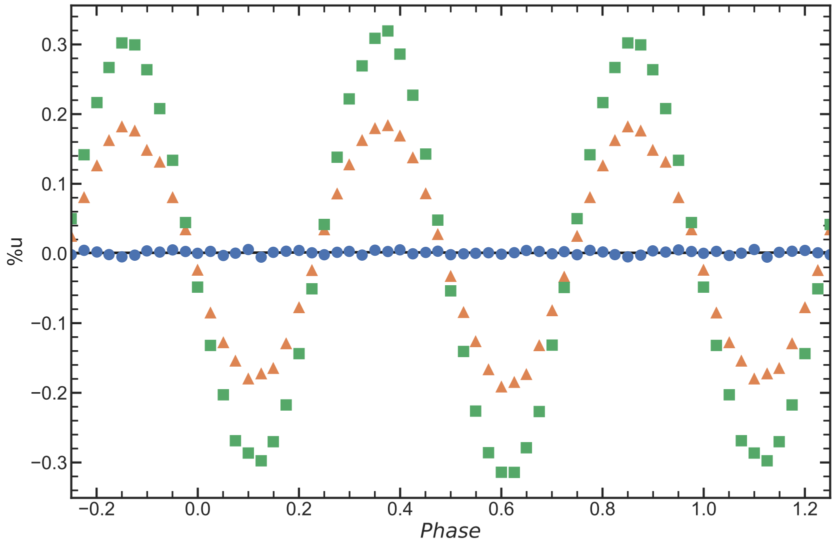

Figure 4.3: Comparison of *SLIP* results for a prolate ellipsoid (extended in the direction perpendicular to the orbital plane) to the analytical model of Brown, McLean, and Emslie (1978). The blue circles represent $i = 90^{\circ} \pm 4$, orange triangles represent $i = 58.7^{\circ} \pm 4$ and the green squares represent $i = 27.4^{\circ} \pm 4$. The $i = 90^{\circ} \pm 4$ output has been fit by the model of Brown, McLean, and Emslie (1978) (black line).

Table 4.1: Fitted models of Brown, McLean, and Emslie (1978) compared to the expected output from three *SLIP* models at three specific inclination angles. The top row shows the inclination angles of the *SLIP* models. $\Omega = 0$ for all *SLIP* models.

SLIP output i:	$i = 27.4° \pm 4$	$i = 58.7° \pm 4$	$i = 90° \pm 4$
Disklike			
i (°)	52.4	62.4	90
Ω (°)	6.9	-1.8	0.1
Spherical			
i (°)	30.9	58.8	90
Ω	-8.3	-0.1	0.1
Prolate			
i (°)	27.8	60.2	90
Ω (°)	-14.3	-0.6	0

4.3 Results

4.3.1 Continuum polarization model

V444 Cygni is a well-studied WN5 + O6 system that is at an inclination angle of $\sim 80°$ to our line of sight. This makes it an excellent subject to compare with models, because there are plenty of data available both photo- and polarimetrically, and most of the system parameters are well defined. From the data in St-Louis et al. (1993), we know that the system exhibits sinusoidal continuum polarization variation with phase typical of WR + O binary systems. However, it also has rapid polarization changes during the secondary eclipse when the O star eclipses the WR star and its wind.

I used parameters from the eclipse polarization model of St-Louis et al. (1993) for the relative emission from each source f_{WR} and f_{O}, as well as for the stellar radii R_{WR} and R_{O}. To approximate the WR + O wind collision effects, I used a spherical density distribution to represent the WR wind with a spherical cavity with no density to represent the O star wind. The cavity is a void because the WR star's mass-loss rate is ~ 10 times higher than the O star's mass-loss rate and therefore dominates the polarization signal. This is of course a first-order approximation, and future models will include an O star wind and a more physical wind-wind collision region shape.

The values for orbital separation a, cavity size, and cavity (x, y) location were taken from Lomax et al. (2015) (also see Section 1.3. The simulation radius $r_{\max}$ was taken to be approximately double the stellar separation; this marks the region of the WR wind where polarization will be important due to the high optical depths. The WR wind density itself was taken from the Potsdam Wolf-Rayet (PoWR) models (Todt et al. 2015). I chose the model with the parameters closest to those derived by Lomax et al. (2015), i.e., $R_{\mathrm{WR}} = 2.9R_{\odot}$, $\dot{M}_{\mathrm{WR}} = 6.76 \times 10^{-6} M_{\odot}$ yr^{-1}, and $M_{\mathrm{WR}} = 12.4M_{\odot}$. The 10-12 (in PoWR grid coordinates) model was the closest match, with $R_{\mathrm{WR}} = 2.977R_{\odot}$, $\dot{M}_{\mathrm{WR}} = 7.35 \times 10^{-6} M_{\odot}$ yr^{-1}, and $M_{\mathrm{WR}} = 12.02M_{\odot}$. Note that the cavity around the O star uses the spherical subtraction noted in §4.2, so the density in that region is zero. Table 4.2 lists the overall parameters I used for the model. Figure 4.4 shows a to-scale representation of the model in the $x - y$ plane. The grid resolution of the figure is reduced compared to the true model for clarity. The size of the grid versus the star sizes is unimportant because photon positions are not tracked per-grid cell but rather stepped short distances to integrate optical depth (see Section 1.7 for details). This means that the photon position is tracked finely enough to intercept the stellar surfaces accurately.

For additional points of comparison, I increased the orbital separation and decreased the cavity size to match the Fahed and Moffat (2012) model of WR 21, a similar WN5 + O7V type system with an orbital period of 8.2546 days. I also tested a third model, with changed stellar radii and emission fractions to match model E from Kurosawa, Hillier, and Pittard (2002), one of the two best fitting V444 Cygni models from those authors.

To create each of the models shown here, I ran 1.28×10^{10} photons across 64 CPUs, which took approximately 2 hours on the University of Denver high-performance computing cluster (HPC). The density grid was made up of 100 r, 101 θ and 101 ϕ cells. The photon sources emit at a single wavelength because of the grey nature of Thomson scattering. They act as perfect absorbers if a photon path intersects one of their surfaces. The output was

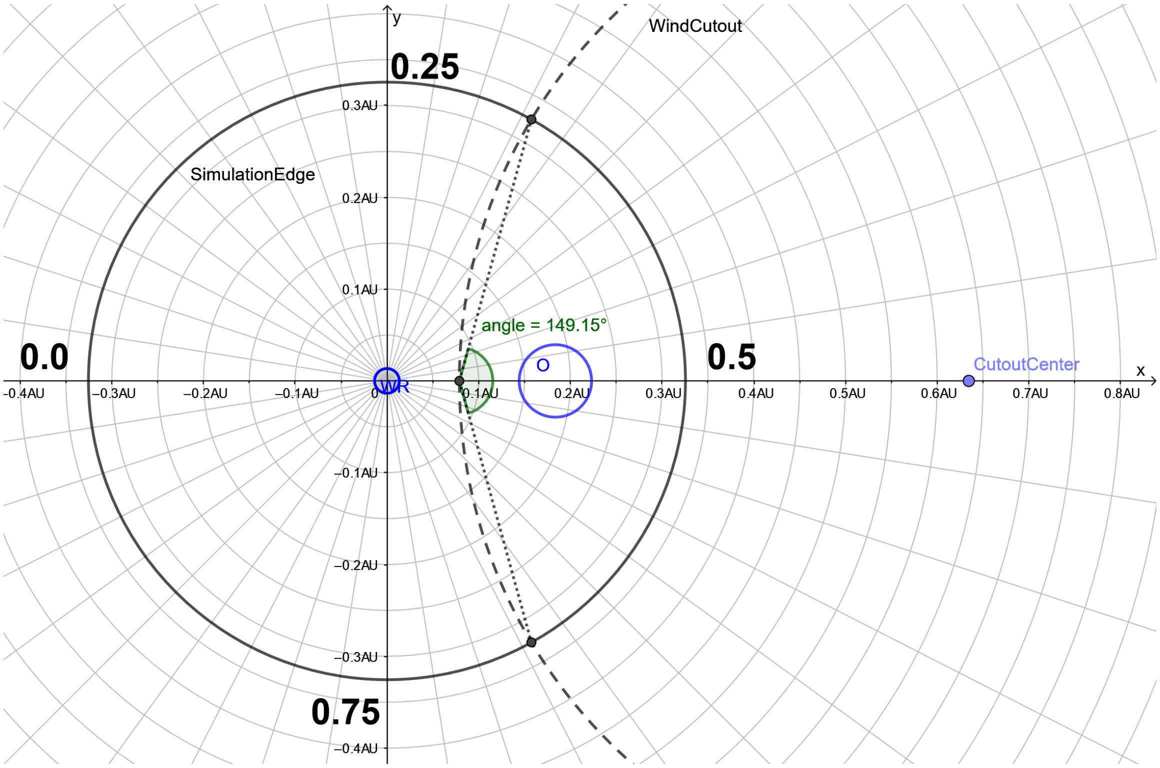

Figure 4.4: V444 Cygni polarization model schematic, to scale. The WR and O star are labeled in blue and emit photons from their surfaces. The WR wind density is arranged radially outwards from the WR star surface and scatters photons. The solid black line shows the edge of the simulation. The dashed black line shows where the cavity begins, and its center location is marked as CutoutCenter. Between the cavity and the simulation edge in the positive x-direction is void. The dotted black line shows an approximation of the X-ray model shock cone from Lomax et al. (2015) with the opening angle highlighted in green. Phases are marked around the exterior of the simulation grid in boldface.

binned to 23 inclination angle and 80 orbital phase bins, the latter to ensure that sufficient resolution could be provided for the secondary eclipse behavior.

I show the polarimetric results of the Figure 4.4 model in Figure 4.5, with the polarimetric data from St-Louis et al. (1993) shown for comparison. I used the Johnson R-band data because it has the lowest uncertainty of all the bands, and is less likely to be contaminated with emission lines from the WR star wind. I rotated the polarimetric data by its uncertainty-weighted mean position angle so that the average position angle is 0°, as in the *SLIP* model. The phase region 0.4–0.6 was excluded from the mean position angle calculation because of the eclipse behavior (as in St-Louis et al. 1993). I also subtracted the ISP in the R-band from the polarimetric data, by -0.24% in q and -0.04% in u (see Chapter 2).

By visual inspection of Figure 4.5, the typical double-sinusoid behavior expected from Brown, McLean, and Emslie (1978) is represented by the St-Louis parameter derived model in both $\%q$ and $\%u$ (with an overestimate of the magnitude of variation in q), and some of the secondary eclipse polarization behavior is accounted for.

The Kurosawa, Hillier, and Pittard (2002) model shown in Figure 4.6 improves the modeling of the eclipse behavior, but the double peak in q at the secondary eclipse is still not produced by the model. The Stokes q variation is still overestimated. The WR 21 model shown in Figure 4.7 performs similarly to the Kurosawa, Hillier, and Pittard (2002) model. At an inclination angle of 58.7°, within the range of estimated inclination angles for WR 21 (Fahed and Moffat 2012), the secondary eclipse polarization behavior disappears. Instead, the simpler double-sinusoid behavior is visible. This result is shown in Figure 4.8.

4.3.2 Shortcomings of initial models

V444 Cygni offers a convenient point of comparison for the continuum models due to its good phase coverage in polarization by St-Louis et al. (1993). As can be seen in the residuals of the data$-$model (Figure 4.5), there are two areas where the basic continuum

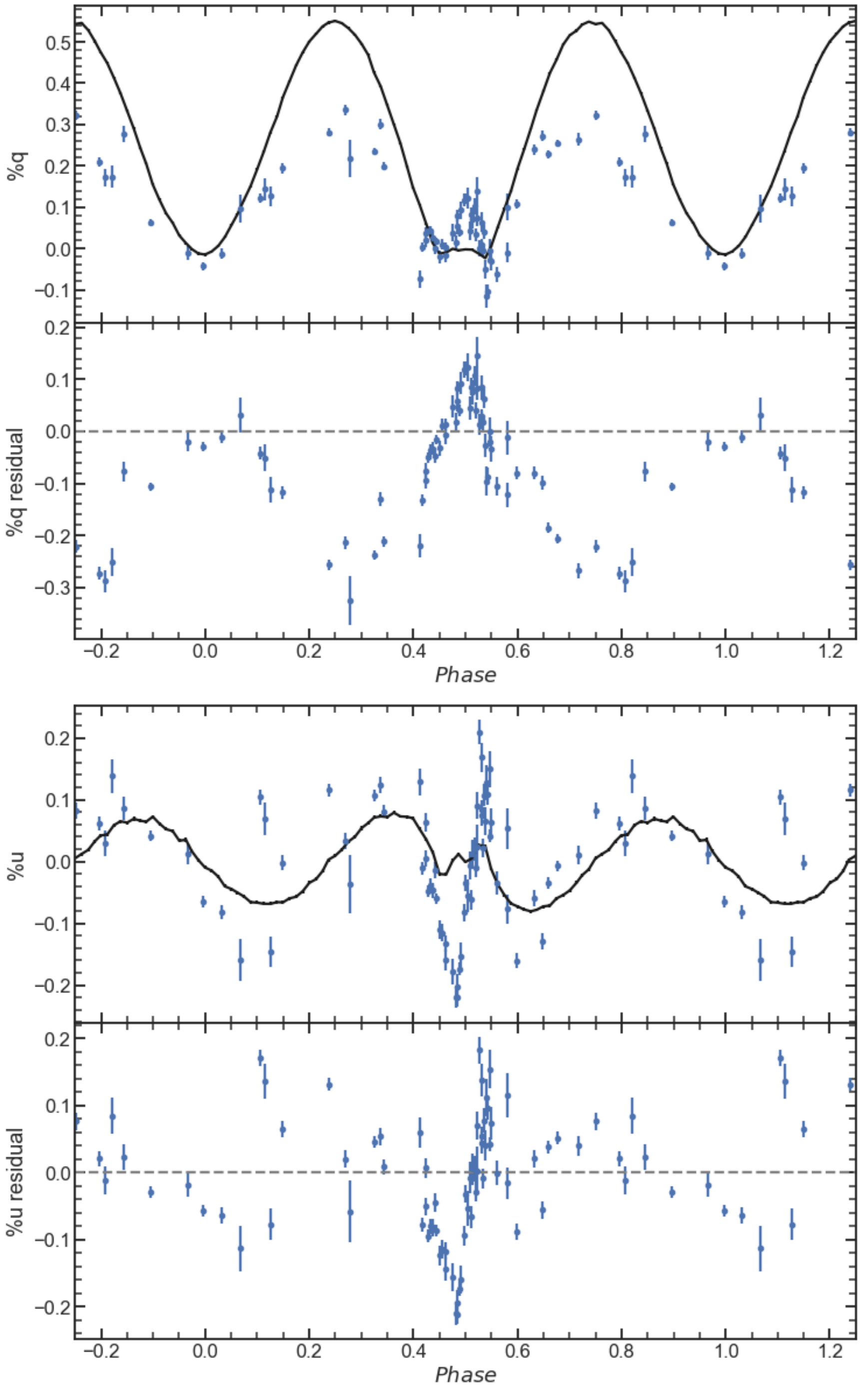

Figure 4.5: V444 Cygni polarization (blue points) compared to the closest model inclination angle of 82.2° (black line). The *R*-band polarization data are taken from St-Louis et al. (1993). Residuals are also presented below each plot.

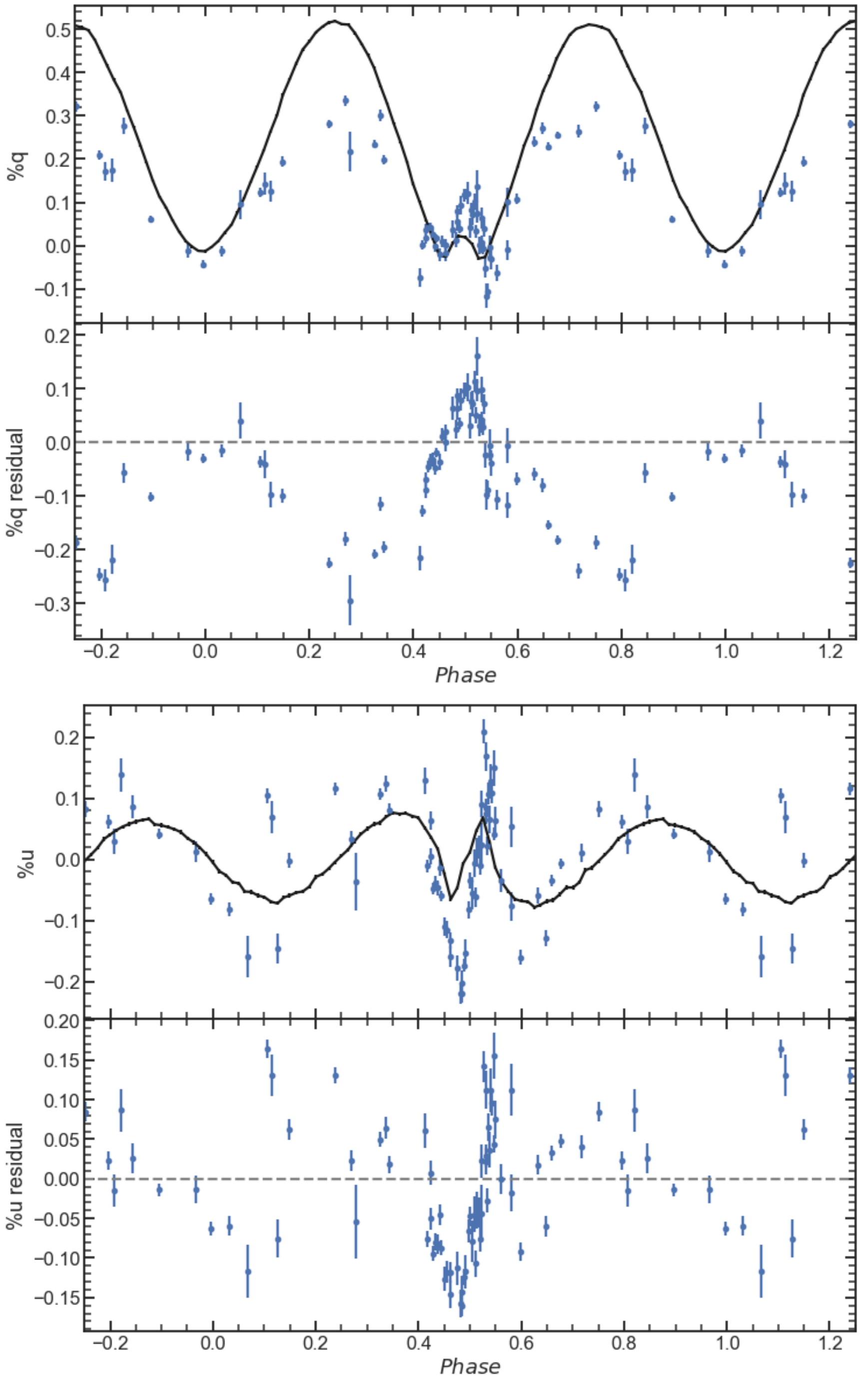

Figure 4.6: V444 Cygni polarization (blue points) compared to the Kurosawa, Hillier, and Pittard (2002) E model at an inclination angle of 82.2° (black line). The *R*-band polarization data are taken from St-Louis et al. (1993). Residuals are also presented below each plot.

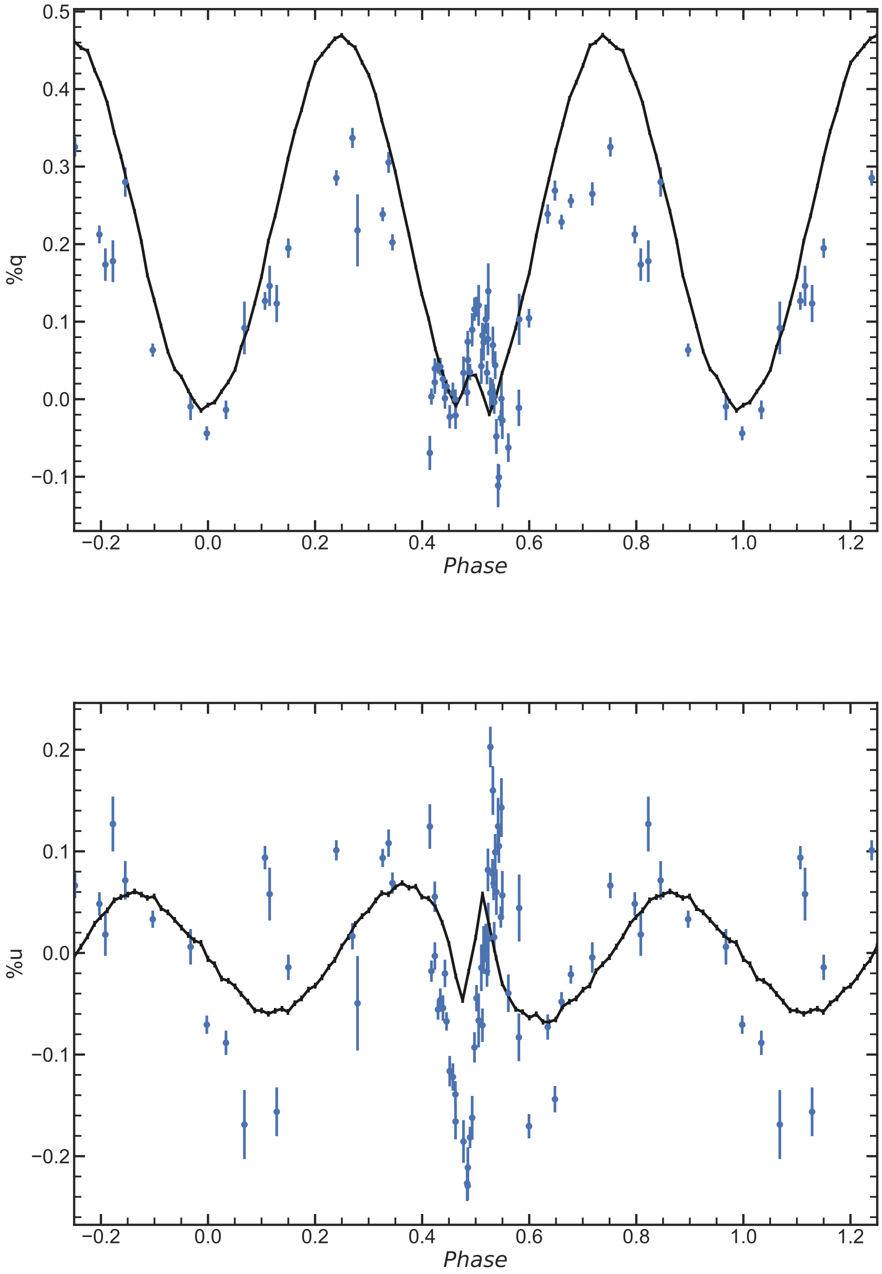

Figure 4.7: V444 Cygni polarization (blue points) compared to a model based on the WR 21 system at an inclination angle of 82.2° (black line). The *R*-band polarization data are taken from St-Louis et al. (1993).

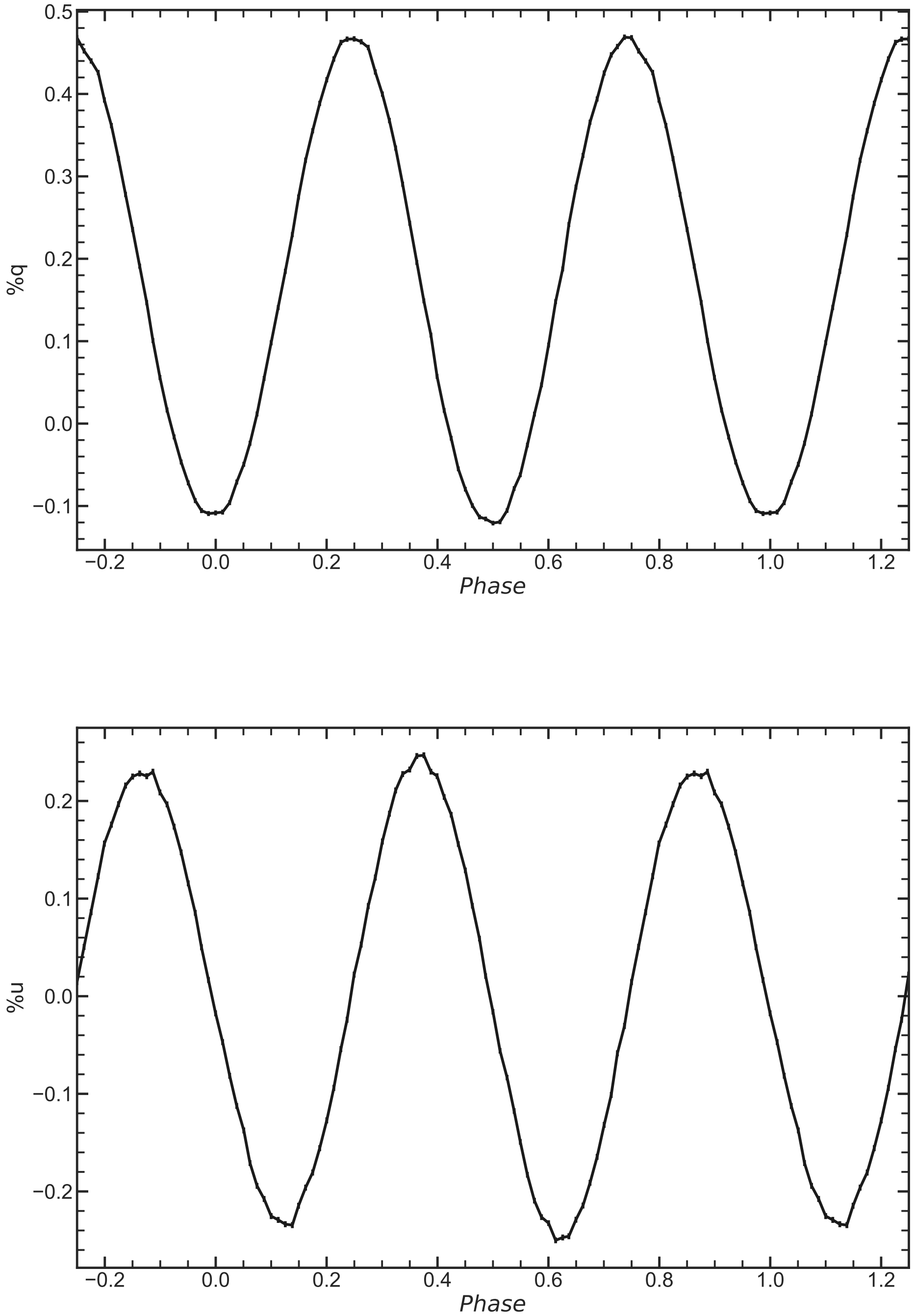

Figure 4.8: A model based on the WR 21 system at an inclination angle of 58.7° (black line).

Table 4.2: V444 Cygni model parameters for continuum and line polarization simulations. St-Louis model parameters from St-Louis et al. (1993). Kurosawa E model parameters from Kurosawa, Hillier, and Pittard (2002).

Parameter	St-Louis	WR 21	Kurosawa E	Emission line
$R_{\rm WR}$ ($M_\odot$)	2.9	2.9	2.5	2.9
$R_{\rm O}$ ($M_\odot$)	8.5	8.5	6.9	8.5
$f_{\rm WR}$	0.15	0.15	0.2	0.0
$f_{\rm O}$	0.85	0.85	0.8	0.0
$f_{\rm wind}$	0.0	0.0	0.0	0.9
$f_{\rm shock}$	0.0	0.0	0.0	0.1
$r_{\rm max}$ (AU)	0.3255	0.3255	0.3255	0.3255
a (AU)	0.16728	0.2681	0.16728	0.16728
Cavity size (AU)	0.5555	0.0900	0.5555	0.5555
Cavity x position (AU)	0.65084	0.2400	0.65084	0.5961
Cavity y position (AU)	0.0	0.0	0.0	-0.1879

model fails to adequately match the V444 Cygni data: the secondary eclipse in q and u, and the q polarization peaks at phases ~ 0.3 and ~ 0.8. The eclipse behavior is very sensitive to both inclination angle and the size of the O star (Kurosawa, Hillier, and Pittard 2002). This is clearly seen in the difference between Figure 4.5 and Figure 4.6: the model with the smaller O star from Kurosawa, Hillier, and Pittard (2002) shows a much stronger eclipse effect in u. The models presented here have a limited range of output inclination angles, with a bin size on the order of $\sim 8°$. Kurosawa, Hillier, and Pittard (2002) commented that even $\sim 1°$ difference in inclination angle changes the results of St-Louis et al. (1993), so it is not surprising that the eclipse behavior is not well fit by any of these simulations. This problem can be solved by increasing the inclination angle bin count with a commensurate (squared, to account for Poisson statistics) increase in photon count and therefore runtime, requiring the use of more CPUs simultaneously. I plan to run these simulations on the Stampede supercomputer, which has 36,892 available compute nodes.

The basic continuum behavior in q is strongly dependent on the WR mass-loss rate, because that along with the velocity structure of the wind determines the WR star wind density. However, the PoWR model I used to represent the V444 WN5 star matches all the parameters derived from well-fit spectroscopic models, including closely matching the mass-loss rate, so there must be another cause for the discrepancy between the model and data in Stokes q. The opacity value I used in these simulations was $\kappa = 0.4$ (from $\kappa = 0.2(1 + X_H)$; Paczynski 1983), assuming a pure hydrogen gas. The PoWR models are produced for WN5 stars using a helium fraction of 98%, so the correct value for κ should be 0.204 instead. Implementing this adjusted value for κ will increase the integration path length required to reach a given optical depth, reducing the number of possible scattering events and therefore the polarization fraction.

4.3.3 Model improvements

Following the initial models presented above, I ran a new set of models to investigate possible improvements. The output θ bin count was increased to 180, i.e. one bin per degree of inclination. Photon counts were doubled to 2.56×10^{10} total photons to reduce the increased uncertainty of the smaller bins. Density grid resolution remained unchanged. For all the new models, the hydrogen fraction was reduced to the 2% fraction discussed above. This immediately resulted in an improved result, as can be seen in Figure 4.9 where the Kurosawa, Hillier, and Pittard (2002) E model is compared to the R-band polarization data. Although the amplitude of the residuals has not improved greatly in $\%u$, the amplitude of the variability across the secondary eclipse is reproduced.

Following the improvements, I investigated the impact that a rotation of the O star wind cavity would have. I located the cavity center in the same place as the emission line model in Table 4.2. The results are presented in Figure 4.10. The difference between the unrotated and rotated case is negligible; therefore the precise location of the cavity initially appears have little effect on the continuum polarization variability.

I ran another model to investigate the impact of mass-loss rate on the amplitude of the continuum polarization variability with phase. In this case, a PoWR model of the same type but with a mass-loss rate of 10^{-5} $\mathrm{M}_{\odot}$ yr^{-1} (compare to the previous model with a mass-loss

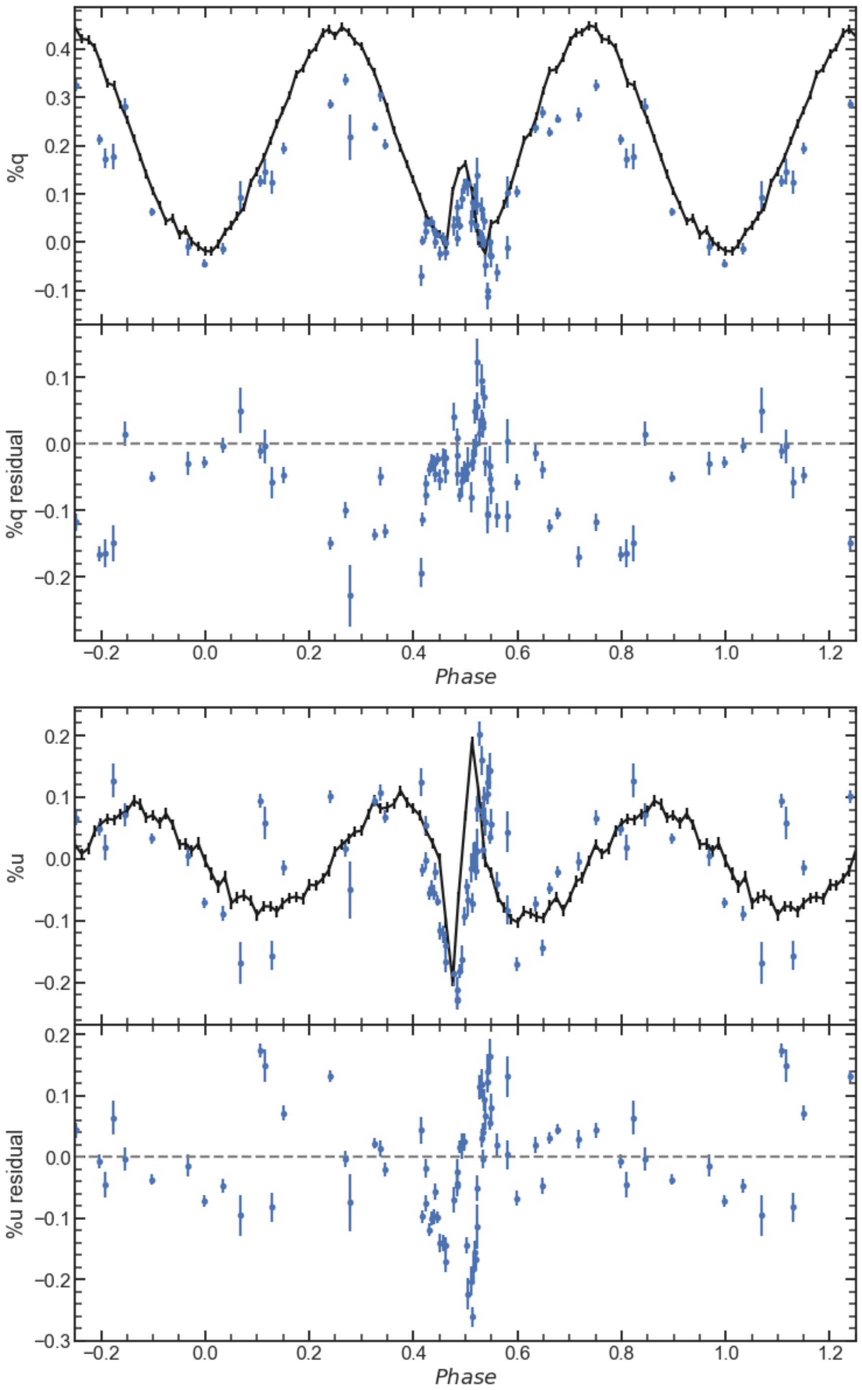

Figure 4.9: V444 Cygni polarization (blue points) compared to the Kurosawa, Hillier, and Pittard (2002) E model at an inclination angle of 82.2° (black line). The *R*-band polarization data are taken from St-Louis et al. (1993). Residuals are also presented below each plot.

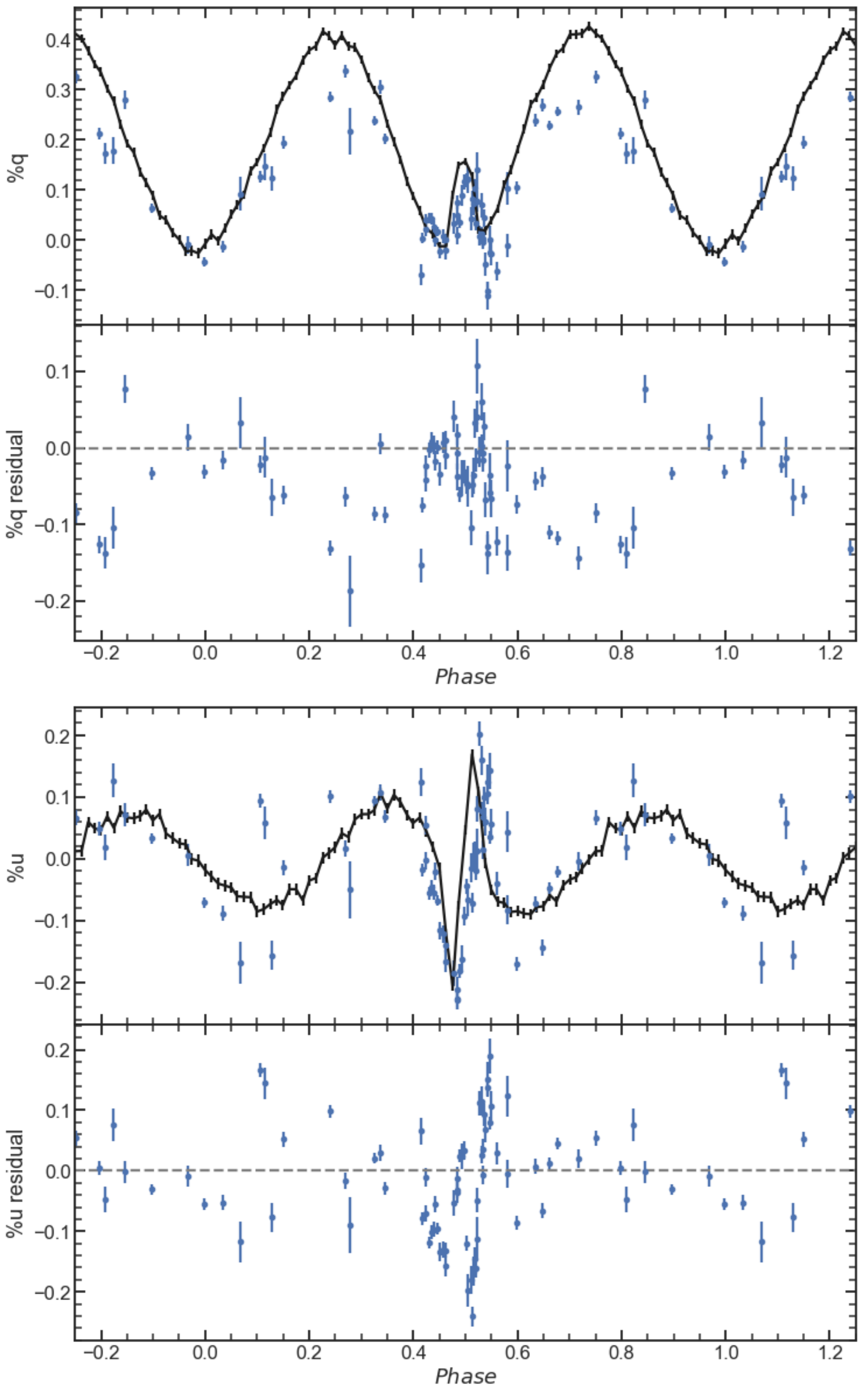

Figure 4.10: V444 Cygni polarization (blue points) compared to the Kurosawa, Hillier, and Pittard (2002) E model at an inclination angle of 82.2° (black line), with rotated O star wind cavity as in the emission line model (Table 4.2). The *R*-band polarization data are taken from St-Louis et al. (1993). Residuals are also presented below each plot.

rate of 7×10^{-6} $M_{\odot}$ yr^{-1}). The result is shown in Figure 4.11. While the eclipse behavior remains similar, the amplitude of polarization variation is increased by 0.2% polarization in $\%q$. This is expected given the direct relationship between $\dot{M}$ and polarization variation amplitude derived by St-Louis et al. (1988).

4.3.4 Line polarization model

V444 Cygni (as well as WR 42 and WR 79, see Chapter 3) has been studied using spectropolarimetry (Lomax et al. 2015). Modeling the polarization behavior of line emission regions is important to fully characterize the system and investigate its mass loss properties. As a first test, I devised a model to represent the spectroscopically-derived model of Marchenko et al. (1997) for the He II $\lambda4686$ line, found to exist in shocked regions in the colliding wind of V444 Cygni and observed polarimetrically by Hoffman et al. (2017). This will allow the use of polarimetry as an independent test of the spectroscopic model. Figure 4.12 shows a scale diagram of the model in a top-down view. The stars act only as absorbing surfaces, while emission occurs in two regions: the WR wind, and the shocked regions behind the wind-wind collision zone. The WR wind density is the same as for continuum models, but the O star cavity has been located so that it follows the shock emission regions. The stellar continuum emission can be neglected because Stokes parameters are additive, therefore the effects of multiple sources can be separately modeled and combined if desired. The shock emission regions are located somewhat arbitrarily along the O star wind cavity edge so that they match the phase locations of the Marchenko et al. (1997) model, and their ϕ extent of 15° in the model matches the angular width of the regions suggested by Marchenko et al. (1997).

To separate the effects of the shocked emission and the WR wind emission, I ran two different models. The first included both wind and shock emission in a ratio of 9:1 (see Table 4.2 for other parameters), following the estimate of Marchenko et al. (1997) that $\sim$ 10% of the He II $\lambda4686$ emission originates in the shocked region. The results of this

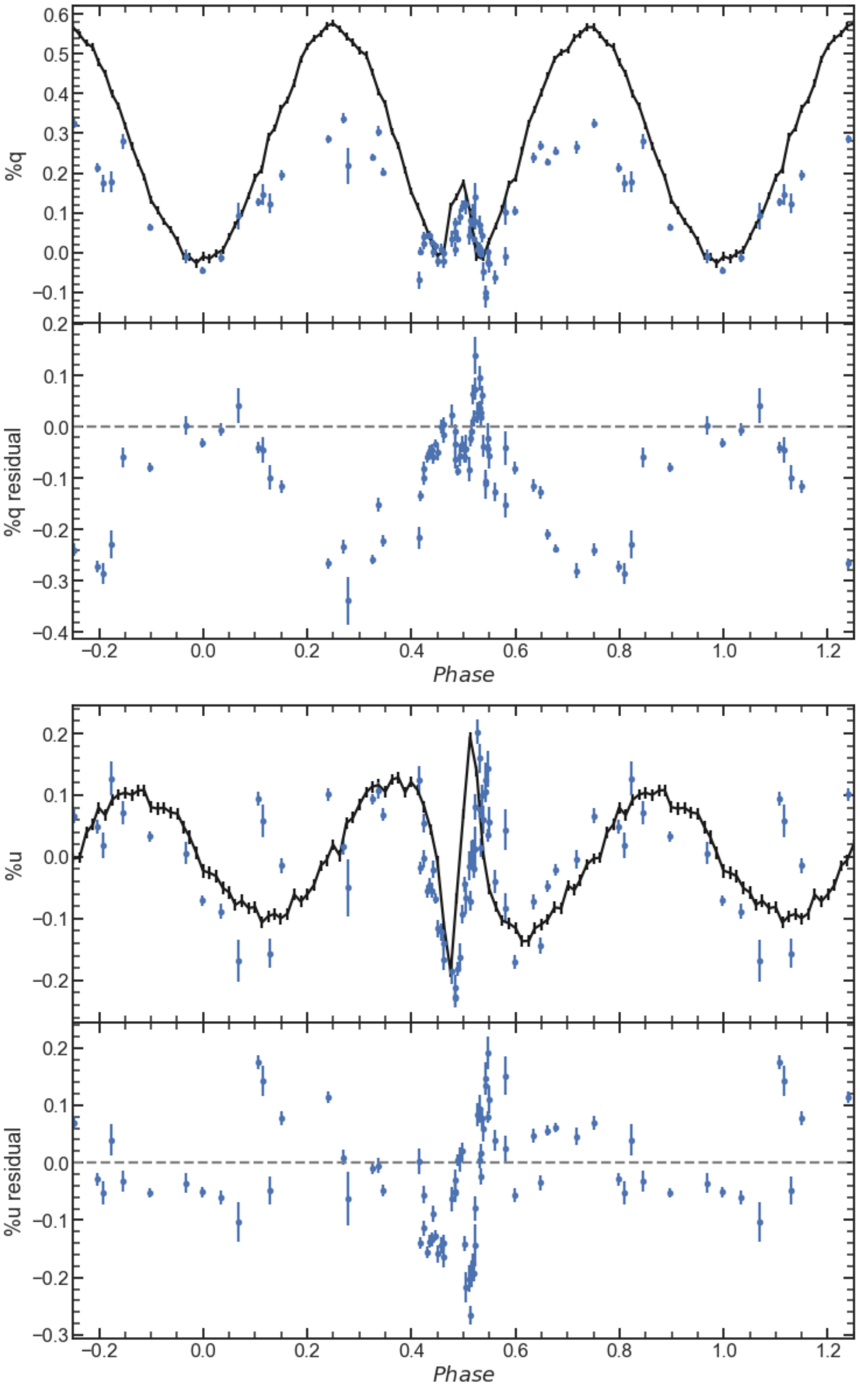

Figure 4.11: V444 Cygni polarization (blue points) compared to the Kurosawa, Hillier, and Pittard (2002) E model at an inclination angle of 82.2° (black line), with a higher mass-loss rate PoWR model (10^{-5} $M_\odot$ yr^{-1}). The *R*-band polarization data are taken from St-Louis et al. (1993). Residuals are also presented below each plot.

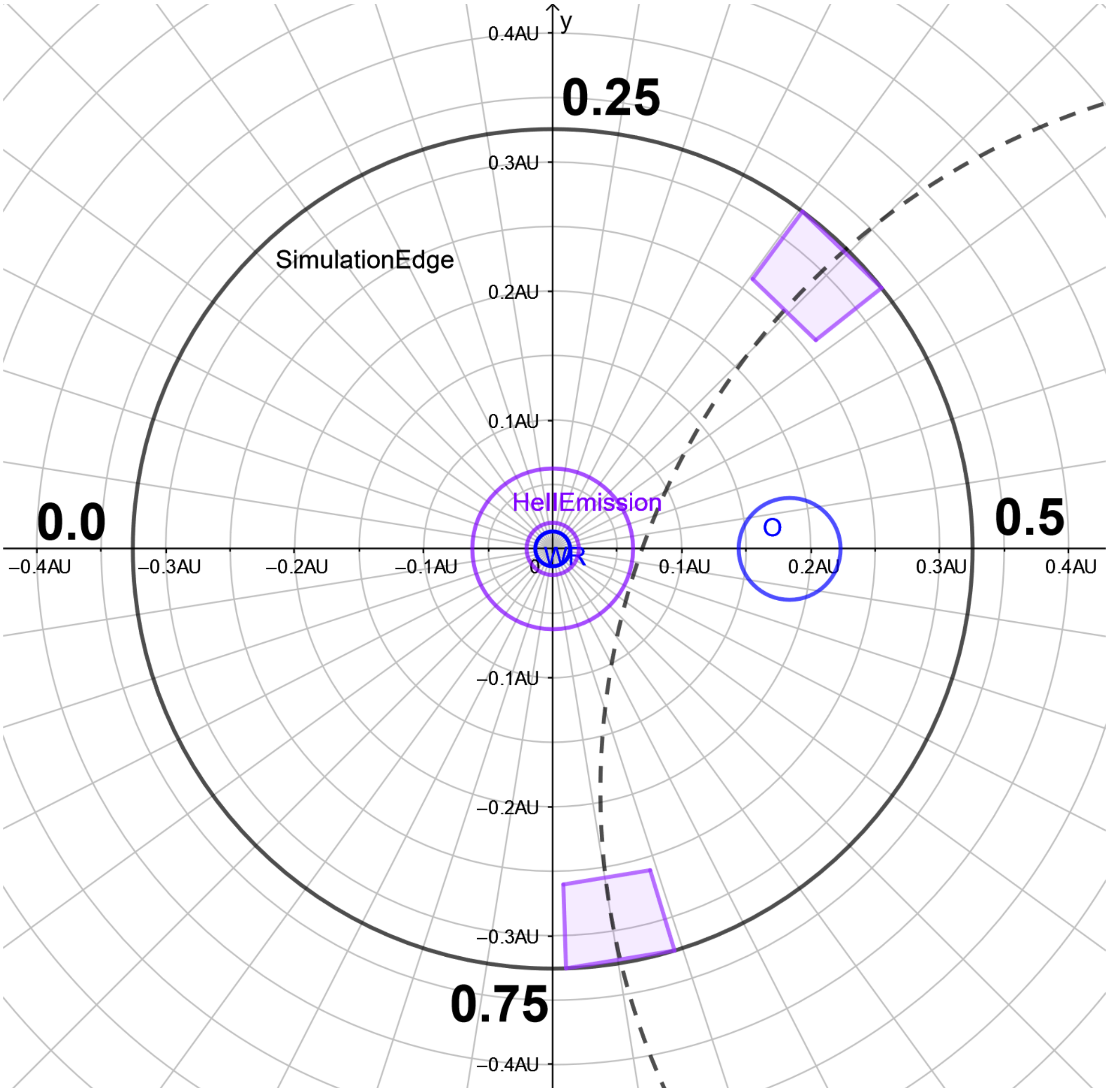

Figure 4.12: V444 Cygni line polarization model schematic, to scale. Same as Figure 4.4, but instead emission originates from the shaded areas in a shell around the WR star and two ends of the shock region, based on the spectroscopically derived model of Marchenko et al. (1997). The cavity has been relocated so that it lines up with the shock emission while maintaining the same stagnation point. The leading shock is located at phase ∼ 0.12 while the trailing shock is at phase ∼ 0.75 in this static image (where phase 0 occurs when the WR star is in front of the O star and 0.5 occurs in the reverse case).

can be seen in Figure 4.13, with the R-band continuum polarization data of St-Louis et al. (1993) plotted on top to show how differently the line polarization behaves with phase. The second model only emitted from the shock, and the results of this are shown in Figure 4.14, again compared to the continuum data.

1.28×10^{10} photons were run across 64 CPUs to produce each model output in a run time of approximately 2 hours on the University of Denver HPC cluster. The output was binned to 23 inclination angle and 80 orbital phase bins.

The result in Figure 4.13 shows almost no polarization variation in q, with the majority in u, including a "flat top" to the sinusoid around secondary eclipse, phase 0.5. In contrast, Figure 4.14 has very strong variation in q and u, with multiple peaks between phases 0.25 and 0.6. I discuss these results in more detail in the next section.

4.4 Discussion and conclusions

4.4.1 Continuum polarization models

The updated continuum models in Section 4.3.3 show significant improvements over the prior set. However, further improvements need to be made, regarding the reproduction of the $\%q$ polarization amplitude and the secondary eclipse. The former could be solved using a reduced mass-loss rate for the WR star wind model. Figure 4.11 shows that the model is (as expected) sensitive to mass-loss rate changes, so a reduction in mass-loss rate to perhaps 1×10^{-6} $\mathrm{M}_\odot$ yr^{-1} may be sufficient to reduce the maximum $\%q$ by 0.1% polarization. The issues with the secondary eclipse may be solved by changing the radius of the O star. To increase the phase range over which the eclipse manifests in the model, a larger O star size would be required. Despite the problems with the model in Figure 4.5, the phase range of the secondary eclipse appears more accurate than the Kurosawa, Hillier, and Pittard (2002) model E result. Both of these improvements can be easily tested with future model runs.

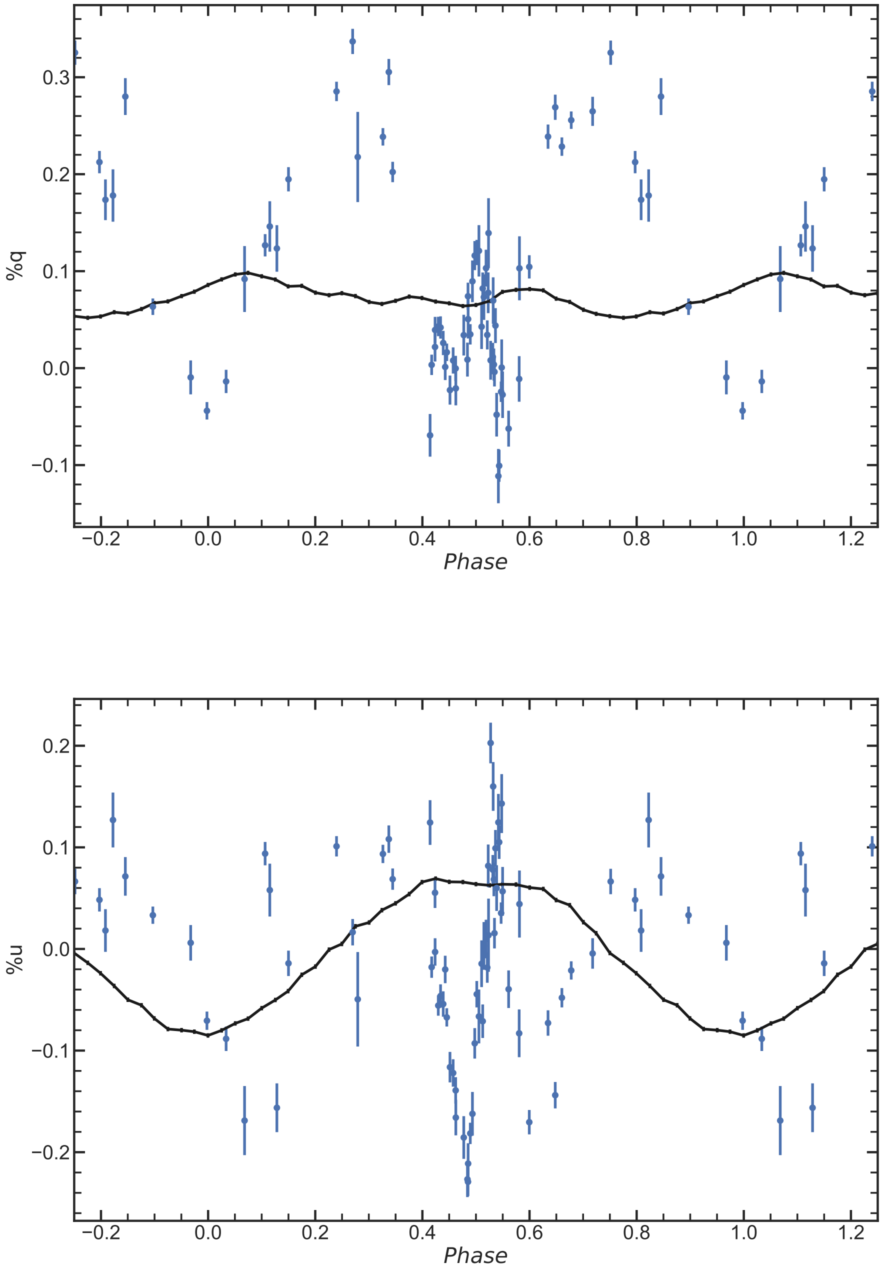

Figure 4.13: V444 Cygni polarization (blue points) compared to a wind + shock emission line region model at an inclination angle of 82.2° (black line). The *R*-band polarization data are taken from St-Louis et al. (1993).

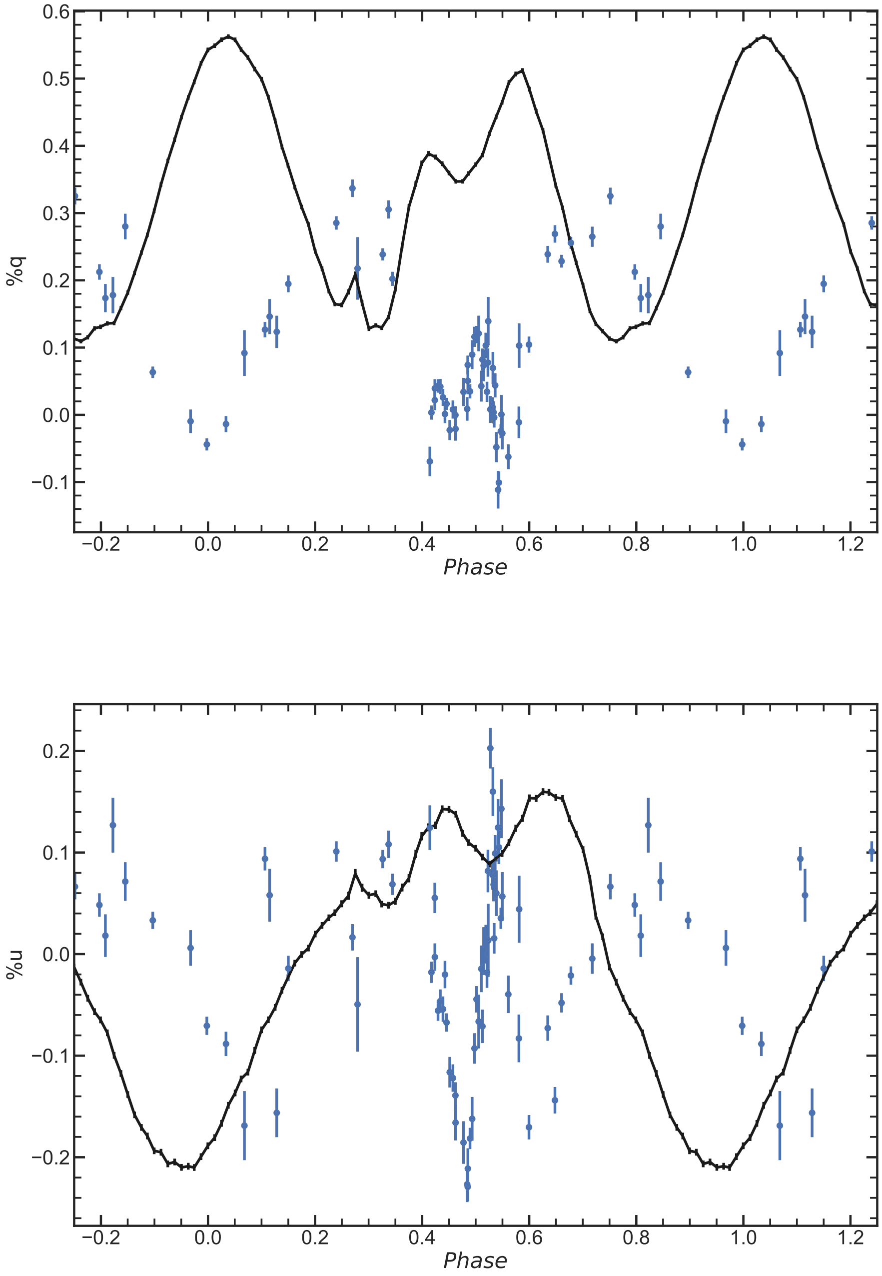

Figure 4.14: V444 Cygni polarization (blue points) compared to a shock emission line region model at an inclination angle of 82.2° (black line). The *R*-band polarization data are taken from St-Louis et al. (1993).

An interesting prediction arises from the model based on the WR 21 stellar separation: the basic V444 Cygni model, with only adjustments to the stellar separation, can produce simple double sinusoids with no strong eclipse effects in q or u. Therefore, continuum polarization alone is not a sufficient diagnostic to tightly constrain the inclination angle and O star radius for non-eclipsing systems (especially for low inclination angles, see §4.2).

4.4.2 Line polarization models

Section 4.3.4 shows the results of the model described in Figure 4.12, intended to represent the He II emission in V444 Cygni. I separated the effects of the shocked emission that follows the wind-wind collision region by limiting photon emission from those regions.

Figure 4.14 shows the result, which is quite startling: the polarized light from these regions varies almost completely out-of-phase with the continuum polarization variation. The constant 0.1% q polarization that shifts up the curve is likely due to the asymmetry of the scattering region coupled with the asymmetric illumination by two separated sources. The out-of-phase nature of the polarization is not too surprising given that the leading shock region is ~ 0.12 ahead in phase while the trailing emission is ~ 0.25 out of phase. Therefore, at primary eclipse, the observer sees light primarily from the trailing shock scattered in the WR wind (because it is perpendicular to the line-of-sight, as opposed to parallel to the line-of-sight at phase 0.75) while at secondary eclipse, the polarization creates two separate peaks (at phases 0.4 and 0.6) as each emission region aligns perpendicular to the observer. There is also a small peak at phase 0.25, though the cause of this is unclear and needs to be investigated with additional modeling. The predictions I mention here can be easily tested with minor changes to the model, e.g. the asymmetric WR wind imparting a constant polarization can be tested by removing the O star; the out-of-phase behavior can be tested by changing the phase location of the shock emission regions.

Figure 4.13 shows the case where emission originates from both the shocked regions and the WR wind. The magnitude of the polarization variations in q drops to $\sim 0.05\%$, and the clear out-of-phase behavior almost disappears. The fact that Lomax et al. (2015) measured some significant departures from a low mean polarization in multiple lines suggests that the ratio of 10% shock emission to 90% WR wind emission proposed by Marchenko et al. (1997) may not account for the spectropolarimetric behavior of the system. Further study of the effects of varying the balance between the emission regions is warranted to explore this possibility.

What is most interesting about the phase variation in the shock-only emission case is that it appears very similar to the line polarization behavior measured for WR 42 and WR 79 in Chapter 3 (though of course additional tests need to be conducted to investigate degeneracy in the models). This is despite the significantly lower inclination angle of those two systems, longer orbits, and WC type. This simple model suggests that in those stars, the majority of the emission in the lines showing this phase variation (C III $\lambda5696$, C IV $\lambda5800$) is originating in the shocked region. This means we can diagnose the location of these shocked regions in the wind once these models have been sufficiently tested. It is not unexpected that these lines are markers for the wind-wind collision. Hill et al. (2000) used C III $\lambda5696$ to investigate the shape of the O star wind cavity in both WR 42 and WR 79. The SLIP model and the data from SALT can therefore provide an independent test of the spectroscopic models: can they explain the polarimetric behavior?

Altogether, it seems plausible that a single class of models with different stellar separations, shock opening angles, and WR wind densities could explain the polarimetric behavior of some different WR + O binary systems. This hypothesis can be tested by expanding the parameter space of the initial models and using data for more objects from RSS (e.g. Chapter 3). The magnitude of continuum polarization variation with phase provides a strong constraint on the mass-loss rate of the WR star, and in cases where the O star eclipses the dense parts of the WR wind it is very sensitive to inclination angle. The phase behavior of line polarization, on the other hand, probes the geometry of the O star wind cavity, which is a function of the relative speeds of the two stellar winds.

In particular, these models can be applied to the spectropolarimetric data from SALT. WR 42 and WR 79 are excellent candidates, as mentioned earlier, because their strong line polarization should allow for constraints on the geometry of their wind-wind collision regions. WR 21 is another obvious choice, because it has such similar spectral types to V444 Cygni, and I already have a preliminary model. Using both continuum and line polarization data to constrain its mass-loss rate and wind-wind collision geometry will tell us a lot about the future evolution of the system.

Chapter 5

Conclusions and Future Work

5.1 Concluding remarks

In Chapter 2, I presented my analysis of a large sample of 47 WR stars, both single and binary, to investigate their possible intrinsic polarization. To do so, I estimated the ISP for each object using a straightforward fitting procedure. Some of the binary systems in the sample had multiple observations, so I performed analytical model fits to determine salient characteristics such as inclination angle. Unfortunately, the phase coverage and uncertainty was often not good enough to recover precise system parameters. Ten of the systems exhibit significant intrinsic polarization. I attributed this to binary interaction, wind clumping, or complex wind structures. Five of the targets showed a significant residual in the narrow Strömgren *b* filter, an indication of line polarization different to that of the continuum. WR 90 stood out as an interesting case of a single star with a strong position angle rotation of the *b* filter polarization, possibly indicating a previously undetected structure in its wind. This work also resulted in an ISP survey across a large region of the Milky Way, providing additional evidence that there can be a polarization position angle dependence on wavelength. I attributed this behaviour to dust clouds of varying density and orientation along the line of sight. This chapter was published in *The Astronomical Journal* as Fullard et al. (2020).

In Chapter 3, I used data from RSS/SALT to investigate two very similar binary systems in detail: WR 42 and WR 79. These stars both have nearly identical periods, inclination angle, and stellar classifications. I found that they also behave similarly polarimetrically. Both of them follow the analytical model of Brown, McLean, and Emslie (1978) in continuum polarization, though the uncertainty on the data is currently too high to use the model to extract system parameters. Of greater interest is the integrated line polarization behavior, which shows a phase difference between the continuum and the line region of C IV λ5800. I attributed this to the collision region between the WR and O star winds passing the observer, based on existing flux spectra models by Hill, Moffat, and St-Louis (2002). The other line regions that I investigated did not show as much variation with phase, suggesting that they are diluted by unpolarized emission from the WR wind. WR 42 shows a strong constant intrinsic polarization component which may indicate a rapidly rotating WR star. However, I was not able to rule out an underestimated ISP contribution, which can be investigated with future observations.

In Chapter 4, I described the preliminary stages of modeling WR + O binary systems using *SLIP*, a pre-existing MCRT code that I modifed to treat colliding-wind binary systems. I validated the modified code against the analytical model of Brown, McLean, and Emslie (1978), confirming the findings of Wolinski and Dolan (1994) that the analytical model tends to overestimate the inclination angle of binary systems. I compared results from the code against the well-studied WR + O system V444 Cyg, and found that the output did not have sufficient inclination angle bins to accurately match continuum polarization data from St-Louis et al. (1993), but otherwise the general behavior of the polarization matched expectations from the data. I changed the stellar separation and O star wind cavity size to approximate the WR 21 system, and found that simple double-sinusoidal polarization behavior with phase is produced. I also created a simple model of line polarization, restricting photon emission to regions known to produce emission lines based on spectroscopy (Marchenko et al. 1997). The results showed very strong polarization behavior that is out-of-phase with the continuum polarization, caused by emission from shocked gas in the wind-wind collision region. Emission from the WR wind itself dilutes the polarization to a low level, but stars such as WR 42 and WR 79 (Chapter 3) show similar behavior with phase in their line polarization. These line polarization simulations, along with spectropolarimetric data from SALT, can be used to constrain the geometrical properties of the wind-wind collision region, telling us about the relative wind strengths of the two stars and quantifying the mass lost from the system.

5.2 Future work

I plan to continue investigating WR + O binary systems using data from RSS/SALT and numerical models. There are a number of areas that could be improved in our current understanding of the analysis of spectropolarimetric data.

Firstly, the instrumental polarization spectrum of RSS/SALT makes drawing robust conclusions from its data output difficult, and certainly does not do justice to the 11-m telescope. I am working closely with Kenneth Nordsieck, the instrument designer, to find methods to remove the instrumental polarization at the data calibration stage so that more fundamental parameters than polarization position angle can be used.

Secondly, the ISP estimates produced in Chapter 2 are not as robust as they need to be to accurately determine ISP for binary systems. There was not enough time-dependent data to produce accurate analytical model fits to all the binaries in the sample, nor were the filter data free of large uncertainties, especially in the U band. Furthermore, the existence of strong, differently-polarized emission lines in WR spectra mean that broad filters can be biased towards (usually lower) polarization values. To resolve these issues, I am planning to use the multi-object spectropolarimetry mode of RSS to obtain simultaneous low-resolution of all the nearby field stars, so that the ISP can be well-characterized across the entire field near a given target. This novel method for rapidly determining ISP with a single observation will be very important for any instrument user who wishes to define the ISP towards their target.

Thirdly, I have still not unlocked the full potential of the RSS/SALT data, namely the ability to investigate the polarized line profiles of emission lines in the polarimetric spectra. The information in these lines can tell us about the detailed behavior of the colliding wind regions, which can be linked to more detailed models to put strong constraints on the wind geometry. This has already been accomplished with flux spectra (e.g., Hill, Moffat, and St-Louis 2002) so it should be achievable with polarized spectra as well. Simply using polarimetry as an independent test of these spectral models would be valuable.

Finally, the updated version of *SLIP* remains in its preliminary stages. More validation of the model needs to be performed versus other existing models (e.g. Fox 1994b; Wood et al. 1996c), and a wider range of optical depths should be considered to compare with the analytical model of Brown, McLean, and Emslie (1978). Some discrepancies between the numerical and analytical model need to be addressed (e.g. Fig. 4.3). Further tests including emission from both stars and line emission regions may help disentangle the different contributions to the polarization. Placing the shock emission regions at different phases should also be done to test the effects on the line polarization variation with phase. Testing the effects of the asymmetric wind (with cavity) with central illumination should be done to determine its impact on the polarzation. I have also obtained the detailed density predictions of the hydrodynamical model that Lomax et al. (2015) developed to explain the X-ray signatures of V444 Cyg, and I intend to test it using the existing spectropolarimetric data to provide an independent determination of the model's success in explaining the system. The model could also benefit from improvements to its grid setup. An octree grid, for example, would improve the density resolution of areas of interest such as the wind collision region.

Bibliography

Adams, S. M., Kochanek, C. S., Gerke, J. R., Stanek, K. Z., and Dai, X. (2017). “The search for failed supernovae with the Large Binocular Telescope: confirmation of a disappearing star”. *Monthly Notices of the Royal Astronomical Society* 468, pp. 4968–4981. DOI: `10.1093/mnras/stx816`.

Aldoretta, E. J., St-Louis, N., Richardson, N. D., Moffat, A. F. J., Eversberg, T., Hill, G. M., Shenar, T., Artigau, É., Gauza, B., Knapen, J. H., Kubát, J., Kubátová, B., Maltais-Tariant, R., Muñoz, M., Pablo, H., Ramiaramanantsoa, T., Richard-Laferrière, A., Sablowski, D. P., Simón-Díaz, S., St-Jean, L., Bolduan, F., Dias, F. M., Dubreuil, P., Fuchs, D., Garrel, T., Grutzeck, G., Hunger, T., Küsters, D., Langenbrink, M., Leadbeater, R., Li, D., Lopez, A., Mauclaire, B., Moldenhawer, T., Potter, M., Santos, E. M. dos, Schanne, L., Schmidt, J., Sieske, H., Strachan, J., Stinner, E., Stinner, P., Stober, B., Strandbaek, K., Syder, T., Verilhac, D., Waldschläger, U., Weiss, D., and Wendt, A. (2016). “An extensive spectroscopic time series of three Wolf-Rayet stars - I. The lifetime of large-scale structures in the wind of WR 134”. *Monthly Notices of the Royal Astronomical Society* 460.3, p. 3407. DOI: `10.1093/mnras/stw1188`.

Alzner, A. and Argyle, R. W. (2012). “The Orbital Elements of a Visual Binary Star”. In: *Observing and Measuring Visual Double Stars*. Ed. by R. W. Argyle. Patrick Moore’s Practical Astronomy Series. New York, NY: Springer, pp. 71–79. ISBN: 978-1-4614-3945-5. DOI: `10.1007/978-1-4614-3945-5_7`.

Annuk, K. (1990). “The long period Wolf-Rayet star HD 193077.” *Acta Astronomica* 40, p. 267.

Arora, B., Pandey, J. C., Joshi, A., and De Becker, M. (2019). “Polarization study of massive binaries with the ARIES-1.04 m telescope”. *Bulletin de la Societe Royale des Sciences de Liege* 88, pp. 287–290.

Aspin, C., Simmons, J. F. L., and Brown, J. C. (1981). "Polarimetric Accuracy Required for the Determination of Binary Inclinations". *Monthly Notices of the Royal Astronomical Society* 194, p. 283. DOI: `10.1093/mnras/194.2.283`.

Bagnulo, S., Cox, N. L. J., Cikota, A., Siebenmorgen, R., Voshchinnikov, N. V., Patat, F., Smith, K. T., Smoker, J. V., Taubenberger, S., Kaper, L., and Cami, J. (2017). "Large Interstellar Polarisation Survey (LIPS) - I. FORS2 spectropolarimetry in the Southern Hemisphere". *Astronomy & Astrophysics* 608, A146. DOI: `10.1051/0004-6361/201731459`.

Bartzakos, P., Moffat, A. F. J., and Niemela, V. S. (2001). "Magellanic Cloud WC/WO Wolf-Rayet stars - I. Binary frequency and Roche lobe overflow formation". *Monthly Notices of the Royal Astronomical Society* 324.1, p. 18. DOI: `10.1046/j.1365-8711.2001.04126.x`.

Böhm-Vitense, E. (1992). *Introduction to stellar astrophysics. Vol. 3 - Stellar structure and evolution.* Vol. 3. Cambridge (UK): Cambridge University Press. ISBN: 0-521-34404-2.

Bowen, D. V., Jenkins, E. B., Tripp, T. M., Sembach, K. R., Savage, B. D., Moos, H. W., Oegerle, W. R., Friedman, S. D., Gry, C., Kruk, J. W., Murphy, E., Sankrit, R., Shull, J. M., Sonneborn, G., and York, D. G. (2008). "The Far Ultraviolet Spectroscopic Explorer Survey of O VI Absorption in the Disk of the Milky Way". *The Astrophysical Journal Supplement Series* 176.1, p. 59. DOI: `10.1086/524773`.

Brott, I., Mink, S. E. de, Cantiello, M., Langer, N., Koter, A. de, Evans, C. J., Hunter, I., Trundle, C., and Vink, J. S. (2011). "Rotating massive main-sequence stars. I. Grids of evolutionary models and isochrones". *Astronomy and Astrophysics* 530, A115. DOI: `10.1051/0004-6361/201016113`.

Brown, J. C., Aspin, C., Simmons, J. F. L., and McLean, I. S. (1982). "The effect of orbital eccentricity on polarimetric binary diagnostics." *Monthly Notices of the Royal Astronomical Society* 198, p. 787. DOI: `10.1093/mnras/198.3.787`.

Brown, J. C. and McLean, I. S. (1977). “Polarisation by Thomson Scattering in Optically Thin Stellar Envelopes. I. Source Star at Centre of Axisymmetric Envelope”. *Astronomy and Astrophysics* 57.

Brown, J. C., McLean, I. S., and Emslie, A. G. (1978). “Polarisation by Thomson scattering in optically thin stellar envelopes. II - Binary and multiple star envelopes and the determination of binary inclinations”. *Astronomy and Astrophysics* 68, pp. 415–427.

Buckley, D. A. H., Swart, G. P., and Meiring, J. G. (2006). “Completion and commissioning of the Southern African Large Telescope”. In: *Proceedings of the SPIE.* Vol. 6267. Society of Photo-Optical Instrumentation Engineers (SPIE) Conference Series, 62670Z. DOI: `10.1117/12.673750`.

Burgh, E. B., Nordsieck, K. H., Kobulnicky, H. A., Williams, T. B., O’Donoghue, D., Smith, M. P., and Percival, J. W. (2003). “Prime focus imaging spectrograph for the Southern African Large Telescope: optical design”. In: *Instrument Design and Performance for Optical/Infrared Ground-based Telescopes.* Vol. 4841. International Society for Optics and Photonics, pp. 1463–1471. DOI: `10.1117/12.460312`.

Callingham, J. R., Crowther, P. A., Williams, P. M., Tuthill, P. G., Han, Y., Pope, B. J. S., and Marcote, B. (2020). “Two Wolf-Rayet stars at the heart of colliding-wind binary Apep”. *Monthly Notices of the Royal Astronomical Society* 495, pp. 3323–3331. DOI: `10.1093/mnras/staa1244`.

Callingham, J. R., Tuthill, P. G., Pope, B. J. S., Williams, P. M., Crowther, P. A., Edwards, M., Norris, B., and Kedziora-Chudczer, L. (2019). “Anisotropic winds in Wolf-Rayet binary identify potential gamma-ray burst progenitor”. *Nature Astronomy* 3.1, pp. 82–87. DOI: `10.1038/s41550-018-0617-7`.

Cano, Z., Wang, S.-Q., Dai, Z.-G., and Wu, X.-F. (2017). “The Observer’s Guide to the Gamma-Ray Burst Supernova Connection”. *Advances in Astronomy* 2017, p. 8929054. DOI: `10.1155/2017/8929054`.

Carlos-Leblanc, D., St-Louis, N., Bjorkman, J. E., and Ignace, R. (2019). "Monte Carlo simulations of polarimetric and light variability from corotating interaction regions in hot stellar winds". *Monthly Notices of the Royal Astronomical Society* 489.2, pp. 2873–2886. DOI: `10.1093/mnras/stz2273`.

Cassinelli, J. P. (1992). "Models for the Winds of Rapidly Rotating Early-Type Stars (Invited Paper)". *Nonisotropic and Variable Outflows from Stars* 22, p. 134.

Castor, J. I., Abbott, D. C., and Klein, R. I. (1975). "Radiation-driven winds in Of stars". *The Astrophysical Journal* 195, pp. 157–174. DOI: `10.1086/153315`.

Chandrasekhar, S. (1947). "On the Radiative Equilibrium of a Stellar Atmosphere. XV." *The Astrophysical Journal* 105, p. 424. DOI: `10.1086/144917`.

Chandrasekhar, S. (1960). *Radiative transfer.* New York: Dover.

Chené, A.-N. and St-Louis, N. (2011). "A Systematic Search for Corotating Interaction Regions in Apparently Single Galactic Wolf-Rayet Stars. II. A Global View of the Wind Variability". *The Astrophysical Journal* 736.2, p. 140. DOI: `10.1088/0004-637X/736/2/140`.

Chevalier, R. A. (2012). "Common Envelope Evolution Leading to Supernovae with Dense Interaction". *The Astrophysical Journal Letters* 752, p. L2. DOI: `10.1088/2041-8205/752/1/L2`.

Chevrotière, A. de la, St-Louis, N., Moffat, A. F. J., and Collaboration, M. (2014). "Searching for Magnetic Fields in 11 Wolf-Rayet Stars: Analysis of Circular Polarization Measurements from ESPaDOnS". *The Astrophysical Journal* 781.2, p. 73. DOI: `10.1088/0004-637X/781/2/73`.

Clarke, D. (2010). *Stellar Polarimetry.* Wiley. ISBN: 978-3-527-40895-5.

Cohen, M., Barlow, M. J., and Kuhi, L. V. (1975). "Wolf-Rayet stars. VI - The nature of the optical and infrared continua". *Astronomy and Astrophysics* 40, pp. 291–302.

Collado, A., Gamen, R., and Barbá, R. H. (2013). "The new Wolf-Rayet binary system WR62a". *Astronomy and Astrophysics* 552, A22. DOI: `10.1051/0004-6361/201118460`.

Crawford, S. M., Still, M., Schellart, P., Balona, L., Buckley, D. A. H., Dugmore, G., Gulbis, A. A. S., Kniazev, A., Kotze, M., Loaring, N., Nordsieck, K. H., Pickering, T. E., Potter, S., Romero Colmenero, E., Vaisanen, P., Williams, T., and Zietsman, E. (2010). "PySALT: the SALT science pipeline". *Observatory Operations: Strategies, Processes, and Systems III* 7737, p. 773725. DOI: `10.1117/12.857000`.

Crowther, P. A. (2015). "Wolf-Rayet content of the Milky Way". *Wolf-Rayet Stars: Proceedings of an International Workshop held in Potsdam*, p. 21.

Crowther, P. A., De Marco, O., and Barlow, M. J. (1998). "Quantitative classification of WC and WO stars". *Monthly Notices of the Royal Astronomical Society* 296, pp. 367–378. DOI: `10.1046/j.1365-8711.1998.01360.x`.

Crowther, P. A. (2007). "Physical Properties of Wolf-Rayet Stars". *Annual Review of Astronomy and Astrophysics* 45.1, pp. 177–219. DOI: `10.1146/annurev.astro.45.051806.110615`.

David-Uraz, A., Moffat, A. F. J., Chené, A.-N., Rowe, J. F., Lange, N., Guenther, D. B., Kuschnig, R., Matthews, J. M., Rucinski, S. M., Sasselov, D., and Weiss, W. W. (2012). "Using MOST to reveal the secrets of the mischievous Wolf-Rayet binary CV Ser". *Monthly Notices of the Royal Astronomical Society* 426.3, p. 1720. DOI: `10.1111/j.1365-2966.2012.21736.x`.

De Becker, M. and Raucq, F. (2013). "Catalogue of particle-accelerating colliding-wind binaries". *Astronomy and Astrophysics* 558, A28. DOI: `10.1051/0004-6361/201322074`.

Demers, H., Moffat, A. F. J., Marchenko, S. V., Gayley, K. G., and Morel, T. (2002). "The Quadruple Wolf-Rayet System GP Cephei: Spectral Types, Masses, Mass-Loss Rate, and Colliding Winds". *The Astrophysical Journal* 577.1, p. 409. DOI: `10.1086/342142`.

Dolan, J. F. and Tapia, S. (1986). "Wavelength Dependence of Position Angle in Polarization Standards". *Bulletin of the American Astronomical Society* 18, p. 968.

Dorn-Wallenstein, T. Z. and Levesque, E. M. (2020). "A Comparison of Rotating and Binary Stellar Evolution Models: Effects on Massive Star Populations". *The Astrophysical Journal* 896, p. 164. DOI: `10.3847/1538-4357/ab8d28`.

Drissen, L., Moffat, A. F. J., Bastien, P., Lamontagne, R., and Tapia, S. (1986). "Polarimetric observations of the WN7 binary CQ Cephei". *The Astrophysical Journal* 306, p. 215. DOI: `10.1086/164333`.

Drissen, L., Robert, C., and Moffat, A. F. J. (1992). "Polarization Variability among Wolf-Rayet Stars. VII. The Single Stars WR 14, WR 25, and WR 69". *The Astrophysical Journal* 386, p. 288. DOI: `10.1086/171014`.

Drissen, L., St.-Louis, N., Moffat, A. F. J., and Bastien, P. (1987). "Polarization variability among Wolf-Rayet stars. II. Linear polarization of a complete sample of southern Galactic WN stars". *The Astrophysical Journal* 322, pp. 888–901. DOI: `10.1086/165783`.

Duchêne, G. and Kraus, A. (2013). "Stellar Multiplicity". *Annual Review of Astronomy and Astrophysics* 51, pp. 269–310. DOI: `10.1146/annurev-astro-081710-102602`.

Duderstadt, J. J. and Martin, W. R. (1979). *Transport theory.* New York: Wiley.

Ekström, S., Georgy, C., Eggenberger, P., Meynet, G., Mowlavi, N., Wyttenbach, A., Granada, A., Decressin, T., Hirschi, R., Frischknecht, U., Charbonnel, C., and Maeder, A. (2012). "Grids of stellar models with rotation - I. Models from 0.8 to 120 Msun at solar metallicity (Z = 0.014)". *Astronomy & Astrophysics* 537. arXiv: 1110.5049, A146. DOI: `10.1051/0004-6361/201117751`.

Eldridge, J. J., Stanway, E. R., Xiao, L., McClelland, L. A. S., Taylor, G., Ng, M., Greis, S. M. L., and Bray, J. C. (2017). "Binary Population and Spectral Synthesis Version 2.1: Construction, Observational Verification, and New Results". *Publications of the Astronomical Society of Australia* 34, e058. DOI: `10.1017/pasa.2017.51`.

Eldridge, J. J., Fraser, M., Smartt, S. J., Maund, J. R., and Crockett, R. M. (2013). "The death of massive stars - II. Observational constraints on the progenitors of Type Ibc supernovae". *Monthly Notices of the Royal Astronomical Society* 436, pp. 774–795. DOI: `10.1093/mnras/stt1612`.

Eriș, F. Z. and Ekmekçi, F. (2011). "A 2007 photometric study and UV spectral analysis of the Wolf-Rayet binary V444 Cyg". *Astronomische Nachrichten* 332.6, p. 616. DOI: `10.1002/asna.201011564`.

Fahed, R. and Moffat, A. F. J. (2012). "Colliding winds in five WR+O systems of the Southern hemisphere". *Monthly Notices of the Royal Astronomical Society* 424.3, pp. 1601–1613. DOI: `10.1111/j.1365-2966.2012.20494.x`.

Filippenko, A. V. (1997). "Optical Spectra of Supernovae". *Annual Review of Astronomy and Astrophysics* 35, pp. 309–355. DOI: `10.1146/annurev.astro.35.1.309`.

Foellmi, C., Moffat, A. F. J., and Guerrero, M. A. (2003a). "Wolf—Rayet binaries in the Magellanic Clouds and implications for massive-star evolution — I. Small Magellanic Cloud". *Monthly Notices of the Royal Astronomical Society* 338.2. Publisher: Oxford Academic, pp. 360–388. DOI: `10.1046/j.1365-8711.2003.06052.x`.

— (2003b). "Wolf—Rayet binaries in the Magellanic Clouds and implications for massive-star evolution — II. Large Magellanic Cloud". *Monthly Notices of the Royal Astronomical Society* 338.4. Publisher: Oxford Academic, pp. 1025–1056. DOI: `10.1046/j.1365-8711.2003.06161.x`.

Foreman-Mackey, D., Hogg, D. W., Lang, D., and Goodman, J. (2013). "emcee: The MCMC Hammer". *Publications of the Astronomical Society of the Pacific* 125, p. 306. DOI: `10.1086/670067`.

Fox, G. K. (1994a). "Stellar occultation of polarized light from circumstellar electrons. 4: Detached binary systems". *The Astrophysical Journal* 432, pp. 262–273. DOI: `10.1086/174567`.

— (1994b). "The theoretical polarization of pure scattering axisymmetric circumstellar envelopes". *The Astrophysical Journal* 435, pp. 372–378. DOI: `10.1086/174819`.

Friend, D. B. and Abbott, D. C. (1986). “The theory of radiatively driven stellar winds. III - Wind models with finite disk correction and rotation”. *The Astrophysical Journal* 311, pp. 701–707. DOI: `10.1086/164809`.

Fryer, C. L. and Heger, A. (2005). “Binary Merger Progenitors for Gamma-Ray Bursts and Hypernovae”. *The Astrophysical Journal* 623, pp. 302–313. DOI: `10.1086/428379`.

Fullard, A. G., Hoffman, J. L., DeKlotz, S., Luchtan, D. A., Cooper, K., and Nordsieck, K. H. (2018). “Spectropolarimetry of the WR + O Binary WR42”. *Research Notes of the AAS* 2.2, p. 37. DOI: `10.3847/2515-5172/aac5fb`.

Fullard, A. G., St-Louis, N., Moffat, A. F. J., Piirola, V. E., Manset, N., and Hoffman, J. L. (2020). “A Multiwavelength Search for Intrinsic Linear Polarization in Wolf–Rayet Winds”. *The Astronomical Journal* 159.5. Publisher: American Astronomical Society, p. 214. DOI: `10.3847/1538-3881/ab8293`.

Gaia Collaboration et al. (2018). “Gaia Data Release 2. Summary of the contents and survey properties”. *Astronomy and Astrophysics* 616, A1. DOI: `10.1051/0004-6361/201833051`.

Gamen, R., Gosset, E., Morrell, N., Niemela, V., Sana, H., Nazé, Y., Rauw, G., Barbá, R., and Solivella, G. (2006). “The first orbital solution for the massive colliding-wind binary HD 93162 (=WR 25)”. *Astronomy and Astrophysics* 460.3, p. 777. DOI: `10.1051/0004-6361:20065618`.

Gamen, R. and Niemela, V. S. (1999). “Wolf-Rayet binaries revisited.” *Revista Mexicana de Astronomia y Astrofisica Conference Series* 8, p. 55.

Gayley, K. G. (2004). “Inhibition of Wind-Compressed Disk Inhibition in Optically Thick Winds”. In: *Stellar Rotation.* Ed. by A. Maeder and P. Eenens. Vol. 215. IAU Symposium, p. 527.

Georgiev, L. N., Koenigsberger, G., Ivanov, M. M., St. -Louis, N., and Cardona, O. (1999). “Long-term coherent variations in the WR system EZ Canis Majoris: the binary scenario revisited”. *Astronomy and Astrophysics* 347, p. 583.

Georgy, C., Ekström, S., Meynet, G., Massey, P., Levesque, E. M., Hirschi, R., Eggenberger, P., and Maeder, A. (2012). "Grids of stellar models with rotation - II. WR populations and supernovae/GRB progenitors at Z = 0.014". *Astronomy & Astrophysics* 542. Publisher: EDP Sciences, A29. DOI: `10.1051/0004-6361/201118340`.

Gräfener, G., Koesterke, L., and Hamann, W.-R. (2002). "Line-blanketed model atmospheres for WR stars". *Astronomy and Astrophysics* 387, pp. 244–257. DOI: `10.1051/0004-6361:20020269`.

Gräfener, G., Vink, J. S., Harries, T. J., and Langer, N. (2012). "Rotating Wolf-Rayet stars in a post RSG/LBV phase. An evolutionary channel towards long-duration GRBs?" *Astronomy and Astrophysics* 547, A83. DOI: `10.1051/0004-6361/201118664`.

Grassitelli, L., Langer, N., Grin, N. J., Mackey, J., Bestenlehner, J. M., and Gräfener, G. (2018). "Subsonic structure and optically thick winds from Wolf-Rayet stars". *Astronomy and Astrophysics* 614, A86. DOI: `10.1051/0004-6361/201731542`.

Green, R. M. (1985). *Spherical astronomy*. Cambridge [Cambridgeshire] ; New York: Cambridge University Press. ISBN: 978-0-521-23988-2.

Gullberg, D. and Lindegren, L. (2002). "Determination of accurate stellar radial-velocity measures". *Astronomy and Astrophysics* 390, pp. 383–395. DOI: `10.1051/0004-6361:20020660`.

Hamann, W.-R. and Gräfener, G. (2004). "Grids of model spectra for WN stars, ready for use". *Astronomy and Astrophysics* 427, pp. 697–704. DOI: `10.1051/0004-6361:20040506`.

Hamann, W.-R., Gräfener, G., Liermann, A., Hainich, R., Sander, A. a. C., Shenar, T., Ramachandran, V., Todt, H., and Oskinova, L. M. (2019). "The Galactic WN stars revisited. Impact of Gaia distances on fundamental stellar parameters". *Astronomy and Astrophysics* 625, A57. DOI: `10.1051/0004-6361/201834850`.

Hamann, W.-R., Leuenhagen, U., Koesterke, L., and Wessolowski, U. (1992). “Modelling the spectrum of WC-type Wolf-Rayet stars”. *Astronomy and Astrophysics* 255, pp. 200–214.

Harries, T. J., Hillier, D. J., and Howarth, I. D. (1998). “A spectropolarimetric survey of northern hemisphere Wolf-Rayet stars”. *Monthly Notices of the Royal Astronomical Society* 296, pp. 1072–1088. DOI: `10.1046/j.1365-8711.1998.01508.x`.

Harries, T. J., Howarth, I. D., Schulte-Ladbeck, R. E., and Hillier, D. J. (1999). “The interstellar and intrinsic polarizations of EZ CMa”. *Monthly Notices of the Royal Astronomical Society* 302, pp. 499–511. DOI: `10.1046/j.1365-8711.1999.02126.x`.

Harrington, J. P. and Collins George W., I. (1968). “Intrinsic Polarization of Rapidly Rotating Early-Type Stars”. *ApJ* 151, p. 1051. DOI: `10.1086/149504`.

Heuvel, V. D., J, E. P., Zwart, P., F, S., Mink, D., and E, S. (2017). “Forming short-period Wolf-Rayet X-ray binaries and double black holes through stable mass transfer”. *Monthly Notices of the Royal Astronomical Society* 471.4, p. 4256. DOI: `10.1093/mnras/stx1430`.

Hill, G. M., Moffat, A. F. J., and St-Louis, N. (2002). “Modelling the colliding-winds spectra of the 19-d WR + OB binary in the massive triple system θ Muscae”. *Monthly Notices of the Royal Astronomical Society* 335.4, p. 1069. DOI: `10.1046/j.1365-8711.2002.05694.x`.

— (2018). “Modelling the colliding-wind spectra of the WC8d+O8-9IV binary CV Ser (WR 113)”. *Monthly Notices of the Royal Astronomical Society* 474.3, pp. 2987–2999. DOI: `10.1093/mnras/stx2943`.

Hill, G. M., Moffat, A. F. J., St-Louis, N., and Bartzakos, P. (2000). “Modelling the spectra of colliding winds in the Wolf-Rayet WC7+O binaries WR 42 and WR 79”. *Monthly Notices of the Royal Astronomical Society* 318.2, pp. 402–410. DOI: `10.1046/j.1365-8711.2000.03705.x`.

Hill, G. M., Moffat, A. F. J., and St-Louis, N. (2003). "Colliding winds in the WR+OB binary θ Muscae (WR 48, WC5+O6-7V)". *A Massive Star Odyssey: From Main Sequence to Supernova* 212, p. 204.

Hillier, D. J. (1989). "WC stars - Hot stars with cold winds". *The Astrophysical Journal* 347, p. 392. DOI: `10.1086/168127`.

Hillier, D. J. (2011). "The atomic physics underlying the spectroscopic analysis of massive stars and supernovae". *Astrophysics and Space Science* 336, pp. 87–93. DOI: `10.1007/s10509-010-0590-9`.

Hoffman, J. L. (2007). "Polarized Line Profiles as Diagnostics of Circumstellar Geometry in Type IIn Supernovae". In: vol. 30. eprint: arXiv:astro-ph/0612244, pp. 57–63.

— (2015). "Mass Flows in Massive Binaries: Clues from Spectropolarimetry". 71. Conference Name: EAS Publications Series, pp. 163–167. DOI: `10.1051/eas/1571036`.

Hoffman, J. L., Ashley, S. F., Ornelas, J. L., Fullard, A., Lomax, J. R., Shrestha, M., Babler, B. L., Bjorkman, J. E., Bjorkman, K. S., Davidson, J. W., Meade, M., Nordsieck, K. H., and Richardson, N. (2017). "The Distorted Winds of V444 Cygni: New Insights from Spectropolarimetry". In: *American Astronomical Society Meeting Abstracts.* Vol. 229, p. 344.02.

Hoffman, J. L., Nordsieck, K. H., and Fox, G. K. (1998). "Spectropolarimetric Evidence for a Bipolar Flow in beta Lyrae". *The Astronomical Journal* 115, pp. 1576–1591. DOI: `10.1086/300274`.

Hoffman, J. L., Whitney, B. A., and Nordsieck, K. H. (2003). "The Effect of Multiple Scattering on the Polarization from Binary Star Envelopes. I. Self- and Externally Illuminated Disks". *The Astrophysical Journal* 598, pp. 572–587. DOI: `10.1086/378770`.

Hough, J. (2006). "Polarimetry: a powerful diagnostic tool in astronomy". *Astronomy & Geophysics* 47.3. Publisher: Oxford Academic, pp. 3.31–3.35. DOI: `10.1111/j.1468-4004.2006.47331.x`.

Hoyle, F. (1946). “The synthesis of the elements from hydrogen”. *Monthly Notices of the Royal Astronomical Society* 106, p. 343. DOI: `10.1093/mnras/106.5.343`.

Huber, P. J. (1964). “Robust Estimation of a Location Parameter”. *Annals of Mathematical Statistics* 35.1. Publisher: Institute of Mathematical Statistics, pp. 73–101. DOI: `10.1214/aoms/1177703732`.

Hubrig, S., Scholz, K., Hamann, W.-R., Schöller, M., Ignace, R., Ilyin, I., Gayley, K. G., and Oskinova, L. M. (2016). “Searching for a magnetic field in Wolf-Rayet stars using FORS 2 spectropolarimetry”. *Monthly Notices of the Royal Astronomical Society* 458, pp. 3381–3393. DOI: `10.1093/mnras/stw558`.

Huk, L. N. (2017). “Time-Dependent Spectropolarimetric Modeling of Interacting Core Collapse Supernovae”. ISSN: 9780355110982 Journal Abbreviation: Ph.D. Thesis Publication Title: Ph.D. Thesis. PhD thesis.

Ignace, R., Cassinelli, J. P., and Bjorkman, J. E. (1996). “Equatorial Wind Compression Effects across the H-R Diagram”. *The Astrophysical Journal* 459, p. 671. DOI: `10.1086/176932`.

Irwin, J. A. (2007). *Astrophysics: decoding the cosmos*. OCLC: ocm85830856. Chichester, England ; Hoboken, NJ: John Wiley. ISBN: 978-0-470-01305-2.

Isserstedt, J., Moffat, A. F. J., and Niemela, V. S. (1983). “The runaway Wolf-rayet star HD 143414 : evidence for a low-mass companion.” *Astronomy and Astrophysics* 126, p. 183.

Jackson, J. D. (1998). *Classical Electrodynamics, 3rd Edition*. 3rd. Wiley-VCH. ISBN: 0-471-30932-X.

Johnson, R. A., Fullard, A. G., Lomax, J. R., Cooper, K., Leon-Alvarez, D., Hoffman, J. L., and Nordsieck, K. H. (2019). “A Comparison of the Well-constrained Geometry of V444 Cygni and Two Possible Analogs: WR 21 and WR 62a”. *Research Notes of the American Astronomical Society* 3, p. 146. DOI: `10.3847/2515-5172/ab4a12`.

Kasen, D., Nugent, P., Thomas, R. C., and Wang, L. (2004). “Could There Be a Hole in Type Ia Supernovae?” *The Astrophysical Journal* 610, pp. 876–887. DOI: `10.1086/421699`.

Kippenhahn, R. and Weigert, A. (1967). “Entwicklung in engen Doppelsternsystemen I. Massenaustausch vor und nach Beendigung des zentralen Wasserstoff-Brennens”. *Zeitschrift fur Astrophysik* 65, p. 251.

Koenigsberger, G., Schmutz, W., and Skinner, S. L. (2017). “Does the Wolf-Rayet binary CQ Cephei undergo sporadic mass transfer events?” *Astronomy and Astrophysics* 601, A121. DOI: `10.1051/0004-6361/201630360`.

Korhonen, T., Piirola, V., and Reiz, A. (1984). “Polarization Measurements at La-Silla”. *The Messenger* 38, p. 20.

Kurosawa, R., Hillier, D. J., and Pittard, J. M. (2002). “Mass-loss rate determination for the massive binary V444 Cygni using 3-D Monte-Carlo simulations of line and polarization variability”. *Astronomy and Astrophysics* 388, pp. 957–977. DOI: `10.1051/0004-6361:20020443`.

La Chevrotière, A. de, Moffat, A. F. J., and Chené, A.-N. (2011). “Spectroscopic study of the short-period WN5o + O8.5V binary system WR127 (HD 186943)”. *Monthly Notices of the Royal Astronomical Society* 411.1, p. 635. DOI: `10.1111/j.1365-2966.2010.17710.x`.

Lafon, J.-P. J. and Berruyer, N. (1991). “Mass loss mechanisms in evolved stars”. *Astronomy and Astrophysics Review* 2.3-4, p. 249. DOI: `10.1007/BF00872769`.

Lamers, H. J. G. L. M. and Cassinelli, J. P. (1999). *Introduction to Stellar Winds.*

Lamers, H. J. G. L. M., Maeder, A., Schmutz, W., and Cassinelli, J. P. (1991). “Wolf-Rayet stars as starting points or as endpoints of the evolution of massive stars?” *The Astrophysical Journal* 368, pp. 538–544. DOI: `10.1086/169717`.

Lamontagne, R., Moffat, A. F. J., Drissen, L., Robert, C., and Matthews, J. M. (1996). “Photometric Determination of Orbital Inclinations and Mass Loss Rates for Wolf-

Rayet Stars in WR+O Binaries". *The Astronomical Journal* 112, p. 2227. DOI: `10.1086/118175`.

Langer, N. (2012). "Presupernova Evolution of Massive Single and Binary Stars". *Annual Review of Astronomy and Astrophysics* 50.1, pp. 107–164. DOI: `10.1146/annurev-astro-081811-125534`.

Lau, R. M., Hankins, M. J., Schödel, R., Sanchez-Bermudez, J., Moffat, A. F. J., and Ressler, M. E. (2017). "Stagnant Shells in the Vicinity of the Dusty Wolf-Rayet-OB Binary WR 112". *The Astrophysical Journal Letters* 835, p. L31. DOI: `10.3847/2041-8213/835/2/L31`.

Lefèvre, L., Marchenko, S. V., Lépine, S., Moffat, A. F. J., Acker, A., Harries, T. J., Annuk, K., Bohlender, D. A., Demers, H., Grosdidier, Y., Hill, G. M., Morrison, N. D., Knauth, D. C., Skalkowski, G., and Viti, S. (2005). "Spectroscopic study of the long-period dust-producing WC7pd+O9 binary HD 192641". *Monthly Notices of the Royal Astronomical Society* 360.1, p. 141. DOI: `10.1111/j.1365-2966.2005.09017.x`.

Leonard, D. C. (2007). "A Supernova Riddle". *Science* 315.5809. Publisher: American Association for the Advancement of Science Section: Perspective, pp. 193–194. DOI: `10.1126/science.1123373`.

Lomax, J. R., Nazé, Y., Hoffman, J. L., Russell, C. M. P., De Becker, M., Corcoran, M. F., Davidson, J. W., Neilson, H. R., Owocki, S., Pittard, J. M., and Pollock, A. M. T. (2015). "V444 Cygni X-ray and polarimetric variability: Radiative and Coriolis forces shape the wind collision region". *Astronomy and Astrophysics* 573, A43. DOI: `10.1051/0004-6361/201424468`.

Lomax, J. R., Fullard, A. G., Malatesta, M. A., Babler, B., Bednarski, D., Berdis, J. R., Bjorkman, K. S., Bjorkman, J. E., Carciofi, A. C., Davidson Jr., J. W., Keil, M., Meade, M. R., Nordsieck, K., Scheffler, M., Hoffman, J. L., and Wisniewski, J. P. (2017). "The complex circumstellar and circumbinary environment of V356 Sgr". *Monthly Notices of the Royal Astronomical Society* 464, pp. 1936–1947. DOI: `10.1093/mnras/stw2457`.

Lomax, J. R., Hoffman, J. L., Elias II, N. M., Bastien, F. A., and Holenstein, B. D. (2012). “Geometrical Constraints on the Hot Spot in Beta Lyrae”. *The Astrophysical Journal* 750, p. 59. DOI: `10.1088/0004-637X/750/1/59`.

St-Louis, N. (2013). “Revealing the Asymmetry of the Wind of the Variable Wolf-Rayet Star WR1 (HD 4004) through Spectropolarization”. *The Astrophysical Journal* 777.1, p. 9. DOI: `10.1088/0004-637X/777/1/9`.

St-Louis, N., Chené, A.-N., Schnurr, O., and Nicol, M.-H. (2009). “A Systematic Search for Corotating Interaction Regions in Apparently Single Galactic Wolf-Rayet Stars. I. Characterizing the Variability”. *The Astrophysical Journal* 698.2, p. 1951. DOI: `10.1088/0004-637X/698/2/1951`.

St-Louis, N., Moffat, A. F. J., Lapointe, L., Efimov, Y. S., Shakhovskoj, N. M., Fox, G. K., and Piirola, V. (1993). “Polarization Eclipse Model of the Wolf-Rayet Binary V444 Cygni with Constraints on the Stellar Radii and an Estimate of the Wolf-Rayet Mass-Loss Rate”. *The Astrophysical Journal* 410, p. 342. DOI: `10.1086/172751`.

St-Louis, N., Piaulet, C., Richardson, N. D., Shenar, T., Moffat, A. F. J., Eversberg, T., Hill, G. M., Gauza, B., Knapen, J. H., Kubat, J., Kubatova, B., Sablowski, D. P., Simon-Diaz, S., Bolduan, F., Dias, F. M., Dubreuil, P., Fuchs, D., Garrel, T., Grutzeck, G., Hunger, T., Kusters, D., Langenbrink, M., Leadbeater, R., Li, D., Lopez, A., Mauclaire, B., Moldenhawer, T., Potter, M., Santos, E. M. d., Schanne, L., Schmidt, J., Sieske, H., Strachan, J., Stinner, E., Stinner, P., Stober, B., Strandbaek, K., Syder, T., Verilhac, D., Waldschlager, U., Weiss, D., and Wendt, A. (2020). “An extensive spectroscopic time series of three Wolf-Rayet stars – II. A search for wind asymmetries in the dust-forming WC7 binary WR137”. *arXiv:2007.09239 [astro-ph]*. arXiv: 2007.09239.

St-Louis, N., Tremblay, P., and Ignace, R. (2018). “Polarization light curve modelling of corotating interaction regions in the wind of the Wolf–Rayet star WR 6”. *Monthly Notices of the Royal Astronomical Society* 474.2, pp. 1886–1899. DOI: `10.1093/mnras/stx2813`.

St-Louis, N., Drissen, L., Moffat, A. F. J., Bastien, P., and Tapia, S. (1987). “Polarization variability among Wolf-Rayet stars. I. Linear polarization of a complete sample of southern Galactic WC stars”. *The Astrophysical Journal* 322, pp. 870–887. DOI: `10.1086/165782`.

St-Louis, N., Moffat, A. F. J., Drissen, L., Bastien, P., and Robert, C. (1988). “Polarization Variability among Wolf-Rayet Stars. III. A New Way to Derive Mass-Loss Rates for Wolf-Rayet Stars in Binary Systems”. *The Astrophysical Journal* 330, p. 286. DOI: `10.1086/166472`.

Luehrs, S. (1997). “A Colliding-Wind Model for the Wolf-Rayet System HD 152270”. *Publications of the Astronomical Society of the Pacific* 109, p. 504. DOI: `10.1086/133907`.

Maeder, A. and Meynet, G. (2012). “Rotating massive stars: From first stars to gamma ray bursts”. *Reviews of Modern Physics* 84, pp. 25–63. DOI: `10.1103/RevModPhys.84.25`.

Marchenko, S. V., Moffat, A. F. J., Eenens, P. R. J., Cardona, O., Echevarria, J., and Hervieux, Y. (1997). “The Wolf-Rayet Binary V444 Cygni Under the Spectroscopic Microscope. II. Physical Parameters of the Wolf-Rayet Wind and the Zone of Wind Collision”. *The Astrophysical Journal* 485.2, p. 826. DOI: `10.1086/304435`.

Marchenko, S. V., Arias, J., Barbá, R., Balona, L., Moffat, A. F. J., Niemela, V. S., Shara, M. M., and Sterken, C. (2000). “The Puzzle of HD 104994 (WR 46)”. *The Astronomical Journal* 120.4, p. 2101. DOI: `10.1086/301580`.

Marchenko, S. V., Moffat, A. F. J., and Eenens, P. R. J. (1998). “The Wolf-Rayet Binary WR 141 (WN5O + O5 V-III) Revisited”. *Publications of the Astronomical Society of the Pacific* 110.754, p. 1416. DOI: `10.1086/316280`.

Marchenko, S. V., Moffat, A. F. J., and Koenigsberger, G. (1994). “The Wolf-Rayet Binary V444 Cygni under the Spectroscopic Microscope. I. Improved Characteristics of the Components and Their Interaction Seen in He i”. *The Astrophysical Journal* 422, p. 810. DOI: `10.1086/173773`.

Marle, A. J. van, Langer, N., and García-Segura, G. (2005). "Constraints on gamma-ray burst and supernova progenitors through circumstellar absorption lines". *Astronomy and Astrophysics* 444, pp. 837–847. DOI: `10.1051/0004-6361:20053520`.

Massey, P. (1981). "The masses of Wolf-Rayet stars". *The Astrophysical Journal* 246, p. 153. DOI: `10.1086/158908`.

— (1984). "Absolute spectrophotometry of northern Wolf-Rayet stars - How similar are the colors?" *The Astrophysical Journal* 281, pp. 789–799. DOI: `10.1086/162157`.

McLean, I. S., Coyne, G. V., Frecker, S. J. J. E., and Serkowski, K. (1979). "Detection of polarization structure across the emission lines of the Wolf-Rayet star HD 50896." *The Astrophysical Journal* 231, p. L141. DOI: `10.1086/183021`.

Metzger, B. D., Giannios, D., Thompson, T. A., Bucciantini, N., and Quataert, E. (2011). "The protomagnetar model for gamma-ray bursts". *Monthly Notices of the Royal Astronomical Society* 413, pp. 2031–2056. DOI: `10.1111/j.1365-2966.2011.18280.x`.

Meynet, G. and Maeder, A. (2005). "Stellar evolution with rotation. XI. Wolf-Rayet star populations at different metallicities". *Astronomy and Astrophysics* 429, p. 581. DOI: `10.1051/0004-6361:20047106`.

Meynet, G. and Maeder, A. (2017). "Supernovae from Rotating Stars". *Handbook of Supernovae*, p. 601. DOI: `10.1007/978-3-319-21846-5_122`.

Michaux, Y. J. L., Moffat, A. F. J., Chené, A.-N., and St-Louis, N. (2014). "On the origin of variable structures in the winds of hot luminous stars". *Monthly Notices of the Royal Astronomical Society* 440.1, pp. 2–9. DOI: `10.1093/mnras/stt2102`.

Milne, E. A. (1926). "On the possibility of the emission of high-speed atoms from the sun and stars". *Monthly Notices of the Royal Astronomical Society* 86, pp. 459–473. DOI: `10.1093/mnras/86.7.459`.

Moffat, A. F. J., Marchenko, S. V., Bartzakos, P., Niemela, V. S., Cerruti, M. A., Magalhães, A. M., Balona, L., St-Louis, N., Seggewiss, W., and Lamontagne, R. (1998). "The Luminous Eclipsing SMC OB + WN Binary HD 5980 before and during the Recent

LBV-like Outburst: An Extreme Case of Colliding Winds". *The Astrophysical Journal* 497, pp. 896–911. DOI: `10.1086/305475`.

Moffat, A. F. J. and Seggewiss, W. (1977). "The Wolf-Rayet binary theta Muscae." *Astronomy and Astrophysics* 54, p. 607.

Moffat, A. F. J., St-Louis, N., Carlos-Leblanc, D., Richardson, N. D., Pablo, H., and Ramiaramanantsoa, T. (2018). "Wolf-Rayet Stars with BRITE". In: *3rd BRITE Science Conference*. Ed. by G. A. Wade, D. Baade, J. A. Guzik, and R. Smolec. Vol. 8. Auberge du Lac Taureau, QC, Canada: Polish Astronomical Society, pp. 37–42.

Moffat, A. F. J. and Piirola, V. (1993). "Polarization Variability among Wolf-Rayet Stars. VIII. Emission Lines versus Continuum in WR+O Binaries". *The Astrophysical Journal* 413, p. 724. DOI: `10.1086/173040`.

Montier, L., Plaszczynski, S., Levrier, F., Tristram, M., Alina, D., Ristorcelli, I., and Bernard, J.-P. (2015). "Polarization measurement analysis: I. Impact of the full covariance matrix on polarization fraction and angle measurements*". *Astronomy & Astrophysics* 574, A135. DOI: `10.1051/0004-6361/201322271`.

Morel, T., Marchenko, S. V., Eenens, P. R. J., Moffat, A. F. J., Koenigsberger, G., Antokhin, I. I., Eversberg, T., Tovmassian, G. H., Hill, G. M., Cardona, O., and St-Louis, N. (1999). "A 2.3 Day Periodic Variability in the Apparently Single Wolf-Rayet Star WR 134: Collapsed Companion or Rotational Modulation?" *The Astrophysical Journal* 518, pp. 428–441. DOI: `10.1086/307250`.

Motte, F., Bontemps, S., and Louvet, F. (2018). "High-Mass Star and Massive Cluster Formation in the Milky Way". *Annual Review of Astronomy and Astrophysics* 56, pp. 41–82. DOI: `10.1146/annurev-astro-091916-055235`.

Müller, H. (1948). "The foundation of optics". *Journal of the Optical Society of America* A38.661, p. 63.

Munoz, M., Moffat, A. F. J., Hill, G. M., Shenar, T., Richardson, N. D., Pablo, H., St-Louis, N., and Ramiaramanantsoa, T. (2017). "WR 148: identifying the companion of an extreme runaway massive binary¡SUP¿*¡/SUP¿". *Monthly Notices of the Royal Astronomical Society* 467.3, p. 3105. DOI: `10.1093/mnras/stw2283`.

Newville, M., Stensitzki, T., Allen, D. B., and Ingargiola, A. (2014). "LMFIT: Non-Linear Least-Square Minimization and Curve-Fitting for Python". *Zenodo.* DOI: `10.5281/zenodo.11813`.

Niedzielski, A. and Skorzynski, W. (2002). "Kinematical Structure of Wolf-Rayet Winds. I.Terminal Wind Velocity". *Acta Astronomica* 52, p. 81.

Niemela, V. S. and Gamen, R. C. (2000). "The massive Wolf-Rayet binary LSS 1964 (= WR 29)". *Astronomy and Astrophysics* 362, p. 973.

Nordsieck, K. H., Jaehnig, K. P., Burgh, E. B., Kobulnicky, H. A., Percival, J. W., and Smith, M. P. (2003). "Instrumentation for high-resolution spectropolarimetry in the visible and far-ultraviolet". In: *Polarimetry in Astronomy.* Vol. 4843. International Society for Optics and Photonics, pp. 170–179. DOI: `10.1117/12.459288`.

Owocki, S. P., Cranmer, S. R., and Gayley, K. G. (1996). "Inhibition FO Wind Compressed Disk Formation by Nonradial Line-Forces in Rotating Hot-Star Winds". *The Astrophysical Journal Letters* 472. tex.ids: owocki_inhibition_1996, p. L115. DOI: `10.1086/310372`.

Packet, W. (1981). "On the spin-up of the mass accreting component in a close binary system". *Astronomy and Astrophysics* 102, pp. 17–19.

Paczynski, B. (1983). "Models of X-ray bursters with radius expansion". *The Astrophysical Journal* 267, pp. 315–321. DOI: `10.1086/160870`.

Paczyński, B. (1971). "Evolutionary Processes in Close Binary Systems". *Annual Review of Astronomy and Astrophysics* 9, p. 183. DOI: `10.1146/annurev.aa.09.090171.001151`.

Parkin, E. R. and Pittard, J. M. (2008). "A 3D dynamical model of the colliding winds in binary systems". *Monthly Notices of the Royal Astronomical Society* 388.3, p. 1047. DOI: `10.1111/j.1365-2966.2008.13511.x`.

Pauldrach, A., Puls, J., and Kudritzki, R. P. (1986). "Radiation-driven winds of hot luminous stars - Improvements of the theory and first results". *Astronomy and Astrophysics* 164, pp. 86–100.

Petrovic, J., Langer, N., and Hucht, K. A. van der (2005). "Constraining the mass transfer in massive binaries through progenitor evolution models of Wolf-Rayet+O binaries". *Astronomy and Astrophysics* 435, pp. 1013–1030. DOI: `10.1051/0004-6361:20042368`.

Piirola, V. (1973). "A double image chopping polarimeter." *Astronomy and Astrophysics* 27, p. 383.

Piirola, V. (1988). "Simultaneous five-colour (UBVRI) photopolarimeter." *Polarized Radiation of Circumstellar Origin*, p. 735.

Podsiadlowski, P., Joss, P. C., and Hsu, J. J. L. (1992). "Presupernova evolution in massive interacting binaries". *The Astrophysical Journal* 391, pp. 246–264. DOI: `10.1086/171341`.

Poe, C. H., Friend, D. B., and Cassinelli, J. P. (1989). "A Rotating, Magnetic, Radiation-driven Wind Model for Wolf-Rayet Stars". *The Astrophysical Journal* 337, p. 888. DOI: `10.1086/167159`.

Potter, S. B., Nordsieck, K., Romero-Colmenero, E., Crawford, S., Vaisanen, P., Depagne, É., Buckley, D., Koeslag, A., Brink, J., Hetlage, C., Browne, K., Crause, L., Schier, A., and Allington, J. (2016). "Commissioning the polarimetric modes of the Robert Stobie spectrograph on the Southern African Large Telescope". In: *Proc. SPIE.* Vol. 9908. Society of Photo-Optical Instrumentation Engineers (SPIE) Conference Series, 99082K. DOI: `10.1117/12.2232391`.

Pourbaix, D., Tokovinin, A. A., Batten, A. H., Fekel, F. C., Hartkopf, W. I., Levato, H., Morrell, N. I., Torres, G., and Udry, S. (2004). "SB9: The ninth catalogue of spectroscopic binary orbits". *Astronomy and Astrophysics* 424, pp. 727–732. DOI: `10.1051/0004-6361:20041213`.

Quirrenbach, A., Bjorkman, K. S., Bjorkman, J. E., Hummel, C. A., Buscher, D. F., Armstrong, J. T., Mozurkewich, D., Elias N. M., I., and Babler, B. L. (1997). "Constraints on the Geometry of Circumstellar Envelopes: Optical Interferometric and Spectropolarimetric Observations of Seven Be Stars". *ApJ* 479.1, pp. 477–496. DOI: `10.1086/303854`.

Ramiaramanantsoa, T., Ignace, R., Moffat, A. F. J., St-Louis, N., Shkolnik, E. L., Popowicz, A., Kuschnig, R., Pigulski, A., Wade, G. A., Handler, G., Pablo, H., and Zwintz, K. (2019). "The chaotic wind of WR 40 as probed by BRITE*". *Monthly Notices of the Royal Astronomical Society*, p. 2491. DOI: `10.1093/mnras/stz2895`.

Ramiaramanantsoa, T., Ratnasingam, R., Shenar, T., Moffat, A. F. J., Rogers, T. M., Popowicz, A., Kuschnig, R., Pigulski, A., Handler, G., Wade, G. A., Zwintz, K., and Weiss, W. W. (2018). "A BRITE view on the massive O-type supergiant V973 Scorpii: hints towards internal gravity waves or sub-surface convection zones". *Monthly Notices of the Royal Astronomical Society* 480.1, p. 972. DOI: `10.1093/mnras/sty1897`.

Reeve, D. and Howarth, I. D. (2018). "Are the O stars in WR+O binaries exceptionally rapid rotators?" *Monthly Notices of the Royal Astronomical Society* 478, pp. 3133–3137. DOI: `10.1093/mnras/sty1296`.

Repolust, T., Puls, J., and Herrero, A. (2004). "Stellar and wind parameters of Galactic O-stars. The influence of line-blocking/blanketing". *Astronomy and Astrophysics* 415, pp. 349–376. DOI: `10.1051/0004-6361:20034594`.

Robert, C., Moffat, A. F. J., Bastien, P., Drissen, L., and St-Louis, N. (1989). "Polarization Variability among Wolf-Rayet Stars. V. Linear Polarization of the Bright Cygnus Stars and an Anticorrelation of Variability with Wind Speed". *The Astrophysical Journal* 347, p. 1034. DOI: `10.1086/168194`.

Robert, C., Moffat, A. F. J., Drissen, L., Lamontagne, R., Seggewiss, W., Niemela, V. S., Cerruti, M. A., Barrett, P., Bailey, J., Garcia, J., and Tapia, S. (1992). "Photometry, Polarimetry, Spectroscopy, and Spectropolarimetry of the Enigmatic Wolf-Rayet Star EZ Canis Majoris". *The Astrophysical Journal* 397, p. 277. DOI: `10.1086/171786`.

Robitaille, T. P. (2011). "HYPERION: an open-source parallelized three-dimensional dust continuum radiative transfer code". *Astronomy & Astrophysics* 536. Publisher: EDP Sciences, A79. DOI: `10.1051/0004-6361/201117150`.

Rybicki, G. B. and Lightman, A. P. (1986). *Radiative Processes in Astrophysics.* ISBN: 9780471827597 Num Pages: 400. Wiley-VCH. ISBN: 0-471-82759-2.

Sana, H., Mink, S. E. de, Koter, A. de, Langer, N., Evans, C. J., Gieles, M., Gosset, E., Izzard, R. G., Le Bouquin, J.-B., and Schneider, F. R. N. (2012). "Binary Interaction Dominates the Evolution of Massive Stars". *Science* 337.6093, p. 444. DOI: `10.1126/science.1223344`.

Sander, A. A. C., Hamann, W.-R., Todt, H., Hainich, R., Shenar, T., Ramachandran, V., and Oskinova, L. M. (2019). "The Galactic WC and WO stars: The impact of revised distances from Gaia DR2 and their role as massive black hole progenitors". *Astronomy & Astrophysics* 621. arXiv: 1807.04293, A92. DOI: `10.1051/0004-6361/201833712`.

Sander, A. A. C., Vink, J. S., and Hamann, W.-R. (2020). "Driving classical Wolf-Rayet winds: a Γ- and Z-dependent mass-loss". *Monthly Notices of the Royal Astronomical Society* 491, pp. 4406–4425. DOI: `10.1093/mnras/stz3064`.

Schmutz, W., Hamann, W.-R., and Wessolowski, U. (1989). "Spectral analysis of 30 Wolf-Rayet stars". *Astronomy and Astrophysics* 210, pp. 236–248.

Schmutz, W. and Koenigsberger, G. (2019). "Long uninterrupted photometric observations of the Wolf-Rayet star EZ CMa by the Toronto BRITE satellite reveal a very fast apsidal motion". *Astronomy and Astrophysics* 624, p. L3. DOI: `10.1051/0004-6361/201935094`.

Schnurr, O., Casoli, J., Chené, A.-N., Moffat, A. F. J., and St-Louis, N. (2008). "The very massive binary NGC 3603-A1". *Monthly Notices of the Royal Astronomical Society: Letters* 389.1, pp. L38–L42. DOI: `10.1111/j.1745-3933.2008.00517.x`.

Schulte-Ladbeck, R. E., Nordsieck, K. H., Taylor, M., Nook, M. A., Bjorkman, K. S., Magalhaes, A. M., and Anderson, C. M. (1991). "On the Wind Geometry of the Wolf-Rayet Star EZ Canis Majoris". *The Astrophysical Journal* 382, p. 301. DOI: `10.1086/170717`.

Serkowski, K., Mathewson, D. S., and Ford, V. L. (1975). “Wavelength dependence of interstellar polarization and ratio of total to selective extinction”. *The Astrophysical Journal* 196, pp. 261–290. DOI: `10.1086/153410`.

Shara, M. M., Crawford, S. M., Vanbeveren, D., Moffat, A. F. J., Zurek, D., and Crause, L. (2017). “The spin rates of O stars in WR + O binaries – I. Motivation, methodology, and first results from SALT”. *Monthly Notices of the Royal Astronomical Society* 464.2, pp. 2066–2074. DOI: `10.1093/mnras/stw2450`.

Shenar, T., Hamann, W.-R., and Todt, H. (2014). “The impact of rotation on the line profiles of Wolf-Rayet stars”. *Astronomy and Astrophysics* 562, A118. DOI: `10.1051/0004-6361/201322496`.

Shenar, T., Sablowski, D. P., Hainich, R., Todt, H., Moffat, A. F. J., Oskinova, L. M., Ramachandran, V., Sana, H., Sander, A. A. C., Schnurr, O., St-Louis, N., Vanbeveren, D., Goetberg, Y., and Hamann, W.-R. (2019). “The Wolf-Rayet binaries of the nitrogen sequence in the Large Magellanic Cloud: spectroscopy, orbital analysis, formation, and evolution”. *arXiv:1905.09296 [astro-ph]*. arXiv: 1905.09296.

Shrestha, M., Neilson, H. R., Hoffman, J. L., and Ignace, R. (2018). “Polarization simulations of stellar wind bow-shock nebulae - I. The case of electron scattering”. *Monthly Notices of the Royal Astronomical Society* 477.1, p. 1365. DOI: `10.1093/mnras/sty724`.

Simmons, J. F. L., Aspin, C., and Brown, J. C. (1982). “Bias of polarimetric estimators for binary star inclinations”. *Monthly Notices of the Royal Astronomical Society* 198, pp. 45–57. DOI: `10.1093/mnras/198.1.45`.

Simmons, J. F. L. and Boyle, C. B. (1984). “Interpretation of the variable linear polarization of X-ray transientAO 538-66.” *Astronomy and Astrophysics* 134, p. 368.

Smartt, S. J. (2015). “Observational Constraints on the Progenitors of Core-Collapse Supernovae: The Case for Missing High-Mass Stars”. *Publications of the Astronomical Society of Australia* 32, e016. DOI: `10.1017/pasa.2015.17`.

Smartt, S. J. (2009). "Progenitors of Core-Collapse Supernovae". *Annual Review of Astronomy and Astrophysics* 47.1, p. 63. DOI: `10.1146/annurev-astro-082708-101737`.

Smith, L. F. (1968). "A revised spectral classification system and a new catalogue for galactic Wolf-Rayet stars". *Monthly Notices of the Royal Astronomical Society* 138, p. 109. DOI: `10.1093/mnras/138.1.109`.

Smith, N. (2014). "Mass Loss: Its Effect on the Evolution and Fate of High-Mass Stars". *Annual Review of Astronomy and Astrophysics* 52.1, pp. 487–528. DOI: `10.1146/annurev-astro-081913-040025`.

— (2017). "Luminous blue variables and the fates of very massive stars". *Philosophical Transactions of the Royal Society of London Series A* 375.2105, p. 20160268. DOI: `10.1098/rsta.2016.0268`.

Smith, N. and Conti, P. S. (2008). "On the Role of the WNH Phase in the Evolution of Very Massive Stars: Enabling the LBV Instability with Feedback". *The Astrophysical Journal* 679, pp. 1467–1477. DOI: `10.1086/586885`.

Smith, N., Götberg, Y., and Mink, S. E. de (2018). "Extreme isolation of WN3/O3 stars and implications for their evolutionary origin as the elusive stripped binaries". *Monthly Notices of the Royal Astronomical Society* 475, pp. 772–782. DOI: `10.1093/mnras/stx3181`.

Smith, N., Li, W., Filippenko, A. V., and Chornock, R. (2011). "Observed fractions of core-collapse supernova types and initial masses of their single and binary progenitor stars". *Monthly Notices of the Royal Astronomical Society* 412, pp. 1522–1538. DOI: `10.1111/j.1365-2966.2011.17229.x`.

Stevance, H. F., Ignace, R., Crowther, P. A., Maund, J. R., Davies, B., and Rate, G. (2018). "Probing the rotational velocity of Galactic WO stars with spectropolarimetry". *Monthly Notices of the Royal Astronomical Society* 479.4, pp. 4535–4543. DOI: `10.1093/mnras/sty1827`.

Stevens, I. R., Blondin, J. M., and Pollock, A. M. T. (1992). "Colliding Winds from Early-Type Stars in Binary Systems". *The Astrophysical Journal* 386, p. 265. DOI: `10.1086/171013`.

Stokes, G. G. (1851). "On the Composition and Resolution of Streams of Polarized Light from different Sources". *Transactions of the Cambridge Philosophical Society* 9, p. 399.

Sukhbold, T. and Woosley, S. E. (2016). "The Most Luminous Supernovae". *The Astrophysical Journal Letters* 820, p. L38. DOI: `10.3847/2041-8205/820/2/L38`.

Tigé, J., Motte, F., Russeil, D., Zavagno, A., Hennemann, M., Schneider, N., Hill, T., Nguyen Luong, Q., Di Francesco, J., Bontemps, S., Louvet, F., Didelon, P., Könyves, V., André, P., Leuleu, G., Bardagi, J., Anderson, L. D., Arzoumanian, D., Benedettini, M., Bernard, J.-P., Elia, D., Figueira, M., Kirk, J., Martin, P. G., Minier, V., Molinari, S., Nony, T., Persi, P., Pezzuto, S., Polychroni, D., Rayner, T., Rivera-Ingraham, A., Roussel, H., Rygl, K., Spinoglio, L., and White, G. J. (2017). "The earliest phases of high-mass star formation, as seen in NGC 6334 by Herschel-HOBYS". *Astronomy and Astrophysics* 602, A77. DOI: `10.1051/0004-6361/201628989`.

Todt, H., Sander, A., Hainich, R., Hamann, W. .-.-R., Quade, M., and Shenar, T. (2015). "Potsdam Wolf-Rayet model atmosphere grids for WN stars". *Astronomy and Astrophysics* 579, A75. DOI: `10.1051/0004-6361/201526253`.

Tramper, F., Straal, S. M., Sanyal, D., Sana, H., Koter, A. de, Gräfener, G., Langer, N., Vink, J. S., Mink, S. E. de, and Kaper, L. (2015). "Massive stars on the verge of exploding: the properties of oxygen sequence Wolf-Rayet stars". *Astronomy and Astrophysics* 581, A110. DOI: `10.1051/0004-6361/201425390`.

Underhill, A. B. and Hill, G. M. (1994). "A Study of the Moderately Wide Wolf-Rayet Spectroscopic Binary HD 190918". *The Astrophysical Journal* 432, p. 770. DOI: `10.1086/174615`.

Van Der Hucht, K. A. (2001a). "The VIIth catalogue of galactic Wolf-Rayet stars". *New Astronomy Reviews* 45.3, p. 135. DOI: `10.1016/S1387-6473(00)00112-3`.

Van Der Hucht, K. A. (2001b). "The VIIth catalogue of galactic Wolf-Rayet stars". *New Astronomy Reviews* 45.3, p. 135. DOI: `10.1016/S1387-6473(00)00112-3`.

— (2006). "New Galactic Wolf-Rayet stars, and candidates. An annex to The VIIth Catalogue of Galactic Wolf-Rayet Stars". *Astronomy and Astrophysics* 458.2, p. 453. DOI: `10.1051/0004-6361:20065819`.

Vanbeveren, D. and Conti, P. S. (1980). "On the binary frequency distribution and evolution of Wolf-Rayet stars ." *Astronomy and Astrophysics* 88, p. 230.

Vanbeveren, D., Mennekens, N., Shara, M. M., and Moffat, A. F. J. (2018). "Spin rates and spin evolution of O components in WR+O binaries". *Astronomy & Astrophysics* 615, A65. DOI: `10.1051/0004-6361/201732212`.

Villar-Sbaffi, A., St-Louis, N., Moffat, A. F. J., and Piirola, V. (2005). "First Ever Polarimetric Detection of a Wind-Wind Interaction Region and a Misaligned Flattening of the Wind in the Wolf-Rayet Binary CQ Cephei". *The Astrophysical Journal* 623, pp. 1092–1104. DOI: `10.1086/428830`.

— (2006). "An Extreme Case of a Misaligned Highly Flattened Wind in the Wolf-Rayet Binary CX Cephei". *ApJ* 640.2, pp. 995–1004. DOI: `10.1086/499224`. arXiv: `astro-ph/0507616 [astro-ph]`.

Vink, J. S., Gräfener, G., and Harries, T. J. (2011). "In pursuit of gamma-ray burst progenitors: the identification of a sub-population of rotating Wolf-Rayet stars". *Astronomy and Astrophysics* 536, p. L10. DOI: `10.1051/0004-6361/201118197`.

Vink, J. S. and Harries, T. J. (2017a). "Wolf-Rayet spin at low metallicity and its implication for black hole formation channels". *Astronomy and Astrophysics* 603, A120. DOI: `10.1051/0004-6361/201730503`.

— (2017b). "Wolf-Rayet spin at low metallicity and its implication for black hole formation channels". *A&A* 603, A120, A120. DOI: `10.1051/0004-6361/201730503`. arXiv: `1703.09857 [astro-ph.SR]`.

Wang, L. and Wheeler, J. C. (2008). “Spectropolarimetry of Supernovae”. *Annual Review of Astronomy and Astrophysics* 46, pp. 433–474. DOI: `10.1146/annurev.astro.46.060407.145139`.

Wardle, J. F. C. and Kronberg, P. P. (1974). “The linear polarization of quasi-stellar radio sources at 3.71 and 11.1 centimeters”. *The Astrophysical Journal* 194, pp. 249–255. DOI: `10.1086/153240`.

Whitney, B. A. (2011). “Monte Carlo radiative transfer”. *Bulletin of the Astronomical Society of India* 39, pp. 101–127.

Whittet, D. C. B., Martin, P. G., Hough, J. H., Rouse, M. F., Bailey, J. A., and Axon, D. J. (1992). “Systematic Variations in the Wavelength Dependence of Interstellar Linear Polarization”. *The Astrophysical Journal* 386, p. 562. DOI: `10.1086/171039`.

Wilking, B. A., Lebofsky, M. J., Kemp, J. C., Martin, P. G., and Rieke, G. H. (1980). “The wavelength dependence of interstellar linear polarization”. *The Astrophysical Journal* 235, pp. 905–910. DOI: `10.1086/157694`.

Williams, P. M. (2014). “Eclipses and dust formation by WC9 type Wolf-Rayet stars”. *Monthly Notices of the Royal Astronomical Society* 445.2, p. 1253. DOI: `10.1093/mnras/stu1779`.

— (2019). “Variable dust emission by WC type Wolf-Rayet stars observed in the NEOWISE-R survey”. *Monthly Notices of the Royal Astronomical Society* 488.1, p. 1282. DOI: `10.1093/mnras/stz1784`.

Wolf, C. J. E. and Rayet, G. (1867). “Spectroscopie stellaire”. *Academie des Sciences Paris Comptes Rendus* 65, pp. 292–296.

Wolinski, K. G. and Dolan, J. F. (1994). “Confidence intervals for orbital parameters determined polarimetrically .” *Monthly Notices of the Royal Astronomical Society* 267, p. 5. DOI: `10.1093/mnras/267.1.5`.

Wood, K., Bjorkman, J. E., Whitney, B. A., and Code, A. D. (1996a). “The Effect of Multiple Scattering on the Polarization from Axisymmetric Circumstellar Envelopes.

I. Pure Thomson Scattering Envelopes". *The Astrophysical Journal* 461, p. 828. DOI: `10.1086/177105`.

Wood, K., Bjorkman, J. E., Whitney, B., and Code, A. (1996b). "The Effect of Multiple Scattering on the Polarization from Axisymmetric Circumstellar Envelopes. II. Thomson Scattering in the Presence of Absorptive Opacity Sources". *ApJ* 461, p. 847. DOI: `10.1086/177106`.

— (1996c). "The Effect of Multiple Scattering on the Polarization from Axisymmetric Circumstellar Envelopes. II. Thomson Scattering in the Presence of Absorptive Opacity Sources". *The Astrophysical Journal* 461, p. 847. DOI: `10.1086/177106`.

Woosley, S. E. (1993). "Gamma-ray bursts from stellar mass accretion disks around black holes". *The Astrophysical Journal* 405, pp. 273–277. DOI: `10.1086/172359`.

Woosley, S. E. and Bloom, J. S. (2006). "The Supernova Gamma-Ray Burst Connection". *Annual Review of Astronomy and Astrophysics* 44.1, p. 507. DOI: `10.1146/annurev.astro.43.072103.150558`.

Woosley, S. E. and Heger, A. (2006). "The Progenitor Stars of Gamma-Ray Bursts". *The Astrophysical Journal* 637.2. tex.ids: woosley_progenitor_2006-1, p. 914. DOI: `10.1086/498500`.

Woosley, S. E., Langer, N., and Weaver, T. A. (1993). "The evolution of massive stars including mass loss - Presupernova models and explosion". *The Astrophysical Journal* 411, pp. 823–839. DOI: `10.1086/172886`.

Appendix A

Appendices

A.1 Radiative transfer

A brief overview of radiative transfer is given to aid the reader in understanding WR star winds and MCRT. The classic equation of radiative transfer is:

$$\frac{dI_\nu}{d\tau_\nu} = I_\nu - S_\nu \tag{A.1}$$

where I_ν is the incident intensity at frequency ν, τ_ν is the optical depth at frequency ν and S_ν is the source function, which is the ratio of emission to absorption in a given material (Irwin 2007). The infinitesimal optical depth $d\tau_\nu$ is defined as the mass absorption coefficient κ_ν in a path length dr with mass density ρ, i.e., $d\tau_\nu = -\kappa_\nu \rho dr$. The negative sign reflects the fact that τ and r increase in opposite directions. This can also be written as $d\tau = -\sigma n dr$, where σ is the scattering cross-section and n is the number density of scattering particles. In the case of electron (Thomson) scattering, the cross-section is $\sigma_T = 6.65 \times 10^{-25}$ cm^2, a quantity derived from the classical electron radius; σ_T is independent of wavelength for photon energies less than the electron rest mass, 0.511 MeV (Rybicki and Lightman 1986).

The total electron-scattering optical depth τ is found by integrating over distance along the path length l:

$$\tau = -\int_{l}^{0} \sigma_T n dr = \sigma_T n l. \tag{A.2}$$

Optical depth can be interpreted as the average number of mean free paths (i.e. paths with no interaction) traveled by a photon through a scattering or absorbing material. If $\tau_\nu < 1$, the material is optically thin because the probability that a photon will be absorbed or scattered is less than 1. The optically thick case occurs when $\tau_\nu > 1$.

Solving the radiative transfer equation is generally very difficult, but the assumption of local thermodynamic equilibrium (LTE) can be used to simplify the solution. In LTE, a specific size scale is chosen in which thermodynamic equilibrium holds, i.e. the radiation field at the chosen scale is the same as the kinetic temperature of the gas particles in the volume. This means that Equation A.1 can be solved as

$$I_\nu = I_{\nu 0} e^{-\tau_\nu} + B_\nu(\mathrm{T})(1 - e^{-\tau_\nu}), \tag{A.3}$$

where $I_{\nu 0}$ is the background intensity and $B_\nu(\mathrm{T})$ is the Planck function at temperature T. LTE is not the case for stellar winds, where the equations of statistical equilibrium must be solved for each atomic energy level (Hillier 2011).

All of the above quantities are frequency-dependent in general. However, it is useful to define a frequency-averaged optical depth for optically thick emission when $\tau_\nu >> 1$ (i.e. $I_\nu = B_\nu(\mathrm{T})$). In this case, the frequency-weighted Rosseland mean opacity $\overline{\kappa_R}$ can be used to calculate the optical depth, resulting in a Rosseland mean optical depth $d\tau_{\mathrm{Ross}} = -\overline{\kappa_R}\rho dr$ (Rybicki and Lightman 1986).

A.2 Line formation

Spectral lines, observed features that produce an intensity maximum or minimum at a specific wavelength, can reveal the ionization levels of atoms in a gas. They can be observed in emission, where the line intensity is greater than the continuum intensity, or absorption, the opposite case. Emission lines are observed when the blackbody temperature intensity $B_\nu(T)$ of the emitter is greater than the intensity of the continuum source I_ν, and vice versa for absorption lines (Irwin 2007). The physical processes that produce lines include bound-bound, bound-free, free-bound, and free-free interactions between electrons and atomic nuclei.

This dissertation is focused on optical observations of WR stars, so the dominant line formation processes in this wavelength range (4000 - 7500 Å for RSS/SALT; see Section 1.6) are bound-bound (electron energy level) transitions (Hillier 2011). Bound-bound emission occurs when an electron moves from a higher energy state to a lower energy state while remaining captured by the atomic nucleus. Because of the quantization of atomic energy levels, this process emits a photon at a defined frequency based on the particular levels and atomic state (Irwin 2007). In a fully ionized gas, this process can only occur after a free electron recombines with a nucleus or ion (free-bound interaction), which gives rise to the term “recombination lines” for these emission features. Note that the free-bound interaction produces a continuum of photons because a free electron can have, in principle, any energy before it recombines with a nucleus or ion. The rate of recombination N_r is integral to this process; it is defined by

$$N_r = n_e n_p \alpha_r V \tag{A.4}$$

where n_e and n_p are the electron and proton density respectively, V is the volume of the ionized region, and α_r is the total recombination coefficient (Irwin 2007).

A.3 Massive star wind structure

The basic model for the velocity structure of stellar winds of massive stars is the CAK theory, named for Castor, Abbott, and Klein (1975). In this model, optically thick lines provide radiative acceleration by absorbing photon momentum (Milne 1926). The CAK formulation relies on a single-scattering limit because there can be a maximum of c/v_∞ thick lines, where v_∞ is the terminal wind velocity (i.e. v at infinite radius). This limit is given by

$$\dot{M} v_\infty \leq L/c, \tag{A.5}$$

where $\dot{M}$ is the mass-loss rate and L is the stellar luminosity. CAK developed a solution for the velocity as a function of radius:

$$v \frac{dv}{dr} = v_\infty (1 - \frac{R_*}{r})^\beta, \tag{A.6}$$

where r is the distance from the stellar surface and β is a dimensionless constant. For O stars, $\beta = 0.8$ (Pauldrach, Puls, and Kudritzki 1986). CAK has been modified by a number of authors since Castor, Abbott, and Klein (1975). These modified versions have improved the theory's match to observed O star winds (Friend and Abbott 1986; Pauldrach, Puls, and Kudritzki 1986). Figure A.1, taken from Pauldrach, Puls, and Kudritzki (1986), shows the velocity and density structure of an O star wind as an example comparing CAK and modified CAK. For an in-depth discussion of wind driving by lines, see Chapter 8 of Lamers and Cassinelli (1999).

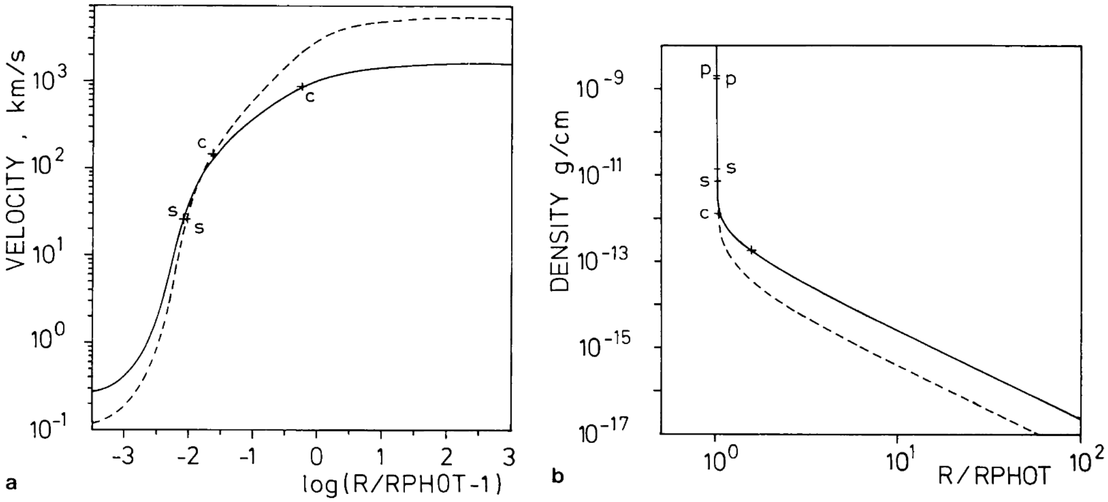

Figure A.1: O star wind velocity and density structure from Pauldrach, Puls, and Kudritzki (1986). RPHOT is the photospheric radius. C, S and P label important points in the wind relevant to the discussion in Pauldrach, Puls, and Kudritzki (1986). The dashed line is basic CAK theory (equation A.6), while the solid line is the modified CAK theory from Pauldrach, Puls, and Kudritzki (1986).

A.4 RSS instrumental signal fitting code

```
#!/usr/bin/env python
# coding: utf-8

# Imports

# In[ ]:



import seaborn as sns
import numpy as np
import scipy as sp
import matplotlib.pyplot as plt
from astropy.io import ascii
import astropy.io.fits as fits
import polTools
import glob
import lmfit
import xarray as xr



# Seaborn
```

```
# In[ ]:


sns.set()
sns.set_style("white")
sns.set_context("paper", font_scale=1.0)
sns.set_style("ticks")

filePattern = '/*.fits'


# Function defs

# In[ ]:


def viewstokes(stokes_Sw,err2_Sw,ok_w=[True],tcenter=0.):
    """Compute normalized stokes parameters, converts Q-U to P-T, for viewing
    Parameters
    ----------
    stokes_Sw: 2d float nparray(stokes,wavelength bin)
       unnormalized stokes parameters vs wavelength
    var_Sw: 2d float nparray(stokes,wavelength bin)
       variance for stokes_sw
    ok_w: 1d boolean nparray(stokes,wavelength bin)
       marking good stokes values. default all ok.
    Output: normalized stokes parameters and errors, linear stokes converted to pol %, PA
       Ignore covariance.  Assume binned first if necessary.
    """
    stokess,wavs = stokes_Sw.shape
    stokes_vw = np.zeros((stokess-1,wavs))
    err_vw = np.zeros((stokess-1,wavs))
    if (len(ok_w) == 1): ok_w = np.ones(wavs,dtype=bool)

    stokes_vw[:,ok_w] = 100.*stokes_Sw[1:,ok_w]/stokes_Sw[0,ok_w]                # in
    ↪  percent
    err_vw[:,ok_w] = 100.*np.sqrt(err2_Sw[1:stokess,ok_w])/stokes_Sw[0,ok_w]      # error
    ↪  bar ignores covariance

    if (stokess >2):
        stokesP_w = np.zeros((wavs))
        stokesT_w = np.zeros((wavs))
        varP_w = np.zeros((wavs))
        varT_w = np.zeros((wavs))
```

```
        varpe_dw = np.zeros((2,wavs))
        varpt_w = np.zeros((wavs))
        # unnormalized linear polarization
        stokesP_w[ok_w] = np.sqrt(stokes_Sw[1,ok_w]**2 + stokes_Sw[2,ok_w]**2)
        # PA in radians
        stokesT_w[ok_w] = (0.5*np.arctan2(stokes_Sw[2,ok_w],stokes_Sw[1,ok_w]))
        # optimal PA folding
        stokesT_w[ok_w] = (stokesT_w[ok_w]-(tcenter+np.pi/2.)+np.pi) % np.pi +
        ↪  (tcenter-np.pi/2.)
     # variance matrix eigenvalues, ellipse orientation
        varpe_dw[:,ok_w] = 0.5*(err2_Sw[1,ok_w]+err2_Sw[2,ok_w]
        ↪  + np.array([1,-1])[:,None]*np.sqrt((err2_Sw[1,ok_w]-err2_Sw[2,ok_w])**2 +
        ↪  4*err2_Sw[-1,ok_w]**2))
        varpt_w[ok_w] = 0.5*np.arctan2(2.*err2_Sw[-1,ok_w],err2_Sw[1,ok_w]-err2_Sw[2,ok_w])
     # linear polarization variance along p, PA
        varP_w[ok_w] = varpe_dw[0,ok_w]*(np.cos(2.*stokesT_w[ok_w]-varpt_w[ok_w]))**2
        ↪  + varpe_dw[1,ok_w]*(np.sin(2.*stokesT_w[ok_w]-varpt_w[ok_w]))**2
        varT_w[ok_w] = varpe_dw[0,ok_w]*(np.sin(2.*stokesT_w[ok_w]-varpt_w[ok_w]))**2
        ↪  + varpe_dw[1,ok_w]*(np.cos(2.*stokesT_w[ok_w]-varpt_w[ok_w]))**2

        stokes_vw[0,ok_w] = 100*stokesP_w[ok_w]/stokes_Sw[0,ok_w]                  #
        ↪  normalized % linear polarization
        err_vw[0,ok_w] =  100*np.sqrt(err2_Sw[1,ok_w])/stokes_Sw[0,ok_w]
        stokes_vw[1,ok_w] = np.degrees(stokesT_w[ok_w])                            # PA in
        ↪  degrees
        err_vw[1,ok_w] =  0.5*np.degrees(np.sqrt(err2_Sw[2,ok_w])/stokesP_w[ok_w])

    return stokes_vw,err_vw

def binDataAngstrom(wave, stokes, goodData, error, binSize=10):
    binWavelength = (wave / binSize-0.5).astype(int) - int((wave / binSize-0.5).min())
    Bins = binWavelength.max()
    binWavelength[~goodData[1]] = -1

    stokesShape, empty = stokes.shape

    binArray = np.arange(Bins)
    binArrayOk = (binArray[:,None] == binWavelength[None,:])
    stokesBinned = (stokes[:,None,:] * binArrayOk).sum(axis=2)
    errorBinned = ((error[:stokesShape,None,:] + 2. * covar[:,None,:]) *
    ↪  binArrayOk).sum(axis=2)
    wavelengthBinned = (wave[None,:] * binArrayOk).sum(axis=1) / binArrayOk.sum(axis=1)

    return stokesBinned, errorBinned, wavelengthBinned
```

```
def binDataError(wave, stokes, goodData, error, covar, bpm_Sw, binError=0.01):
    allowedgap = 5

    wgap0_g = np.where((bpm_Sw[0,:-1]==0) & (bpm_Sw[0,1:]!=0))[0] + 1
    wgap1_g = np.where((bpm_Sw[0,wgap0_g[0]:-1]!=0) & (bpm_Sw[0,wgap0_g[0]+1:]==0))[0]
    ↪  +  wgap0_g[0] + 1
    wgap0_g = wgap0_g[0:wgap1_g.shape[0]]

    isbad_g = ((wgap1_g - wgap0_g) > allowedgap)

    stokes_sw, err_sw = viewstokes(stokes, error, ok_w=goodData,tcenter=np.pi/2)

    binvar_w = err_sw[0]**2
    bincovar_w = np.zeros_like(binvar_w)
    bincovar_w[goodData] = binvar_w[goodData]*covar[1,goodData]/error[1,goodData]

    ww = -1
    b = 0
    binWavelength = -1*np.ones((wavs))

    while (bpm_Sw[0,ww+1:]==0).sum() > 0:

        w = ww+1+np.where(bpm_Sw[0,ww+1:]==0)[0][0]

        cumsvar_W = np.cumsum((binvar_w[w:]+2.*bincovar_w[w:])*(bpm_Sw[0,w:]==0))
        ↪  /np.cumsum((bpm_Sw[0,w:]==0))**2

        err_W = np.sqrt(cumsvar_W)
        ww = wavs                                       # stopping point override: end

        nextbadgap = np.where(isbad_g & (wgap0_g > w))[0]

        if nextbadgap.size: ww = wgap0_g[nextbadgap[0]] - 1   # stopping point override:
        ↪  before bad gap

        dw = np.where(err_W[:ww-w] < binError)[0]

        if dw.size: ww = w + dw[0]                      # err goal is reached first

        binWavelength[w:ww+1] = b
        b += 1

    binWavelength[bpm_Sw[0]>0] = -1
    Bins  = b
```

```
    stokesShape, empty = stokes.shape

    binArray = np.arange(Bins)
    binArrayOk = (binArray[:,None] == binWavelength[None,:])
    stokesBinned = (stokes[:,None,:]*binArrayOk).sum(axis=2)
    errorBinned = ((error[:stokesShape,None,:] +
    ↪  2.*covar[:,None,:])*binArrayOk).sum(axis=2)
    wavelengthBinned = (wave[None,:]*binArrayOk).sum(axis=1)/binArrayOk.sum(axis=1)

    return stokesBinned, errorBinned, wavelengthBinned


# In[ ]:


def fileLoad(folder):
    '''Loads a fits file'''
    dataFile = glob.glob(folder+filePattern)

    #Open fits file
    with fits.open(dataFile[0]) as hdul:

       # stokes I, Q, U values in [0, :], [1, :], [2, :]
        stokesSw = hdul['SCI'].data[:,0,:]
        #stokes errors (I, Q, U)
        varSw = hdul['VAR'].data[:,0,:]
        covarSw = hdul['COV'].data[:,0,:]
        deltaWave = float(hdul['SCI'].header['CDELT1'])
        #get starting wavelength
        wave0 = float(hdul['SCI'].header['CRVAL1'])
        #get wavelength axis size
        waves = int(hdul['SCI'].header['NAXIS1'])

        bpm_Sw = hdul['BPM'].data[:,0,:]
        ok_Sw = (bpm_Sw==0)

        wavelengths = wave0 + deltaWave*np.arange(waves)

        return stokesSw, varSw, covarSw, wavelengths, ok_Sw, bpm_Sw

def fileWrite(folder, stokesSw):
    '''Loads a fits file'''
    dataFile = glob.glob(folder+filePattern)

    #Open fits file
```

```
    with fits.open(dataFile[0]) as hdul:

        # stokes I, Q, U values in [0, :], [1, :], [2, :]
        hdul['SCI'].data[:,0,:] = stokesSw

        hdul.writeto(dataFile[0]+"_ripple_removed")

        return

def readData(fileName):
    data = []
    dataError = []
    dataCovar = []
    dataWave = []
    dataOk = []
    dataBPM = []

    #folder = "F:/Andrew's Dropbox/Dropbox/"
    folder = ""
    fileNameTotal = folder + fileName

    folderList = glob.glob(fileNameTotal)

    for folder in folderList:
        print(folder)
        stokes, stokesError, stokesCovar, waves, ok, bpm = fileLoad(folder)
        data.append(stokes)
        dataError.append(stokesError)
        dataCovar.append(stokesCovar)
        dataWave.append(waves)
        dataOk.append(ok)
        dataBPM.append(bpm)

    return data, dataError, dataCovar, dataWave, dataOk, dataBPM

def writeData(fileName, data):
    #folder = "F:/Andrew's Dropbox/Dropbox/"
    folder = ""
    fileNameTotal = folder + fileName

    folderList = glob.glob(fileNameTotal)

    for (folder, stokes) in zip(folderList, data):
        print(folder)
        fileWrite(folder, stokes)
```

```
    return


# In[ ]:


data2017, dataError2017, dataCovar2017, dataWave2017, dataOk2017, dataBPM2017 =
↪  readData("D:/WR_Data/WR042/20*")
#data2018, dataError2018, dataCovar2018, dataWave2018, dataOk2018, dataBPM2018 =
↪  readData("/RSS 2018-1/observations/WR113/20*")


# In[ ]:


fig, ax = plt.subplots(figsize = (6,4), dpi=150)

ripple = ascii.read("PA_Ripple.txt", data_start=2)

ripple_interp = np.polynomial.polynomial.polyfit(ripple["wavl"][(ripple["wavl"] > 4100) &
↪  (ripple["wavl"]<7800)], ripple["dPA"][(ripple["wavl"] > 4100) & (ripple["wavl"]<7800)],
↪  deg=15)
ripple_interp2 = sp.interpolate.interp1d(ripple["wavl"], ripple["dPA"], kind='cubic',
↪  fill_value='extrapolate')

wavs = np.linspace(4000, 10000, 1000)
#pp = sp.interpolate.PPoly.from_spline(ripple_interp2)

ax.plot(ripple["wavl"], ripple["dPA"], "ko")
ax.plot(wavs, ripple_interp2(wavs))
#ax.plot(wavs, np.polyval(ripple_interp[::-1], wavs))
#ax.plot(wavs, sp.interpolate.splev(wavs, ripple_interp2))
#ax.plot([4300, 4600, 4850, 5200, 5600, 6150, 6650, 7000, 8600, 9180], np.ones(10), "rx")
ax.set_xlim(3500, 10500)
ax.set_ylim(-2, 2)
ax.set_xlabel("$\lambda~(\AA)$")
ax.set_ylabel("Position angle ($\degree$)")


fig, ax = plt.subplots(figsize = (6,4), dpi=150)

ripple = ascii.read("PA_Ripple.txt", data_start=2)

q_ripple = 2*np.cos(2 * np.deg2rad(ripple["dPA"] + 22.5))
```

```
u_ripple = 2*np.sin(2 * np.deg2rad(ripple["dPA"] + 22.5))

ripple_q_interp = sp.interpolate.interp1d(ripple["wavl"], q_ripple, kind='cubic',
↪  fill_value='extrapolate')
ripple_u_interp = sp.interpolate.interp1d(ripple["wavl"], u_ripple, kind='cubic',
↪  fill_value='extrapolate')

ax.plot(ripple["wavl"], q_ripple, "ko")
ax.plot(ripple["wavl"], u_ripple, "ko")
ax.plot(wavs, ripple_q_interp(wavs))
ax.plot(wavs, ripple_u_interp(wavs))
ax.set_xlim(3500, 10500)
#ax.set_ylim(-2, 2)

fig, ax = plt.subplots(figsize = (6,6), dpi=150)
ax.plot(ripple_q_interp(wavs), ripple_u_interp(wavs))

# In[ ]:

def nan_helper(y):
    """Helper to handle indices and logical indices of NaNs.

    Input:
        - y, 1d numpy array with possible NaNs
    Output:
        - nans, logical indices of NaNs
        - index, a function, with signature indices= index(logical_indices),
          to convert logical indices of NaNs to 'equivalent' indices
    Example:
        >>> # linear interpolation of NaNs
        >>> nans, x= nan_helper(y)
        >>> y[nans]= np.interp(x(nans), x(~nans), y[~nans])
    """

    return np.isnan(y), lambda z: z.nonzero()[0]

def fitting_poly(params, x, q=None, qerr=None, u=None, uerr=None, size=309):

    model_q = np.zeros((len(q), size))
    model_u = np.zeros((len(u), size))
    i=0

    for i in range(len(q)):
        model_q[i] = params["A_%i"%(i+1)] * np.cos(2 * np.deg2rad(ripple_interp2(x[i] +
        ↪  params["x"]) + params["rot_%i"%(i+1)])) \
```

```
        + params["q00_%i"%(i+1)] + params["P_max"] * np.cos(2 * (params["theta0"] +
        ↪  params["k"] * 1./(x[i]*1e-4))) \
         * np.exp(-1.7 * params["lambda_max"] * np.log(params["lambda_max"] *
         ↪  1./(x[i]*1e-4))**2)

        model_u[i] = params["A_%i"%(i+1)] * np.sin(2 * np.deg2rad(ripple_interp2(x[i] +
        ↪  params["x"]) + params["rot_%i"%(i+1)])) \
        + params["u00_%i"%(i+1)] + params["P_max"] * np.sin(2 * (params["theta0"] +
        ↪  params["k"] * 1./(x[i]*1e-4))) \
         * np.exp(-1.7 * params["lambda_max"] * np.log(params["lambda_max"] *
         ↪  1./(x[i]*1e-4))**2)

    if q is None:
        return model_q, model_u

    residual_q = np.zeros((len(q), size))
    residual_u = np.zeros((len(u), size))

    weighted_q = np.zeros((len(q), size))
    weighted_u = np.zeros((len(u), size))

    for i, date in enumerate(q):
        residual_q[i] = date - model_q[i]
        weighted_q[i] = np.sqrt(residual_q[i]**2/qerr[i]**2)

    for i, date in enumerate(u):
        residual_u[i] = date - model_u[i]
        weighted_u[i] = np.sqrt(residual_u[i]**2/uerr[i]**2)

    return np.concatenate((weighted_q.flatten(), weighted_u.flatten()))

def fitting_poly_no_isp(params, x, q=None, qerr=None, u=None, uerr=None, size=309):

    model_q = np.zeros((len(q), size))
    model_u = np.zeros((len(u), size))
    i=0

    for i in range(len(q)):
        model_q[i] = np.cos(2 * (params["A_%i"%(i+1)] * np.deg2rad(ripple_interp2(x[i] *
        ↪  params["x_%i"%(i+1)])) + params["rot_%i"%(i+1)])) \
        + params["q00_%i"%(i+1)]

        model_u[i] = np.sin(2 * (params["A_%i"%(i+1)] * np.deg2rad(ripple_interp2(x[i] *
        ↪  params["x_%i"%(i+1)])) + params["rot_%i"%(i+1)])) \
        + params["u00_%i"%(i+1)]
```

```
    if q is None:
        return model_q, model_u

    residual_q = np.zeros((len(q), size))
    residual_u = np.zeros((len(u), size))

    weighted_q = np.zeros((len(q), size))
    weighted_u = np.zeros((len(u), size))

    for i, date in enumerate(q):
        residual_q[i] = date - model_q[i]
        weighted_q[i] = np.sqrt(residual_q[i]**2/qerr[i]**2)

    for i, date in enumerate(u):
        residual_u[i] = date - model_u[i]
        weighted_u[i] = np.sqrt(residual_u[i]**2/uerr[i]**2)

    return np.concatenate((weighted_q.flatten(), weighted_u.flatten()))

def fitting_isp(params, x, q=None, qerr=None, u=None, uerr=None, size= 309):

    model_q = np.zeros((len(q), size))
    model_u = np.zeros((len(u), size))
    i=0

    for i in range(len(q)):
        model_q[i] = params["q00_%i"%(i+1)] + params["P_max"] * np.cos(2 *
        ↪   (params["theta0"] + params["k"] * 1./(x[i]*1e-4)))         * np.exp(-1.7 *
        ↪   params["lambda_max"] * np.log(params["lambda_max"] * 1./(x[i]*1e-4))**2)

        model_u[i] = params["u00_%i"%(i+1)] + params["P_max"] * np.sin(2 *
        ↪   (params["theta0"] + params["k"] * 1./(x[i]*1e-4)))         * np.exp(-1.7 *
        ↪   params["lambda_max"] * np.log(params["lambda_max"] * 1./(x[i]*1e-4))**2)

    if q is None:
        return model_q, model_u

    residual_q = np.zeros((len(q), size))
    residual_u = np.zeros((len(u), size))

    weighted_q = np.zeros((len(q), size))
    weighted_u = np.zeros((len(u), size))

    for i, date in enumerate(q):
```

```
        residual_q[i] = date - model_q[i]
        weighted_q[i] = residual_q[i]/qerr[i]

    for i, date in enumerate(u):
        residual_u[i] = date - model_u[i]
        weighted_u[i] = residual_u[i]/uerr[i]

    return np.concatenate((weighted_q.flatten(), weighted_u.flatten()))

def fit_position_angle(params, x, pa=None, err=None, size= 309):

    model = np.zeros((len(pa), size))
    i=0

    for i in range(len(pa)):
        model[i] = params["A_%i"%(i+1)] * np.deg2rad(ripple_interp2(x[i] +
        ↪  params["x_%i"%(i+1)])) + params["rot_%i"%(i+1)]

    if q is None:
        return model

    residual = np.zeros((len(pa), size))

    weighted = np.zeros((len(pa), size))

    for i, date in enumerate(pa):
        residual[i] = date - model[i]
        weighted[i] = residual[i]/err[i]

    return weighted.flatten()

def fitting_poly_q_i(params, x, i):

    model_q = np.cos(2 * (np.deg2rad(ripple_interp2(x + params["x"]) +
    ↪  params["rot_%i"%(i+1)])))     + params["q00_%i"%(i+1)] + params["P_max"] * np.cos(2
    ↪  * (params["theta0"] + params["k"] * 1./(x*1e-4)))     * np.exp(-1.7 *
    ↪  params["lambda_max"] * np.log(params["lambda_max"] * 1./(x*1e-4))**2)

    return model_q

def fitting_position_angle_out(params, x, i):

    model = params["A_%i"%(i+1)] * np.deg2rad(ripple_interp2(x + params["x_%i"%(i+1)])) +
    ↪  params["rot_%i"%(i+1)]
```

```
    return model

def fitting_poly_u_i(params, x, i):

    model_u = np.sin(2 * (np.deg2rad(ripple_interp2(x + params["x"]) +
    ↪  params["rot_%i"%(i+1)])))     + params["u00_%i"%(i+1)] + params["P_max"] * np.sin(2
    ↪  * (params["theta0"] + params["k"] * 1./(x*1e-4)))     * np.exp(-1.7 *
    ↪  params["lambda_max"] * np.log(params["lambda_max"] * 1./(x*1e-4))**2)

    return model_u

def fitting_q_i(params, x, i):

    model_q = np.cos(2 * (params["A_%i"%(i+1)] * np.deg2rad(ripple_interp2(x +
    ↪  params["x_%i"%(i+1)])) + params["rot_%i"%(i+1)]))\
               #+ params["q00_%i"%(i+1)]

    return model_q

def fitting_u_i(params, x, i):

    model_u = np.sin(2 * (params["A_%i"%(i+1)] * np.deg2rad(ripple_interp2(x +
    ↪  params["x_%i"%(i+1)])) + params["rot_%i"%(i+1)]))\
               #+ params["u00_%i"%(i+1)]

    return model_u

def fitting_q_isp_i(params, x, i):

    model_q = params["P_max"] * np.cos(2 * (params["theta0"] + params["k"] * 1./(x*1e-4)))
    ↪  * np.exp(-1.7 * params["lambda_max"] * np.log(params["lambda_max"] *
    ↪  1./(x*1e-4))**2)

    return model_q

def fitting_u_isp_i(params, x, i):

    model_u = params["P_max"] * np.sin(2 * (params["theta0"] + params["k"] * 1./(x*1e-4)))
    ↪  * np.exp(-1.7 * params["lambda_max"] * np.log(params["lambda_max"] *
    ↪  1./(x*1e-4))**2)

    return model_u

min_waves_table = []
max_waves_table = []
```

```
for wave in dataWave2017:
    min_waves_table.append(np.min(wave))
    max_waves_table.append(np.max(wave))

min_wave = np.min(min_waves_table)
max_wave = np.max(max_waves_table)

qu_table = []

#WR42 ISP
par = lmfit.Parameters()
par.add('P_max', value = 1.177)
par.add('theta0', value = np.deg2rad(-46.3), min=-np.pi, max=np.pi)
par.add('k', value= np.deg2rad(0), vary=False)
par.add('lambda_max', value = 0.568)

#WR79 ISP
#par = lmfit.Parameters()
#par.add('P_max', value = 0.376)
#par.add('theta0', value = np.deg2rad(-81.5), min=-np.pi, max=np.pi)
#par.add('k', value= np.deg2rad(4.7), vary=False)
#par.add('lambda_max', value = 0.595)

i=0
for (stokes, error, covar, wave, goodData) in zip(data2017, dataError2017, dataCovar2017,
↪   dataWave2017, dataOk2017):

    if np.min(wave) > min_wave or np.max(wave) < max_wave:
        padded_wave = np.pad(wave, (int(np.min(wave) - min_wave), int(max_wave -
        ↪   np.max(wave))), mode='linear_ramp', end_values=(min_wave, max_wave))

        goodData = np.array((np.pad(goodData[0], (int(np.min(wave) - min_wave),
        ↪   int(max_wave - np.max(wave))), mode='edge'), \
                             np.pad(goodData[1], (int(np.min(wave) - min_wave),
                             ↪   int(max_wave - np.max(wave))), mode='edge'), \
                             np.pad(goodData[2], (int(np.min(wave) - min_wave),
                             ↪   int(max_wave - np.max(wave))), mode='edge')))

        stokes = np.array((np.pad(stokes[0], (int(np.min(wave) - min_wave), int(max_wave -
        ↪   np.max(wave))), mode='edge'), \
                           np.pad(stokes[1], (int(np.min(wave) - min_wave), int(max_wave -
                           ↪   np.max(wave))), mode='edge'), \
                           np.pad(stokes[2], (int(np.min(wave) - min_wave), int(max_wave -
                           ↪   np.max(wave))), mode='edge')))
```

```
    error = np.array((np.pad(error[0], (int(np.min(wave) - min_wave), int(max_wave -
    ↪   np.max(wave))), mode='edge'), \
                      np.pad(error[1], (int(np.min(wave) - min_wave), int(max_wave -
                      ↪   np.max(wave))), mode='edge'), \
                      np.pad(error[2], (int(np.min(wave) - min_wave), int(max_wave -
                      ↪   np.max(wave))), mode='edge')))

    covar = np.array((np.pad(covar[0], (int(np.min(wave) - min_wave), int(max_wave -
    ↪   np.max(wave))), mode='edge'), \
                      np.pad(covar[1], (int(np.min(wave) - min_wave), int(max_wave -
                      ↪   np.max(wave))), mode='edge'), \
                      np.pad(covar[2], (int(np.min(wave) - min_wave), int(max_wave -
                      ↪   np.max(wave))), mode='edge')))

binSize = 10
stokesBinned, errorBinned, wavelengthBinned = binDataAngstrom(padded_wave, stokes,
↪   goodData, error, binSize=binSize)

q, u = (stokesBinned[1]/stokesBinned[0])*100, (stokesBinned[2]/stokesBinned[0])*100

q_err = (np.sqrt(errorBinned[1])/stokesBinned[0])*100
u_err = (np.sqrt(errorBinned[2])/stokesBinned[0])*100

q_isp = fitting_q_isp_i(par, wavelengthBinned, i)
u_isp = fitting_u_isp_i(par, wavelengthBinned, i)

q -= q_isp
u -= u_isp

mask1 = np.where((wavelengthBinned > 4570) & (wavelengthBinned < 4760))
mask2 = np.where((wavelengthBinned > 5620) & (wavelengthBinned < 5900))
mask3 = np.where((wavelengthBinned > 6525) & (wavelengthBinned < 6615))
mask4 = np.where((wavelengthBinned > 6700) & (wavelengthBinned < 6800))
mask5 = np.where((wavelengthBinned > 6990) & (wavelengthBinned < 7100))
mask6 = np.where((wavelengthBinned > 7200) & (wavelengthBinned < 7260))

q[mask1] = np.nan
q[mask2] = np.nan
q[mask3] = np.nan
q[mask4] = np.nan
q[mask5] = np.nan
q[mask6] = np.nan

u[mask1] = np.nan
```

```
    u[mask2] = np.nan
    u[mask3] = np.nan
    u[mask4] = np.nan
    u[mask5] = np.nan
    u[mask6] = np.nan

    pa = np.deg2rad(polTools.calculate_PA(q, u))
    pa_err = np.deg2rad(polTools.calculate_PA_error(q, u, q_err, u_err))

    #for WR79
    #if i == 0:
    #    for j, PA in enumerate(pa):
    #        if PA < np.pi/2:
    #            pa[j] += np.pi

    nans, x_nans= nan_helper(wavelengthBinned)
    wavelengthBinned[nans]= np.interp(x_nans(nans), x_nans(~nans), wavelengthBinned[~nans])

    qu_da = np.array((wavelengthBinned, q, q_err, u, u_err, pa, pa_err))

    qu_table.append(qu_da)

    i+=1

size = len(wavelengthBinned)

qu_table = np.stack(qu_table)

qu_da2 = xr.DataArray(qu_table, dims=['date', 'data', 'rows'], coords={'data':
↪  ['wavelength', 'q', 'qerr', 'u', 'uerr', 'PA', 'PAerr']})

par = lmfit.Parameters()
for i in range(len(qu_da2.loc[:, 'q'])):
    par.add('A_%i'%(i+1), value = 0.0)
    #par.add('P_%i'%(i+1), value = 1.0)
    par.add('rot_%i'%(i+1), value = np.mean(qu_da2.loc[i, 'PA']), min=0, max=np.pi)
    #par.add('xu_%i'%(i+1), value = 1.0)
    #par.add('q00_%i'%(i+1), value = np.mean(qu_da2.loc[i, 'q'])-1)
    #par.add('u00_%i'%(i+1), value = np.mean(qu_da2.loc[i, 'u'])+1)
    par.add('x_%i'%(i+1), value = 0.0)

#par.add('P_max', value = 1.177)
#par.add('theta0', value = np.deg2rad(-46.3), min=-np.pi, max=np.pi)
#par.add('k', value= 0.0, vary=False)
#par.add('lambda_max', value = 0.568)
```

```
#mini = lmfit.Minimizer(fitting_poly_no_isp, par, fcn_args=(qu_da2.loc[:, 'wavelength'],),\
#                        fcn_kws={'q':qu_da2.loc[:, 'q'], 'qerr':qu_da2.loc[:, 'qerr'], \
#                                 'u':qu_da2.loc[:, 'u'], 'uerr':qu_da2.loc[:, 'uerr'], \
#                                 'size':size}, nan_policy='omit')

mini = lmfit.Minimizer(fit_position_angle, par, fcn_args=(qu_da2.loc[:, 'wavelength'],),\
                       fcn_kws={'pa': qu_da2.loc[:, 'PA'], 'err': qu_da2.loc[:, 'PAerr'], \
                                'size':size}, nan_policy='omit')

out = mini.least_squares(loss='huber', f_scale = 1.345)

#out = mini.minimize(method='nelder')


# In[ ]:


print(lmfit.fit_report(out, show_correl=False))

wavs = np.linspace(4200, 7250, 1000)

fig, subplots = plt.subplots(20, 1, figsize = (5, 20), sharex=True, dpi=150)

fig.subplots_adjust(hspace=0.0)

for i in range(len(qu_da2.loc[:, 'PA'])):
    ax = subplots.flat[i]
    ax.step(qu_da2.loc[i, 'wavelength'], qu_da2.loc[i, 'PA'], where='mid')
    ax.plot(wavs, fitting_position_angle_out(out.params, wavs, i))
    ax.set_xlim(4000, 7500)
    ax.set_ylabel('PA')

ax.set_xlabel('Wavelength')

fig, subplots = plt.subplots(20, 1, figsize = (5, 20), sharex=True, dpi=150)

fig.subplots_adjust(hspace=0.0)

for i in range(len(qu_da2.loc[:, 'q'])):
    p = np.mean(np.sqrt(qu_da2.loc[i, 'u']**2 + qu_da2.loc[i, 'q']**2))

    ax = subplots.flat[i]
    ax.step(qu_da2.loc[i, 'wavelength'], qu_da2.loc[i, 'q'], where='mid')
    ax.plot(wavs, p.data * fitting_q_i(out.params, wavs, i))
```

```
    ax.set_xlim(4000, 7500)
    ax.set_ylabel('%q')

ax.set_xlabel('Wavelength')

fig.savefig("ripple_fit_q.eps")

fig, subplots = plt.subplots(20, 1, figsize = (5, 20), sharex=True, dpi=150)

fig.subplots_adjust(hspace=0.0)

for i in range(len(qu_da2.loc[:, 'u'])):
    p = np.mean(np.sqrt(qu_da2.loc[i, 'u']**2 + qu_da2.loc[i, 'q']**2))

    ax = subplots.flat[i]
    ax.step(qu_da2.loc[i, 'wavelength'], qu_da2.loc[i, 'u'], where='mid')
    ax.plot(wavs, p.data * fitting_u_i(out.params, wavs, i))
    ax.set_xlim(4000, 7500)
    ax.set_ylabel('%u')

ax.set_xlabel('Wavelength')

fig.savefig("ripple_fit_u.eps")

# In[ ]:

for i in range(len(qu_da2.loc[:, 'q'])):
    out.params['rot_%i'%(i+1)].set(0.0)
    #out.params['q00_%i'%(i+1)].set(0.0)
    #out.params['u00_%i'%(i+1)].set(0.0)

fig, subplots = plt.subplots(20, 1, figsize = (5, 10), sharex=True, dpi=150)

fig.subplots_adjust(hspace=0.0)
print('q')
for i in range(len(qu_da2.loc[:, 'q'])):
    pa = qu_da2.loc[i, 'PA'] - fitting_position_angle_out(out.params, qu_da2.loc[i,
    ↪  'wavelength'], i)
    p = np.sqrt(qu_da2.loc[i, 'u']**2 + qu_da2.loc[i, 'q']**2)

    ax = subplots.flat[i]
    #ax.step(qu_da2.loc[i, 'wavelength'], qu_da2.loc[i, 'q'] - fitting_q_i(out.params,
    ↪  qu_da2.loc[i, 'wavelength'], i), where='mid')
    ax.step(qu_da2.loc[i, 'wavelength'], p * np.cos(2 * pa), where='mid')
    ax.set_xlim(4000, 7500)
```

```
    ax.set_ylabel('%q')

    p = np.ma.array(p, mask=np.isnan(p))
    print(np.ptp(p * fitting_q_i(out.params, qu_da2.loc[i, 'wavelength'], i))/2)


ax.set_xlabel('Wavelength')

fig, subplots = plt.subplots(20, 1, figsize = (5, 10), sharex=True, dpi=150)

fig.subplots_adjust(hspace=0.0)
print('u')
for i in range(len(qu_da2.loc[:, 'u'])):
    pa = qu_da2.loc[i, 'PA'] - fitting_position_angle_out(out.params, qu_da2.loc[i,
    ↪  'wavelength'], i)
    p = np.sqrt(qu_da2.loc[i, 'u']**2 + qu_da2.loc[i, 'q']**2)

    ax = subplots.flat[i]
    #ax.step(qu_da2.loc[i, 'wavelength'], qu_da2.loc[i, 'u'] - fitting_u_i(out.params,
    ↪  qu_da2.loc[i, 'wavelength'], i), where='mid')
    ax.step(qu_da2.loc[i, 'wavelength'], p * np.sin(2 * pa), where='mid')
    ax.set_xlim(4000, 7500)
    ax.set_ylabel('%u')

    p = np.ma.array(p, mask=np.isnan(p))
    print(np.ptp(p * fitting_u_i(out.params, qu_da2.loc[i, 'wavelength'], i))/2)
    q = p * fitting_q_i(out.params, qu_da2.loc[i, 'wavelength'], i)
    u = p * fitting_u_i(out.params, qu_da2.loc[i, 'wavelength'], i)
    X = np.ma.stack((q, u), axis=0)
    print(np.ma.cov(X))

ax.set_xlabel('Wavelength')

# In[ ]:

i=0

data_out = []

for (stokes, wave) in zip(data2017, dataWave2017):

    q, u = (stokes[1]/stokes[0])*100, (stokes[2]/stokes[0])*100

    nans, x_nans= nan_helper(wave)
    wave[nans]= np.interp(x_nans(nans), x_nans(~nans), wave[~nans])
```

```
    pa = (0.5 * np.arctan2(u, q)) - fitting_position_angle_out(out.params, wave, i)
    p = np.sqrt(q**2 + u**2)

    q = p * np.cos(2 * pa)
    u = p * np.sin(2 * pa)

    stokes[1] = q/100*stokes[0]
    stokes[2] = u/100*stokes[0]

    data_out.append(stokes)

    i+=1

writeData("D:/WR_Data/WR079/20*", data_out)


# In[ ]:
```

A.5 Continuum filter extraction from reduced SALT data

```
# -*- coding: utf-8 -*-
"""
Created on Mon Mar  4 14:43:50 2019

@author: Andrew
"""

import seaborn as sns
import numpy as np
import scipy as sp
import matplotlib.pyplot as plt
from astropy.io import ascii
import astropy.io.fits as fits
from astropy.table import Table
from scipy.interpolate import interpolate
import polTools
import os
import glob

sns.set()
sns.set_style("white")
sns.set_context("paper", font_scale=2.0)
sns.set_style("ticks")

filePattern = '/*.fits'

syserr = 0.035

print(syserr)

def fileLoad(folder):
    '''Loads a fits file'''
    dataFile = glob.glob(folder+filePattern)

    #Open fits file
    with fits.open(dataFile[0]) as hdul:
       # stokes I, Q, U values in [0, :], [1, :], [2, :]
        stokesSw = hdul['SCI'].data[:,0,:]
        #stokes errors (I, Q, U)
        varSw = hdul['VAR'].data[:,0,:]
        covarSw = hdul['COV'].data[:,0,:]
        deltaWave = float(hdul['SCI'].header['CDELT1'])
```

```
        #get starting wavelength
        wave0 = float(hdul['SCI'].header['CRVAL1'])
        #get wavelength axis size
        waves = int(hdul['SCI'].header['NAXIS1'])


        bpm_Sw = hdul['BPM'].data[:,0,:]
        ok_Sw = (bpm_Sw==0)

        wavelengths = wave0 + deltaWave*np.arange(waves)

        return stokesSw, varSw, covarSw, wavelengths, ok_Sw, bpm_Sw

def readData(fileName):
    data = []
    dataError = []
    dataCovar = []
    dataWave = []
    dataOk = []
    dataBPM = []

    folderList = glob.glob(fileName)

    for folder in folderList:
        print(folder[-8:])

        data.append(stokes)
        dataError.append(stokesError)
        dataCovar.append(stokesCovar)
        dataWave.append(waves)
        dataOk.append(ok)
        dataBPM.append(bpm)

    return data, dataError, dataCovar, dataWave, dataOk, dataBPM

filter_Path = "Filters/"

filter_B_Standard = ascii.read(filter_Path + "B Filter Standard")
filter_V_Standard = ascii.read(filter_Path + "V Filter Standard")
filter_R_Standard = ascii.read(filter_Path + "R Filter Standard")
filter_B_Stroemgren = ascii.read(filter_Path + "Stroemgren_b.txt")
filter_B_WN = ascii.read(filter_Path + "B Filter WN")
filter_V_WN = ascii.read(filter_Path + "V Filter WN")
filter_R_WN = ascii.read(filter_Path + "R Filter WN")
filter_B_WC = ascii.read(filter_Path + "B Filter WC")
```

```
filter_V_WC = ascii.read(filter_Path + "V Filter WC")
filter_R_WC = ascii.read(filter_Path + "R Filter WC")
filter_B_WR = ascii.read(filter_Path + "B Filter WR")
filter_V_WR = ascii.read(filter_Path + "V Filter WR")
filter_R_WR = ascii.read(filter_Path + "R Filter WR")

filter_B_Standard.sort('Wavelength')
filter_V_Standard.sort('Wavelength')
filter_R_Standard.sort('Wavelength')
filter_B_Stroemgren.sort('Wavelength')
filter_B_WN.sort('Wavelength')
filter_V_WN.sort('Wavelength')
filter_R_WN.sort('Wavelength')
filter_B_WC.sort('Wavelength')
filter_V_WC.sort('Wavelength')
filter_R_WC.sort('Wavelength')

#data2017, dataError2017, dataCovar2017, dataWave2017, dataOk2017, dataBPM2017 =
↪  readData("C:/Users/Andrew/Dropbox/RSS 2017/observations/WR113/2017*")

datapath = input("Enter the name of the star: ")
Star_type = input("Enter star type: ")

skipnum = 4

final_result = Table(names=("Date", "BQ", "BU", "BQerr", "BUerr", "VQ", "VU", "VQerr",
↪  "VUerr", "RQ", "RU", "RQerr", "RUerr"), dtype=('S8', 'f8',
↪  'f8','f8','f8','f8','f8','f8','f8','f8','f8','f8','f8'))

folderList = glob.glob("F:/Andrew's Dropbox/Dropbox/RSS2019-1/observations/WR079/20190810")

for folder in folderList:

    date = int(folder[-8:])

    err = syserr

    stokes, stokesError, stokesCovar, waves, ok, bpm = fileLoad(folder)

    for i, errorarray in enumerate(stokesError):
        for k, error in enumerate(errorarray):
            if np.sqrt(error)/stokes[0,k] < err:
                stokesError[i,k] = err

    #extract data columns
```

```
    lam= waves[ok[0]]
    flux = stokes[0,ok[0]]

    if Star_type == 'Standard':
        filters = [(0, filter_B_Standard), (4, filter_V_Standard), (8, filter_R_Standard)]
    elif Star_type == 'Stroemgren':
        filters = [(0, filter_B_Stroemgren), (4, filter_V_Standard), (8, filter_R_Standard)
        ↪  ]
    elif Star_type == 'WN':
        filters = [(0, filter_B_WN), (4, filter_V_WN), (8, filter_R_WN)]
    elif Star_type == 'WC':
        filters = [(0, filter_B_WC), (4, filter_V_WC), (8, filter_R_WC)]
    elif Star_type == 'WR':
        filters = [(0, filter_B_WR), (4, filter_V_WR), (8, filter_R_WR)]
    else:
        print('Wrong filter type')
        break

    newrow = [date]
#
#    plt.plot(lam, flux/np.max(flux), "k-")
#    plt.plot(filter_array_B[:,0], filter_array_B[:,1], "b--")
#    plt.plot(filter_array_V[:,0], filter_array_V[:,1], "g--")
#    plt.plot(filter_array_R[:,0], filter_array_R[:,1], "r--")
#    plt.xlabel("Wavelength £\AA£")
#    plt.ylabel("Normalized flux")
#    break

    for j, colour in filters:
        #extract filter info
        wave = colour['Wavelength']
        weight = colour['Filter']

        #Interpolate filter
        interp = interpolate.interp1d(wave, weight, bounds_error=False, fill_value=0.0)
        weightpol = interp(lam)
        filterregion = np.where(weightpol > 0)

        #standard columns from polsalt reduction output
        cols = [('%Q', 1), ('%U', 2)]
        errcols = [('%Qerr', 1), ('%Uerr', 2)]

        #cols = [('%Q', 1), ('%U', 2), ('%err', 3)]
        filter_result = []
        #repeat for each stokes value
```

```
        for column, i in cols:

            #load appropriate column
            pol = stokes[i, ok[0]]/stokes[0,ok[0]]

            #plt.plot(wave, pol)
            #plt.plot(wave, weight)

            #integrate and convolve
            top = np.trapz((flux[filterregion]*weightpol[filterregion]*pol[filterregion]),
            ↪  x=lam[filterregion])
            bottom = np.trapz((flux[filterregion]*weightpol[filterregion]),
            ↪  x=lam[filterregion])
            measure = top/bottom

            #print results
            print(column, measure)

            filter_result.append(measure)

        for column, i in errcols:

            #load appropriate column
            pol = stokesError[i,:]

            #integrate and convolve
            top = np.trapz((flux[filterregion]*weightpol[filterregion]*pol[filterregion]),
            ↪  x=lam[filterregion])
            bottom = np.trapz((flux[filterregion]*weightpol[filterregion]),
            ↪  x=lam[filterregion])
            measure = top/bottom

            #error calculation for error columns
            measure = measure/np.sqrt(len(lam[filterregion]))

            #print results
            print(column, measure)

            filter_result.append(measure)

        print(filter_result)
        newrow = np.concatenate((newrow, filter_result))

    print(newrow)
    final_result.add_row(newrow)
```

```
if Star_type == 'Standard':
    final_result.write(datapath+"_BVR_mod_HighRes_S.txt", format='ascii')
if Star_type == 'Stroemgren':
    final_result.write(datapath+"_BVR_mod_HighRes_Stroemgren.txt", format='ascii')
elif Star_type == 'WR':
    final_result.write(datapath+"_BVR_mod_HighRes.txt", format='ascii')
```

A.6 Line polarization extraction from reduced SALT data, *pfew* method

A.6.1 Calculations

```
# -*- coding: utf-8 -*-
"""
Created on Tue Oct  9 15:07:47 2018

@author: Andrew
"""

#-----------------------------------------------------------------
# Program to measure polarization, q, u and theta, with errors, for an
# emission line.   JRL, 4/13/2010
# Will rotate q and u values to a user specified angle and accepts
# two input files for 1 spectra (ie. HPOL blue and red CCD files).
# Also still accepts only one file.     JRL, 6/10/2010
# Accepts two files, does errors correctly.    JRL, 6/23/2010
# Fixed problem with not calculating underlying absorption
# correctly. (EW inputed by user needs to be negative, but I
# ran it through the math as a positive number before). JRL, 3/26/2013
#
# 170722 jlh modified for RSS data
# 82018 agf written in Python
#------------------------------------------------------------------

import astropy.io.fits as fits
import astropy.io.ascii as ascii
from astropy.table import Table
import glob
import numpy as np
from scipy import interpolate

class LinePol():
    def __init__(self):
        #-----------------------------------------------------------------
        # Pixel correlation value (different for each detector)
        #----------------------------------------------------------------_
        self.__pixelCorrelation = 1.0  #RSS
        self.__folderPath = str()
        self.__folderList = str()
        self.__path = str()
```

```
self.__objectName = str()
self.__currentFolderIndex = 0
self.__outputTable = None

self.__filePattern = '*.fits'
self.__positionAngleRotate = 0.0
self.__absorptionDeltaWave = 0.0

self.__indexBlueContinuumMin = 0
self.__indexBlueContinuumMax = 0
self.__indexRedContinuumMin = 0
self.__indexRedContinuumMax = 0
self.__indexLineMin = 0
self.__indexLineMax = 0

self.__closestBlueContinuumMin = 0.0
self.__closestBlueContinuumMax = 0.0
self.__closestRedContinuumMin = 0.0
self.__closestRedContinuumMax = 0.0
self.__closestLineMin = 0.0
self.__closestLineMax = 0.0

self.blueContinuumMin = 0.0
self.blueContinuumMax = 0.0
self.redContinuumMin = 0.0
self.redContinuumMax = 0.0
self.lineMin = 0.0
self.lineMax = 0.0

self.meanBlueContinuumLam = 0.0
self.meanRedContinuumLam = 0.0

self.meanQBlueContinuum = 0.0
self.meanUBlueContinuum = 0.0

self.meanQRedContinuum = 0.0
self.meanURedContinuum = 0.0

self.meanErrBlueContinuum = 0.0
self.meanErrRedContinuum = 0.0

self.meanLineLam = 0.0
self.meanQLine = 0.0
self.meanULine = 0.0
self.meanErrLine = 0.0
```

```
        self.blueContinuumCenter = 0.0
        self.redContinuumCenter = 0.0

        self.wavelengths = np.ndarray(0)

        self.i = np.ndarray(0)
        self.q = np.ndarray(0)
        self.u = np.ndarray(0)

        self.iErr = np.ndarray(0)
        self.qErr = np.ndarray(0)
        self.uErr = np.ndarray(0)

        self.iMeanTotal = 0.0
        self.qMeanTotal = 0.0
        self.uMeanTotal = 0.0
        self.errMeanTotal = 0.0

        self.iLineFlux = 0.0
        self.qLineFlux = 0.0
        self.uLineFlux = 0.0
        self.errLineFlux = 0.0

        self.qContOutput = 0.0
        self.uContOutput = 0.0
        self.errContOutput = 0.0
        self.pContOutput = 0.0
        self.PAContOutput = 0.0

        self.qLineOutput = 0.0
        self.uLineOutput = 0.0
        self.errLineOutput = 0.0
        self.pLineOutput = 0.0
        self.PALineOutput = 0.0

        self.qDiffOutput = 0.0
        self.uDiffOutput = 0.0
        self.errDiffOutput = 0.0

        self.rotation = False

    def loadOneFile(self, path, objectName):
        '''Loads a file for display'''
        self.getInput(path, objectName)
```

```
        if (len(self.__folderList) > 0) and (self.__currentFolderIndex <
        ↪   len(self.__folderList)):
            self.fileLoad(self.__folderList[self.__currentFolderIndex])
        else:
            print("No files found at location: ", path)

    def doLinePolExtraction(self, folder):
        '''Runs line polarization extraction on one folder'''
        self.fileLoad(folder)

        if self.rotation == True:
            self.PARotation()

        self.setClosestValues()

        waveBlueContinuum = self.sliceWavelengths(self.wavelengths,
        ↪   self.__indexBlueContinuumMin, self.__indexBlueContinuumMax)
        iBlueContinuum = self.sliceWavelengths(self.i, self.__indexBlueContinuumMin,
        ↪   self.__indexBlueContinuumMax)
        qBlueContinuum = self.sliceWavelengths(self.q, self.__indexBlueContinuumMin,
        ↪   self.__indexBlueContinuumMax)
        uBlueContinuum = self.sliceWavelengths(self.u, self.__indexBlueContinuumMin,
        ↪   self.__indexBlueContinuumMax)
        errBlueContinuum = self.sliceWavelengths(self.qErr, self.__indexBlueContinuumMin,
        ↪   self.__indexBlueContinuumMax)

        waveRedContinuum = self.sliceWavelengths(self.wavelengths,
        ↪   self.__indexRedContinuumMin, self.__indexRedContinuumMax)
        iRedContinuum = self.sliceWavelengths(self.i, self.__indexRedContinuumMin,
        ↪   self.__indexRedContinuumMax)
        qRedContinuum = self.sliceWavelengths(self.q, self.__indexRedContinuumMin,
        ↪   self.__indexRedContinuumMax)
        uRedContinuum = self.sliceWavelengths(self.u, self.__indexRedContinuumMin,
        ↪   self.__indexRedContinuumMax)
        errRedContinuum = self.sliceWavelengths(self.qErr, self.__indexRedContinuumMin,
        ↪   self.__indexRedContinuumMax)

        waveLine = self.sliceWavelengths(self.wavelengths, self.__indexLineMin,
        ↪   self.__indexLineMax)
        iLine = self.sliceWavelengths(self.i, self.__indexLineMin, self.__indexLineMax)
        qLine = self.sliceWavelengths(self.q, self.__indexLineMin, self.__indexLineMax)
        uLine = self.sliceWavelengths(self.u, self.__indexLineMin, self.__indexLineMax)
        errLine = self.sliceWavelengths(self.qErr, self.__indexLineMin,
        ↪   self.__indexLineMax)
```

```
lineCenter = self.findCenter(waveLine)
blueContinuumCenter = self.findCenter(waveBlueContinuum)
redContinuumCenter = self.findCenter(waveRedContinuum)

self.meanBlueContinuumLam = np.mean(iBlueContinuum)
self.meanRedContinuumLam = np.mean(iRedContinuum)

self.meanQBlueContinuum = np.mean(qBlueContinuum)
self.meanUBlueContinuum = np.mean(uBlueContinuum)

self.meanQRedContinuum = np.mean(qRedContinuum)
self.meanURedContinuum = np.mean(uRedContinuum)

self.meanErrBlueContinuum = self.findErrorAverage(errBlueContinuum)
self.meanErrRedContinuum = self.findErrorAverage(errRedContinuum)

self.meanLineLam = np.mean(iLine)
self.meanQLine = np.mean(qLine)
self.meanULine = np.mean(uLine)
self.meanErrLine = self.findErrorAverage(errLine)

errorWeight = self.findErrorWeight(waveLine, lineCenter, waveBlueContinuum,
↪  blueContinuumCenter, waveRedContinuum, redContinuumCenter)

self.iMeanTotal = self.findTotalAverage(waveBlueContinuum,
↪  self.meanBlueContinuumLam, blueContinuumCenter, \
                                        waveRedContinuum, self.meanRedContinuumLam,
                                        ↪  redContinuumCenter, \
                                        waveLine, lineCenter)
self.qMeanTotal = self.findTotalAverage(waveBlueContinuum, self.meanQBlueContinuum,
↪  blueContinuumCenter, \
                                        waveRedContinuum, self.meanQRedContinuum,
                                        ↪  redContinuumCenter, \
                                        waveLine, lineCenter)
self.uMeanTotal = self.findTotalAverage(waveBlueContinuum, self.meanUBlueContinuum,
↪  blueContinuumCenter, \
                                        waveRedContinuum, self.meanURedContinuum,
                                        ↪  redContinuumCenter, \
                                        waveLine, lineCenter)
self.errMeanTotal = self.findErrorWeightedAverage(errorWeight,
↪  self.meanErrBlueContinuum, self.meanErrRedContinuum)

lineWidth = self.findLineWidth(self.lineMin, self.lineMax)

self.iLineFlux = self.calcLineFlux(self.meanLineLam, self.iMeanTotal, lineWidth)
```

```
        self.qLineFlux = self.calcLineFlux(self.meanQLine, self.qMeanTotal, lineWidth)
        self.uLineFlux = self.calcLineFlux(self.meanULine, self.uMeanTotal, lineWidth)
        self.errLineFlux = self.calcLineFluxError(self.meanErrLine, self.errMeanTotal,
        ↪  lineWidth)

        self.qContOutput = self.qMeanTotal / self.iMeanTotal * 100
        self.uContOutput = self.uMeanTotal / self.iMeanTotal * 100
        self.errContOutput = self.errMeanTotal / self.iMeanTotal * 100
        self.pContOutput = self.calcPolarization(self.qContOutput, self.uContOutput)
        self.PAContOutput = self.calcPA(self.qContOutput, self.uContOutput)

        self.qLineOutput = self.qLineFlux / self.iLineFlux * 100
        self.uLineOutput = self.uLineFlux / self.iLineFlux * 100
        self.errLineOutput = self.errLineFlux / self.iLineFlux * 100
        self.pLineOutput = self.calcPolarization(self.qLineOutput, self.uLineOutput)
        self.PALineOutput = self.calcPA(self.qLineOutput, self.uLineOutput)

        self.qDiffOutput = (self.qContOutput - self.qLineOutput) * 100
        self.uDiffOutput = (self.uContOutput - self.uLineOutput) * 100
        #not actually calculating polarization here, but does the same thing
        self.errDiffOutput = self.calcPolarization(self.errContOutput, self.errLineOutput)

        self.printOutput(folder)
        self.addToTable()

        return lineCenter

    def doLinePolExtractionAll(self):
        '''Runs line polarization extraction automatically for all data'''
        self.constructOutputTable()

        lineCenter = 0

        for folder in self.__folderList:
            lineCenter = self.doLinePolExtraction(folder)

        self.writeTable(lineCenter)

    def doLinePolExtractionSequence(self):
        '''Runs line polarization extraction for one observation and then move to the
        ↪  next'''
        if not self.__outputTable:
            self.constructOutputTable()

        lineCenter = 0
```

```
        if self.__currentFolderIndex > (len(self.__folderList) - 1):
            print("End of file list")
            self.__outputTable = None
            return

        lineCenter = self.doLinePolExtraction(self.__folderList[self.__currentFolderIndex])
        self.__currentFolderIndex += 1

        if self.__currentFolderIndex == (len(self.__folderList)):
            self.writeTable(lineCenter)

        return

    def valueLocate(self, array, value):
        '''Locates nearest value in array'''
        index = (np.abs(array - value)).argmin()
        output = array[index]
        return output, index

    def IDLInterpol(self, inputArray, inputAbscissa, outputAbscissa):
        '''Wrapper for scipy interpolate to match IDL style'''
        interpfunc = interpolate.interp1d(inputAbscissa, inputArray, kind='linear')
        return interpfunc(outputAbscissa)

    def constructOutputTable(self) -> None:
        '''Sets up the output astropy table'''
        self.__outputTable = Table(names = ["Date", "%Q", "%U", "%Err", "%P", "PA"])

        self.__outputTable["%Q"].format = "{:.5f}"
        self.__outputTable["%U"].format = "{:.5f}"
        self.__outputTable["%Err"].format = "{:.7f}"
        self.__outputTable["%P"].format = "{:.3f}"
        self.__outputTable["PA"].format = "{:.1f}"

    def getInput(self, path, objectName) -> None:
        '''Gets file and folder locations'''
        #get path to folder
        self.__path = path
        #pick star
        self.__objectName = objectName
        #find dated folders using dropbox naming format
        self.__folderPath = self.__path+"/"+self.__objectName+'/20*/'
        self.__folderList = glob.glob(self.__folderPath)
        #fits file search pattern
```

```
def wavelengthErrorCheck(self) -> None:
    '''If continuum extends into the line ask for values again.'''
    if (self.blueContinuumMin > self.blueContinuumMax) or (self.lineMin > self.lineMax)
    ↪  or (self.redContinuumMin > self.redContinuumMax):
        print('Error! Min < Max')

    if self.lineMin < self.blueContinuumMax:
        print('Error! Continuum extends into line region. Please reenter values.')

    if self.redContinuumMin < self.lineMax:
        print('Error! Continuum extends into line region. Please reenter values.')

def fileLoad(self, folder) -> None:
    '''Loads a fits file'''
    dataFile = glob.glob(folder+self.__filePattern)

    #Open fits file
    hdul = fits.open(dataFile[0])
    #get wavelength spacing
    deltaWave = float(hdul['SCI'].header['CDELT1'])
    #get starting wavelength
    wave0 = float(hdul['SCI'].header['CRVAL1'])
    #get wavelength axis size
    waves = int(hdul['SCI'].header['NAXIS1'])

   # stokes I, Q, U values
    stokesSw = hdul['SCI'].data[:,0,:]
    #stokes errors
    varSw = hdul['VAR'].data[:,0,:]
    #wavelength axis
    self.wavelengths = wave0 + deltaWave*np.arange(waves)

    print("\n"+folder)

    self.i = stokesSw[0, :]
    self.q = stokesSw[1, :]#[i > 0]/i[i > 0]
    self.u = stokesSw[2, :]#[i > 0]/i[i > 0]

    self.iErr = np.sqrt(varSw[0, :])
    self.qErr = np.sqrt(varSw[1, :])#[iErr > 0])/i[i > 0]
    self.uErr = np.sqrt(varSw[2, :])#[iErr > 0])/i[i > 0]

def PARotation(self) -> None:
```

```
    '''Rotate the data in a file if need be. Errors do not need to be rotated since
    ↪   they will be essentially the same.'''
    positionAngleArray = np.rad2deg(0.5*np.arctan2(self.q, self.u))
    deltaPositionAngle = []
    qRotated = []
    uRotated = []

    for i in range(len(positionAngleArray)):
        if positionAngleArray[i] < 0:
            positionAngleArray[i] += 180

    polarization = np.sqrt(self.q**2 + self.u**2)

    #Find the angle to rotate by and then convert that angle to radians so you can use
    ↪   sine and cosine later.
    for angle in positionAngleArray:
        deltaPositionAngle.append(np.deg2rad(angle - self.__positionAngleRotate))

    #compute q values for the rotated data
    for i in range(len(deltaPositionAngle)):
        qRotated.append(polarization[i] * np.cos(2 * deltaPositionAngle[i]))

    #compute u values for the rotated data
    for i in range(len(deltaPositionAngle)):
        uRotated.append(polarization[i] * np.cos(2 * deltaPositionAngle[i]))

    self.q = qRotated
    self.u = uRotated

def setClosestValues(self) -> None:
    '''Find the wavelength values closest to C1, C2, L1, L2, C3 and C4.'''
    self.__closestBlueContinuumMin, self.__indexBlueContinuumMin =
    ↪   self.valueLocate(self.wavelengths, self.blueContinuumMin)
    self.__closestBlueContinuumMax, self.__indexBlueContinuumMax =
    ↪   self.valueLocate(self.wavelengths, self.blueContinuumMax)
    self.__closestLineMin, self.__indexLineMin = self.valueLocate(self.wavelengths,
    ↪   self.lineMin)
    self.__closestLineMax, self.__indexLineMax = self.valueLocate(self.wavelengths,
    ↪   self.lineMax)
    self.__closestRedContinuumMin, self.__indexRedContinuumMin =
    ↪   self.valueLocate(self.wavelengths, self.redContinuumMin)
    self.__closestRedContinuumMax, self.__indexRedContinuumMax =
    ↪   self.valueLocate(self.wavelengths, self.redContinuumMax)

def sliceWavelengths(self, wavelengths, indexMin, indexMax) -> None:
```

```
        '''Pull out the wavelengths'''
        return wavelengths[indexMin:indexMax]

    def findCenter(self, wave) -> float:
        '''Find center.'''
        center = len(wave)/2
        #later I subtract one from the center values. This is because if the center
        #is 3 that means it is element 2 in the array (0,1,2,...). However if it is element
        #one element array than 1/2=0 (integers) so then when I subtract later on I get -1.
        #Here I correct for that.

        if center == 0: center = 1

        return center

    def findErrorAverage(self, err) -> float:
        '''Finds the average error'''
        return np.sqrt(np.sum((err)**2.) * self.__pixelCorrelation / (len(err)**2))

    def findErrorWeight(self, waveLine, lineCenter, waveBlueContinuum, blueContinuumCenter,
    ↪   waveRedContinuum, redContinuumCenter) -> float:
        '''Find how much to weight the blue continuum region by. The red is
        one minus this value. This is needed instead of the interpolate
        function, which does not work for the errors.'''

        return (waveLine[int(lineCenter) - 1] - waveBlueContinuum[int(blueContinuumCenter)
        ↪   - 1]) \
                        /(waveRedContinuum[int(redContinuumCenter) - 1] -
                        ↪   waveBlueContinuum[int(blueContinuumCenter) - 1])

    def findTotalAverage(self, waveBlueContinuum, meanBlueContinuum, blueContinuumCenter,
    ↪   waveRedContinuum, meanRedContinuum, redContinuumCenter, waveLine, lineCenter) ->
    ↪   None:
        '''Find total average of both regions'''
        return self.IDLInterpol([meanBlueContinuum, meanRedContinuum],
        ↪   [waveBlueContinuum[int(blueContinuumCenter) - 1], \
                                 waveRedContinuum[int(redContinuumCenter) - 1]],
                                 ↪   waveLine[int(lineCenter) - 1])

    def findErrorWeightedAverage(self, errorWeight, meanErrBlueContinuum,
    ↪   meanErrRedContinuum) -> float:
        '''Finds the error weighted average'''
        return np.sqrt((errorWeight * meanErrBlueContinuum)**2 + ((1 - errorWeight) *
        ↪   meanErrRedContinuum)**2)
```

```
def findLineWidth(self, lineMin, lineMax) -> float:
    '''Calculate line width here. It
    goes into the equation used to calculate the line pol.'''
    return lineMax - lineMin

def calcLineFlux(self, mean, total, lineWidth) -> float:
    '''Calculate the flux in the line.'''
    return (mean - total) * lineWidth

def calcLineFluxError(self, mean, total, lineWidth) -> float:
    '''Calculate the flux error in the line.'''
    return np.sqrt(mean**2 + total**2) * lineWidth

def contOutput(self, stokesMeanTotal, iMeanTotal) -> float:
    '''Continuum percentage output'''
    return stokesMeanTotal / iMeanTotal * 100

def calcPolarization(self, q, u) -> float:
    '''Calculates total polarization'''
    return np.sqrt(q**2 + u**2)

def calcPA(self, q, u) -> float:
    '''Calculates position angle'''
    return np.rad2deg(0.5 * np.arctan2(u, q))

def addToTable(self) -> None:
    '''Adds a new row to the output table'''
    newrow = [self.date, self.qLineOutput, self.uLineOutput, self.errLineOutput,
    ↪  self.pLineOutput, self.PALineOutput]
    self.__outputTable.add_row(newrow)

def writeTable(self, lineCenter) -> None:
    '''Writes the output table to file'''
    self.__outputTable.write(self.__objectName+'_'+str(lineCenter+self.lineMin)+'.txt',
    ↪  format='ascii', overwrite=True)

def printOutput(self, folder) -> None:
    '''Prints output to console'''
    self.date = folder[-10:]
    self.date = self.date.replace("\\", "")

    print('Date: ', self.date, '\n')
    print('C1 ', 'C2 ', 'L1 ', 'L2 ', 'C3 ', 'C4')
```

```
print(self.__closestBlueContinuumMin, self.__closestBlueContinuumMax,
↪  self.__closestLineMin, self.__closestLineMax, self.__closestRedContinuumMin,
↪  self.__closestRedContinuumMax)
print( ' ', ' - ', 'I ', 'Q ', 'U ', 'Err ', '%Pol ', 'PA ')
print('Flam Left ', self.meanBlueContinuumLam,' ', self.meanQBlueContinuum,' ',
↪  self.meanUBlueContinuum ,' ', self.meanErrBlueContinuum,' ', \
      self.calcPolarization(self.meanQBlueContinuum, self.meanUBlueContinuum),' ',
      ↪  self.calcPA(self.meanQBlueContinuum, self.meanUBlueContinuum))
print('Flam Cntr ', self.meanLineLam,' ', self.meanQLine,' ', self.meanULine,' ',
↪  self.meanErrLine,' ', self.calcPolarization(self.meanQLine, self.meanULine),'
↪  ', \
      self.calcPA(self.meanQLine, self.meanULine))
print('Flam Right ', self.meanRedContinuumLam,' ', self.meanQRedContinuum,' ',
↪  self.meanURedContinuum ,' ', self.meanErrRedContinuum,' ', \
      self.calcPolarization(self.meanQRedContinuum, self.meanURedContinuum),' ',
      ↪  self.calcPA(self.meanQRedContinuum, self.meanURedContinuum))
print('Flam Cont ', self.iMeanTotal,' ',self.qMeanTotal,' ', self.uMeanTotal ,' ',
↪  self.errMeanTotal,' ', \
      self.calcPolarization(self.qMeanTotal, self.uMeanTotal),' ',
      ↪  self.calcPA(self.qMeanTotal, self.uMeanTotal))
print('Flux Line ', self.iLineFlux,' ', self.qLineFlux,' ', self.uLineFlux,' ',
↪  self.errLineFlux,' ', \
      self.calcPolarization(self.qLineFlux, self.uLineFlux),' ',
      ↪  self.calcPA(self.qLineFlux, self.uLineFlux))
print('EW Line ', self.iLineFlux/self.iMeanTotal,' ',
↪  self.qLineFlux*(self.iLineFlux/self.iMeanTotal)/self.iLineFlux,' ', \
    self.uLineFlux*(self.iLineFlux/self.iMeanTotal)/self.iLineFlux,' ',
    ↪  self.errLineFlux*(self.iLineFlux/self.iMeanTotal)/self.iLineFlux,' ',\
    np.sqrt((self.qLineFlux*(self.iLineFlux/self.iMeanTotal)/self.iLineFlux)**2 +
    ↪  (self.uLineFlux*(self.iLineFlux/self.iMeanTotal)/self.iLineFlux)**2),' ')
print('% Cont ', ' - ', self.qContOutput,' ', self.uContOutput,' ',
↪  self.errContOutput,' ', self.pContOutput,' ', self.PAContOutput)
print('% Line ', ' - ', self.qLineOutput,' ', self.uLineOutput,' ',
↪  self.errLineOutput,' ', self.pLineOutput,' ', self.PALineOutput)
print('% Cnt-Line ', ' - ', self.qDiffOutput,' ', self.uDiffOutput,' ',
↪  self.errDiffOutput)
```

A.6.2 User interface

```
# -*- coding: utf-8 -*-
"""
Created on Tue Oct  9 14:44:30 2018

@author: Andrew
"""
import sys

import numpy as np
from PyQt5.QtCore import *
from PyQt5.QtGui import *
from PyQt5.QtWidgets import QApplication, QDialog, QPushButton, QCheckBox, QFormLayout,
↪  QHeaderView, QHBoxLayout, QLabel, QLineEdit, QMainWindow, QSplitter, \
QTextEdit, QVBoxLayout, QWidget
from matplotlib.backends.backend_qt5agg import FigureCanvas, NavigationToolbar2QT as
↪  NavigationToolbar
from matplotlib.figure import Axes, Figure

import lines_pol_module as lpm

class EmittingStream(QObject):

    textWritten = pyqtSignal(str)

    def write(self, text):
        self.textWritten.emit(str(text))

class MainWindow():
    def __init__(self):

        sys.stdout = EmittingStream(textWritten = self.normalOutputWritten)

        self.__lpm = lpm.LinePol()

        self.__loaded = False
        self.__limits = np.zeros(6)
        self.__mouseX = 0.0
        self.__lines = [None, None, None, None, None, None]
        self.__lines_Stokes = [None, None, None, None, None, None]
        self.__recorder = None
        self.__editedWidget = None
```

```
self.__window: QMainWindow = QMainWindow()
self.__window.setWindowTitle("Line Polarization Extractor")
self.__widget: QWidget = QSplitter(self.__window)
self.__window.setCentralWidget(self.__widget)

self.__logOutput: QTextEdit = QTextEdit()

self.__plotWidget: QWidget = QWidget()
self.__plotWidget.setLayout(QVBoxLayout())

self.__plotCanvas: FigureCanvas = FigureCanvas(Figure())
self.__plotNavBar: NavigationToolbar = NavigationToolbar(self.__plotCanvas,
↪  self.__plotWidget)

self.__plotWidget.layout().addWidget(self.__plotNavBar)
self.__plotWidget.layout().addWidget(self.__plotCanvas)

self.__rotatePA: QCheckBox = QCheckBox()
self.__rotatePA.setText('Rotate Position Angle?')
self.__rotatePA.stateChanged.connect(self.PAChecked)

self.__loadButton: QPushButton = QPushButton('Load Files')
self.__runButton: QPushButton = QPushButton('Run Extraction')
self.__runAllButton: QPushButton = QPushButton('Run Extraction (all)')

self.__inputPath: QLineEdit = QLineEdit()
self.__path = self.__inputPath.text()

self.__inputObjectName: QLineEdit = QLineEdit()
self.__objectName = self.__inputObjectName.text()

self.__inputPath.returnPressed.connect(self.__pathSet)
self.__inputObjectName.returnPressed.connect(self.__pathSet)

self.__inputPA: QLineEdit = QLineEdit()
self.__PA = self.__inputPA.text()

self.__inputBlueMin: QLineEdit = QLineEdit()
self.__inputBlueMin.setValidator(QIntValidator())
self.__inputBlueMin.returnPressed.connect(self.recordLimit)
self.__mouseBlueMin: QPushButton = QPushButton('C')
self.__mouseBlueMin.clicked.connect(lambda:
↪  self.recordMouseLimit(self.__inputBlueMin))

self.__inputBlueMax: QLineEdit = QLineEdit()
```

```
self.__inputBlueMax.setValidator(QIntValidator())
self.__inputBlueMax.returnPressed.connect(self.recordLimit)
self.__mouseBlueMax: QPushButton = QPushButton('C')
self.__mouseBlueMax.clicked.connect(lambda:
↪  self.recordMouseLimit(self.__inputBlueMax))

self.__inputLineMin: QLineEdit = QLineEdit()
self.__inputLineMin.setValidator(QIntValidator())
self.__inputLineMin.returnPressed.connect(self.recordLimit)
self.__mouseLineMin: QPushButton = QPushButton('C')
self.__mouseLineMin.clicked.connect(lambda:
↪  self.recordMouseLimit(self.__inputLineMin))

self.__inputLineMax: QLineEdit = QLineEdit()
self.__inputLineMax.setValidator(QIntValidator())
self.__inputLineMax.returnPressed.connect(self.recordLimit)
self.__mouseLineMax: QPushButton = QPushButton('C')
self.__mouseLineMax.clicked.connect(lambda:
↪  self.recordMouseLimit(self.__inputLineMax))

self.__inputRedMin: QLineEdit = QLineEdit()
self.__inputRedMin.setValidator(QIntValidator())
self.__inputRedMin.returnPressed.connect(self.recordLimit)
self.__mouseRedMin: QPushButton = QPushButton('C')
self.__mouseRedMin.clicked.connect(lambda:
↪  self.recordMouseLimit(self.__inputRedMin))

self.__inputRedMax: QLineEdit = QLineEdit()
self.__inputRedMax.setValidator(QIntValidator())
self.__inputRedMax.returnPressed.connect(self.recordLimit)
self.__mouseRedMax: QPushButton = QPushButton('C')
self.__mouseRedMax.clicked.connect(lambda:
↪  self.recordMouseLimit(self.__inputRedMax))

self.__pathLabel: QLabel = QLabel()
self.__pathLabel.setText("Path to objects:")

self.__objectNameLabel: QLabel = QLabel()
self.__objectNameLabel.setText("Object Name:")

self.__PALabel: QLabel = QLabel()
self.__PALabel.setText("Position Angle for rotation (degrees):")

self.__blueLimitsLayout = QHBoxLayout()
self.__lineLimitsLayout = QHBoxLayout()
```

```
self.__redLimitsLayout = QHBoxLayout()

self.__blueLimitsLabel: QLabel = QLabel()
self.__blueLimitsLabel.setText("Blue limits:")

self.__blueLimitsLayout.addWidget(self.__inputBlueMin)
self.__blueLimitsLayout.addWidget(self.__mouseBlueMin)
self.__blueLimitsLayout.addWidget(self.__inputBlueMax)
self.__blueLimitsLayout.addWidget(self.__mouseBlueMax)

self.__lineLimitsLabel: QLabel = QLabel()
self.__lineLimitsLabel.setText("Line region:")

self.__lineLimitsLayout.addWidget(self.__inputLineMin)
self.__lineLimitsLayout.addWidget(self.__mouseLineMin)
self.__lineLimitsLayout.addWidget(self.__inputLineMax)
self.__lineLimitsLayout.addWidget(self.__mouseLineMax)

self.__redLimitsLabel: QLabel = QLabel()
self.__redLimitsLabel.setText("Red limits:")

self.__redLimitsLayout.addWidget(self.__inputRedMin)
self.__redLimitsLayout.addWidget(self.__mouseRedMin)
self.__redLimitsLayout.addWidget(self.__inputRedMax)
self.__redLimitsLayout.addWidget(self.__mouseRedMax)

leftWidget: QWidget = QWidget()
leftWidget.setLayout(QVBoxLayout())
leftWidget.layout().addWidget(self.__pathLabel)
leftWidget.layout().addWidget(self.__inputPath)
leftWidget.layout().addWidget(self.__objectNameLabel)
leftWidget.layout().addWidget(self.__inputObjectName)
leftWidget.layout().addWidget(self.__PALabel)
leftWidget.layout().addWidget(self.__inputPA)
leftWidget.layout().addWidget(self.__rotatePA)

leftWidget.layout().addWidget(self.__blueLimitsLabel)
leftWidget.layout().addLayout(self.__blueLimitsLayout)
leftWidget.layout().addWidget(self.__lineLimitsLabel)
leftWidget.layout().addLayout(self.__lineLimitsLayout)
leftWidget.layout().addWidget(self.__redLimitsLabel)
leftWidget.layout().addLayout(self.__redLimitsLayout)

leftWidget.layout().addWidget(self.__loadButton)
leftWidget.layout().addWidget(self.__runButton)
```

```
        leftWidget.layout().addWidget(self.__runAllButton)

        leftWidget.layout().addWidget(self.__logOutput)

        self.__widget.addWidget(leftWidget)
        self.__widget.addWidget(self.__plotWidget)

        self.__axes: Axes = self.__plotCanvas.figure.add_subplot(211)
        self.__axes.set_ylabel("$F_\lambda$")
        self.__axes_Stokes: Axes = self.__plotCanvas.figure.add_subplot(212)
        self.__axes_Stokes.set_ylabel("$Q$")
        self.__axes_Stokes.set_xlabel("$\lambda (\AA)$")

        print("Enter path to observations, object name, then press enter. Select position
        ↪   angle rotation if desired.\nPress Load Files, then choose your limits on the
        ↪   plot. Press Run Extraction.")

    def __del__(self):
        '''Restore sys.stdout'''
        sys.stdout = sys.__stdout__

    def getWindow(self) -> QMainWindow:
        '''Returns window'''
        return self.__window

    def __pathSet(self) -> None:
        '''Detects button presses and sets variables from text boxes'''
        self.__path = self.__inputPath.text()
        self.__objectName = self.__inputObjectName.text()
        if (self.__path is not None) and (self.__objectName is not None):
            self.__loadButton.clicked.connect(self.loadOneFile)
            self.__runButton.clicked.connect(self.__lpm.doLinePolExtractionSequence)
            self.__runAllButton.clicked.connect(self.__lpm.doLinePolExtractionAll)
            print('Input path: ', self.__path)
            print('Input object: ', self.__objectName)

    def loadOneFile(self):
        '''Loads and plots the first spectrum'''
        self.__lpm.loadOneFile(self.__path, self.__objectName)
        #clear axes
        self.__axes.cla()
        self.__axes_Stokes.cla()
        #replot
        self.__axes.set_ylabel("$F_\lambda$")
        self.__axes_Stokes.set_ylabel("$Q$")
```

```
        self.__axes_Stokes.set_xlabel("$\lambda (\AA)$")

        self.__axes.plot(self.__lpm.wavelengths, self.__lpm.i)
        self.__axes_Stokes.plot(self.__lpm.wavelengths, self.__lpm.q)
        self.plotvLines(self.__limits)
        self.__plotCanvas.draw_idle()
        self.__loaded = True

    def normalOutputWritten(self, text) -> None:
        """Append text to the QTextEdit."""
        # Maybe QTextEdit.append() works as well, but this is how I do it:
        cursor = self.__logOutput.textCursor()
        cursor.movePosition(QTextCursor.End)
        cursor.insertText(text)
        self.__logOutput.setTextCursor(cursor)
        self.__logOutput.ensureCursorVisible()

    def PAChecked(self) -> None:
        '''Records and outputs PA options'''
        if self.__rotatePA.isChecked() == True:
            self.__lpm.rotation = True
            self.__PA = self.__inputPA.text()
            print('PA will be rotated by ', self.__PA, ' deg')
        else:
            self.__lpm.rotation = False
            print('PA will not be rotated')

    def getMousePos(self, event) -> None:
        '''Gets and plots mouse position'''
        if event.button == 1:
            self.__mouseX = int(event.xdata)
            self.__editedWidget.setText(str(self.__mouseX))
            self.__plotCanvas.mpl_disconnect(self.__recorder)
            self.recordLimit()
        else:
            pass

    def plotvLines(self, xList) -> None:
        '''Plots and updates vertical lines to show limits'''
        if self.__loaded:
            for i, x in enumerate(xList):
                if self.__lines[i] is not None:
                    self.__lines[i].remove()

                if self.__lines_Stokes[i] is not None:
```

```
                self.__lines_Stokes[i].remove()

            if x > 0:
                self.__lines[i] = self.__axes.vlines(x, 0, np.max(self.__lpm.i))
                self.__lines_Stokes[i] = self.__axes_Stokes.vlines(x,
                ↪   np.min(self.__lpm.q), np.max(self.__lpm.q))

            self.__plotCanvas.draw_idle()

def recordLimit(self) -> None:
    '''Records limits to variables'''
    if len(self.__inputBlueMin.text()) > 0:
        print("Blue continuum min set to: ", self.__inputBlueMin.text())
        self.__limits[0] = self.__lpm.blueContinuumMin =
        ↪   float(self.__inputBlueMin.text())

    if len(self.__inputBlueMax.text()) > 0:
        print("Blue continuum max set to: ", self.__inputBlueMax.text())
        self.__limits[1] = self.__lpm.blueContinuumMax =
        ↪   float(self.__inputBlueMax.text())

    if len(self.__inputLineMin.text()) > 0:
        print("Line min set to: ", self.__inputLineMin.text())
        self.__limits[2] = self.__lpm.lineMin = float(self.__inputLineMin.text())

    if len(self.__inputLineMax.text()) > 0:
        print("Line max set to: ", self.__inputLineMax.text())
        self.__limits[3] = self.__lpm.lineMax = float(self.__inputLineMax.text())

    if len(self.__inputRedMin.text()) > 0:
        print("Red continuum min set to: ", self.__inputRedMin.text())
        self.__limits[4] = self.__lpm.redContinuumMin =
        ↪   float(self.__inputRedMin.text())

    if len(self.__inputRedMax.text()) > 0:
        print("Red continuum max set to: ", self.__inputRedMax.text())
        self.__limits[5] = self.__lpm.redContinuumMax =
        ↪   float(self.__inputRedMax.text())

    #Once all inputs are given, check for errors
    if len(self.__inputBlueMin.text()) > 0 and len(self.__inputBlueMax.text()) > 0 and
    ↪   len(self.__inputLineMin.text()) > 0 \
        and len(self.__inputLineMax.text()) > 0 and len(self.__inputRedMin.text()) > 0
        ↪   and len(self.__inputRedMax.text()) > 0:
        self.__lpm.wavelengthErrorCheck()
```

```
        #Plot the limits
        self.plotvLines(self.__limits)

    def recordMouseLimit(self, widget) -> None:
        '''Starts mouse connection'''
        self.__recorder = self.__plotCanvas.mpl_connect('button_press_event',
        ↪  self.getMousePos)
        self.__editedWidget = widget
        print("Click on the plot to set a limit")
```

A.6.3 Launcher

```
from lines_pol_gui import MainWindow
from PyQt5.QtWidgets import QApplication
import sys

def main():
    app = QApplication([])

    mainWindow: MainWindow = MainWindow()
    mainWindow.getWindow().show()

    sys.exit(app.exec_() )

if __name__ == "__main__":
    main()
```

A.7 Polarimetric data for stars with multiple observations

I present the data that were used in Section 2.4 in the tables in this section.

Table A.1: Observational data for objects with fewer than 5 observations. All objects in this table were observed at ESO/La Silla.

HJD ($UBVR$)		U			B			V			R	
2,440,000+	q (%)	u (%)	σ_p (%)	q (%)	u (%)	σ_p (%)	q (%)	u (%)	σ_p (%)	q (%)	u (%)	σ_p (%)
WR 16												
412.5653	-1.213	-0.892	0.052	-1.120	-1.118	0.058	-1.010	-1.121	0.081	-1.039	-0.852	0.165
413.5327	-1.144	-0.771	0.029	-1.216	-1.108	0.018	-1.453	-1.161	0.082	-1.041	-1.279	0.024
415.5219	-1.234	-0.657	0.022	-1.304	-0.912	0.023	-1.527	-1.134	0.043	-1.221	-1.075	0.018
417.5685	-1.299	-0.685	0.031	-1.364	-1.011	0.024	-1.508	-1.179	0.048	-1.169	-1.211	0.013
WR 22	.	.	.	.	.	.	.	.	.	.	.	.
412.6005	-1.364	-0.804	0.094	-1.685	-1.095	0.040	-1.538	-0.965	0.080	-1.747	-0.884	0.080
414.5200	-1.475	-0.724	0.018	-1.683	-0.832	0.014	-1.681	-0.940	0.021	-1.768	-0.792	0.019
WR 40	.	.	.	.	.	.	.	.	.	.	.	.
411.5639	-0.624	-0.899	0.043	-0.738	-1.050	0.016	-0.816	-1.157	0.016	-0.805	-1.044	0.009
414.6098	-0.771	-0.587	0.021	-0.802	-0.708	0.018	-0.924	-0.808	0.029	-0.844	-0.753	0.015
416.5346	-0.437	-0.840	0.015	-0.560	-0.969	0.022	-0.718	-1.139	0.045	-0.627	-0.999	0.012
417.6413	-0.578	-0.702	0.032	-0.514	-0.907	0.029	-0.641	-0.932	0.065	-0.577	-0.893	0.025
WR 43	.	.	.	.	.	.	.	.	.	.	.	. .
415.6781	-0.363	-0.530	0.114	-0.104	-1.121	0.056	-0.182	-1.166	0.107	0.154	-1.425	0.127
416.6258	-0.163	-0.918	0.035	-0.091	-1.061	0.042	-0.041	-1.271	0.032	-0.073	-1.186	0.035
WR 48	.	.	.	.	.	.	.	.	.	.	.	. .
411.6689	-1.172	0.413	0.042	-1.288	0.497	0.016	-1.345	0.511	0.030	-1.325	0.472	0.024
417.7561	-1.503	0.271	0.144	-1.398	0.202	0.032	-1.402	0.213	0.060	-1.507	0.313	0.035
WR 71	.	.	.	.	.	.	.	.	.	.	.	. .
415.7723	-0.455	0.995	0.022	-0.566	1.045	0.026	-0.588	1.121	0.036	-0.637	1.081	0.027
417.8569	-0.777	1.073	0.152	-0.924	1.065	0.112	-0.985	0.692	0.087	-0.085	0.896	0.209
WR 103	.	.	.	.	.	.	.	.	.	.	.	. .
411.9105	-0.130	-0.810	0.027	-0.064	-0.853	0.016	-0.038	-0.964	0.026	-0.060	-0.819	0.019
413.9067	-0.077	-0.831	0.037	-0.062	-0.896	0.019	-0.024	-0.909	0.053	-0.092	-0.896	0.019
416.8269	-0.269	-0.780	0.017	-0.192	-0.856	0.018	-0.133	-1.030	0.047	-0.220	-0.812	0.020
417.7832	-0.068	-0.686	0.025	-0.022	-0.842	0.033	-0.109	-0.902	0.040	-0.120	-0.761	0.032
WR 111	.	.	.	.	.	.	.	.	.	.	.	. .
410.9057	-0.184	-0.384	0.183	-0.231	-0.220	0.030	-0.223	-0.313	0.058	-0.298	-0.172	0.033
414.7455	-0.095	-0.099	0.014	-0.162	-0.219	0.011	-0.271	-0.247	0.052	-0.299	-0.222	0.019
WR 113	.	.	.	.	.	.	.	.	.	.	.	. .
410.9282	-3.220	0.161	0.203	-2.632	-0.047	0.045	-2.410	-0.199	0.053	-2.307	-0.099	0.018
414.8588	-2.240	-0.174	0.047	-2.527	-0.285	0.038	-2.607	-0.410	0.029	-2.487	-0.361	0.032

Table A.2: Polarimetric observations of WR 133. Observed at the Crimean Observatory.

HJD	*U*				*B*				*V*			
2,447,000+	q (%)	σ_q	u	σ_u (%)	q (%)	σ_q (%)	u (%)	σ_u (%)	q (%)	σ_q (%)	u (%)	σ_u (%)
320.408	0.446	0.025	-0.310	0.030	0.386	0.048	-0.349	0.013	0.295	0.021	-0.321	0.035
321.460	0.511	0.031	-0.307	0.017	0.466	0.020	-0.350	0.020	0.467	0.026	-0.341	0.032
322.453	0.160	0.047	-0.248	0.089	0.233	0.061	-0.322	0.061	0.039	0.096	-0.486	0.074
325.395	0.192	0.081	-0.325	0.058	0.265	0.069	-0.287	0.029	0.242	0.031	-0.225	0.040
329.412	0.352	0.105	-0.353	0.057	0.329	0.052	-0.350	0.006	0.237	0.040	-0.350	0.024
335.439	0.335	0.033	-0.264	0.031	0.328	0.021	-0.328	0.019	0.323	0.039	-0.362	0.020
338.364	0.316	0.048	-0.646	0.097	0.330	0.023	-0.459	0.043	0.213	0.034	-0.438	0.040
339.357	0.059	0.129	0.073	0.079	0.313	0.076	-0.133	0.063	0.334	0.051	-0.125	0.074
341.536	-0.117	0.303	0.148	0.115	0.064	0.094	0.041	0.124	0.249	0.020	0.001	0.078
348.370	0.335	0.079	-0.119	0.047	0.340	0.031	-0.233	0.021	0.385	0.041	-0.329	0.036
349.361	0.399	0.021	-0.241	0.019	0.386	0.032	-0.329	0.030	0.261	0.055	-0.280	0.011
424.329	0.289	0.040	0.017	0.092	0.342	0.009	-0.208	0.072	0.373	0.019	-0.111	0.062
434.249	0.574	0.038	-0.242	0.037	0.434	0.018	-0.376	0.012	0.358	0.032	-0.370	0.025
435.274	0.459	0.012	-0.268	0.011	0.432	0.015	-0.301	0.033	0.355	0.034	-0.327	0.021
437.263	0.461	0.024	-0.256	0.045	0.434	0.013	-0.254	0.033	0.354	0.025	-0.305	0.019
689.368	0.282	0.032	-0.294	0.020	0.316	0.014	-0.259	0.014	0.303	0.019	-0.244	0.023
690.389	0.359	0.003	-0.308	0.021	0.340	0.020	-0.240	0.012	0.308	0.041	-0.264	0.028
695.377	0.319	0.029	-0.290	0.057	0.331	0.014	-0.285	0.008	0.341	0.008	-0.276	0.017

Table A.2: cont.

HJD		U				B				V		
2,447,000+	q (%)	σ_q	u	σ_u (%)	q (%)	σ_q (%)	u (%)	σ_u (%)	q (%)	σ_q (%)	u (%)	σ_u (%)
722.377	0.375	0.020	-0.231	0.023	0.441	0.030	-0.260	0.019	0.391	0.027	-0.268	0.031
729.336	0.408	0.017	-0.286	0.050	0.384	0.032	-0.297	0.042	0.390	0.024	-0.320	0.049
730.318	0.381	0.032	-0.235	0.033	0.431	0.030	-0.270	0.010	0.372	0.031	-0.266	0.018
757.422	0.563	0.241	-0.900	0.160	0.404	0.035	-0.327	0.058	0.374	0.041	-0.237	0.068
759.463	0.304	0.056	-0.085	0.049	0.333	0.038	-0.168	0.035	0.412	0.031	-0.253	0.050
760.272	0.357	0.030	-0.208	0.035	0.326	0.026	-0.216	0.020	0.335	0.044	-0.313	0.026
760.547	0.212	0.078	-0.144	0.058	0.360	0.025	-0.228	0.043	0.301	0.025	-0.296	0.029
761.304	0.386	0.034	-0.178	0.020	0.405	0.031	-0.212	0.013	0.431	0.059	-0.243	0.014
761.558	0.373	0.054	-0.136	0.060	0.391	0.030	-0.239	0.040	0.298	0.048	-0.221	0.028
762.354	0.408	0.033	-0.138	0.034	0.366	0.033	-0.175	0.027	0.299	0.027	-0.178	0.022
763.531	0.296	0.065	-0.215	0.075	0.367	0.024	-0.229	0.035	0.280	0.038	-0.218	0.046
764.269	0.402	0.025	-0.235	0.025	0.450	0.019	-0.279	0.024	0.396	0.035	-0.268	0.029
764.502	0.444	0.028	-0.299	0.050	0.454	0.038	-0.253	0.031	0.444	0.039	-0.339	0.038
765.365	0.461	0.040	-0.153	0.036	0.487	0.032	-0.193	0.024	0.445	0.038	-0.301	0.030
766.261	0.373	0.027	-0.248	0.021	0.437	0.022	-0.269	0.025	0.353	0.017	-0.335	0.016
766.526	0.384	0.059	-0.088	0.055	0.437	0.036	-0.248	0.030	0.397	0.033	-0.299	0.040
767.252	0.418	0.021	-0.179	0.024	0.435	0.029	-0.275	0.022	0.439	0.035	-0.271	0.029
768.277	0.375	0.013	-0.297	0.016	0.414	0.015	-0.268	0.020	0.371	0.014	-0.293	0.026
768.421	0.408	0.018	-0.240	0.030	0.456	0.025	-0.237	0.025	0.438	0.019	-0.245	0.040
770.276	0.464	0.096	-0.169	0.206	0.566	0.032	-0.249	0.021	0.355	0.025	-0.254	0.079
772.360	0.480	0.058	-0.273	0.048	0.457	0.044	-0.315	0.019	0.440	0.048	-0.334	0.025
773.432	0.396	0.019	-0.243	0.040	0.459	0.022	-0.302	0.041	0.413	0.015	-0.332	0.036
790.397	0.425	0.046	-0.292	0.063	0.400	0.023	-0.314	0.017	0.358	0.019	-0.305	0.014
826.286	0.404	0.011	-0.211	0.033	0.352	0.022	-0.210	0.012	0.335	0.022	-0.338	0.042
835.237	0.457	0.036	-0.138	0.073	0.398	0.021	-0.278	0.040	0.399	0.027	-0.237	0.017
851.212	0.362	0.075	-0.097	0.032	0.302	0.028	-0.203	0.029	0.300	0.032	-0.241	0.049
880.156	0.501	0.063	-0.198	0.119	0.460	0.042	-0.239	0.044	0.370	0.036	-0.296	0.025
880.183	0.678	0.073	-0.344	0.144	0.474	0.026	-0.212	0.036	0.358	0.035	-0.200	0.030
888.209	0.535	0.109	-0.710	0.127	0.445	0.040	-0.326	0.085	0.412	0.042	-0.338	0.058

Table A.3: Polarimetric observations of WR 134. Observed at the Crimean Observatory.

HJD		U				B				V		
2,447,700+	q (%)	σ_q	u	σ_u (%)	q (%)	σ_q (%)	u (%)	σ_u (%)	q (%)	σ_q (%)	u (%)	σ_u (%)
59.3018	1.204	0.048	0.358	0.079	0.946	0.032	0.218	0.048	1.091	0.062	0.303	0.068
60.4033	1.051	0.034	0.265	0.025	0.872	0.039	0.179	0.028	0.912	0.040	0.203	0.026
60.4692	0.946	0.070	0.395	0.060	0.790	0.050	0.229	0.054	0.858	0.046	0.268	0.068
61.2734	1.182	0.059	0.441	0.104	0.990	0.034	0.256	0.077	1.015	0.039	0.275	0.081
61.3306	1.360	0.108	0.340	0.089	1.145	0.044	0.244	0.065	1.261	0.051	0.176	0.071
61.4160	1.284	0.082	0.468	0.086	1.051	0.032	0.331	0.041	1.161	0.060	0.398	0.057
61.5273	1.500	0.097	0.340	0.107	1.009	0.047	0.277	0.019	1.148	0.041	0.292	0.034
62.3887	1.106	0.063	0.191	0.053	0.978	0.034	0.070	0.031	1.035	0.039	0.162	0.058
63.4927	1.182	0.091	0.418	0.111	0.924	0.033	0.286	0.041	1.093	0.066	0.277	0.078
64.4590	1.318	0.061	0.296	0.065	1.025	0.060	0.155	0.039	1.099	0.060	0.159	0.049
65.2705	1.035	0.042	0.224	0.036	0.864	0.023	0.181	0.027	0.898	0.043	0.137	0.038
65.3320	1.065	0.039	0.239	0.038	0.859	0.024	0.111	0.029	0.915	0.042	0.141	0.036
65.3931	1.060	0.054	0.300	0.045	0.880	0.032	0.207	0.035	0.932	0.061	0.163	0.053
65.4751	1.032	0.074	0.291	0.068	0.890	0.043	0.194	0.052	1.041	0.063	0.131	0.062
66.3682	1.187	0.063	0.331	0.029	1.040	0.031	0.223	0.037	1.003	0.056	0.273	0.047
68.3579	1.229	0.031	0.139	0.027	1.056	0.026	0.169	0.027	1.084	0.034	0.109	0.018
72.5010	1.248	0.059	0.194	0.063	1.057	0.046	0.131	0.054	1.132	0.054	0.113	0.045
73.4058	1.068	0.038	0.262	0.055	0.966	0.045	0.169	0.027	1.079	0.036	0.123	0.019

A.8 Interstellar and intrinsic polarization fits

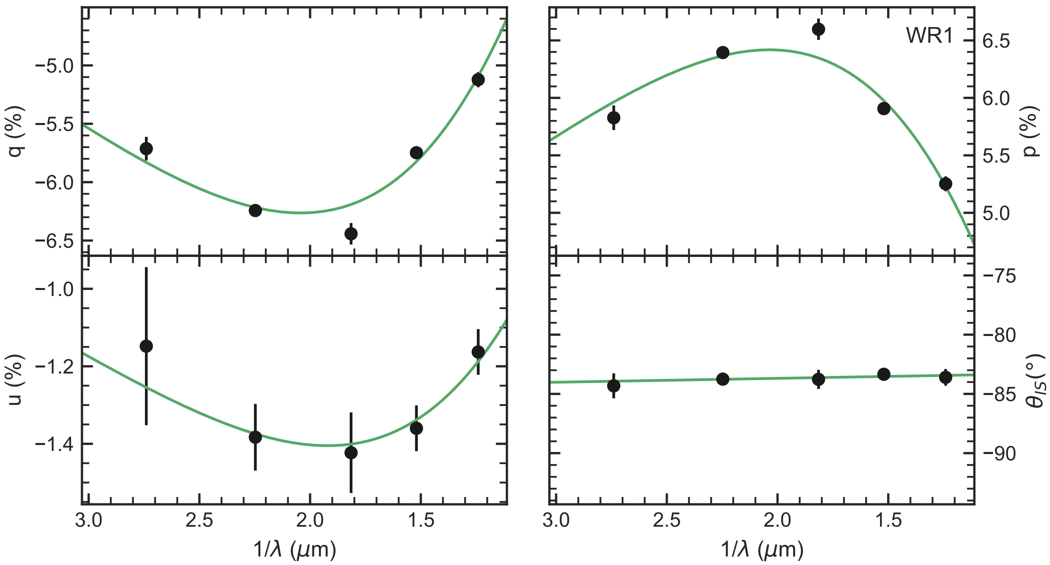

Figure A.2: $UBVRI$ data (black points) fit with equations 2.9 and 2.10 (green curves).

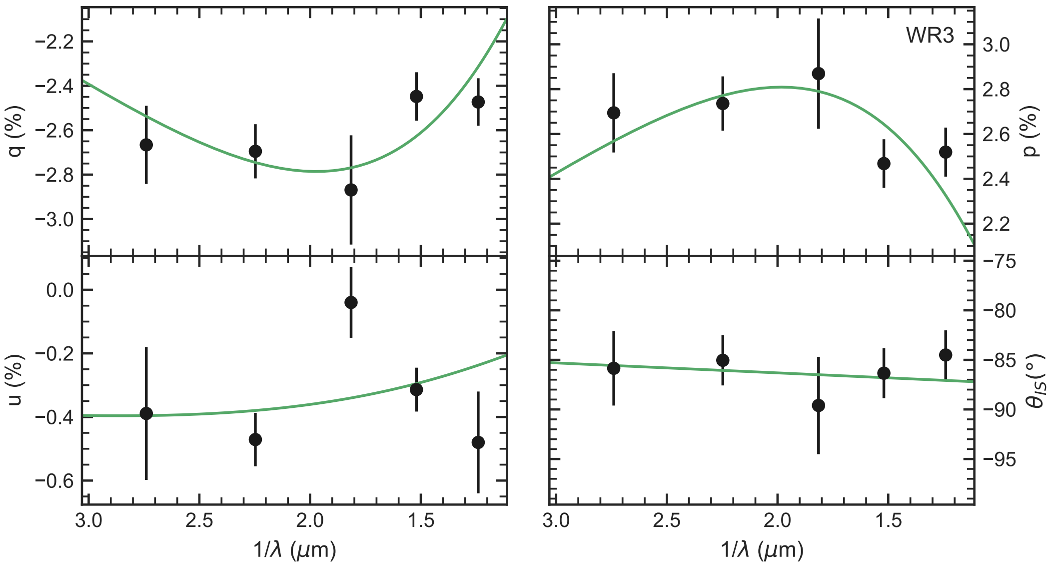

Figure A.3: $UBVRI$ data (black points) fit with equations 2.9 and 2.10 (green curves).

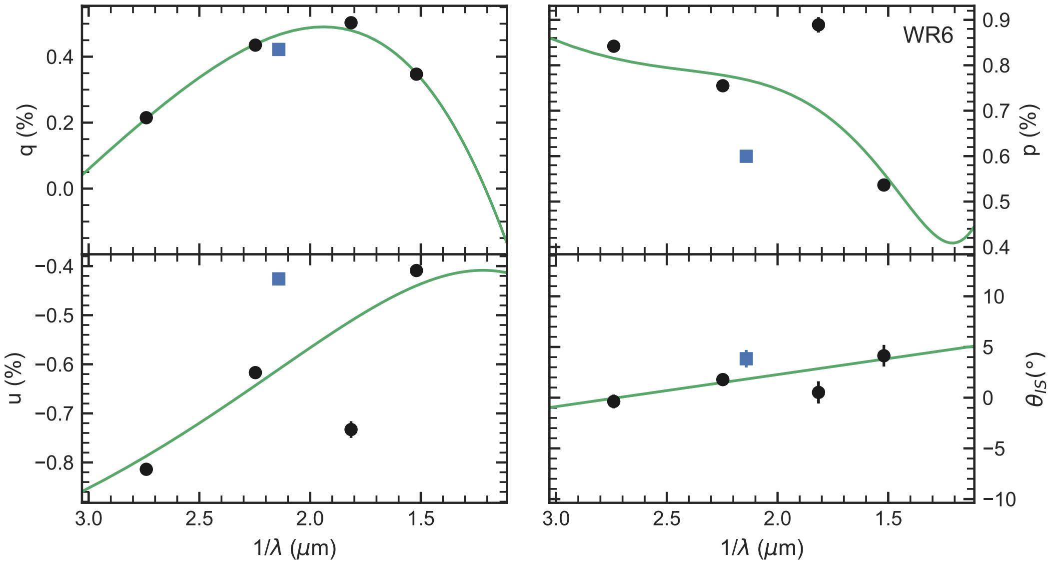

Figure A.4: $UBVRI$ data (black points) fit with equations 2.7 and 2.8 (green curves). b filter data are presented as blue points, but were not included as part of the fit.

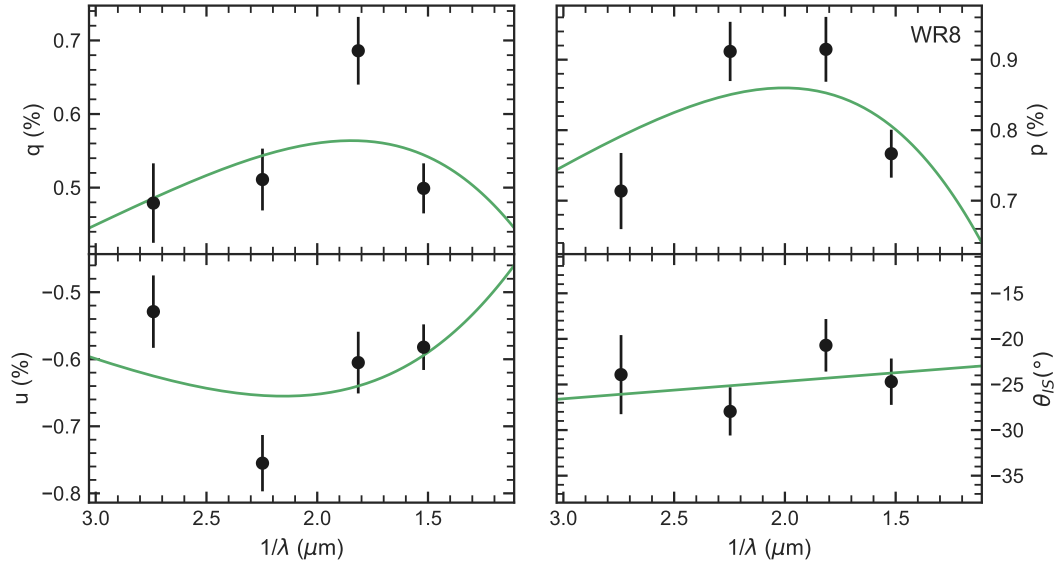

Figure A.5: $UBVRI$ data (black points) fit with equations 2.9 and 2.10 (green curves).

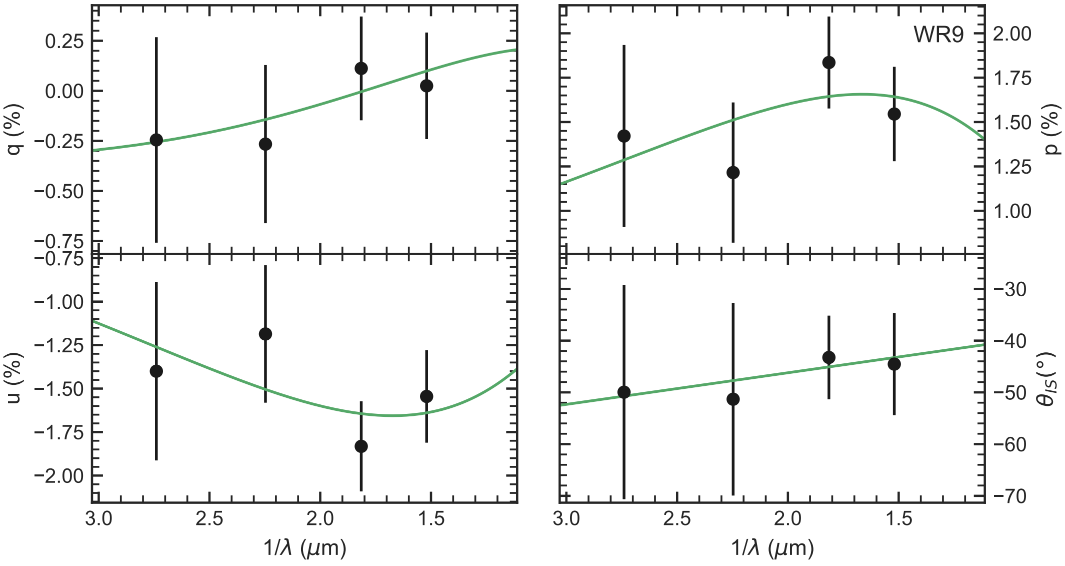

Figure A.6: $UBVRI$ data (black points) fit with equations 2.9 and 2.10 (green curves).

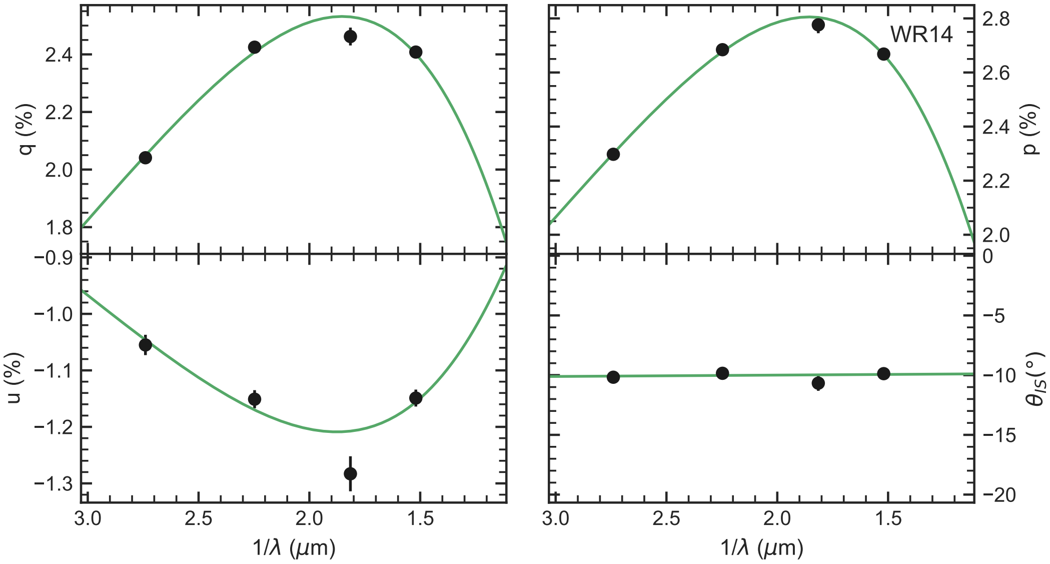

Figure A.7: $UBVRI$ data (black points) fit with equations 2.7 and 2.8 (green curves).

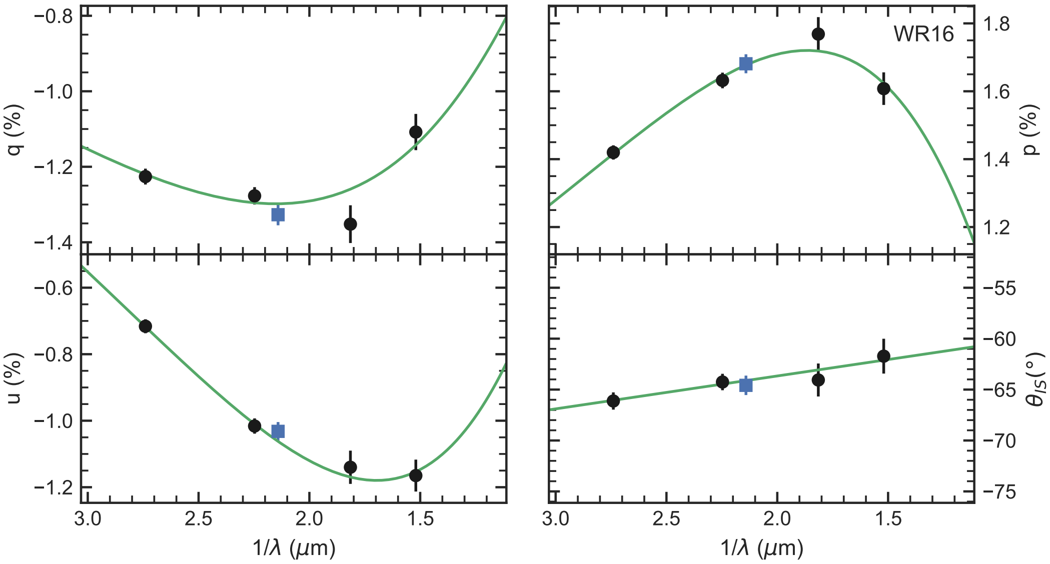

Figure A.8: $UBVRI$ data (black points) fit with equations 2.7 and 2.8 (green curves). b filter data are presented as blue points, but were not included as part of the fit.

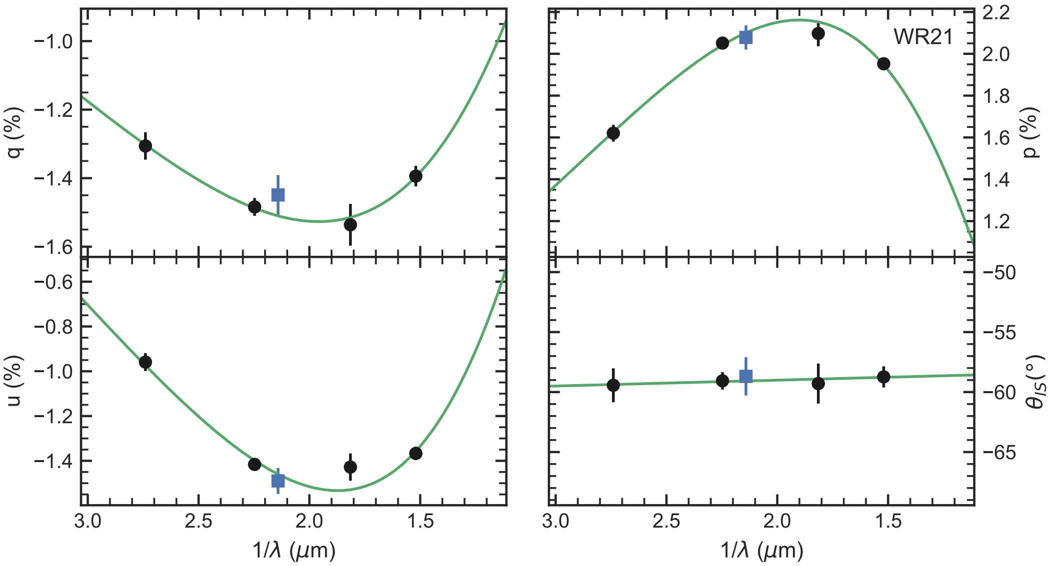

Figure A.9: $UBVRI$ data (black points) fit with equations 2.7 and 2.8 (green curves). b filter data are present as blue points, but were not included as part of the fit.

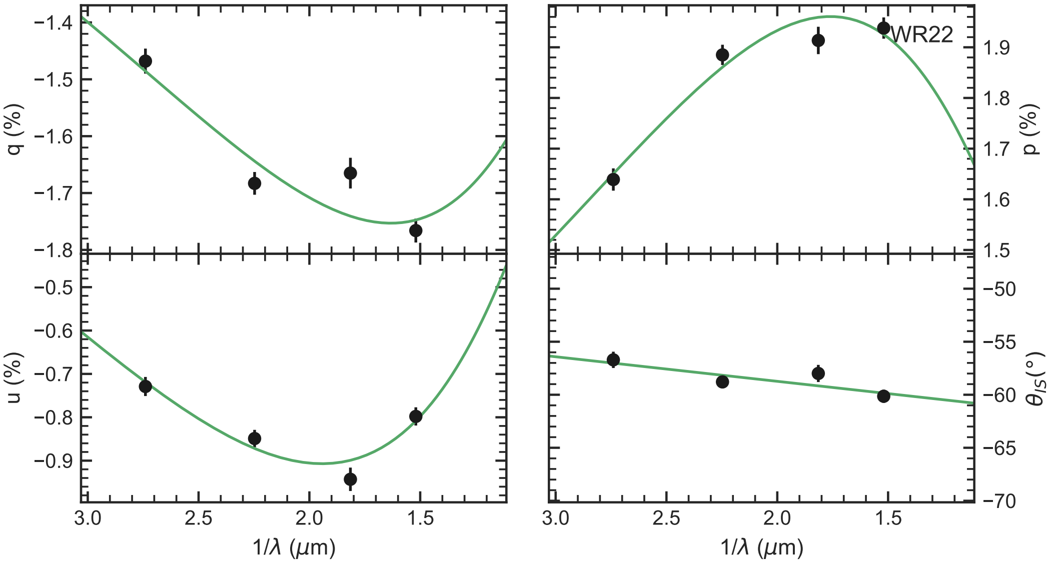

Figure A.10: $UBVRI$ data (black points) fit with equations 2.7 and 2.8 (green curves). b filter data are present as blue points, but were not included as part of the fit.

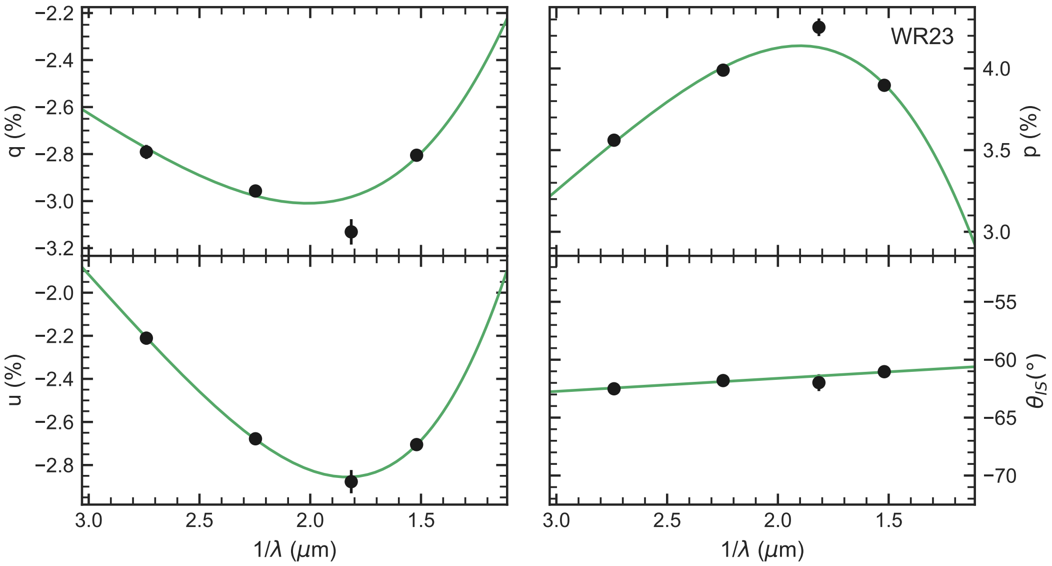

Figure A.11: $UBVRI$ data (black points) fit with equations 2.7 and 2.8 (green curves).

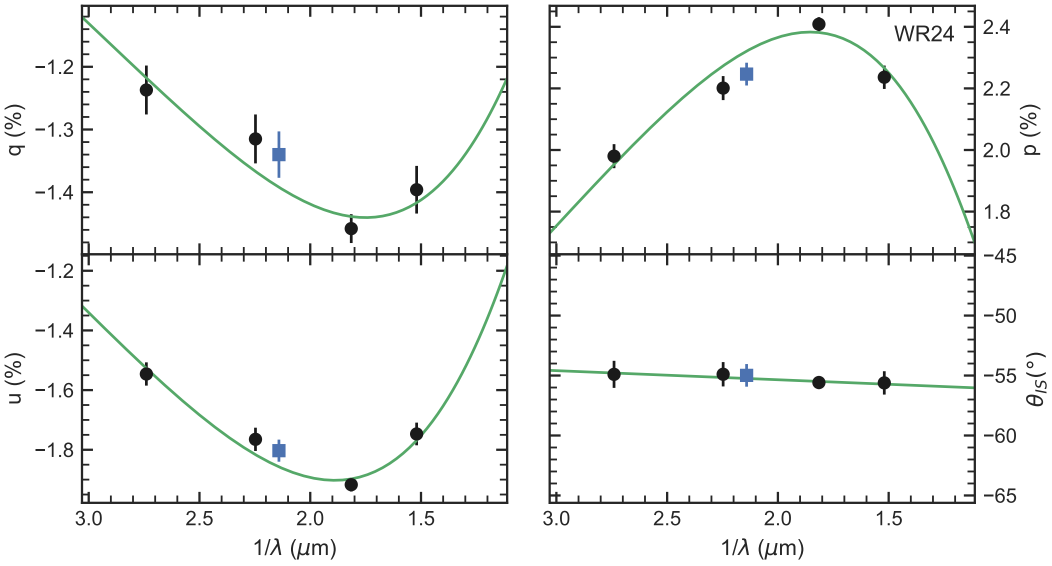

Figure A.12: $UBVRI$ data (black points) fit with equations 2.7 and 2.8 (green curves). b filter data are present as blue points, but were not included as part of the fit.

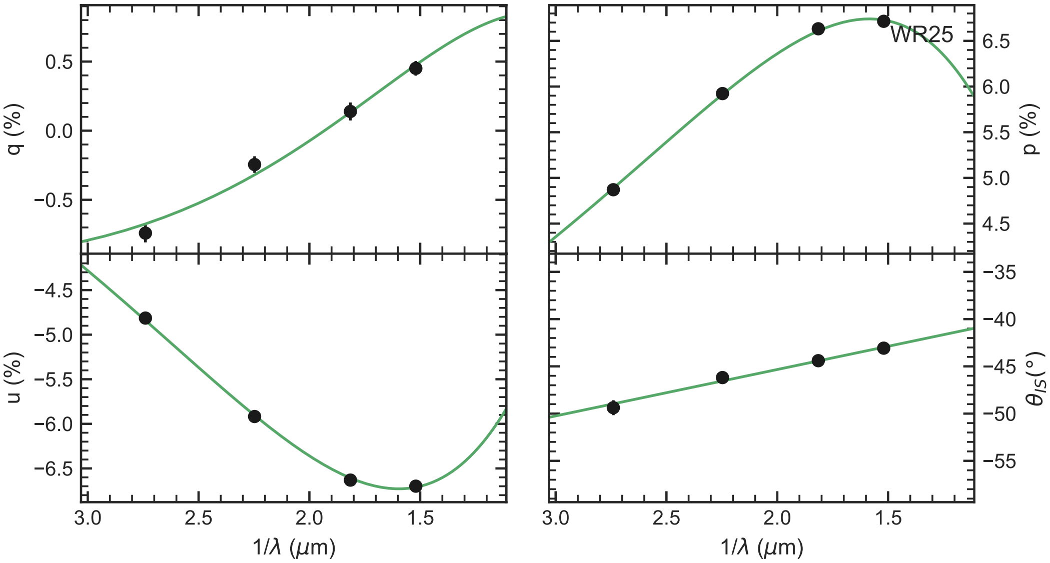

Figure A.13: *UBVRI* data (black points) fit with equations 2.9 and 2.10 (green curves). *b* filter data are present as blue points, but were not included as part of the fit.

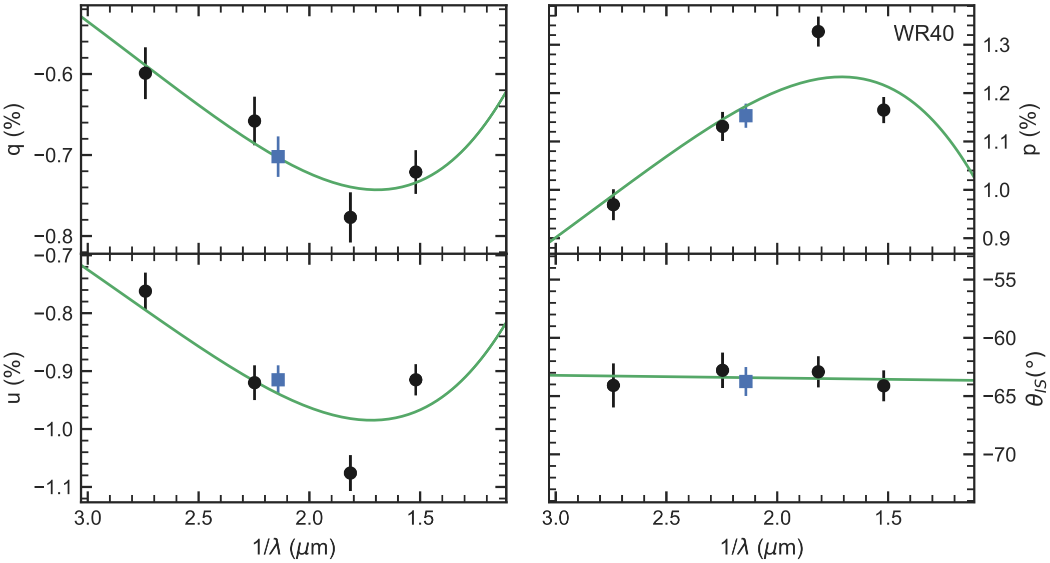

Figure A.14: *UBVRI* data (black points) fit with equations 2.9 and 2.10 (green curves). *b* filter data are present as blue points, but were not included as part of the fit.

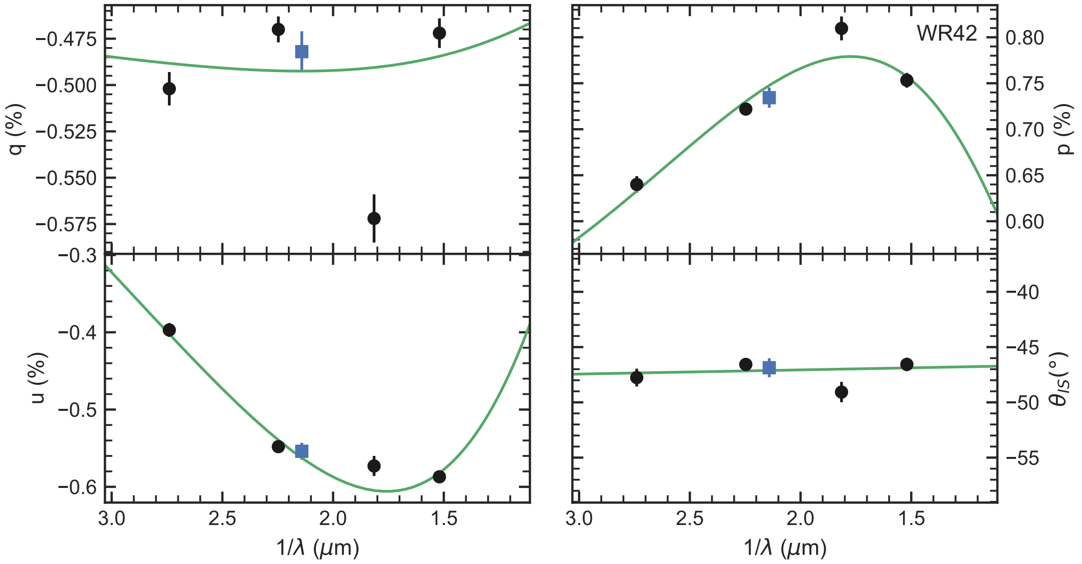

Figure A.15: $UBVRI$ data (black points) fit with equations 2.7 and 2.8 (green curves). b filter data are present as blue points.

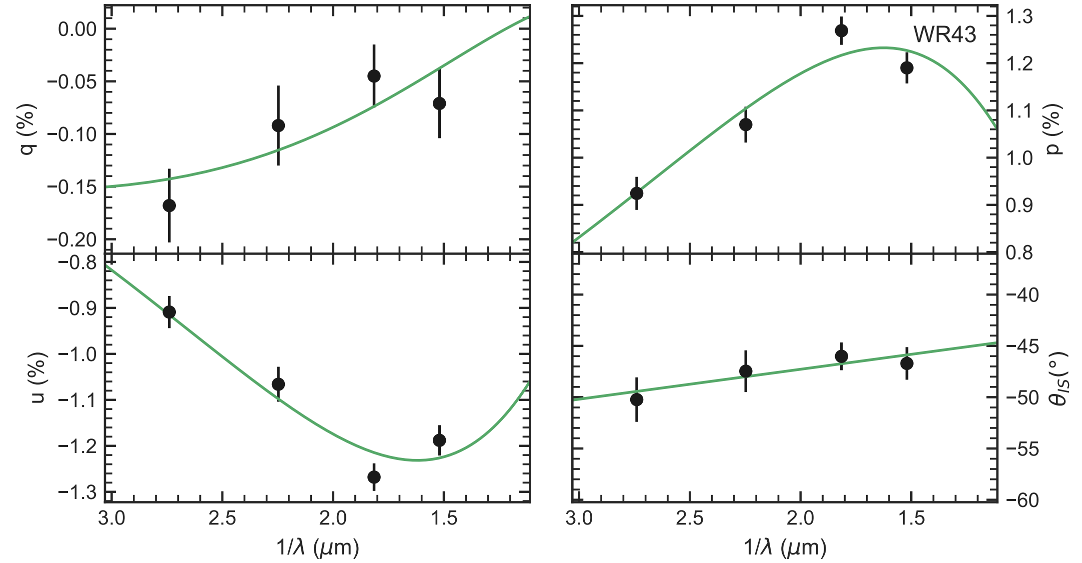

Figure A.16: $UBVRI$ data (black points) fit with equations 2.9 and 2.10 (green curves).

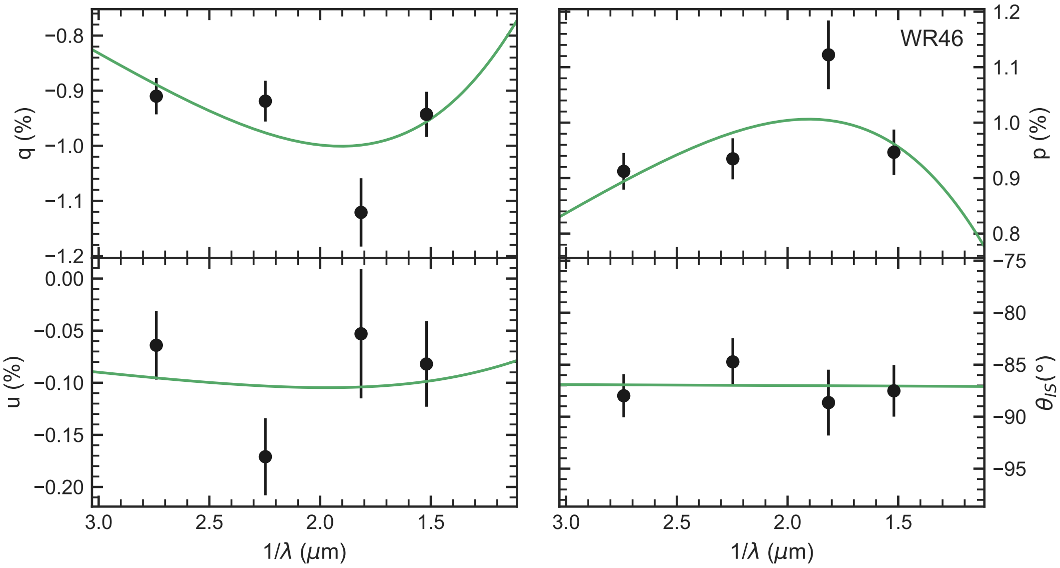

Figure A.17: *UBVRI* data (black points) fit with equations 2.9 and 2.10 (green curves).

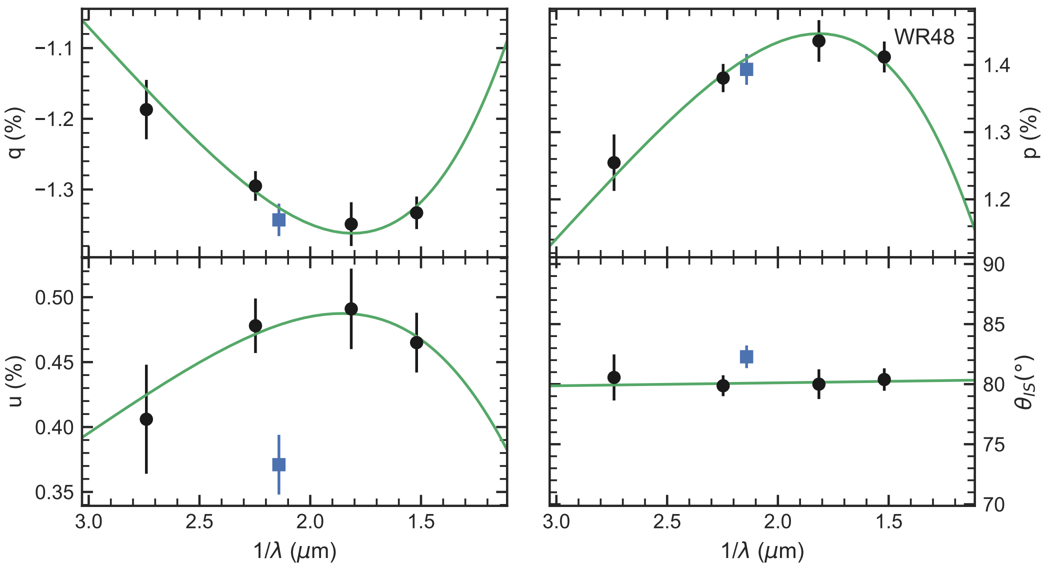

Figure A.18: *UBVRI* data (black points) fit with equations 2.9 and 2.10 (green curves). b filter data are present as blue points, but were not included as part of the fit.

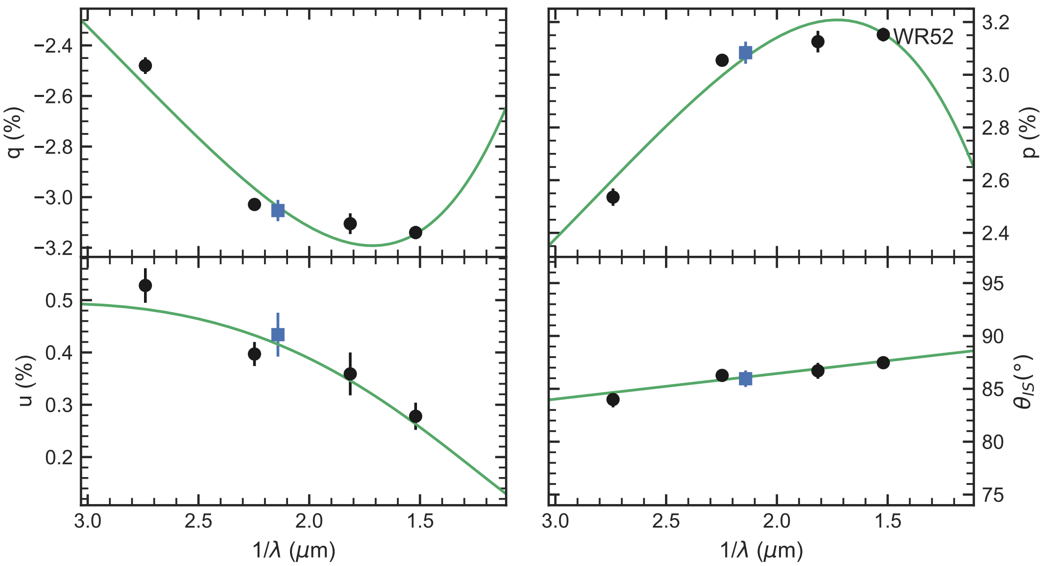

Figure A.19: $UBVRI$ data (black points) fit with equations 2.9 and 2.10 (green curves). b filter data are present as blue points, but were not included as part of the fit.

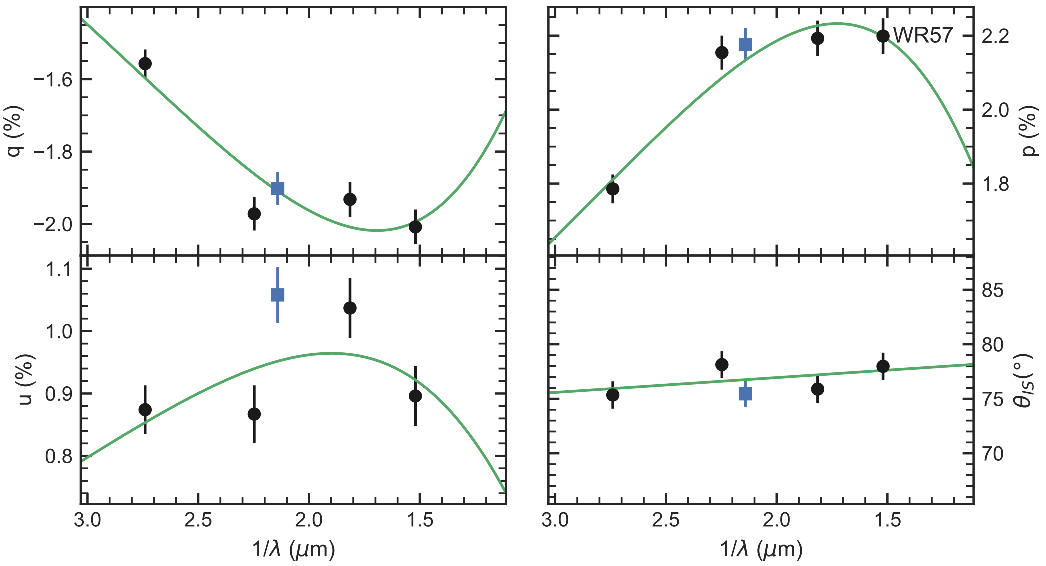

Figure A.20: $UBVRI$ data (black points) fit with equations 2.9 and 2.10 (green curves). b filter data are present as blue points, but were not included as part of the fit.

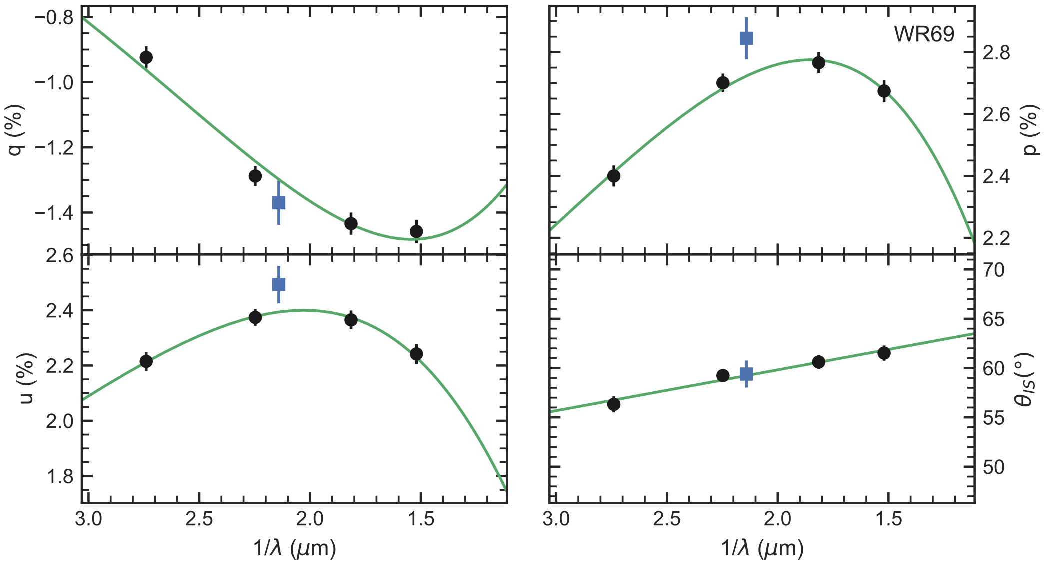

Figure A.21: $UBVRI$ data (black points) fit with equations 2.9 and 2.10 (green curves). b filter data are present as blue points, but were not included as part of the fit.

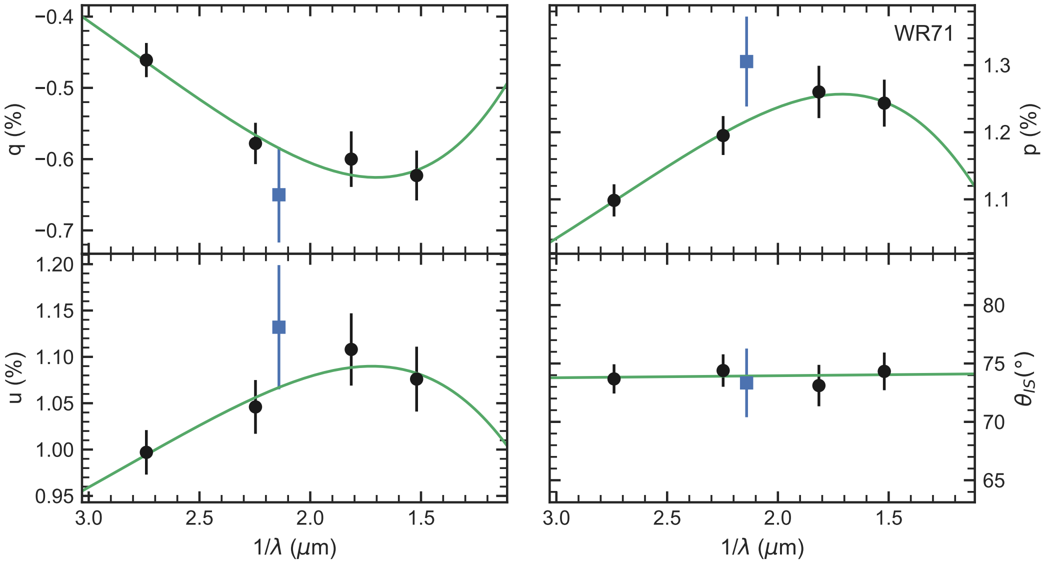

Figure A.22: $UBVRI$ data (black points) fit with equations 2.7 and 2.8 (green curves). b filter data are present as blue points, but were not included as part of the fit.

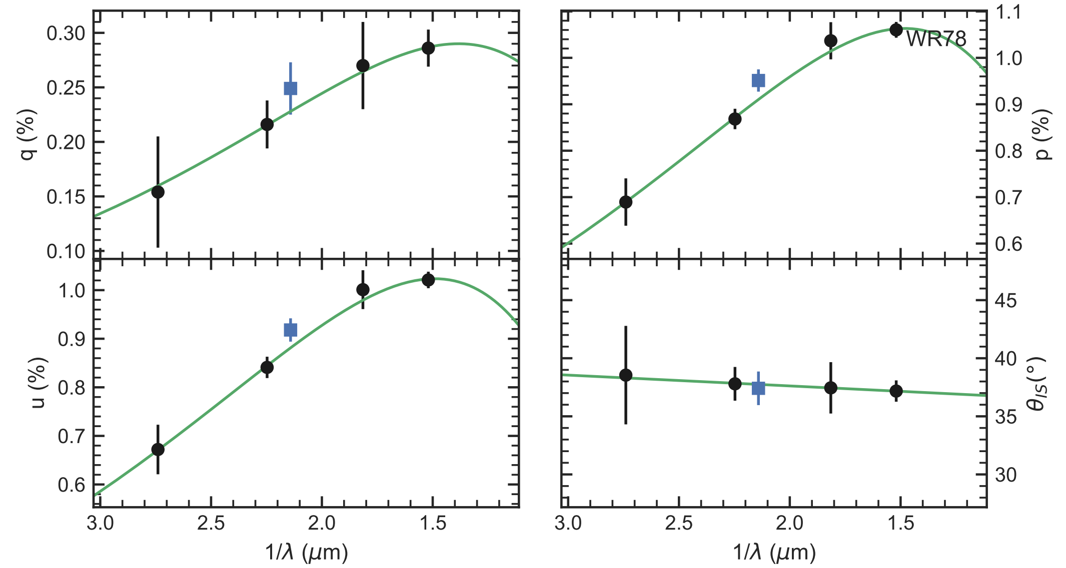

Figure A.23: $UBVRI$ data (black points) fit with equations 2.9 and 2.10 (green curves). b filter data are present as blue points, but were not included as part of the fit.

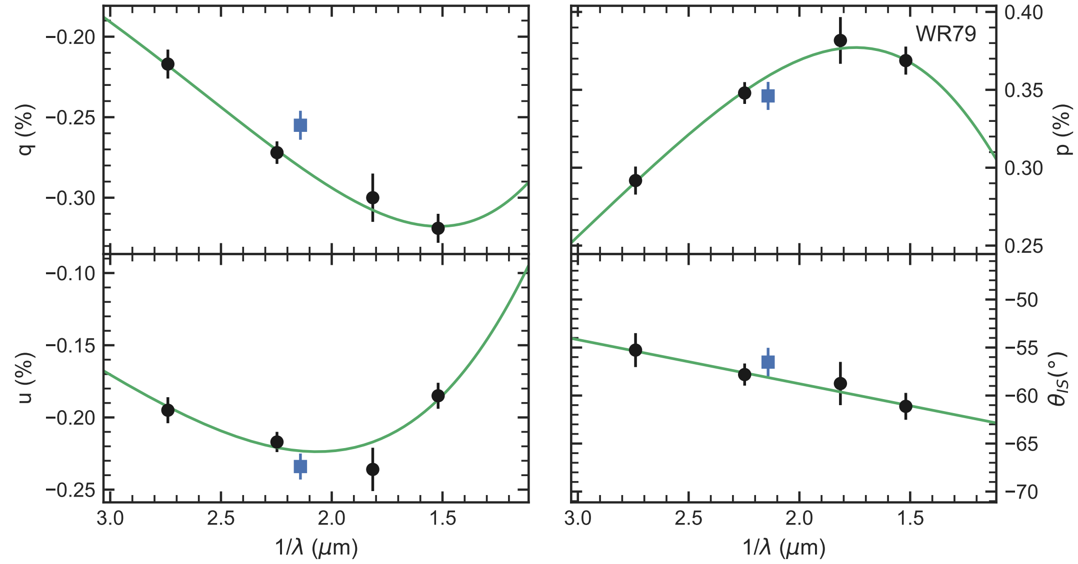

Figure A.24: $UBVRI$ data (black points) fit with equations 2.9 and 2.10 (green curves). b filter data are present as blue points, but were not included as part of the fit.

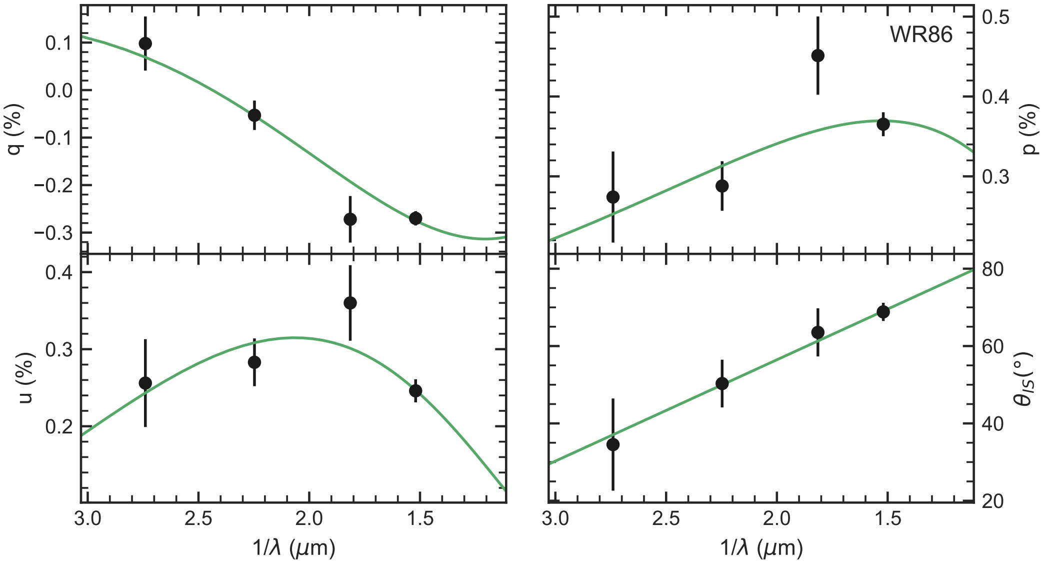

Figure A.25: $UBVRI$ data (black points) fit with equations 2.9 and 2.10 (green curves).

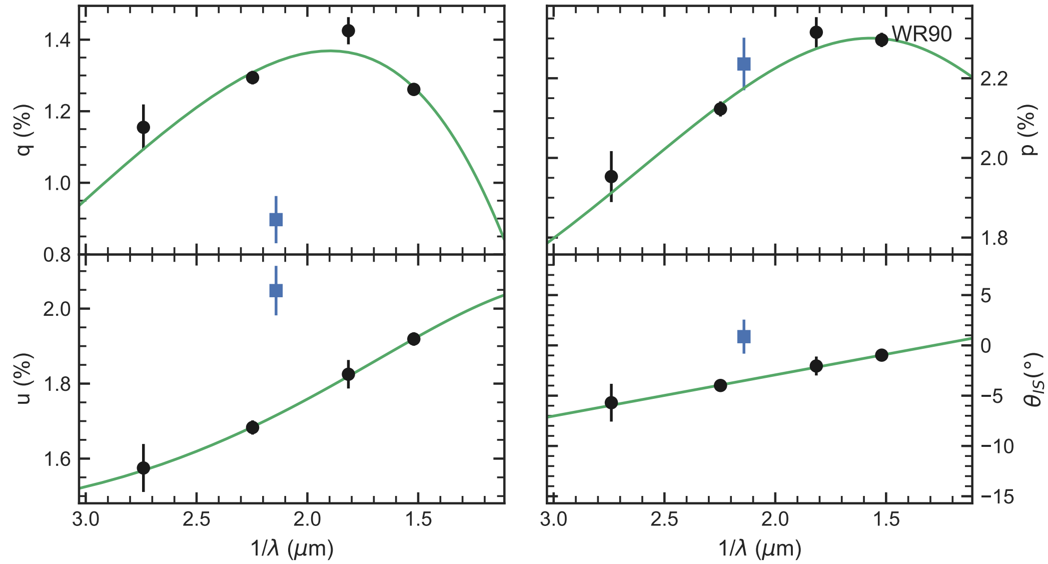

Figure A.26: $UBVRI$ data (black points) fit with equations 2.7 and 2.8 (green curves). b filter data are present as blue points, but were not included as part of the fit.

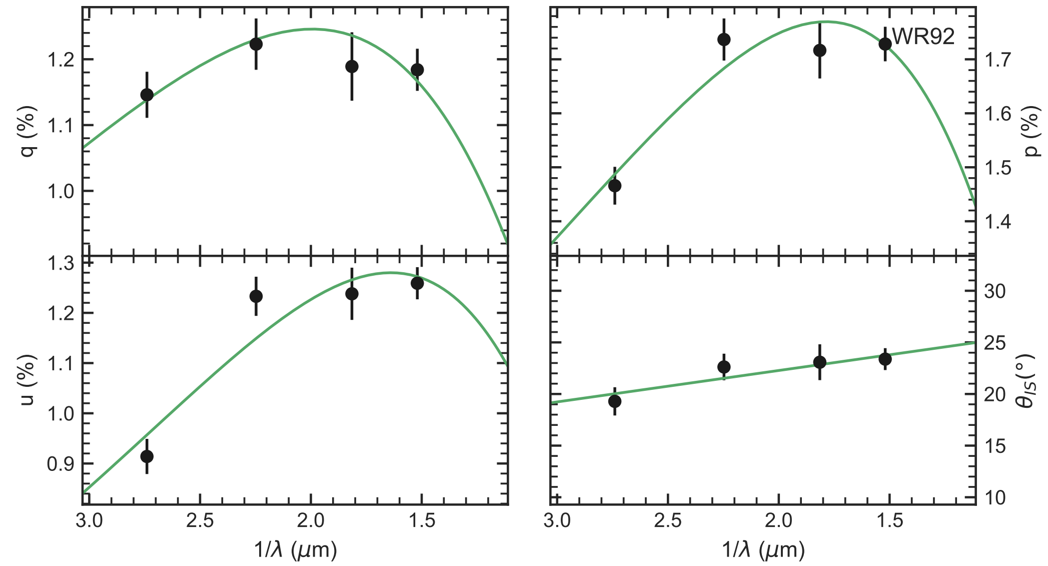

Figure A.27: $UBVRI$ data (black points) fit with equations 2.9 and 2.10 (green curves).

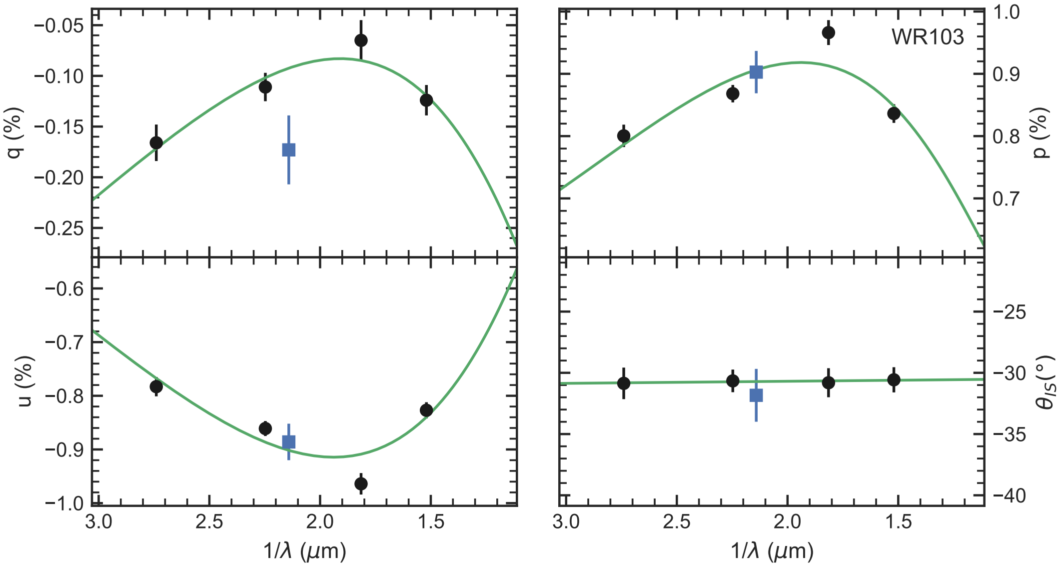

Figure A.28: $UBVRI$ data (black points) fit with equations 2.7 and 2.8 (green curves). b filter data are present as blue points, but were not included as part of the fit.

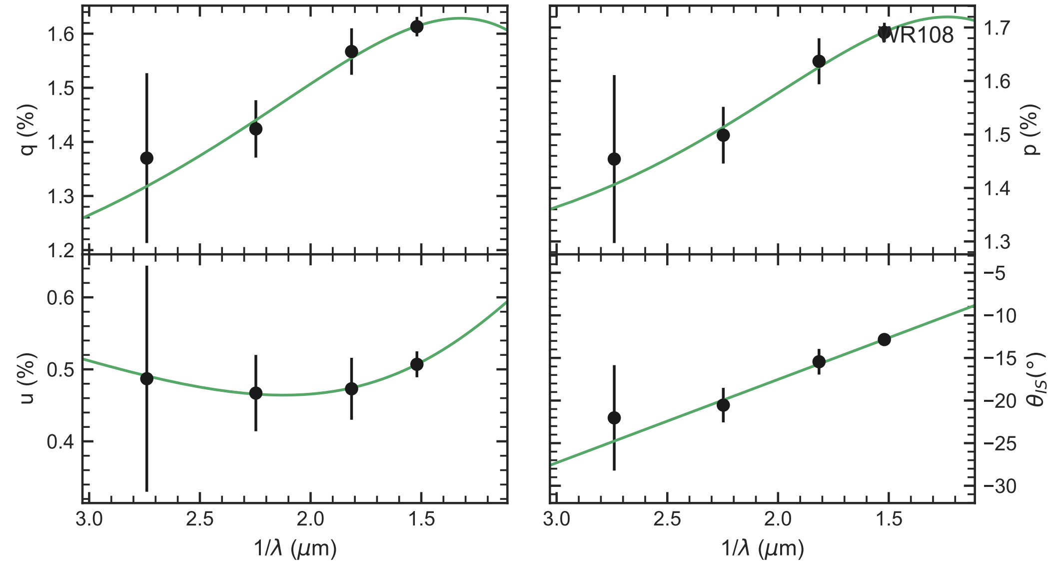

Figure A.29: $UBVRI$ data (black points) fit with equations 2.7 and 2.8 (green curves).

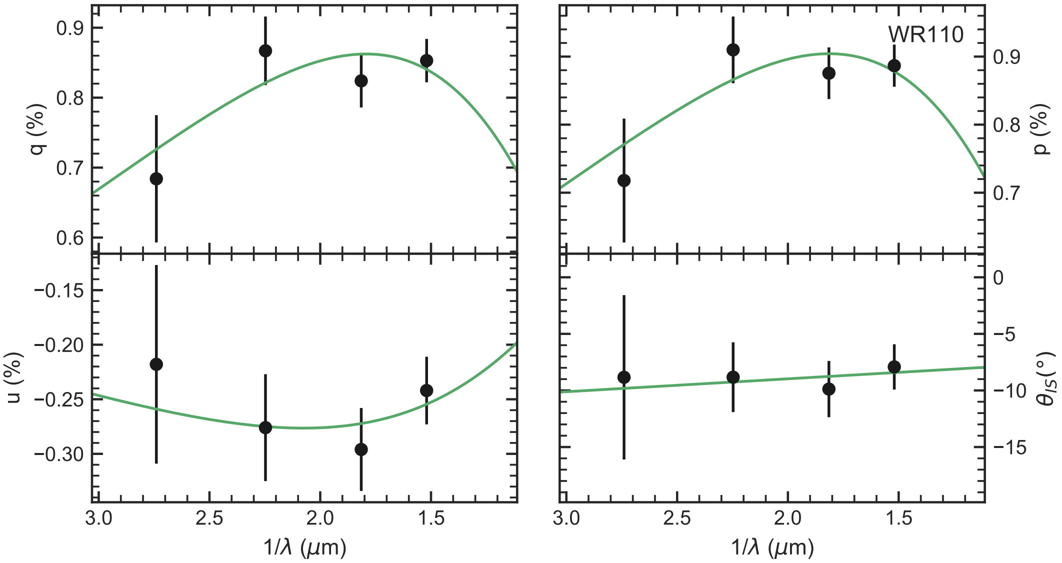

Figure A.30: $UBVRI$ data (black points) fit with equations 2.9 and 2.10 (green curves).

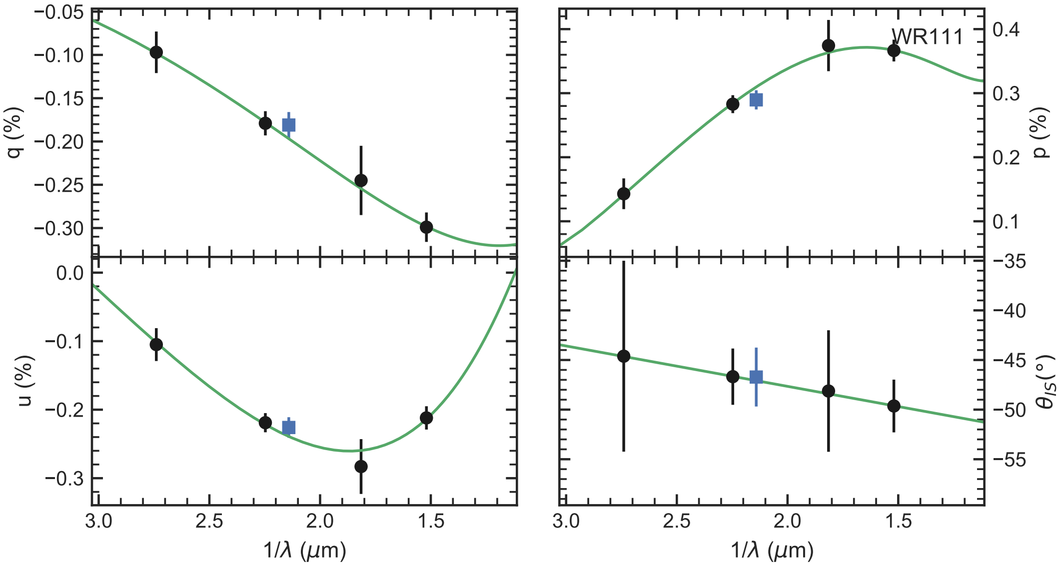

Figure A.31: $UBVRI$ data (black points) fit with equations 2.7 and 2.8 (green curves). b filter data are present as blue points, but were not included as part of the fit.

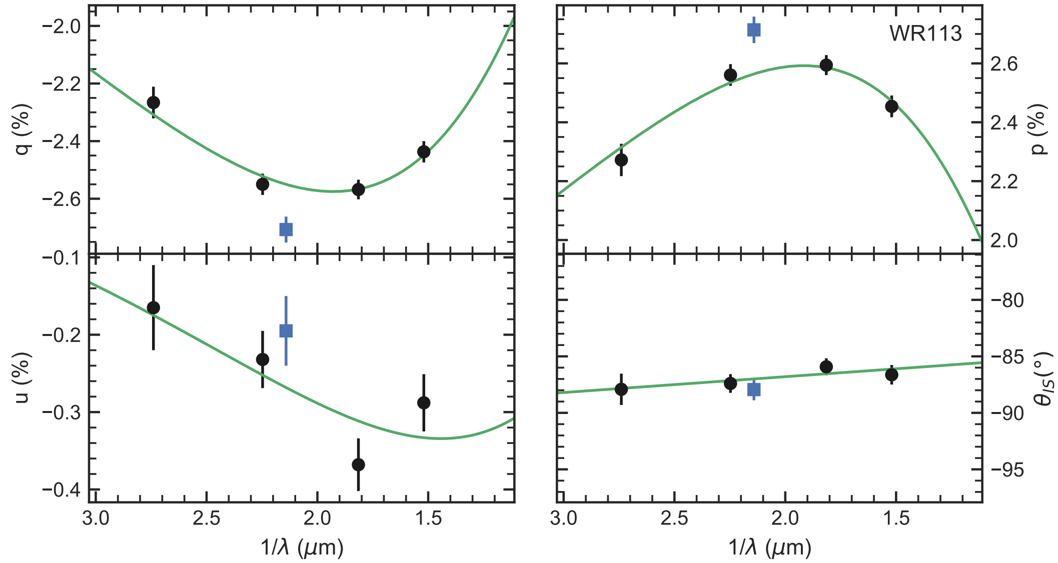

Figure A.32: $UBVRI$ data (black points) fit with equations 2.9 and 2.10 (green curves). b filter data are present as blue points, but were not included as part of the fit.

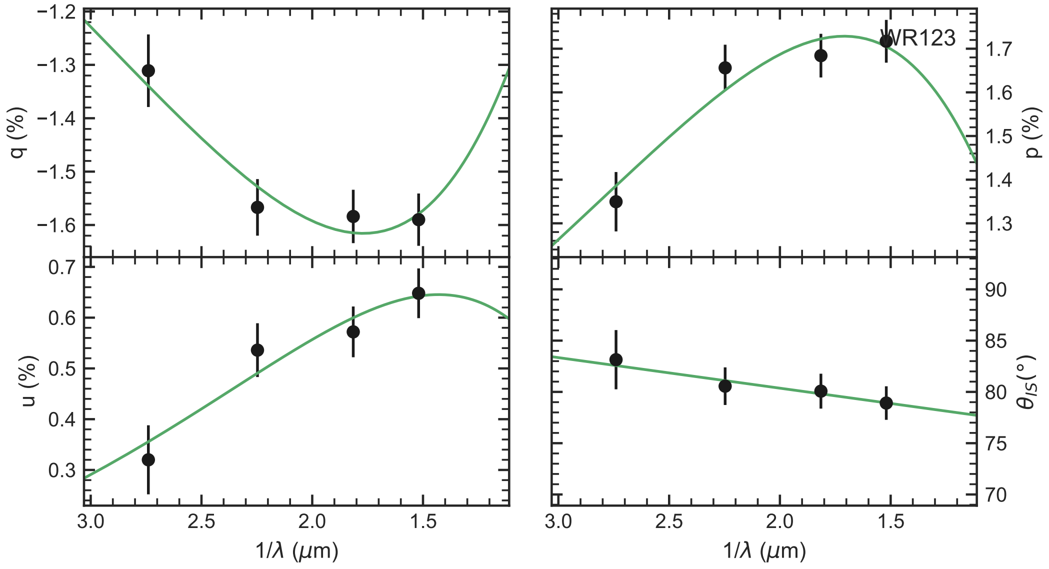

Figure A.33: $UBVRI$ data (black points) fit with equations 2.9 and 2.10 (green curves).

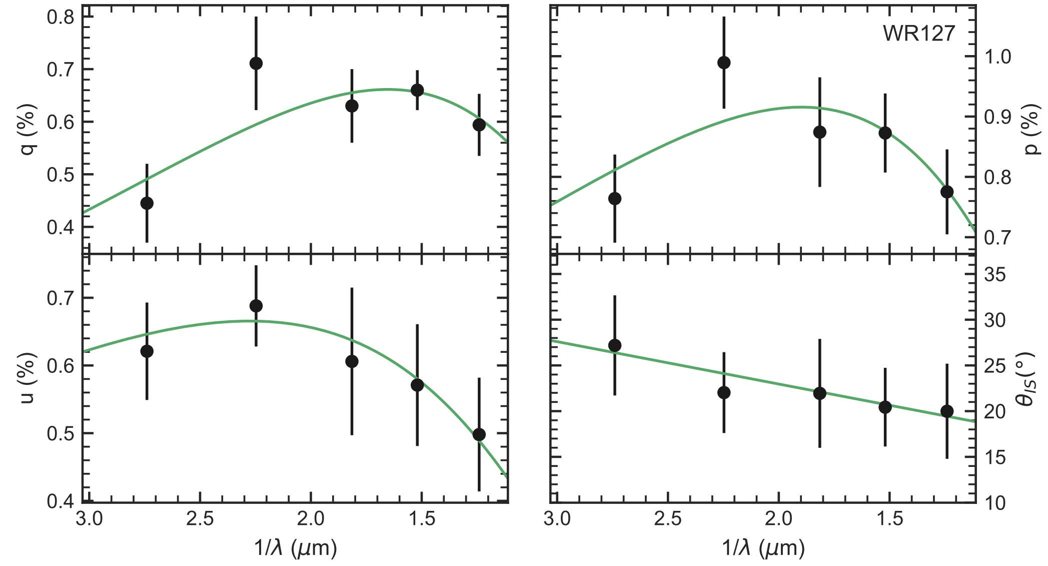

Figure A.34: $UBVRI$ data (black points) fit with equations 2.9 and 2.10 (green curves).

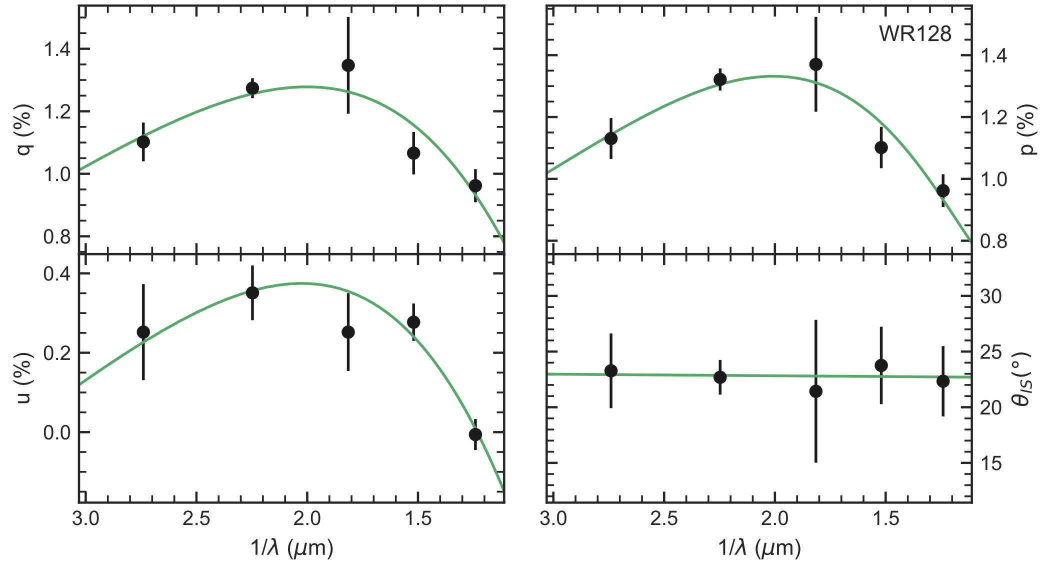

Figure A.35: $UBVRI$ data (black points) fit with equations 2.7 and 2.8 (green curves).

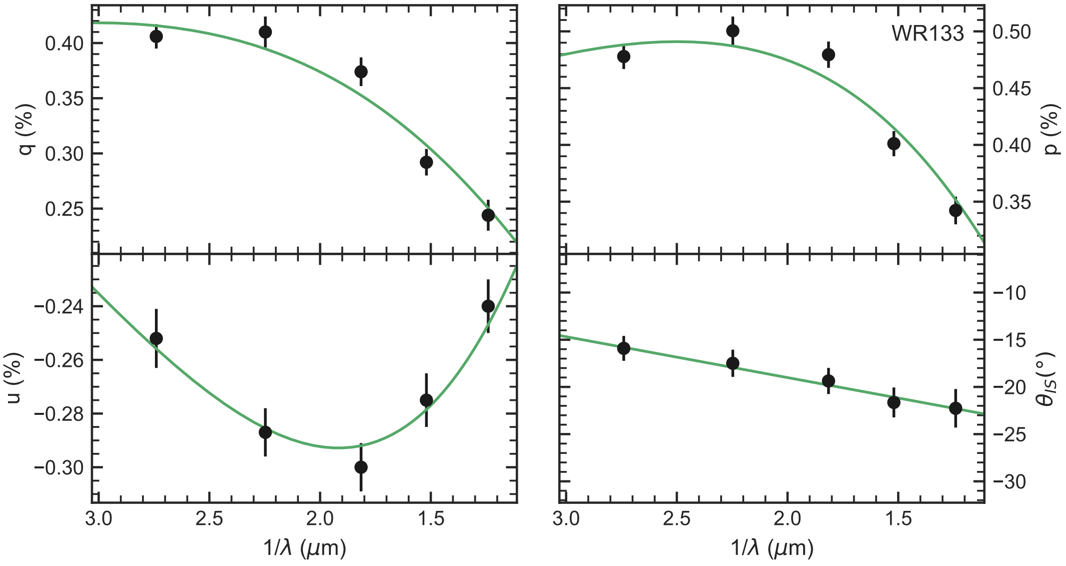

Figure A.36: $UBVRI$ data (black points) fit with equations 2.7 and 2.8 (green curves).

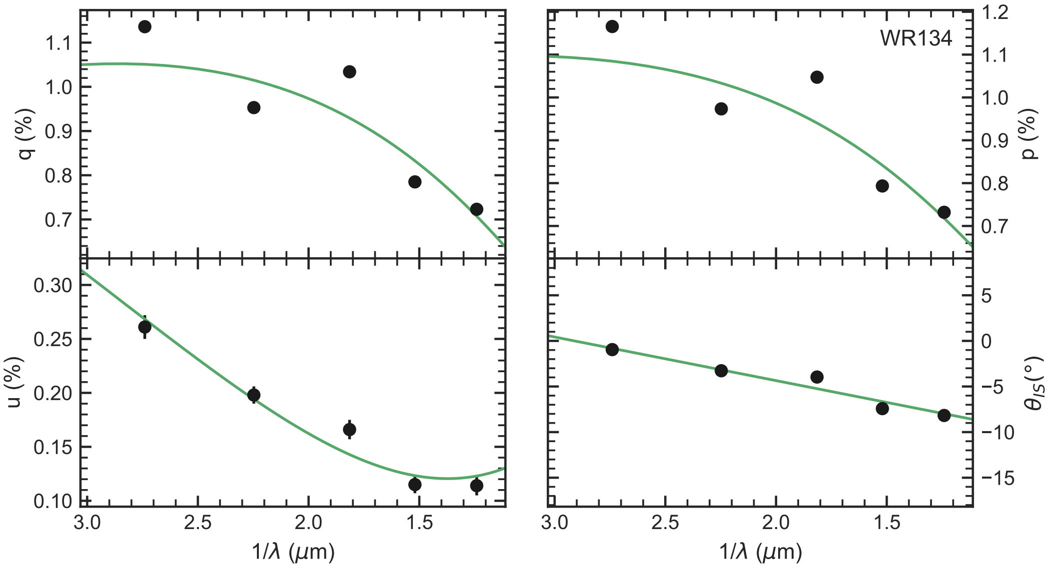

Figure A.37: $UBVRI$ data (black points) fit with equations 2.7 and 2.8 (green curves).

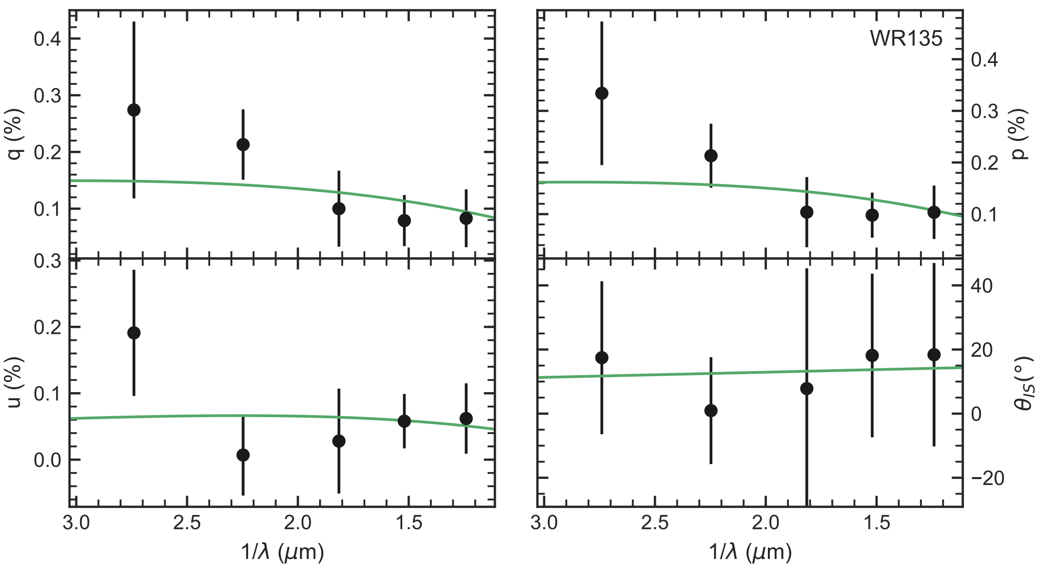

Figure A.38: $UBVRI$ data (black points) fit with equations 2.9 and 2.10 (green curves).

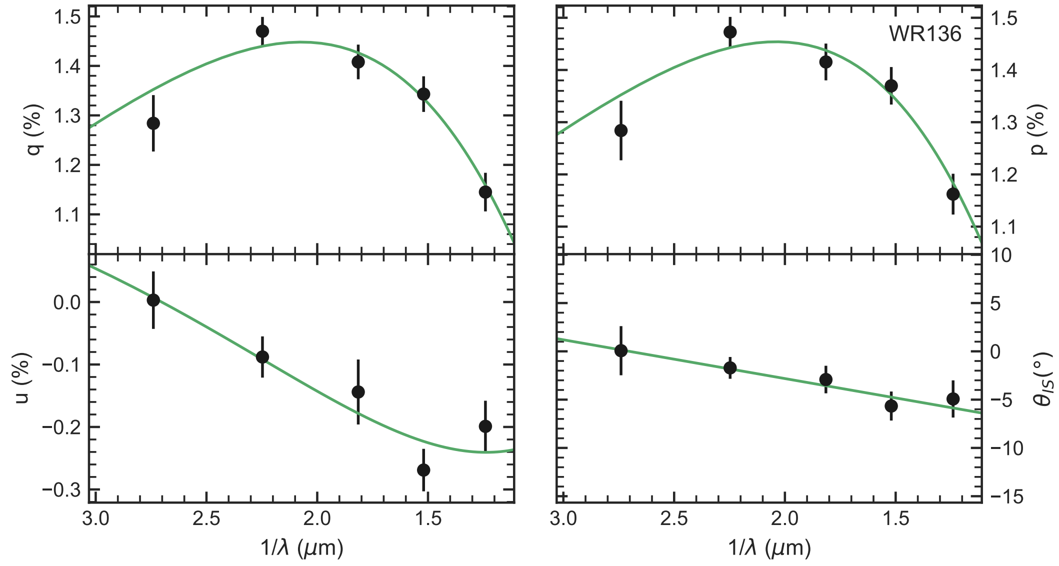

Figure A.39: $UBVRI$ data (black points) fit with equations 2.9 and 2.10 (green curves).

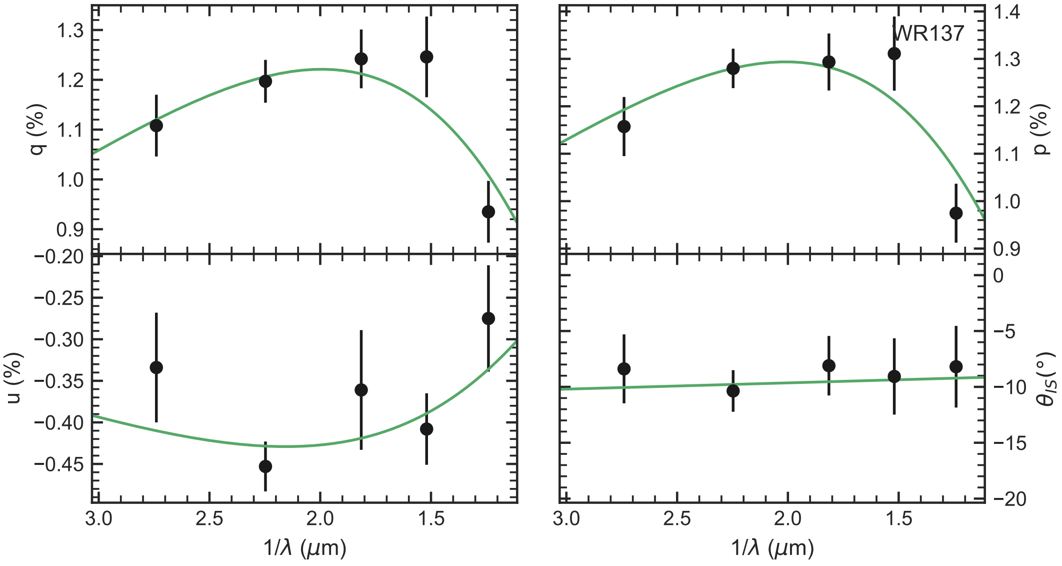

Figure A.40: $UBVRI$ data (black points) fit with equations 2.9 and 2.10 (green curves).

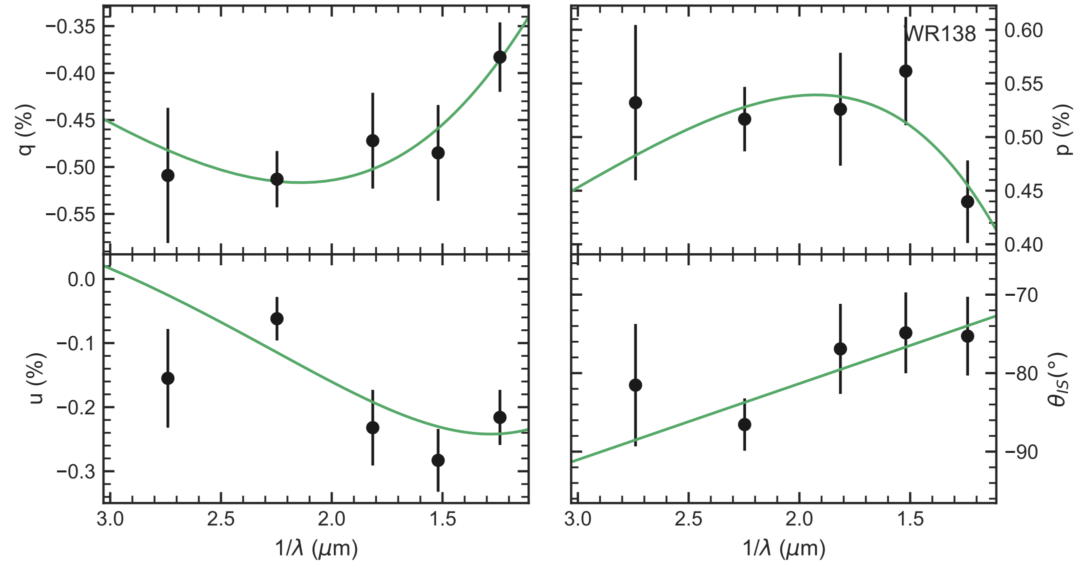

Figure A.41: $UBVRI$ data (black points) fit with equations 2.9 and 2.10 (green curves).

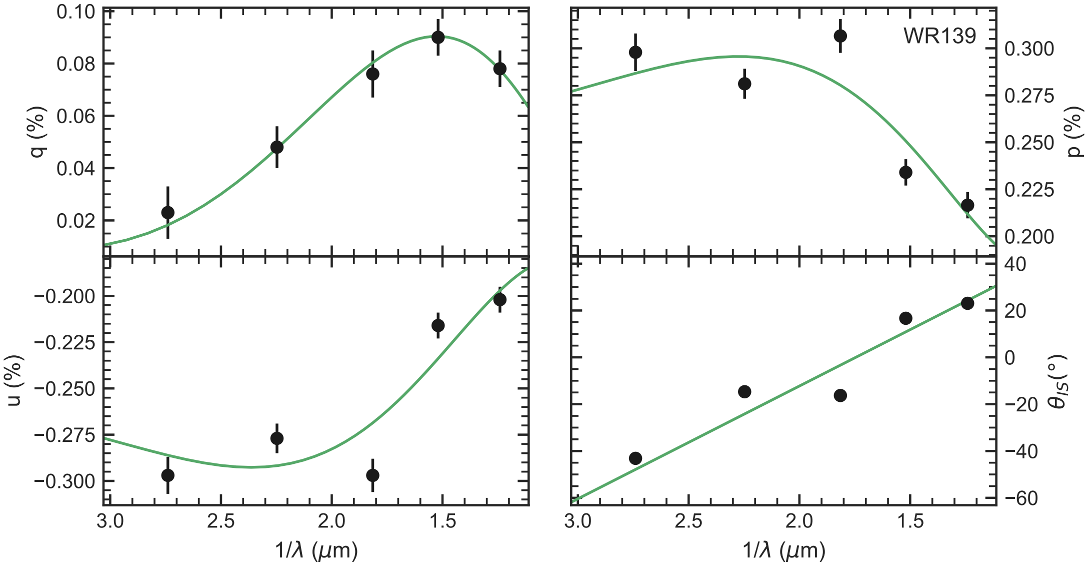

Figure A.42: $UBVRI$ data (black points) fit with equations 2.7 and 2.8 (green curves).

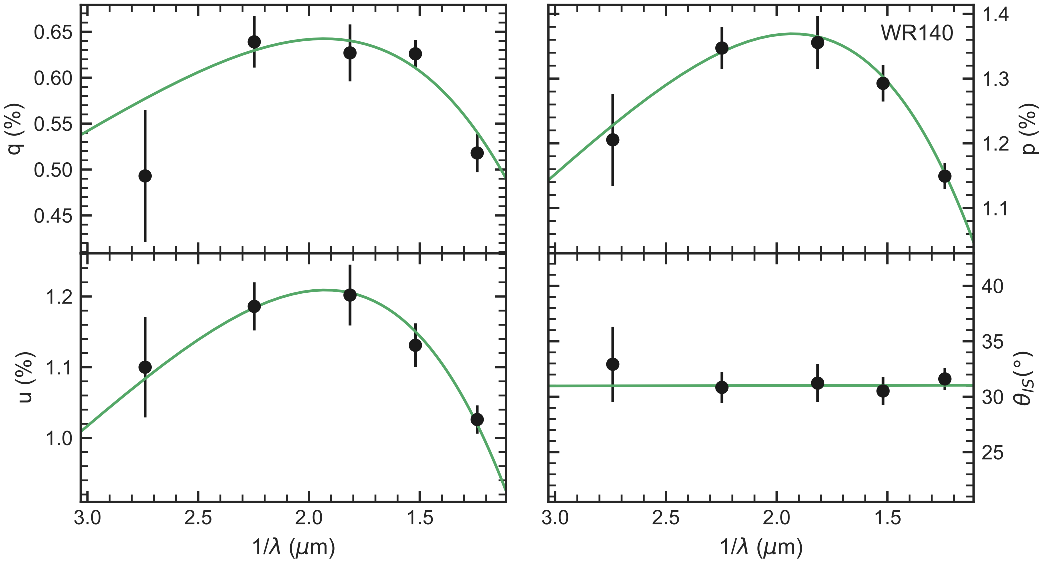

Figure A.43: $UBVRI$ data (black points) fit with equations 2.9 and 2.10 (green curves).

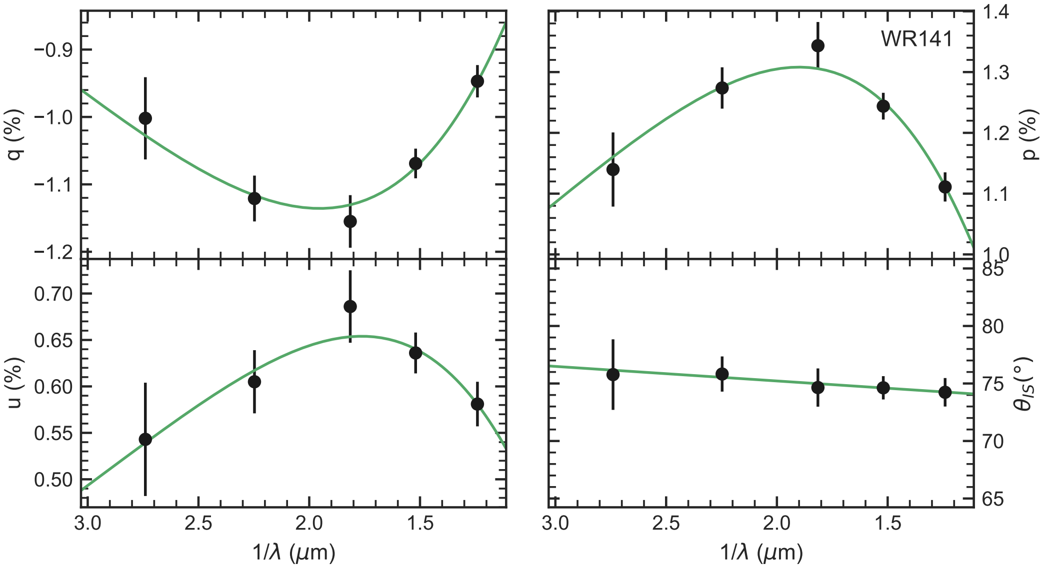

Figure A.44: $UBVRI$ data (black points) fit with equations 2.9 and 2.10 (green curves).

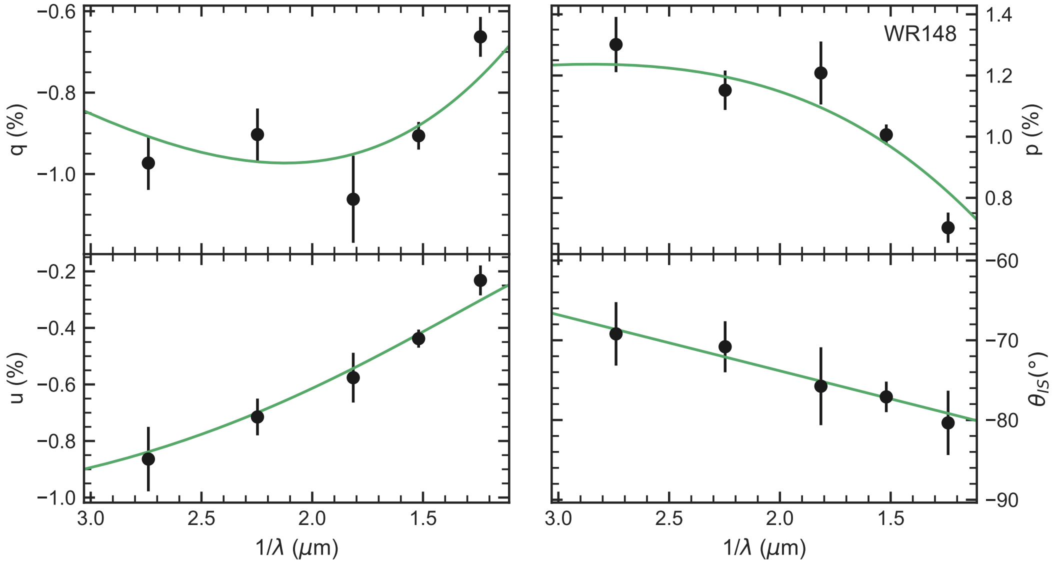

Figure A.45: $UBVRI$ data (black points) fit with equations 2.9 and 2.10 (green curves).

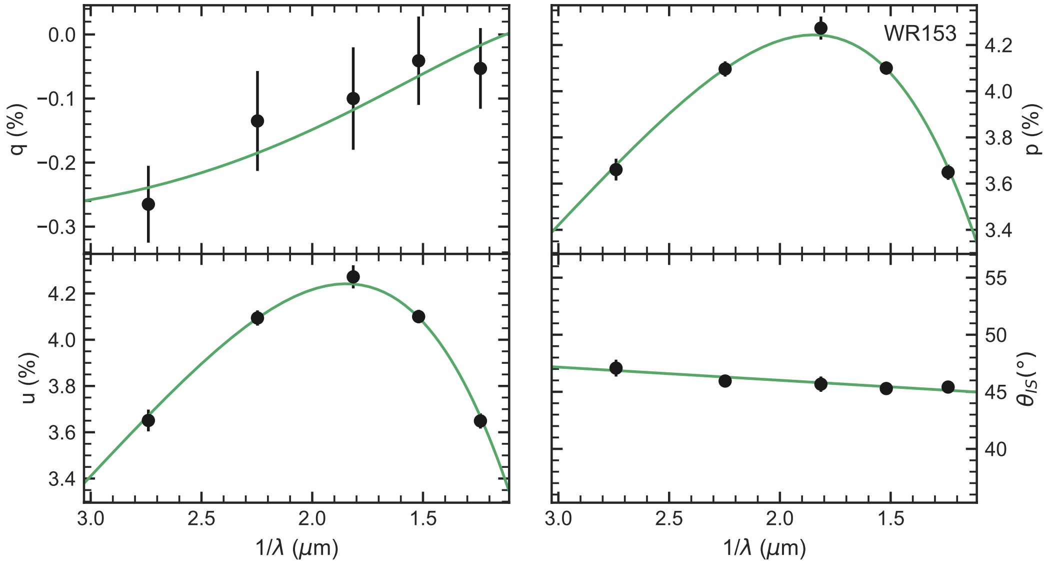

Figure A.46: $UBVRI$ data (black points) fit with equations 2.9 and 2.10 (green curves).

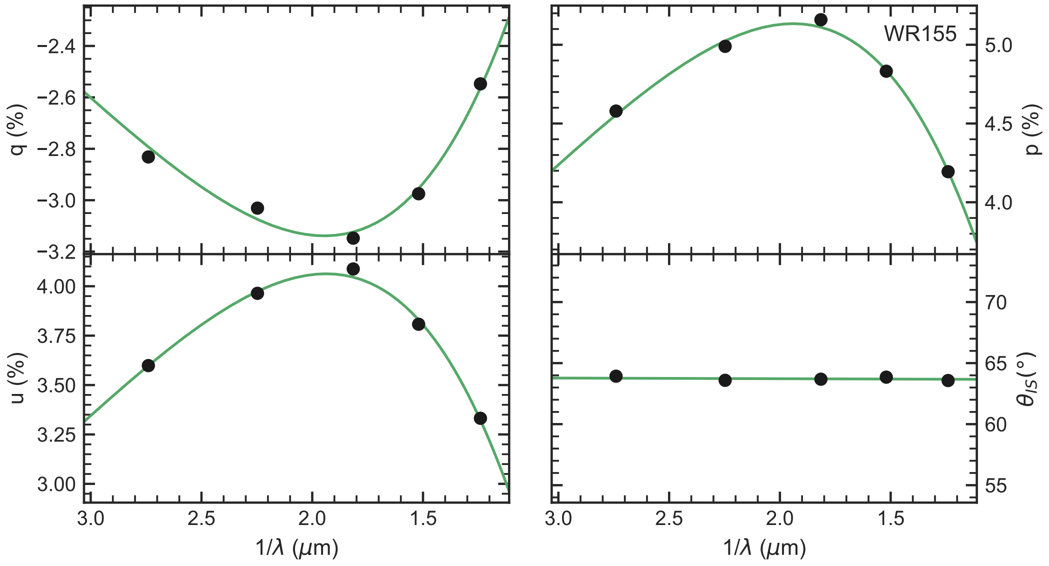

Figure A.47: $UBVRI$ data (black points) fit with equations 2.7 and 2.8 (green curves).

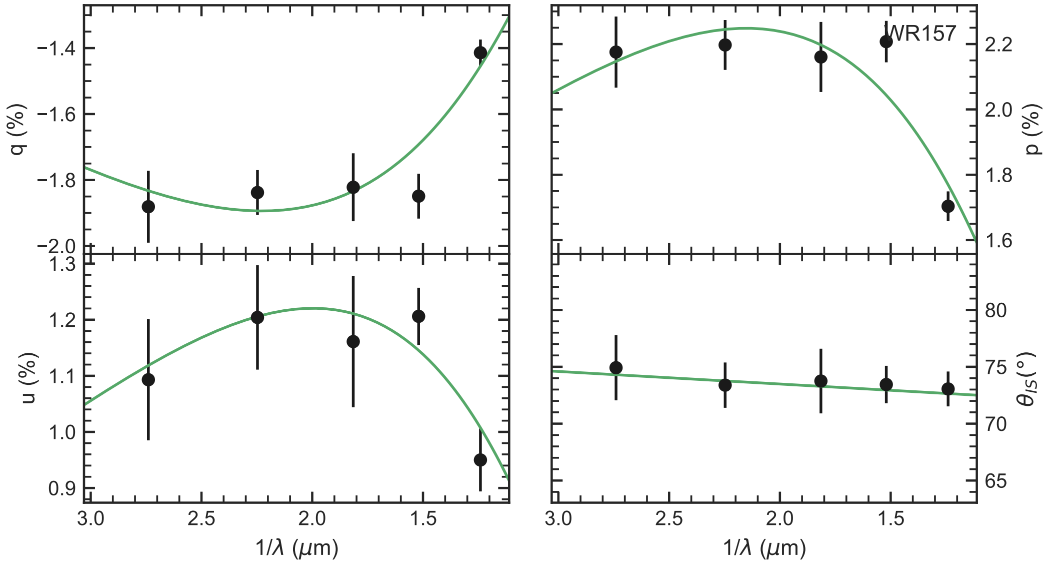

Figure A.48: $UBVRI$ data (black points) fit with equations 2.9 and 2.10 (green curves).